

**Studies on Catalytic Aerobic Oxidation of Organic Molecules:
Development in Activation of Molecular Oxygen and Substrates**

SHINYA FURUKAWA

Department of Molecular Engineering

Graduate School of Engineering

Kyoto University

2011

Preface

Chemical industry is essentially built on transformations of hydrocarbon-based feedstocks derived from petroleum, natural gas, coals, biomass, etc into high-value added products. Within the broad domain of organic molecule, oxygenated products such as alcohols, aldehydes, carboxylic acids, and epoxides are often used as essential building blocks in nearly all branches of industrial chemistry, ranging from polymer synthesis to medicinal chemistry. In this context, oxidation chemistry handling incorporation of oxygen into hydrocarbon and subsequent oxidative conversions, has performed a crucial function and role in industrial chemistry from the last century to today.

In most oxidation processes, an oxidizing agent plays a significant role because the efficiency and selectivity strongly depend on the choice of oxidant. Conventionally, a variety of oxidizing agent such as $K_2Cr_2O_7$, pyridinium chlorochromate and HNO_3 have been used for selective oxidations. Such oxidants, however, not only are toxic, corrosive, and expensive, but also yield equimolar amounts of environmentally-unfriendly wastes. Hydroperoxides such as cumenehydroperoxide and *t*-butylhydroperoxide are used in the field of epoxidation as less harmful oxidants due to production of alcohols as byproducts. Utilizing H_2O_2 as an oxidant is much more environmentally-benign process because it only produces water. But the use of these peroxide species inherently involves a risk of explosion. Moreover, a general problem of the aforementioned oxidants is that they are all manufactured via the oxidation of a precursor with oxygen. Ultimately, therefore, it is always O_2 , which takes up the stoichiometric number of electrons. Utilizing molecular oxygen as a sole oxidant would, in contrast, not only reduce the cost but also eliminate many environmental problems, which also meets the criterion from the viewpoint of green chemistry. However, the perspective of the use of molecular oxygen as an oxidant is not still satisfactory and realizing the effective use of molecular oxygen is even now challenging. The main reason may be that the reactions between molecular oxygen and hydrocarbons are usually very slow due to the fact that they are spin forbidden, or that nonselective radical oxidation often proceeds by reduced active oxygen species. Therefore, appropriate activation of molecular oxygen using a catalyst and successful inhibition of the nonselective radical oxidation are required for efficient aerobic oxidation.

Generally speaking, chemical transformation processes including oxidation consist of two different styles, homogeneous and heterogeneous systems. In homogeneous systems, relatively small molecules such as transition metal complexes, polyoxometalates, and organic compounds which can be dissolved in the reaction medium have been employed as catalysts. Among them, transition metal complexes have been most commonly used due to the variety of choices for metal element and the flexibility of molecular design to dictate the catalytic performance. Unfortunately, molecular catalysts, however, essentially have difficulty in separation of the catalyst from the reaction medium containing products. Moreover, high temperature is not permitted owing to solvent evaporation and thermal stability of catalysts. In heterogeneous systems, on the other hand, insoluble materials such as metal oxides, zeolites, and highly dispersed transition metals on support have been used as catalysts. These materials have practical advantages of not only separability and thermal stability but also reusability. But they have some disadvantages like difficulty in detailed structural design and construction of an active site and in elucidation of reaction mechanism of the catalysis. To develop more effective catalyst, it is significant to appropriately modify the structure of the catalyst and/or to understand the catalytic cycle in detail in both of homogeneous and heterogeneous systems.

In this context, the author developed two type of catalytic aerobic oxidation systems in the present study; homogeneous one using Fe(II) complexes and heterogeneous one based on Nb₂O₅ photocatalyst. In the former, activation of molecular oxygen was investigated from the viewpoints of electronic structure and coordination environment of Fe(II) center of the complex, so that aerobic oxidation of hydrocarbons without any reductant is established. Fine tuning of the electronic structures of the Fe(II) complexes and the effect on the catalytic activity were also studied. In the latter, enhancement in the photocatalytic activity and the selectivity was performed by the consideration of the kinetic aspect and by inhibition of the formation of active oxygen species, respectively. Furthermore, a comprehensive photoactivation mechanism in the photocatalysis of Nb₂O₅ was proposed and discussed in detail.

The studies presented in this thesis were performed at Department of Molecular Engineering, Graduate School of Engineering, Kyoto University from 2006 to 2011 under the supervision of Professor Tsunehiro Tanaka. The author wishes to express his sincere gratitude to Professor

Tsunehiro Tanaka for his exact guidance, fruitful discussions, insightful suggestions and valuable comments, throughout this study. The author makes grateful acknowledgements to Professor Tetsuya Shishido for his instructive discussions, warmhearted advices, and continual encouragement. The author's heartfelt appreciation goes to Professor Yutaka Hitomi at Doshisha University for his precise insight, beneficial suggestions, and helpful supports. The author thanks sincerely from his heart to Lecturer Kentaro Teramura for his valuable suggestions, informative advice, and cheerful messages. Special thanks are made to Professor Sakae Takenaka at Kyushu University for his helpful guidance and kind supports, especially in the measurement of XAFS. The author is deeply grateful to Professor Hiromi Yamashita at Osaka University and Professor Hisao Yoshida at Nagoya University for their fruitful suggestions and kind encouragement. A lot of thanks are dedicated to Dr. Seiji Yamazoe at Ryukoku University, Dr. Junya Ohyama at Nagoya University, and Mr. Toshiaki Miyatake, who were seniors of the laboratory the author belongs to, for their helpful discussions and advices. The author is grateful to Dr. Saburo Hosokawa, Professor Kenji Wada, and Professor Masashi Inoue for their aid in the measuring of X-ray photoelectron spectra. The author shows gratitude to the staffs of Photon Factory at KEK in Ibaraki Prefecture and Spring-8 in Hyogo Prefecture for their technical supports in XAFS measurement. In addition, a great acknowledgement should be shown to JSPS for a grant that made it possible to develop this study.

The author is indebted to Mses. Ayaka Tamura and Manami Satani and Messrs. Daisuke Tsukio and Yasuhiro Ohno for their collaborations and discussions on the studies of the selective photocatalytic oxidation based on Nb_2O_5 described in Part II. The author owes an important debt to Secretary Ms. Ayako Tanaka for her kind official support. The author is grateful to all the members of the group of catalysis research led by Professor Tanaka.

Finally, the author sincerely thanks his parents Taizo and Kayo for their understanding and cheering. The author also would like to express his deepest appreciation to his wife Yuko for her enduring supports, cheerful encouragement, and complete confidence.

Shinya Furukawa

Kyoto,

October, 2011

CONTENTS

Preface

Part I Homogeneous Oxidation Using Mononuclear Non-Heme Fe(II) Complexes

Introduction of Part I	2
Chapter 1 Aerobic Oxidation of Hydrocarbons by High-Spin Fe(II)–TPA Complexes Without Any Reductant	7
Chapter 2 Alkane Oxidation Catalyzed by Fe(II)–TPA Complex and Its Nitro-Substituted Derivatives	25
Chapter 3 Theoretical Study on Electronic Structure of Fe(II)–TPA Complex and Its Nitro-Substituted Derivatives	39

Part II Selective Oxidation Using Heterogeneous Nb₂O₅-Based Photocatalysts

Introduction of Part II	62
Chapter 4 Selective Photooxidation of Amines Using Nb ₂ O ₅	69
Chapter 5 Mechanism of Photooxidation of Hydrocarbons over Nb ₂ O ₅	97
Chapter 6 Solvent-free Aerobic Alcohol Oxidation Using Cu/Nb ₂ O ₅ : Green and Highly Selective Photocatalytic System	119
Chapter 7 Reaction Mechanism of Alcohol Photooxidation over Cu/Nb ₂ O ₅ : Roles of Cu in Enhancement of Photocatalytic Activity	133
Chapter 8 XAFS Study of Cu/Nb ₂ O ₅ : Effects of Electronic States of Cu on Photocatalytic Activity in Alcohol Photooxidation	159
Chapter 9 Selective Photooxidation of Alcohol over TiO ₂ Covered with Nb ₂ O ₅	175
Summary	195
List of publications	199

Part I

Homogeneous Oxidation Using Mononuclear Non-Heme Fe(II) Complexes

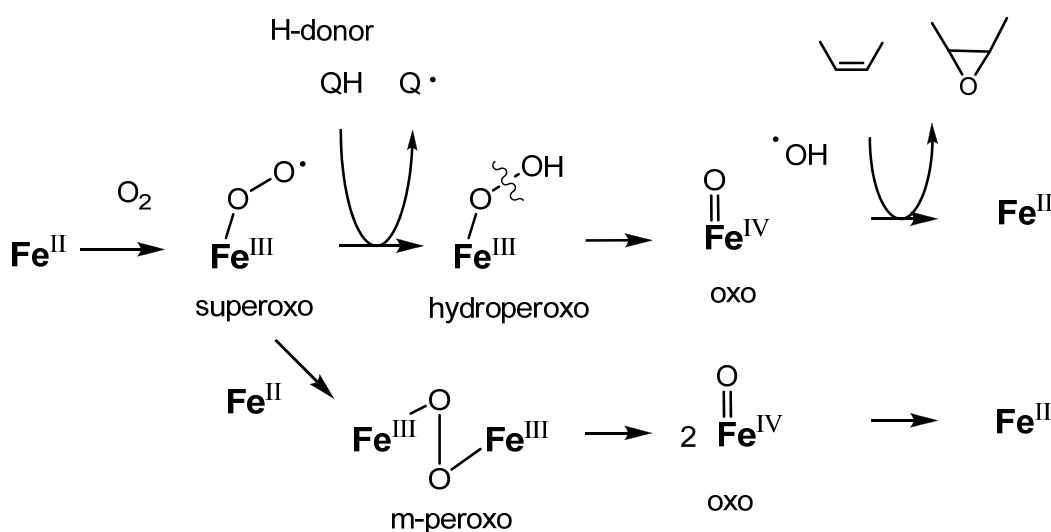
Introduction of Part I

In nature, a variety of oxidation processes using molecular oxygen such as, hydroxylation of hydrocarbons,¹ oxidative cleavage of aromatic rings,^{2,3} or DNA chains^{2,4} are performed under mild conditions by iron-containing enzymes or natural products. For instance, Rieske oxygenases and catechol dioxygenases,² which are mononuclear non-heme iron enzymes, catalyze hydroxylation of several substrates and oxidative cleavage of catechol aromatic rings in metabolic routes, respectively. A natural enzyme, however, generally has a huge molecular weight and can function only in aqueous conditions, which are bottlenecks in view of industrial application or fundamental research. Therefore, a lot of functional model complexes consisted of metal centers and tailor-made ligands which are soluble in organic solvent have been synthesized and investigated in this context.^{3,5,6} For example, mononuclear iron complex bearing a tripodal N4 ligand TPA (Tris(pyrid-2-ylmethyl)amine) and a catecholate is known to be a good functional model of the catechol dioxygenase.^{7,8} Among the researches based on model complexes, much attention has been focused on how to activate molecular oxygen or how to control the reactivity of active species.

Activation of Molecular Oxygen

Generally, molecular oxygen is reductively activated by a ferrous ion to generate superoxide and ferric ion or to form an Fe(III)-superoxo adduct, whereas a ferric ion does not react with molecular oxygen. In the system of an extradiol catechol dioxygenase, the resulting Fe(III)-superoxo species attacks the chelating catecholate followed by oxidative cleavage.² In other systems, the Fe(III)-superoxo species is further transformed into Fe(III)-hydroperoxo, Fe(III)- μ -peroxo dimer, or Fe(IV)-oxo species in a stepwise manner as shown scheme 1.^{5,9,10} High-valent oxo-iron species act as electrophilic oxidants and are active for O-transfer reaction such as sulfoxidation⁹ or olefin epoxidation.¹¹ To be active for the reduction of molecular oxygen, iron centers of the most enzymes and model complexes in the resting-state are indeed in ferrous state.² Cytochrome P450¹ and intradiol catechol dioxygenase² have ferric iron centers in their resting-states. But in the former case, the ferric ion is reduced when substrate comes close to the iron center because of increase in the redox potential of Fe(III)/Fe(II) couple caused by desorption of weakly coordinated water molecule.¹

In the latter case, the chelation of catechol to the ferric center provides an Fe(II)-semiquinonate character which allows to react with molecular oxygen.^{2,12,13} Reactivity of the model complex toward molecular oxygen has been systematically investigated in the light of electronic structure of the iron center. Fukuzumi et al. reported that the reduction potential of ferrous center was a key factor to activate molecular oxygen.¹⁴ Higuchi et al. studied the correlation between the reactivity and spin state of the iron center.^{12,13} A series of Fe(III)-catecholate complexes bearing TPA ligand with various substituents (MeO, H, Cl, NO₂) they employed shows spin crossover phenomenon; the fraction of high-spin species increased with increase in electron-donating ability of the substituent group. In addition, the rate of reaction between the complex and molecular oxygen increased as the fraction of high-spin species increased. This result emphasizes a significance of spin state in the process of dioxygen activation by iron complex.



Scheme 1. Activation of molecular oxygen and formation of active oxygen complexes.

Correlation between the Reactivity of Active Species and Its Electronic State

The reactivity of an iron complex toward substrate also strongly depends on the electronic state of the active oxidizing species. High-valent oxo-iron species are active oxidizing species for not only O-transfer reaction but also H-abstraction reaction. Actually in cyclohexene oxidation by Fe(IV)-oxo porphyrinato complexes,¹⁵ catalytic activity and selectivity to O-transfer product (cyclohexene oxide) or H-abstraction product (2-cyclohexene-1-ol and 2-cyclohexene-1-one) vary

with electron density of the iron center; the more iron porphyrin was electron deficient, the more selectivity to cyclohexene oxide was obtained. The different selectivity of epoxidation versus allylic oxidation was explained by the preference of two-electron reduction process (epoxidation) over one-electron reduction process (allylic oxidation), depending the electronic nature of iron porphyrin complexes. Thus in heme iron systems, the effect of electronic state of iron complex on the reactivity has been deeply investigated. In non-heme iron systems, on the other hand, such studies have been limited. Que et al. synthesized several Fe(II)–TPA complexes having a variety of functional groups at pyridyl moieties of the TPA ligand, and investigated their electronic states and the catalytic activities in alkane hydroxylation.¹⁶ But, the positions of substituent groups they chose were mainly 5- and 6- position of pyridyl ring, which are close to the iron center. Therefore, involvement of steric effect of the substituent in the electronic states did not allow revealing a good correlation between their electronic states and catalytic activities.

Survey of Part I

Although Fe(III)–TPA catecholate complexes conduct aerobic oxidative cleavage of catechol aromatic ring, this system does not respond to oxidation of other substrates. However, the activation of molecular oxygen and the formation of Fe(III)-superoxo species in this system implies the possibility of oxidation of other substrate such as hydrocarbon, if the chelating catecholate ligand is absent. In chapter 1, in this context, the author developed aerobic oxidation of hydrocarbons by using a series of high-spin Fe(II)–TPA complexes. The spin states of the Fe(II)–TPA complexes were controlled by modification of coordination environment such as counter anions and solvents. The author investigated the reaction mechanism of aerobic hydrocarbon oxidation by Fe(II)–TPA complexes and discussed the desired condition of the coordination environment.

In chapter 2, the author synthesized a series of mononuclear nonheme iron(II) complexes supported by TPA and its derivatives that have one to three nitro-groups at 4-position of the pyridine ligand, and evaluated the effect of the nitro-groups on the catalytic oxidation activity of these complexes. In this case, nitro-substitution at 4-position of the pyridine ligand seems to minimize the steric effect to the iron center and to enable a stepwise variation in the electronic state of the catalyst.

The spin crossover phenomenon observed with a series of Fe(III)–TPA catecholate complexes is counterintuitive in the light of coordination chemistry because introduction of electron-withdrawing groups generally makes high-spin state more favorable due to the weaker ligand field.^{17,18} But, an exact evaluation of the substitution effect was prevented by participation of spin crossover and a significant amount of Fe(II)-semiquinonate character of the Fe(III)-catecholate complex. In this context, it seems to be a promising approach to employ Fe(II)–TPA complex and its nitro derivatives which are predominantly in low-spin state. In chapter 3, the author investigated the effects of nitro-substitution to the Fe(II)–TPA complex on the electronic structure in more detail from both experimental and theoretical aspects.

References

- (1) Denisov, I. G.; Makris, T. M.; Sligar, S. G.; Schlichting, I. *Chem. Rev.* **2005**, *105*, 2253.
- (2) Que, L.; Ho, R. Y. N. *Chem. Rev.* **1996**, *96*, 2607.
- (3) Costas, M.; Mehn, M. P.; Jensen, M. P.; Que, L. *Chem. Rev.* **2004**, *104*, 939.
- (4) Burger, R. M. *Chem. Rev.* **1998**, *98*, 1153.
- (5) Nam, W. *Acc. Chem. Res.* **2007**, *40*, 522.
- (6) Rohde, J. U.; Bukowski, M. R.; Que, L. *Curr. Opin. Chem. Biol.* **2003**, *7*, 674.
- (7) Yamahara, R.; Ogo, S.; Masuda, H.; Watanabe, Y. *J. Inorg. Biochem.* **2002**, *88*, 284.
- (8) Jang, H. G.; Cox, D. D.; Que, L. *J. Am. Chem. Soc.* **1991**, *113*, 9200.
- (9) Kim, S. O.; Sastri, C. V.; Seo, M. S.; Kim, J.; Nam, W. *J. Am. Chem. Soc.* **2005**, *127*, 4178.
- (10) Lee, Y. M.; Hong, S.; Morimoto, Y.; Shin, W.; Fukuzumi, S.; Nam, W. *J. Am. Chem. Soc.* **2010**, *132*, 10668.
- (11) Groves, J. T.; Haushalter, R. C.; Nakamura, M.; Nemo, T. E.; Evans, B. J. *J. Am. Chem. Soc.* **1981**, *103*, 2884.
- (12) Higuchi, M.; Hitomi, Y.; Minami, H.; Tanaka, T.; Funabiki, T. *Inorg. Chem.* **2005**, *44*, 8810.
- (13) Hitomi, Y.; Yoshida, M.; Higuchi, M.; Minami, H.; Tanaka, T.; Funabiki, T. *J. Inorg. Biochem.* **2005**, *99*, 755.

- (14) Hong, S.; Lee, Y. M.; Shin, W.; Fukuzumi, S.; Nam, W. *J. Am. Chem. Soc.* **2009**, *131*, 13910.
- (15) Lim, M. H.; Jin, S. W.; Lee, Y. J.; Jhon, G. J.; Nam, W.; Kim, C. *Bull. Korean Chem. Soc.* **2001**, *22*, 93.
- (16) Chen, K.; Que, L. *J. Am. Chem. Soc.* **2001**, *123*, 6327.
- (17) Enamullah, M.; Linert, W. *J. Coord. Chem.* **1996**, *40*, 193-201.
- (18) Linert, W.; Enamullah, M.; Gutmann, V.; Jameson, R. F. *Monatsh. Chem.* **1994**, *125*, 661.

Chapter 1

Aerobic Oxidation of Hydrocarbons by High-Spin Fe(II)–TPA Complexes Without Any Reductant

Abstract

Fe(II)tris(2-pyridylmethyl)amine complexes, Fe(II)–TPA, having different co-existing anions, [Fe(TPA)(MeCN)₂](ClO₄)₂ (**1**), [Fe(TPA)(MeCN)₂](CF₃SO₃)₂ (**2**) and [Fe(TPA)Cl₂] (**3**), were prepared. Effective magnetic moments (evaluated by the Evans method) revealed that while **1–3** in acetone and **3** in acetonitrile (MeCN) have a high-spin Fe(II) ion at 298 K, the Fe(II) ions of **1** and **2** are in the low-spin state in MeCN. The aerobic oxidation of **1–3** was monitored by UV–Vis spectral changes in acetone or MeCN under air at 298 K. Only the high-spin Fe(II)–TPA complexes were oxidized with rate constants of $k_{\text{obs}} = 0.1\text{--}1.3 \text{ h}^{-1}$, while **1** and **2** were stable in MeCN. The aerobic oxidation of **1** or **2** in acetone was greatly accelerated in the presence of pure, peroxide-free cyclohexene (1000 equiv.) and yielded a large amount of oxidized products; 2-cyclohexene-1-ol (A) and 2-cyclohexene-1-one (K) (A+K: 23940% yield based on Fe; A/K = 0.3), and cyclohexene oxide (810%). Besides cyclohexene, aerobic oxidation of norbornene, cyclooctene, ethylbenzene, and cumene proceeded in the presence of **1** in acetone at 348 K without any reductant. Essential factors in the reaction are high-spin Fe(II) ion and labile coordination sites, both of which are required to generate Fe(II)-superoxo species as active species for the H-atom abstraction of hydrocarbons.

Introduction

The catalytic oxidation of hydrocarbons such as alkanes, alkenes and aromatic compounds to oxygen-containing materials is one of the most important chemical transformations in industrial chemistry.¹ For economic and environmental reasons, the use of dioxygen as sole oxidant is highly desirable.² Since it reacts slowly with hydrocarbons owing to its triplet ground state, appropriate activation of dioxygen is required for efficient oxidation of hydrocarbons using dioxygen. In nature, such dioxygen activation is performed by iron- and/or copper-dependent enzymes such as cytochrome P450,³ methane monooxygenase,⁴ tyrosinase,⁵ dopamine β -monooxygenase⁶ and various types of mononuclear nonheme iron dioxygenases,⁷ where dioxygen is reductively activated via the Cu(I) or Fe(II) ion(s). It is noteworthy that a high-spin Fe(II) center activates dioxygen in heme and nonheme iron-dependent enzymes⁸ and model complexes.^{9–11}

Previously, we reported that low spin Fe(III)–TPA catecholate complexes (TPA: tris(2-pyridylmethyl)amine, Figure 1) have a lower dioxygen reactivity than the high-spin species, even though the former has a much higher Fe(II)-semiquinolate character.¹² This result motivated us to examine the spin-state dependency on the dioxygen activation ability of simple Fe(II)–TPA complexes. Diebold and Hagen reported that the spin state of the Fe(II)–TPA complex is different depending on its counter anions.¹³ Therefore, we prepared three Fe(II)–TPA complexes; [Fe(TPA)(MeCN)₂](ClO₄)₂ (**1**), [Fe(TPA)(MeCN)₂](CF₃SO₃)₂ (**2**) and [Fe(TPA)Cl₂] (**3**), and examined their spin states and dioxygen activation ability. We also examined the aerobic oxidation of hydrocarbons in the presence of the Fe(II)–TPA complexes.

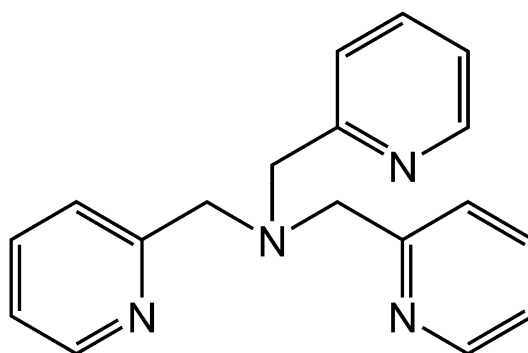


Figure 1. Structure of the tpa ligand.

Experimental

Materials

The TPA ligand was synthesized according to published procedures.¹² All other reagents and dehydrated solvents were purchased from commercial sources. All dehydrated solvents were deoxygenated by N₂ bubbling prior to use. Treatment of the TPA ligand with Fe(ClO₄)₂, Fe(OTf)₂ and FeCl₂ in MeCN gave the corresponding complexes **1–3** as crystalline solids in high yield.

[Fe(TPA)(MeCN)₂](ClO₄)₂ (**1**): ESI-MS calcd. (found): *m/z* 193.6 (193.5) ([Fe^{II}(TPA)(MeCN)]²⁺)

[Fe(TPA)(MeCN)₂](OTf)₂ (**2**): ESI-MS calcd. (found): *m/z* 193.6 (193.5) ([Fe^{II}(TPA)(MeCN)]²⁺)

[Fe(TPA)Cl₂] (**3**): ESI-MS calcd. (found): *m/z* 381.1 (381.4) ([Fe^{II}(TPA)Cl]⁺)

Physical methods

Electrospray ionization mass spectrometry (ESI-MS) spectra were recorded on a PE SCIEX API 2000 mass spectrometer. ¹H and ¹⁹F NMR spectra were recorded on a JEOL ECX400P spectrometer; chemical shifts for ¹H and ¹⁹F NMR are referenced to tetramethylsilane and trifluoroacetic acid, respectively. UV–Vis spectra were recorded on a Hitachi UV-3000 spectrophotometer.

Aerobic oxidation of hydrocarbons

Oxygen was bubbled for 1 min into 5 ml of 1.0 mM Fe(II)–TPA complex solution containing 1000 equiv. of hydrocarbon as substrate, followed by vigorous stirring under 1 atm O₂ in a batch reactor tube equipped with an O₂ balloon. Organic products were analyzed by FID–GC (Shimadzu GC-14B) and GC–MS (Shimadzu GC-MS QP5050). Prior to use, substrates were dried over molecular sieves 4 A and deoxygenated by N₂ bubbling. 2-Butanone was used instead of acetone for the reaction at 348 K to avoid boiling.

Results and discussion

Characterizations of Fe(II)–TPA complexes

The effective magnetic moments of complexes **1–3** were measured in acetonitrile (MeCN) and acetone by the Evans NMR method.¹⁴ The μ_{eff} values, listed in Table 1, indicate that **1** and **2** possess mainly a low spin Fe(II) ion in MeCN, whereas **3** is in the high-spin state in MeCN. The spin states of Fe(II)–TPA type complexes in MeCN have been widely investigated.^{13,15–17} The present results in MeCN are well consistent with the reported data.^{13,15,16} In contrast, all the Fe(II) ions of **1–3** were in the high-spin states in acetone. The complexes **1** and **2** are known to be in the low spin state in the solid state.^{13,15} Therefore, the high spin state in acetone suggests the dissociation of coordinated π -accepting ligand MeCN. Then, we conducted ¹⁹F and ¹H NMR study to clarify the coordination environment of the Fe(II) complex in acetone. The chemical shift of the fluorine atom of triflate anion with paramagnetic Fe(II) complex widely varies based on the chemical environment; ca. +60 (bridging triflate), ca. –10 (terminal) and ca. –80 ppm (free triflate).^{18,19} The ¹⁹F NMR spectrum of **2** in acetone-d₆ exhibited a single broad peak at –41.4 ppm (Figure 2, $\nu_{1/2}$ = 1036 Hz), which suggest that the triflate anions weakly coordinated to Fe(II) and they are equivalent.^{16,20} The observed line broadening indicates a fast exchange between coordinated and free triflate anions.¹⁶ In addition, the ¹H NMR spectrum of **2** in acetone-d₆ shows that the all three pyridylmethyl moieties are equivalent (Figure 3), suggesting a fast exchange between a six-coordinate and a five-coordinate conformation as proposed with the similar Fe(II) complexes by Britovsek et al.,¹⁶ which is shown in Scheme 1a. The electronic states of **1–3** in solution were also investigated by UV-Visible absorption spectroscopy (Table 1). Intense MLCT bands were observed for **1** and **2** in MeCN, but the MLCT bands for **1** and **2** in acetone were weaker in intensity. The MLCT bands of **3** were weak in intensity in both MeCN and acetone, similar to those observed for **1** and **2** in acetone. Thus, the intensity of the MLCT band was higher with low-spin Fe(II)–TPA complexes than with the high-spin. The similar correlation between intensity of the MLCT band and spin states of Fe(II) complexes has been reported by Britovsek et al. without rationale.¹⁶ The correlation suggests that the low spin complex

has the stronger interactions between $d\pi$ and pyridine π^* orbitals compared with the high-spin complexes.

The preferential high spin state of **1** and **2** in acetone can be rationalized by coordination of the counter anions to the Fe(II) ion in acetone. On the other hand, the solvent-independent high spin state of **3** suggests that the two coordinated chloride ions of **3** are not exchanged by MeCN or acetone and result in the Fe(II) ion being in a high spin state.²¹

Table 1. UV-visible absorption properties, effective magnetic moments, rate constant of oxygen activation (k_{obs}) and catalytic activity of cyclohexene oxidation (TON) of Fe(II)-tpa complexes **1–3** in solution states.

entry	solvent	complex	$\lambda_{\text{max}} (\epsilon)^a$	$\mu_{\text{eff}}(\mu_{\text{B}})$	$k_{\text{obs}}(\text{h}^{-1})$	TON ^b
1		1	368 sh, 398 (6379), 506 (150)	0.740	0 ^c	8.7
2	acetonitrile	2	368 sh, 398 (6608), 521 (141)	0.834	0 ^c	8.8
3		3	426 (1468)	5.29	0.529	1.3
4		1	362 (1268)	5.07	1.28	239
5	acetone	2	364 (1476)	5.33	0.118	253
6		3	470 (1331)	5.46	0.311	0.1

^a Units of $\text{M}^{-1}\text{cm}^{-1}$. ^b TON was defined as mol of products (2-cyclohexene-1-ol and 2-cyclohexene-1-one)/mol of complex (5 μmol) after 24 h. ^c No spectral change was observed after 24 h. In the absence of the catalyst, only a small amount of product was evolved (15 μmol in acetone after 24 h).

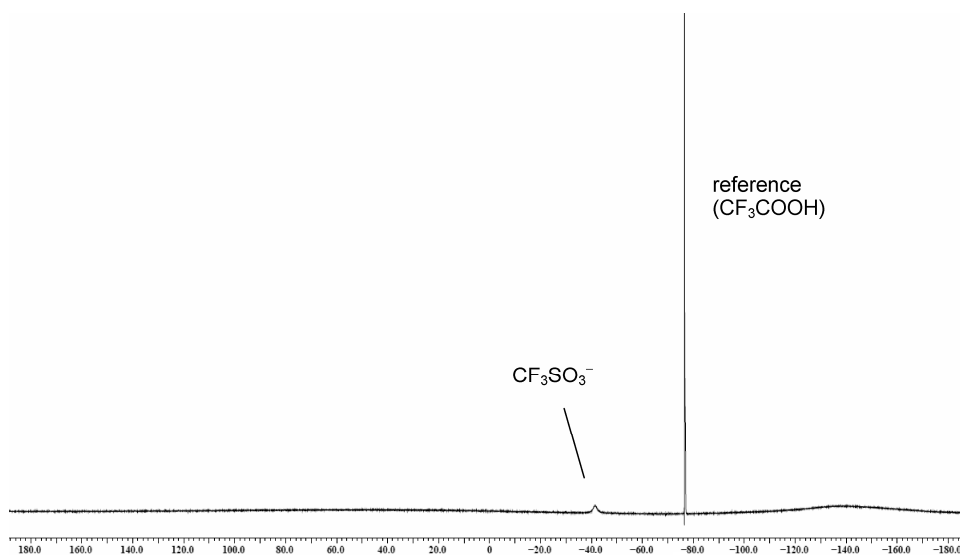


Figure 2. ^{19}F NMR spectrum of **2** in acetone- d_6 .

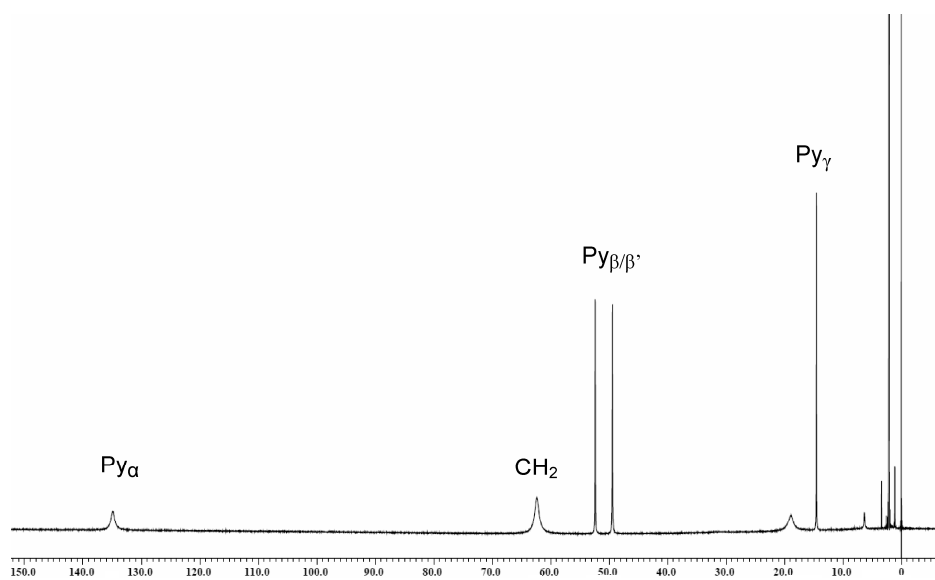


Figure 3. ^1H NMR spectrum of **2** in acetone- d_6 .

Reaction with dioxygen

The reactions of **1–3** with dioxygen were examined by UV-visible spectroscopy. In MeCN, only **3** showed a spectral change upon reaction with O₂ (Figure 4), while **1** and **2** did not show any spectral changes for at least one day. The MLCT band of **3** disappeared in a first-order decay fashion with an isosbestic point at 413 nm over several hours. The observed first-order rate constant k_{obs} is comparable with the reported value (0.68 h⁻¹) by Thallaj et al. (Table 1).¹⁷ In acetone, in contrast to MeCN, all complexes reacted with dioxygen (Table 1). These results clearly show the higher dioxygen reactivity of high spin Fe(II)–TPA complexes rather than low spin. Mandon and his co-workers has proposed that Fe(II)–TPA chloride complex (here in **3**) reacts with dioxygen in a dissociative fashion.^{17,22,23} Our NMR study also supports the possible coordination of dioxygen to Fe(II) in five-coordinate (Scheme 1b). Interestingly, the k_{obs} value of **2** in acetone is smaller than that of **3** in acetone or MeCN, which is contrary to the order of binding strength of the counter anion. This may be due to the difference in steric hindrance between bulky triflate and chloride. The fact that **1**, which has the most weakly coordinating counter anions, showed the fastest oxidation reaction rate indicates that **1** was oxidized preferentially through the formation of a dioxygen adduct of the Fe(II) complex, that is, an Fe(III)-superoxo species (Scheme 1b).^{9,11,24,25} The Fe(III)-superoxo might convert to Fe(III) and superoxide in the presence of a nucleophile such as chloride (Scheme 1c), as found for the autooxidation of oxymyoglobin and oxyhemoglobin.²⁶

Aerobic oxidation of alkenes in the presence of the Fe(II) complexes

To examine the effect of the Fe(III)-superoxo species on the aerobic oxidation of alkenes, we first chose cyclohexene as a substrate with weak allylic C-H bonds; bond dissociation energy (BDE) = 81 kJ/mol.²⁷ The aerobic oxidation of cyclohexene was carried out in the presence of **1–3** (0.1 mol%) both in MeCN and acetone. Gas chromatography analysis of the products revealed that **1** and **2** are capable of promoting aerobic oxidation of cyclohexene in acetone but not in MeCN (Table 1). Thus, these results clearly indicate that the high-spin Fe(II)–TPA complex can be a good promoter in the aerobic oxidation of cyclohexene. Complex **1** gave allylic oxidation products of cyclohexene, 2-cyclohexen-1-ol and 2-cyclohexene-1-one, (y. 23940% based on Fe), and cyclohexene oxide (y. 810%) in acetone after 24 h. The alcohol/ketone (A/K) ratio was ca. 1.0 at the beginning and

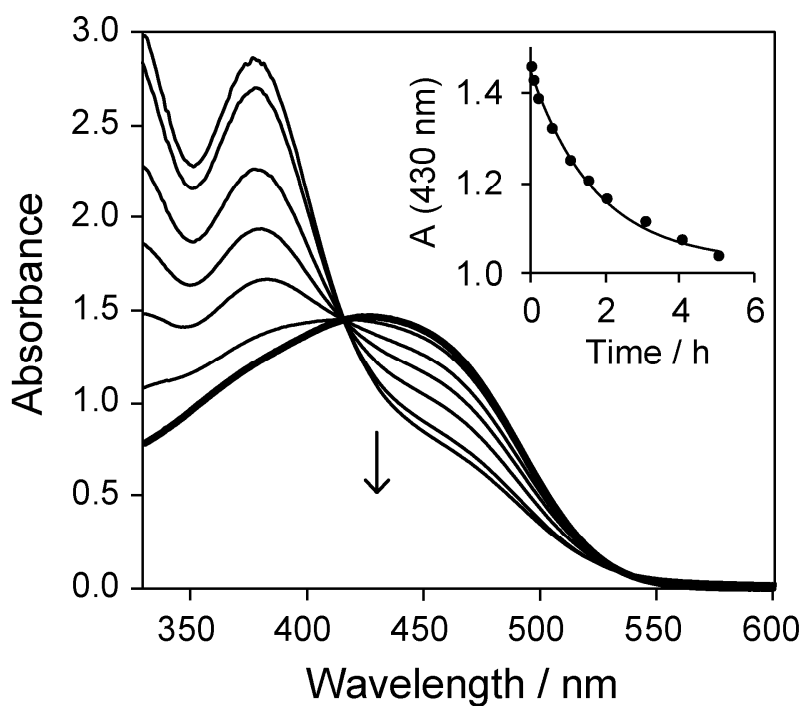
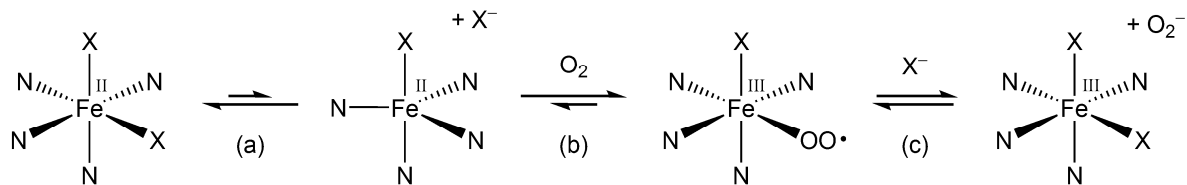


Figure 4. UV-visible spectral changes of **3** in MeCN upon the reaction with O₂. Inset: change in absorbance with time at 430 nm and fitted curve.



Scheme 1. Reaction of dioxygen with the Fe(II) centre via dissociative mechanism; (a) fast ligand exchange, (b) coordination of dioxygen and (c) release of superoxide.

decreased to 0.3 as the reaction proceeded (Figure 5). The decrease in A/K ratio from 1.0 indicates that the allylic oxidation occurs via a radical auto-oxidation process, followed by over-oxidation of the alcohol to ketone by radicals or other oxidants. Production of cyclohexene oxide, however, implies that metal-based oxidants are also formed during the oxidation reaction. Interestingly, **3** is virtually ineffective in initiating the aerobic oxidation of cyclohexene in both MeCN and acetone (Table 1). Thus, these results suggest that labile coordination sites on the high-spin Fe(II) center are a requisite for efficient aerobic oxidation of cyclohexene. In the presence of **1**, oxidation of other alkenes and alkanes with weak or moderate C–H BDE (81–97 kJ/mol) were also examined, whose results are listed in Table 2. At 298 K, cumene (BDE: 83 kJ/mol)²⁸ was oxidized; however, hydrocarbons with C–H BDE of more than 85 kJ/mol such as cyclooctene (85 kJ/mol),²⁷ ethylbenzene (86 kJ/mol)²⁷ and norbornene (97 kJ/mol)²⁹ were intact under these conditions. The latter hydrocarbons were oxidized when the temperature was elevated to 348 K in 2-butanone. The product yield in the oxidation of cumene was effectively enhanced with increase in temperature. These results clearly show that the C–H activation of hydrocarbon is the key step in the catalytic system.

Reaction mechanism

Next, we monitored UV-visible absorption spectral changes of **1** in the presence of cyclohexene in acetone. The abundance fraction of Fe(II) species estimated by intensity of the MLCT band is plotted against reaction time in Figure 6. The Fe(II) species disappeared within 5 s with a small induction period in the presence of cyclohexene, which is significantly faster than the oxidation rate of **1** in the absence of cyclohexene (ca. 2 min). These results indicate that cyclohexene-derived radicals induce the oxidation of Fe(II) species. We propose that H-atom abstraction from cyclohexene by an Fe(III)-superoxo species is the key step in producing cyclohexene-derived radicals, which quickly oxidize Fe(II) species (Scheme 2). The radicals generated would propagate the radical chain oxidation of cyclohexene. Thus, the observed induction period corresponds to the initial dioxygen activation step. The fact that **3** was aerobically oxidized but did not initiate the aerobic oxidation of cyclohexene implies that Fe(III)-superoxo species immediately converts to Fe(III) and superoxide by nucleophilic attack of the chloride anion as discussed above.

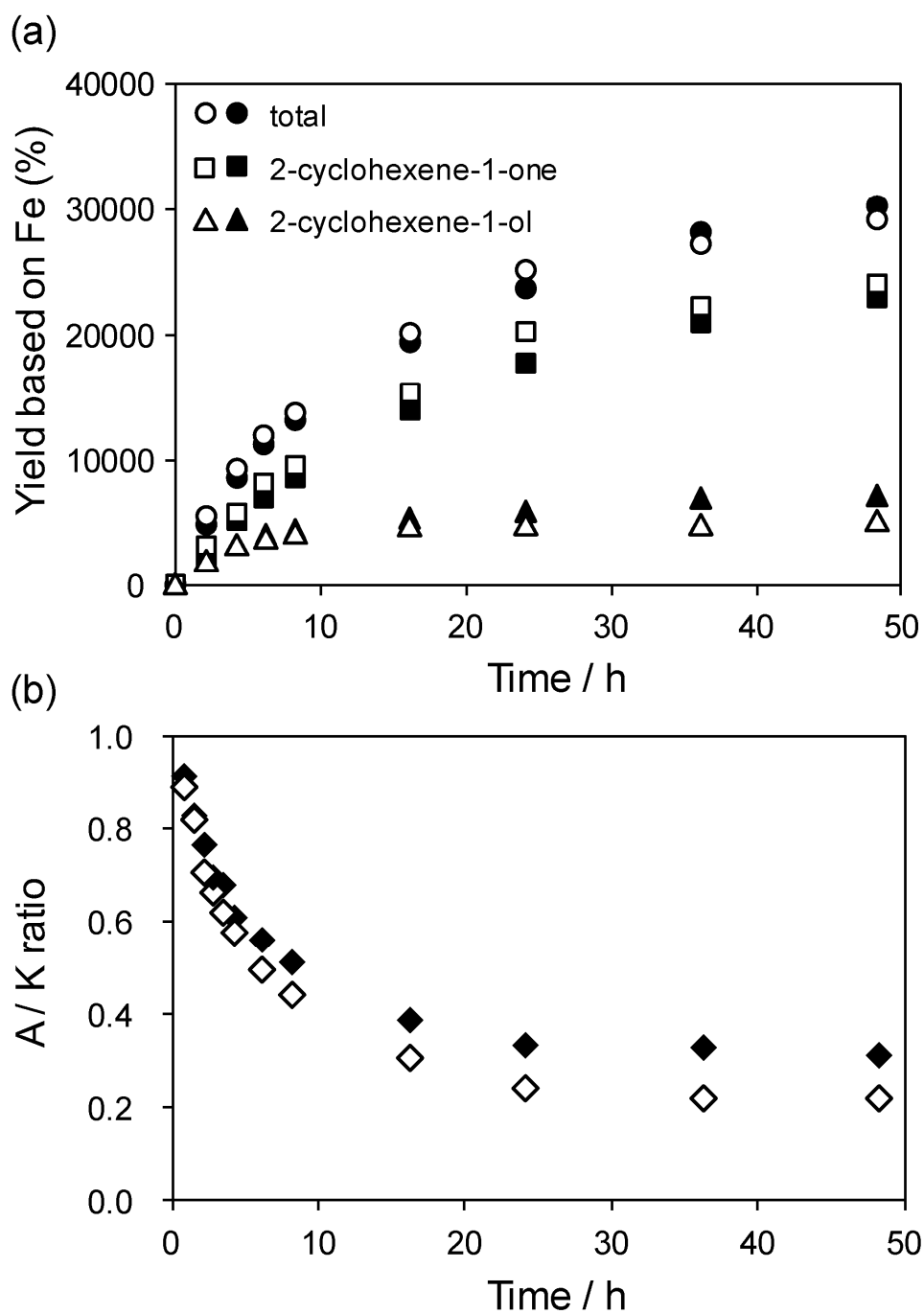


Figure 5. Time course of (a) product yield based on Fe and (b) A/K ratios in the oxidation of cyclohexene with **1** (filled symbols) and **2** (open symbols) in acetone.

Table 2. Product yields in the aerobic oxidation of hydrocarbons in the presence of **1**.

substrate	solvent	T / K	product	yield (%) ^a	sel. (%)	
norbornene ^b	2-butanone	348	norbornene oxide	18340	51 ^c	
cyclooctene	2-butanone	348	cyclooctene oxide	12300	21	
			1,2-cyclooctanediol	13250	23	
			cyclooctanone	14830	26	
cyclohexene	acetone	298	cyclohexene oxide	810	2.9	
			2-cyclohexene-1-ol	6070	22	
			2-cyclohexene-1-one	17870	64	
ethylbenzene	2-butanone	348	acetophenone	2000	54	
			1-phenylethanol	1700	32	
cumene	2-butanone	348	acetophenone	2200	93	
			cumylalcohol	100	4.0	
			acetophenone	940	72	
	acetone	313	313	cumylalcohol	360	28
				acetophenone	130	50
				cumylalcohol	130	50

^a Based on Fe (5 μ mol) after 24 h of reaction. ^b 2100 equiv. of norbornene used. ^c Several byproducts also detected.

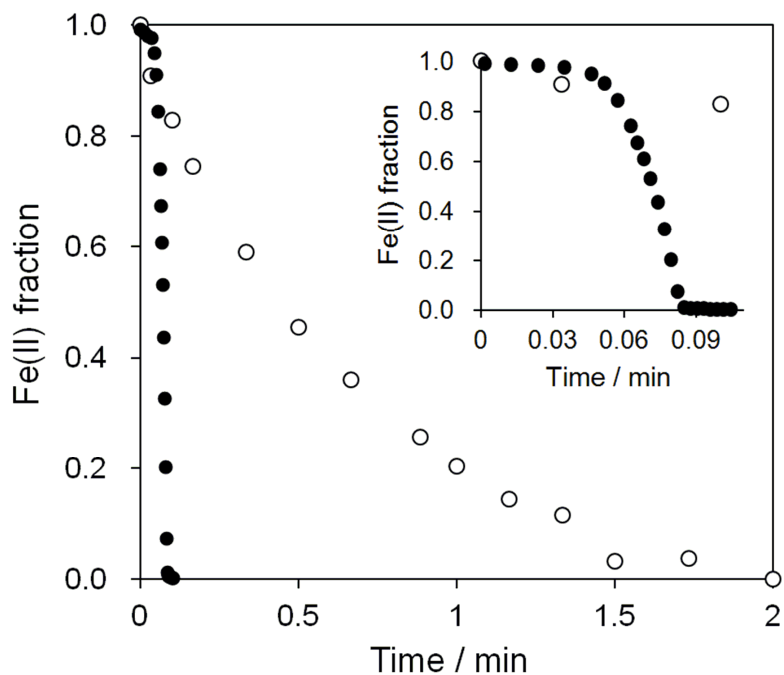
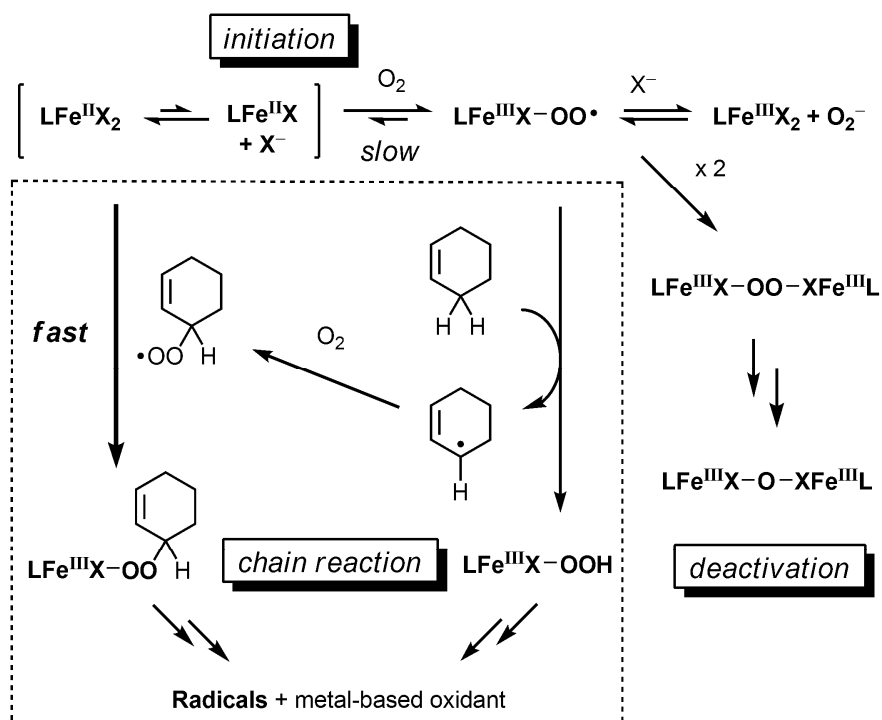


Figure 6. Change in fraction of Fe(II) species with time during oxidation of **1** in acetone in the presence (filled circle) or absence (open circle) of cyclohexene upon the reaction with O₂. The fraction of Fe(II) species was calculated from the MLCT band intensity. Inset shows the initial phase.



Scheme 2. Proposed reaction paths in the initial phase of oxidation of **1** in the presence of cyclohexene.

Superoxide has been reported to perform H-atom abstraction only from weak N–H³⁰ and O–H³¹ bonds. The Fe(III)-superoxo species is also likely to generate a μ -peroxo dimer, followed by formation of a μ -oxo dimer as widely invoked in aerobic oxidation of heme and non-heme Fe(II) complexes.^{32–34} The formation of stable μ -oxo dimer can finally lead to deactivation of the catalysis.

Que and his co-workers have been studying hydrocarbon oxidation catalyzed by the Fe(II)–TPA complex and its derivatives with H₂O₂ or *t*BuOOH as oxidant.^{21,35,36} Recently, they reported that Fe(III)-hydroperoxo and -alkylperoxo species supported by the TPA ligand were transformed to Fe(IV)-oxo species in acetone.³⁷ Production of cyclohexene oxide supports the generation of Fe(IV)-oxo species in our system, although the aerobic oxidation mainly proceeds via radical chain oxidation, as shown by the A/K ratio.

The reactivity of metal-superoxo species involved in hydrocarbon oxidation reactions has attracted much attention recently in the field of bioinorganic chemistry, since Cu(II)-superoxide species have been postulated to initiate H-atom abstraction from substrates in the catalytic cycles of copper-dependent enzymes such as dopamine β -monooxygenase and peptidylglycine α -hydroxylating monooxygenase (PHM),^{38–40} and the Fe(III)-superoxo species have been proposed as active species in a di-iron-dependent enzyme, *myo*-inositol oxygenase.^{41,42} It has been reported by using model complexes that Cu(II)-superoxo species can perform H-atom abstraction from weak O–H and N–H bonds.^{43–45} Recently, Itoh and co-workers synthesized a series of Cu(II) end-on superoxo species which mimic a tetrahedral geometry in the X-ray structure of oxy-PHM reported by Amzel and co-workers,^{46,47} and demonstrated that this species also mimics the H-atom abstraction from aliphatic C–H bonds.⁴⁷ H-atom abstraction by Fe(III)-superoxo species had been reported rarely, but recently, Fukuzumi and Nam et al. reported that Fe(III)-superoxo species generated in the reaction of the mononuclear nonheme Fe(II) complex with dioxygen performs H-atom abstraction from cycloalkenes.^{48,49} We believe that the same mechanism should be operative in the aerobic oxidation reaction promoted by **1** in acetone.

Conclusions

We found that aerobic oxidation of alkenes was efficiently promoted by the Fe(II)–TPA complex, when the Fe center was in the high-spin state. It is noteworthy that the aerobic oxidation proceeded without any reductants, since most of the aerobic oxidation systems catalyzed by heme or nonheme iron complexes require stoichiometric co-reductants such as aldehydes and Zn/AcOH.⁵⁰ We propose that an Fe(III)-superoxo species is a key intermediate in the efficient aerobic oxidation of alkenes. The essential factor in the reaction is the presence of labile coordination sites that provides stable coordination of dioxygen, giving Fe(III)-superoxo species active for the H-atom abstraction; the strong interaction of MeCN with the low-spin iron(II) center would prevent the formation of the Fe(III)-superoxo species, and chloride ion may shorten the life-time of the Fe(III)-superoxo species probably through nucleophilic attack. Thus, the ligand-exchange chemistry including dioxygen should be of important in the performance of the efficient aerobic oxidation.⁵¹ Consequently, high-spin Fe(II)–TPA complexes except for the chloride complex effectively initiated aerobic oxidation of hydrocarbons. We will further study the relationship between spin state and dioxygen activation ability.

References

- (1) Franz, G.; Sheldon, R.A. *Ullmann's encyclopedia of industrial chemistry*, Wiley-VCH, Weinheim, 2005.
- (2) Hermans, I.; Spier, E.S.; Neuenschwander, U.; Turra, N.; Baiker, A. *Top. Catal.* **2009**, *52*, 1162.
- (3) Sono, M.; Roach, M.P.; Coulter, E.D.; Dawson, J.H. *Chem. Rev.* **1996**, *96*, 2841.
- (4) Wallar, B.J.; Lipscomb, J.D. *Chem. Rev.* **1996**, *96*, 2625.
- (5) Solomon, E.I.; Sundaram, U.M.; Machonkin, T.E. *Chem. Rev.* **1996**, *96*, 2563.
- (6) Stewart, L.C.; Klinman, J.P. *Annu. Rev. Biochem.* **1988**, *57*, 551.
- (7) Que, L.; Ho, R.Y.N. *Chem. Rev.* **1996**, *96*, 2607.

- (8) De La Lande, A.; Salahub, D.R.; Maddaluno, J.; Scemama, A.; Pilme, J.; Parisel, O.; Gerard, H.; Caffarel, M.; Piquemal, J.-P. *J. Comput. Chem.* **2010**, *32*, 1178.
- (9) Thibon, A.; England, J.; Martinho, M.; Young, V.; G. Frisch, J.; R. Guillot, R.; Girerd, J.J.; Munck, E.; Que, L.; Banse, F. *Angew. Chem. Int. Ed.* **2008**, *47*, 7064.
- (10) Benhamou, L.; Machkour, A.; Rotthaus, O.; Lachkar, M.; Welter, R.; Mandon, D. *Inorg. Chem.* **2009**, *48*, 4777.
- (11) Martinho, M.; Blain, G.; Banse, F. *Dalton Trans.* **2010**, *39*, 1630.
- (12) Higuchi, M.; Hitomi, Y.; Minami, H.; Tanaka, T.; Funabiki, T. *Inorg. Chem.* **2005**, *44*, 8810.
- (13) Diebold, A.; Hagen, K.S. *Inorg. Chem.* **1998**, *37*, 215.
- (14) Evans, D.F. *J. Chem. Soc.* **1959**, 2003.
- (15) Zang, Y.; Kim, J.; Dong, Y.; Wilkinson, E.C.; Appelman, E.H.; Que, L. *J. Am. Chem. Soc.* **1997**, *119*, 4197.
- (16) Britovsek, G.J.P.; England, J.; White, A.J.P. *Inorg. Chem.* **2005**, *44*, 8125.
- (17) Thallaj, N.K.; Rotthaus, O.; Benhamou, L.; Humbert, N.; Elhabiri, M.; Lachkar, M.; Welter, R.; Albrecht-Gary, A.-M.; Mandon, D. *Chem. Eur. J.* **2008**, *14*, 6742.
- (18) Blakesley, D.W.; Payne, S.C.; Hagen, K.S. *Inorg. Chem.* **2000**, *39*, 1979.
- (19) Börzel, H.; Comba, P.; Hagen, K.S.; Lampeka, Y.D.; Lienke, A.; Linti, G.; Merz, M.; Pritzkow, H.; Tsybmal, L.V. *Inorg. Chim. Acta* **2002**, *337*, 407.
- (20) Jensen, M.P.; Lange, S.J.; Mehn, M.P.; Que, E.L.; Que, L. *J. Am. Chem. Soc.* **2003**, *125*, 2113.
- (21) Kojima, T.; Leising, R.A.; Yan, S.P.; Que, L. *J. Am. Chem. Soc.* **1993**, *115*, 11328.
- (22) Wane, A.; Thallaj, N.K.; Mandon, D. *Chem. Eur. J.* **2009**, *15*, 10593.
- (23) Jaafar, H.; Vileno, B.; Thibon, A.; Mandon, D. *Dalton Trans.* **2011**, *40*, 92.
- (24) Simaan, A.J.; Dopner, S.; Banse, F.; Bourcier, S.; Bouchoux, G.; Boussac, A.; Hildebrandt, P.; Girerd, J.J. *Eur. J. Inorg. Chem.* **2000**, 1627.
- (25) Lefevre-Groboillot, D.; Boucher, J.L.; Mansuy, D.; Stuehr, D.J. *Febs J.* **2006**, *273*, 180.
- (26) Shikama, K. *Cell. Mol. Life Sci.* **1985**, *41*, 701.

- (27) Luo, Y.-R. *Handbook of Bond Dissociation Energies in Organic Compounds*, CRC Press, Boca Raton, 2003.
- (28) Feng, Y.; Gunnoe, T.B.; Grimes, T.V.; Cundari, T.R. *Organometallics* **2006**, *25*, 5456.
- (29) Nunes, P.M.; Estacio, S.G.; Lopes, G.T.; Agapito, F.; Santos, R.C.; Cabral, B.J.C.; dos Santos, R.M.B.; Simoes, J.A.M. *J. Phys. Chem. A* **2009**, *113*, 6524.
- (30) Bernhard, P.; Anson, F.C. *Inorg. Chem.* **1988**, *27*, 4574.
- (31) Frimer, A.A.; Marks, V.; Gilinskysharon, P.; Aljadeff, G.; Gottlieb, H.E. *J. Org. Chem.* **1995**, *60*, 4510.
- (32) Collman, J.P. *Acc. Chem. Res.* **1977**, *10*, 265.
- (33) Balch, A.L.; Chan, Y.W.; Cheng, R.J.; La Mar, G.N.; Latos-Grazynski, L.; Renner, M.W. *J. Am. Chem. Soc.* **1984**, *106*, 7779.
- (34) Kurtz, D.M.; *Chem. Rev.* **1990**, *90*, 585.
- (35) Chen, K.; Que, L. *J. Am. Chem. Soc.* **2001**, *123*, 6327.
- (36) Chen, K.; Costas, M.; Kim, J.H.; Tipton, A.K.; Que, L. *J. Am. Chem. Soc.* **2002**, *124*, 3026.
- (37) Payeras, A.M.I.; Ho, R.Y.N.; Fujita, M.; Que, L. *Chem. Eur. J.* **2004**, *10*, 4944.
- (38) Chen, P.; Solomon, E.I. *Proc. Nat. Acad. Sci.* **2004**, *101*, 13105.
- (39) Itoh, S. *Curr. Opin. Chem. Biol.* **2006**, *10*, 115.
- (40) Klinman, J.P. *J. Biol. Chem.* **2006**, *281*, 3013.
- (41) Xing, G.; Diao, Y.H.; Hoffart, L.M.; Barr, E.W.; Prabhu, K.S.; Arner, R.J.; Reddy, C.C.; Krebs, C.; Bollinger, J.M. *Proc. Nat. Acad. Sci.* **2006**, *103*, 6130.
- (42) Hirao, H.; Morokuma, K. *J. Am. Chem. Soc.* **2009**, *131*, 17206.
- (43) Maiti, D.; Fry, H.C.; Woertink, J.S.; Vance, M.A.; Solomon, E.I.; Karlin, K.D. *J. Am. Chem. Soc.* **2007**, *129*, 264.
- (44) Fujii, T.; Yamaguchi, S.; Hirota, S.; Masuda, H. *Dalton Trans.* **2008**, 164.
- (45) Maiti, D.; Lee, D.H.; Gaoutchenova, K.; Wurtele, C.; Holthausen, M.C.; Sarjeant, A.A.N.; Sundermeyer, J.; Schindler, S.; Karlin, K.D. *Angew. Chem. Int. Ed.* **2008**, *47*, 82.
- (46) Prigge, S.T.; Eipper, B.A.; Mains, R.E.; Amzel, L.M. *Science* **2004**, *304*, 864.

- (47) Kunishita, A.; Kubo, M.; Sugimoto, H.; Ogura, T.; Sato, K.; Takui, T.; Itoh, S. *J. Am. Chem. Soc.* **2009**, *131*, 2788.
- (48) Hong, S.; Lee, Y.M.; Shin, W.; Fukuzumi, S.; Nam, W. *J. Am. Chem. Soc.* **2009**, *131*, 13910.
- (49) Lee, Y.M.; Hong, S.; Morimoto, Y.; Shin, W.; Fukuzumi, S.; Nam, W. *J. Am. Chem. Soc.* **2010**, *132*, 10668.
- (50) Punniyamurthy, T.; Velusamy, S.; Iqbal, J. *Chem. Rev.* **2005**, *105*, 2329.

Chapter 2

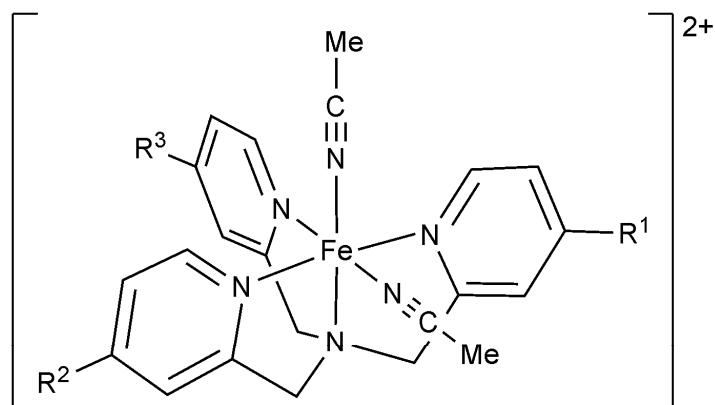
Alkane Oxidation Catalyzed by Fe(II)–TPA Complex and Its Nitro-Substituted Derivatives

Abstract

We have prepared a series of mononuclear nonheme iron(II) complexes supported by TPA (TPA= tris(2-pyridylmethyl)amine) and its derivatives that have one to three nitro-groups at 4-position of the pyridine ligand, and evaluated the effect of the nitro-groups on the catalytic oxidation activity of these complexes. The introduction of nitro-group to the TPA ligand proved to decrease the product yield of cyclohexane oxidation with hydrogen peroxide as well as the product ratio of alcohol to ketone. During the catalytic reaction, a significant amount of Fe(II) species exists in cases of nitro-substituted complexes, while the parent Fe–TPA complex was rapidly oxidized to Fe(III) state. These results suggest that the introduction of nitro-groups prevents from the generation of *cis*-oxo-hydroxo-iron(V) species, but induces homolysis of the Fe O bond of Fe(III)OOH species to initiate radical oxidation of cyclohexane.

Introduction

Mononuclear nonheme iron enzymes catalyze the selective oxidation of unactivated organic substrate under ambient conditions,¹ most of which are still rather difficult tasks for man-made catalysts. For example, naphthalene dioxygenase is able to perform *cis*-dihydroxylation of the aromatic ring of naphthalene,² but such a type of oxidation reactions has never been archived by any catalysts and oxidants. To mimic the oxidation ability of these enzymes, a number of nonheme iron complexes have been synthesized and examined as catalysts for oxidation reactions.³⁻⁵ One of intriguing successes is *cis*-dihydroxylation of alkenes catalyzed by Fe-TPA complex (TPA= tris(2-pyridylmethyl)amine), which was discovered by Que and co-workers in 1999.⁶ Their mechanistic and theoretical studies indicated the involvement of *cis*-oxohydroxo-iron(V) species as an oxidant for *cis*-dihydroxylation.⁷⁻¹¹ The same system, i.e., the reaction with hydrogen peroxide catalyzed by Fe-TPA complex, was also applied for alkane hydroxylation.¹²⁻¹⁴ Although the turnover number was moderate, the reaction took place through hydrogen atom abstraction by a metal based oxidant, *cis*-oxo-hydroxo-iron(V) species. In this study, we focused on the effect of substituent groups on the TPA ligand on the catalytic alkane hydroxylation, since modification of the electronic structure of *cis*-oxo-hydroxo-iron(V) species should make a great impact on the catalytic activity in alkane hydroxylation. Very recently, a theoretical study, that supports our idea, was reported by Ma and Balubuena.¹⁵ In this report, they have proposed that the reactivity of *cis*-oxo-hydroxo-iron(V) species for the hydrogen atom abstraction could be enhanced by introducing electron-withdrawing groups to the aromatic rings of TPA. Enhancement of oxidation power of the active species might enable us to oxidize substrates otherwise difficult to be oxidized, such as methane. Herein, we have synthesized a series of iron(II) complexes (Figure 1, **1-4**) supported by TPA and nitro-substituted TPA ligands, and evaluated how the introduction of nitro-groups to TPA ligand affects the catalytic activity of **1-4** in cyclohexane oxidation with hydrogen peroxide. The introduction of nitro-groups at 4-position of the pyridine ligand of TPA has an advantage in being able to modulate only electronic, but not steric factors that should control the reactivity of metal complexes.¹⁶⁻²¹



- 1:** $R^1 = H, R^2 = H, R^3 = H$
2: $R^1 = NO_2, R^2 = H, R^3 = H$
3: $R^1 = NO_2, R^2 = NO_2, R^3 = H$
4: $R^1 = NO_2, R^2 = NO_2, R^3 = NO_2$

Figure. 1. Structure of the complexes 1–4.

Experimental

Synthesis of tris(4-nitro-pyridin-2-ylmethyl)amine

To a stirred mixture of 2-chloromethyl-4-nitropyridine (0.66 g, 3.8 mmol) and 2-aminomethyl-4-nitropyridine dihydrochloride (0.54 g, 1.9 mmol) in water (1mL) was slowly added 5.0 N NaOH (2.0 mL, 10 mmol). The reaction mixture was stirred at 0 °C for 4 days. The organic layer was separated, and the aqueous layer was extracted with CH₂Cl₂ several times. The combined organic layers were dried over Na₂SO₄, and volatile components were removed. Purification of the product on an alumina column (8:1 CH₂Cl₂/AcOEt) gave a yellow solid of tris(4-nitro-pyridin-2-ylmethyl)amine (0.26 g, yield 32%); ¹H NMR (400 MHz, CDCl₃): 8.78 (3H, d, *J* = 5.5 Hz), 8.22 (3H, d, *J* = 1.8 Hz), 7.85 (3H, dd, *J* = 5.4 Hz, *J*' = 2.3 Hz), 4.11 (6H, s); ¹³C NMR (CDCl₃, 99.5 MHz): 163.7, 155.5, 152.4, 116.6, 115.7 and 60.9.

Synthesis of Fe–TPA and nitro-derivatives

Typical procedure: to a stirred solution of $\text{Fe}(\text{ClO}_4)_2 \cdot n\text{H}_2\text{O}$ (0.109 g, 0.30 mmol) in MeCN was added a solution of TPA or TPA derivatives (0.3 mmol) in MeCN under N_2 . The reaction mixture was stirred for 30 min. The solid was obtained by diffusion of diethyl ether into the MeCN solution.

$[\text{Fe}(\text{TPA})(\text{MeCN})_2](\text{ClO}_4)_2$ (**1**):

^1H NMR (400 MHz, CD_3CN): 11.19 (3H, s, $\text{H}_{\alpha(\text{Py})}$), 8.66 (3H, s, $\text{H}_{\beta/\beta'(\text{Py})}$), 8.57 (3H, s, $\text{H}_{\beta''(\text{Py})}$), 7.26 (3H, t, $J = 7.7$ Hz, $\text{H}_{\gamma(\text{Py})}$), 6.57 (6H, s, H_{Me}). ESI-MS: m/z 193.5 ($[\text{Fe}^{\text{II}}(\text{TPA})(\text{CH}_3\text{CN})]^{2+}$).

$[\text{Fe}(\text{monoNO}_2\text{-TPA})(\text{MeCN})_2](\text{ClO}_4)_2$ (**2**):

^1H NMR (400 MHz, CD_3CN): 10.41 (1H, br s, $\text{H}_{\alpha(\text{NO}_2\text{-Py})}$), 10.02 (2H, br s, $\text{H}_{\alpha(\text{Py})}$), 8.63 (1H, s, $\text{H}_{\beta/\beta'(\text{NO}_2\text{-Py})}$), 8.55 (1H, br s, $\text{H}_{\beta''(\text{NO}_2\text{-Py})}$), 8.02–8.00 (4H, br m, $\text{H}_{\beta+\beta'(\text{Py})}$), 7.54 (2H, t, $J = 7.7$ Hz, $\text{H}_{\gamma(\text{Py})}$), 5.76 (2H, s, $\text{H}_{\text{NO}_2\text{-Me}}$), 5.70 (2H, d, $J = 16.6$ Hz, H_{Me}), 5.40 (2H, d, $J = 16.6$ Hz, H_{Me}). ESI-MS: m/z 216.6 ($[\text{Fe}(\text{monoNO}_2\text{-TPA})(\text{CH}_3\text{CN})]^{2+}$).

$[\text{Fe}(\text{diNO}_2\text{-TPA})(\text{MeCN})_2](\text{ClO}_4)_2$ (**3**):

^1H NMR (400 MHz, CD_3CN): 9.93 (2H, br d, $J = 4.0$ Hz, $\text{H}_{\alpha(\text{NO}_2\text{-Py})}$), 9.95 (1H, br s, $\text{H}_{\alpha(\text{Py})}$), 8.40 (2H, s, $\text{H}_{\beta/\beta'(\text{NO}_2\text{-Py})}$), 8.35 (2H, br d, $J = 4.0$ Hz, $\text{H}_{\beta''(\text{NO}_2\text{-Py})}$), 7.77–7.78 (2H, br m, $\text{H}_{\beta+\beta'(\text{Py})}$), 7.68 (1H, t, $J = 7.7$ Hz, $\text{H}_{\gamma(\text{Py})}$), 5.43 (2H, d, $J = 17.4$ Hz, H_{Me}), 5.20 (2H, d, $J = 17.4$ Hz, H_{Me}), 5.18 (2H, s, $\text{H}_{\text{NO}_2\text{-Me}}$). ESI-MS: m/z 259.2 ($[\text{Fe}(\text{diNO}_2\text{-TPA})(\text{MeCN})_2]^{2+}$).

$[\text{Fe}(\text{triNO}_2\text{-TPA})(\text{MeCN})_2](\text{ClO}_4)_2$ (**4**):

^1H NMR (400 MHz, CD_3CN): 9.68 (3H, br d, $J = 5.1$ Hz, $\text{H}_{\alpha(\text{NO}_2\text{-Py})}$), 9.95 (3H, br s, $\text{H}_{\alpha(\text{Py})}$), 8.30 (3H, s, $\text{H}_{\beta/\beta'(\text{NO}_2\text{-Py})}$), 8.26 (3H, br d, $J = 4.0$ Hz, $\text{H}_{\beta''(\text{NO}_2\text{-Py})}$), 5.20 (3H, d, $J = 17.4$ Hz, $\text{H}_{\text{NO}_2\text{-Me}}$). ESI-MS: m/z 281.9 ($[\text{Fe}(\text{triNO}_2\text{-TPA})(\text{MeCN})_2]^{2+}$).

Results and Discussion

Characterization of a series of iron(II) complexes

TPA and TPA derivatives with one and two nitro-groups were synthesized according to published procedures.¹⁷ Tris(4-nitro-pyridin-2-ylmethyl)amine was readily obtained by coupling 2-(chloromethyl)-4-nitropyridine and 2-(aminomethyl)-4-nitropyridine. Complexation of the ligand with $\text{Fe}(\text{ClO}_4)_2$ in MeCN gave the corresponding complexes **1–4** as a crystalline solid in high yield. These complexes can be formulated as $[\text{Fe}^{\text{II}}(\text{L})(\text{CH}_3\text{CN})_2](\text{ClO}_4)_2$. The NMR spectra of **1–4** in MeCN-d_3 at 298K show proton signals at a range of 4–12, indicating that these complexes predominantly have a diamagnetic low spin ferrous ion (Figure 1).¹⁸

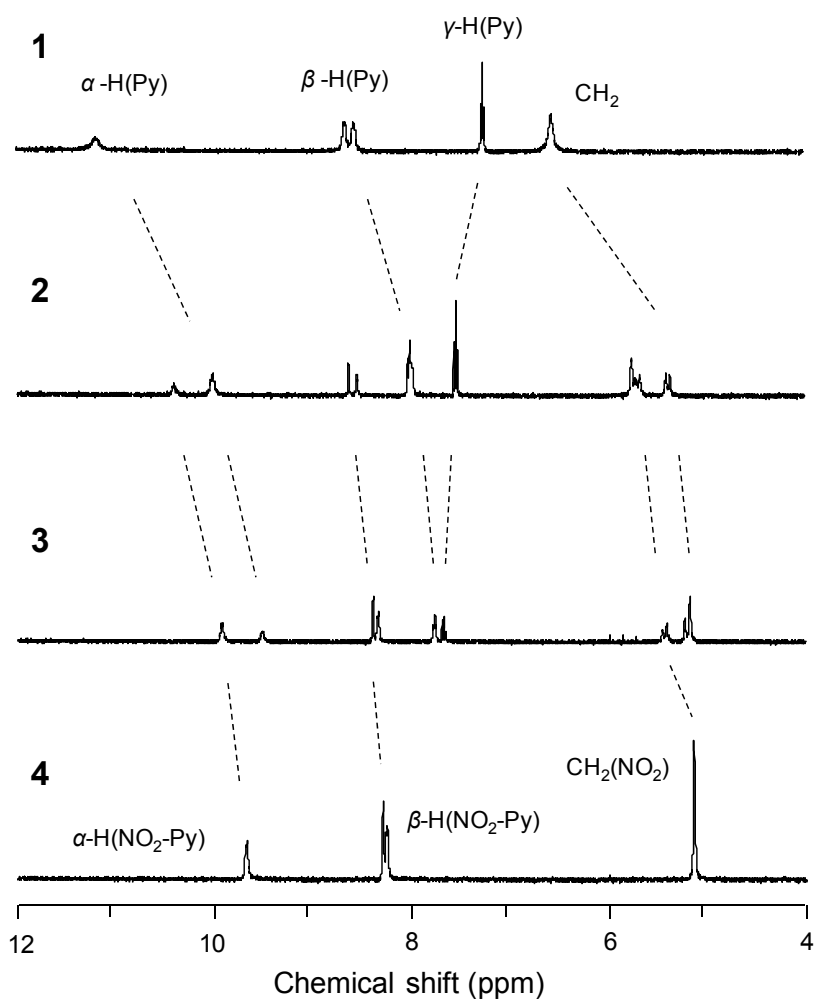


Figure 1. ^1H NMR spectra of **1–4** in MeCN-d_3 at 298 K.

UV-Vis spectra of **2** and **3** in MeCN show two intense broad bands, while one intense broad band was observed for **1** and **4** (Figure 2). As listed in Table 1, the broad bands could be categorized into two classes; lower energy band at around 490 nm and higher energy at around 350 nm. The former is due to charge transfer from iron(II) to a low-lying π^* orbital of 4-nitropyridine ligand, and the latter is assignable to the charge transfer from iron(II) to a low-lying π^* orbital of pyridine ligand, which has been observed for other iron(II) complexes supported by pyridine-based ligands.²²⁻²⁷ Cyclic voltammetry shows a reversible oxidation corresponding to the Fe^{II}/Fe^{III} couple for complexes **1-4**. The oxidation potentials successively increased on going from **1** to **4** (**1**: 1.00V; **2**: 1.12V; **3**: 1.22 V; **4**: 1.32V vs. NHE in MeCN).

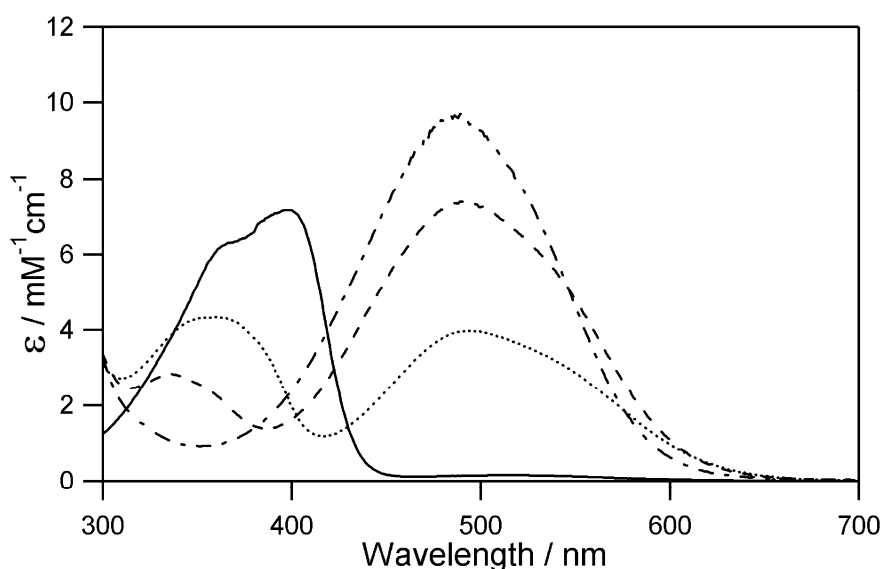


Figure 2. UV-Vis spectra of **1-4** in acetonitrile at 298 K: Solid line (**1**); dotted line (**2**); dashed line (**3**); chain line (**4**).

Table 1. MLCT bands of **1-4** in MeCN at 298 K.^a

Complex	higher energy MLCT band / nm	lower energy MLCT band / nm
1	398 (7040), 370 sh (6350)	–
2	359 (4431)	493 (3972)
3	336 (2828)	489 (7389)
4	–	486 (9656)

^a In parentheses, molar absorption coefficient is expressed in M⁻¹ cm⁻¹.

Catalytic oxidation

The catalytic activities of **1–4** in cyclohexane oxidation was evaluated by the following procedure: to a vigorously stirred solution containing the ferrous complex and 1000 equiv. of cyclohexane in MeCN was slowly supplied 30 equiv. of hydrogen peroxide by using a syringe pump over 90min at room temperature. Samples for GC analysis were taken periodically to determine the time course of the oxidation of cyclohexane. In all the cases, an induction period was observed up to 10 min, and the oxidized products then increased almost linearly until 90 min, at which time the supply of hydrogen peroxide was ended (Figure 3). The reaction mixture contained considerable amounts of the corresponding alcohol and ketone, but the total yields were decreased on going from **1** to **4**. Table 2 shows the yields of cyclohexanol and cyclohexanone with respect to hydrogen peroxide at 90 min. Interestingly, the alcohol/ketone (A/K) ratios shows the highest value of 11 for **2**, which is rather higher even compared with ever reported mononuclear nonheme iron catalysts,⁴ while **3** and **4** show the A/K values close to 1. The results indicate the involvement of radical oxidants for the cyclohexane oxidation in the presence of **3** and **4**.

To gain more insights into the catalytic oxidation, we monitored the UV–Vis spectral changes of **1–4** under the aforementioned catalytic conditions. Figure 4a shows the UV–Vis spectral changes of **1**. The Fe(II)-to-pyridine MLCT band at 398 nm rapidly disappeared, and the spectrum of **1** was converted to that of Fe(III)–TPA species.²⁸ The spectral change clearly demonstrated that an oxidation from Fe(II) to Fe(III) took place within 3 min, which corresponds to the observed induction period of product formation. In contrast to complex **1**, complexes **2–4** showed only a slight to moderate decrease of the corresponding MLCT bands (Figure 4b–d), whose extent became larger as the number of nitro groups increased. Thus, **2–4** retained the Fe(II) state even during the catalytic reaction. Since the iron(III) species is prerequisite to the formation of *cis*-oxo-hydroxo-iron(V) oxidizing species.²⁹ it is conclusive that the decrease in the product yields on going from **1** to **4** should be caused mainly by the ineffective conversion to the iron(III) species. The preference of the iron(II) state of nitro-substituted complexes is in agreement with their high oxidation potentials.

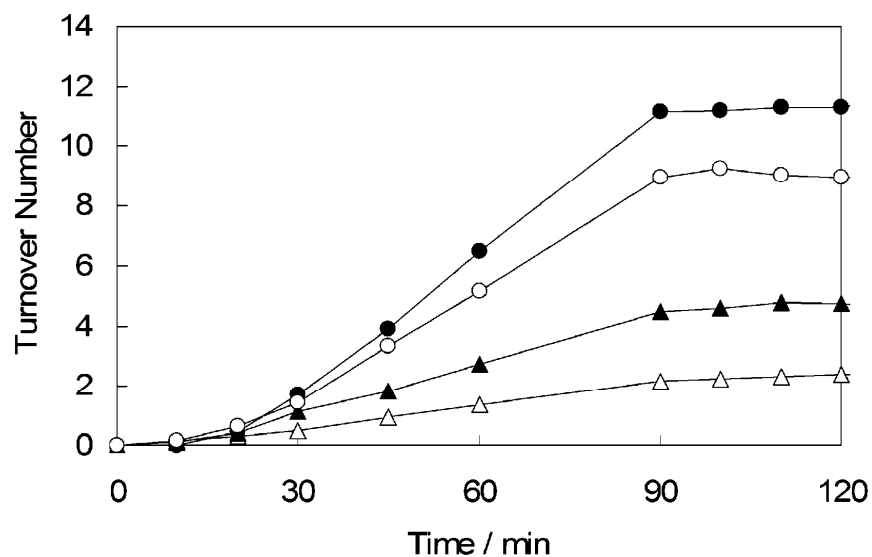


Figure 3. UV-Vis spectra of **1–4** in acetonitrile at 298 K: Solid line (**1**); dotted line (**2**); dashed line (**3**); chain line (**4**).

Table 2. Product yields and A/K ratios in cyclohexane oxidation catalyzed by **1–4**.

Complex	Cyclohexane (%) ^a	Cyclohexanol (%) ^a	A/K ratio
1	32	5.3	6.0
2	27	2.6	11
3	12	2.5	4.9
4	4.6	2.6	1.8

^a Yield at 90 min, with respect to the total hydrogen peroxide.

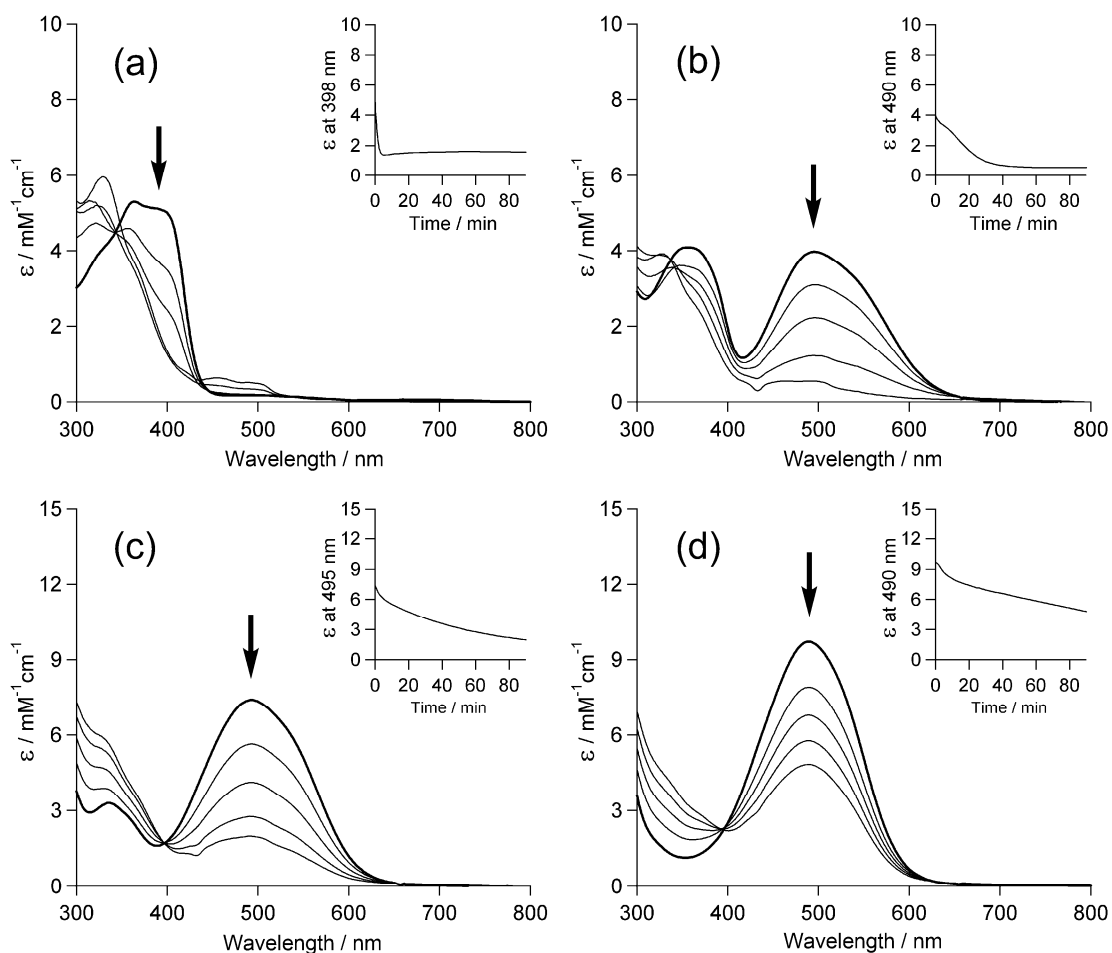


Figure 4. UV-vis spectral changes of **1–4** during the catalytic reaction: (a) **1**, (b) **2**, (c) **3** and (d) **4**.

Proposed reaction cycle

There are two possible mechanisms that can account for the ineffective formation of iron(III) species during the oxidation reaction catalyzed by **2–4**: one is slow-down of the reaction rate of Fe(II) complex with hydrogen peroxide due to the high oxidation potentials of **2–4**. As shown in Figure 2, however, the oxidation reaction was ceased as the supply of hydrogen peroxide was stopped in all the cases. This result suggests that complexes **2–4** have a considerable reactivity with hydrogen peroxide, like complex **1**. The other possible mechanism is regeneration of Fe(II) species by

hydrogen peroxide. To explore this possibility, we added hydrogen peroxide to the solution of **4** after the catalytic reaction, and observed a growth of the MLCT band at around 490 nm, indicating regeneration of ferrous complex **4** (Figure 5). ESI–mass measurements verified the formation of ferrous complex **4** as major species, together with a small amount of Fe(III)-OOH species (Figure 6). The formation of ferrous complex **4** might be through homolytic dissociation of the Fe O bond of Fe(III)-OOH species, which should also produce hydroperoxo radical. Such reduction of metal center by hydrogen peroxide was observed for Cu(II) complexes, especially when the metal center is supported by ligands that stabilize Cu(I) state.^{30,31} Scheme 1 depicted a possible catalytic reaction cycle of complex **4**, together with that for **1**.^{29,32,33} The OH radical in the cycle for **4** would give an explanation for the observed A/K ratio close to 1.

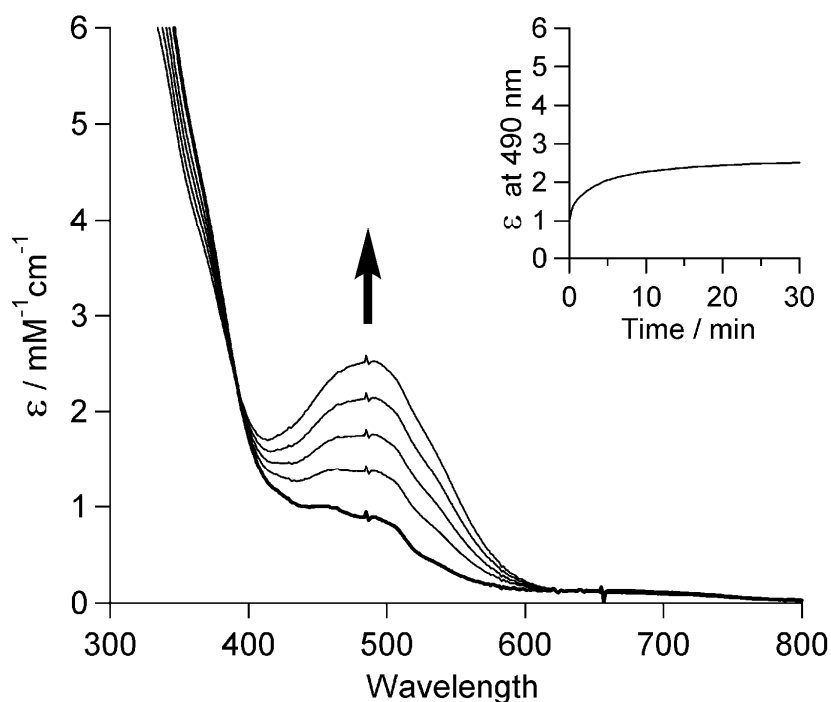


Figure 5. UV–vis spectral changes upon addition of 10 equiv. of hydrogen peroxide to the solution of **4** after the catalytic reaction.

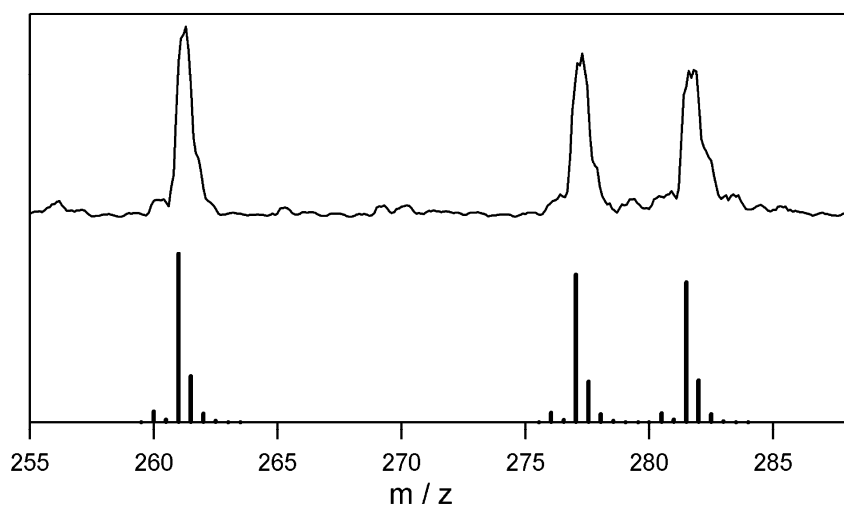
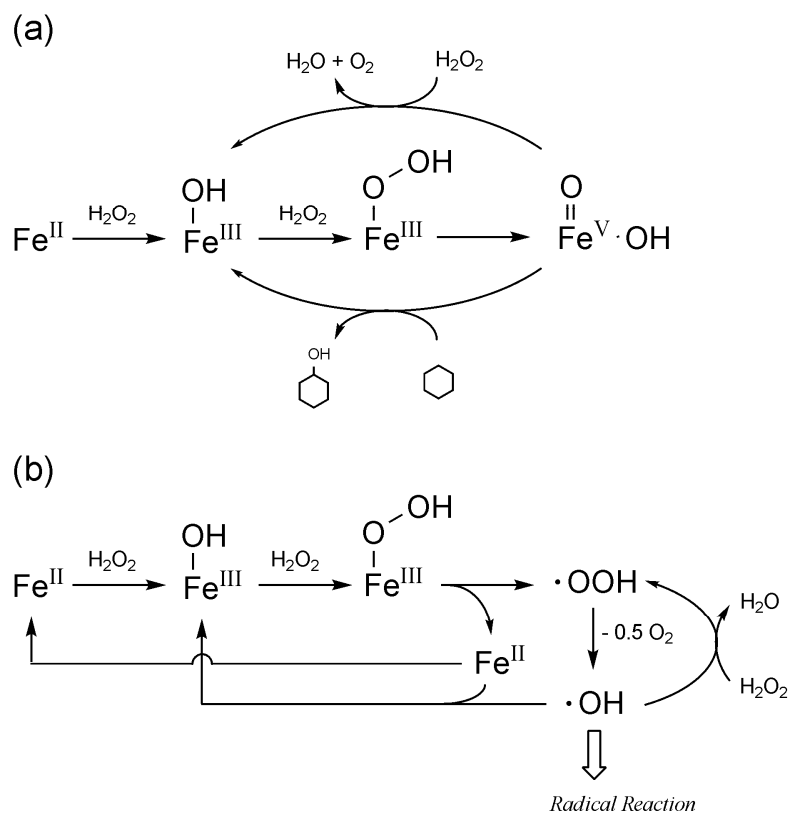


Figure 6. Electron ionization mass spectrum upon addition of 10 equiv. of hydrogen peroxide to the solution of **4** after the catalytic reaction was ended. (a) $[\text{Fe}(\text{triNO}_2\text{-TPA})(\text{MeCN})]^{2+}$ m/z 261.3, (b) $[\text{Fe}(\text{triNO}_2\text{-TPA})(\text{MeCN})(\text{OOH})]^{2+}$ m/z 277.3, (c) $[\text{Fe}(\text{triNO}_2\text{-TPA})(\text{MeCN})_2]^{2+}$ m/z 281.6.



Scheme 1. Proposed catalytic cycles of cyclohexane oxidation catalyzed by **1** (a) and **4** (b).

Conclusions

A number of mononuclear nonheme iron complexes have been prepared and examined as catalysts for alkane hydroxylation with hydrogen peroxide,^{4,5,22,31} but there is no systematic exploration on the effects of the electronic structures of these catalysts on their catalytic oxidation activity. In this study, we have prepared a series of mononuclear nonheme iron(II) complexes supported by TPA and its nitro-derivatives, and evaluated the effect of the nitro-groups on the catalytic oxidation activity. The introduction of nitro-group to the TPA ligand proved to lower the product yields as well as A/K ratio. During the catalytic oxidation, a significant amount of Fe(II) species is present in the cases of nitro-substituted complexes, while the unsubstituted Fe-TPA complex was rapidly oxidized to Fe(III) state. Theoretical calculations predicted that introducing nitro-groups should facilitate H-atom abstraction from alkane by *cis*-oxo-hydroxo-iron(V) species,¹⁵ but our experimental study demonstrated that such energetically unfavorable species cannot be obtained by the reaction with hydrogen peroxide. In fact, it induces homolysis of the Fe O bond of Fe(III)OOH to afford Fe(II) and hydroperoxide radical. The A/K ratio of **3** and **4** decreases dramatically to reach 1, which should be caused by the radical.^{32,33}

References

- (1) Solomon, E.I.; Brunold, T.C.; Davis, M.I.; Kemsley, J.N.; Lee, S.-K.; Lehnert, N.; Neese, F.; Skulan, A.J.; Yang, Y.-S.; Zhou, J. *Chem. Rev.* **2000**, *100*, 235.
- (2) Gibson, D.T.; Parales, R.E. *Curr. Opin. Biotechnol.* **2000**, *11*, 236.
- (3) Que, L.; Ho, R.Y.N. *Chem. Rev.* **1996**, *96*, 2607.
- (4) Costas, M.; Chen, K.; Que, L. *Coord. Chem. Rev.* **2000**, *200*, 517.
- (5) Costas, M.; Mehn, M.P.; Jensen, M.P.; Que, L. *Chem. Rev.* **2004**, *104*, 939.
- (6) Chen, K.; Que, L. *Angew. Chem. Int. Ed.* **1999**, *38*, 2227.
- (7) Chen, K.; Costas, M.; Kim, J.; Tipton, A.K.; Que, L. *J. Am. Chem. Soc.* **2002**, *124*, 3026.
- (8) Mas-Ballesté, R.; Fujita, M.; Hemmila, C.; Que, L. *J. Mol. Catal. A: Chem.* **2006**, *251*, 49.
- (9) Shan, X.; Que, L. *J. Inorg. Biochem.* **2006**, *100*, 421.
- (10) Bassan, A.; Blomberg, M.R.A.; Siegbahn, P.E.M.; Que, L. *J. Am. Chem. Soc.* **2002**, *124*,

11056.

- (11) Bassan, A.; Blomberg, M.R.A.; Siegbahn, P.E.M.; Que, L. *Chem. Eur. J.* **2005**, *11*, 692.
- (12) Kim, C.; Chen, K.; Kim, J.; Que, L. *J. Am. Chem. Soc.* **1997**, *119*, 5964.
- (13) Chen, K.; Que, L. *Chem. Commun.* **1999**, 1375.
- (14) Chen, K.; Que, L. *J. Am. Chem. Soc.* **2001**, *123*, 6327.
- (15) Ma, Y.; Balubuena, P.B. *J. Phys. Chem. B* **2007**, *111*, 2711.
- (16) Hitomi, Y.; Higuchi, M.; Minami, H.; Tanaka, T.; Funabiki, T. *Chem. Commun.* **2005**, 1758.
- (17) Higuchi, M.; Hitomi, Y.; Minami, H.; Tanaka, T.; Funabiki, T. *Inorg. Chem.* **2005**, *44*, 8810.
- (18) Zang, Y.; Kim, J.; Dong, Y.; Wilkinson, E.C.; Appelman, E.H.; Que, L. *J. Am. Chem. Soc.* **1997**, *119*, 4197.
- (19) Mandon, D.; Machkour, A.; Goetz, S.; Welter, R. *Inorg. Chem.* **2002**, *41*, 5364.
- (20) Mandon, D.; Nopper, A.; Litrol, T.; Goetz, S. *Inorg. Chem.* **2001**, *40*, 4803.
- (21) Wada, A.; Ogo, S.; Nagatomo, S.; Kitagawa, T.; Watanabe, Y.; Jitsukawa, K.; Masuda, H. *Inorg. Chem.* **2002**, *41*, 616.
- (22) Diebold, A.; Hagen, K.S. *Inorg. Chem.* **1998**, *37*, 215.
- (23) Al-Obaidi, A.H.R.; Jensen, K.B.; McGarvey, J.J.; Toftlund, H.; Jensen, B.; Bell, S.E.J.; Carroll, J.G. *Inorg. Chem.* **1996**, *35*, 5055.
- (24) Mialane, P.; Nivorojkine, A.; Pratviel, G.; Azéma, L.; Slany, M.; Godde, F.; Simaan, A.J.; Banse, F.; Kargar-Grisel, T.; Bouchoux, G.; Sainton, J.; Horner, O.; Guilhem, J.; Tchertanova, L.; Meunier, B.; Girerd, J.-J. *Inorg. Chem.* **1999**, *38*, 8.
- (25) Toftlund, H.; Yde-Andersen, S. *Acta Chem. Scand.* **1981**, *A35*, 575.
- (26) Bernal, I.; Jensen, I.M.; Jensen, K.B.; McKenzie, C.J.; Toftlund, H.; Tuchagues, J.-P. *J. Chem. Soc., Dalton Trans.* **1995**, 3667.
- (27) Britovsek, G.J.P.; England, J.; White, A.J.P. *Inorg. Chem.* **2005**, *44*, 8125.
- (28) Dong, Y.; Fujii, H.; Hendrich, M.P.; Leising, R.A.; Pan, G.; Randall, C.R.; Wilkinson, E.C.; Zang, Y.; Que, L.; Fox, B.G.; Kauffmann, K.; Münck, E. *J. Am. Chem. Soc.* **1995**, *117*, 2778.
- (29) Zhang, X.; Zhang, D.; Busch, D.H.; van Eldik, R. *J. Chem. Soc., Dalton Trans.* **1999**, 2751.
- (30) Osako, T.; Nagatomo, S.; Tachi, Y.; Kitagawa, T.; Itoh, S. *Angew. Chem. Int. Ed.* **2002**, *41*, 4325.

- (31) Ghattas, W.; Giorgi, M.; Mekmouche, Y.; Tanaka, T.; Rockenbauer, A.; Réglier, M.; Hitomi, Y.; Simaan, A.J. *Inorg. Chem.* **2008**, *47*, 4627.
- (32) Marvel, C.S.; Deanin, R.; Claus, C.J.; Wyld, M.B.; Seitz, R.L. *J. Polym. Sci.* **1948**, *3*, 350.
- (33) Haber, F.; Weiss, J. *Proc. R. Soc. Lond.* **1934**, *A147*, 332.

Chapter 3

Theoretical Study on Electronic Structure of Fe(II)–TPA Complex and Its Nitro-Substituted Derivatives

Abstract

The electronic and geometric structures of a series of iron(II) complexes supported by tetradentate tris(pyrid-2-ylmethyl)amine-type ligands with different number of 4-nitropyridine groups, $[(\text{PyCH}_2)_{3-n}(4\text{-NO}_2\text{PyCH}_2)_n\text{N}]$ ($n = 0\text{--}3$), were examined by X-ray absorption fine-structure and variable-temperature ^1H NMR spectroscopies and theoretical calculations in order to reveal how low-spin state is stabilized through π back-bonding interactions between iron(II) and 4-nitropyridine donor group(s).

Introduction

Transition metal complexes with d^4 – d^7 electronic configurations are capable of exhibiting two spin states (high spin or low spin) depending on the strength of the ligand field. In special cases, the high- and low-spin states are in thermal equilibrium, which can be shifted to either a high-spin or low-spin state by external perturbations such as light, heat, or pressure. Since the change in spin states is accompanied by changes in magnetic moment, color, and molecular geometry, such spin-crossover compounds have attracted much attention for technological applications such as in display devices and data storage.¹ The spin-crossover phenomena have been frequently observed in iron(III) and iron(II) complexes,^{2–5} and the factors that control this behavior have therefore been extensively studied with iron complexes that have a wide variety of supporting ligands.^{6–11} The introduction of substituent groups expected to show steric or electronic effects was traditionally employed as a strategy.^{12–20} The incorporation of either sterically demanding substituents close to the donor atoms^{14,15} or electron-withdrawing ones^{12,13} generally reduces the ligand field strength and makes the high-spin configuration more favorable. For example, M. Enamullah and W. Linert studied the substituent effects of iron(II)-4-X-2,6-bis-(benzimidazol-2'-yl)pyridine complexes (X = H, OH, and Cl) on their spin-crossover phenomena, in which electron-withdrawing substituents made the high spin more favorable.¹³

In previous research,²¹ we prepared a series of iron(III)-catecholate complexes supported by tris(pyrid-2-ylmethyl)amine (TPA)-type ligands having various substituent groups at the 4-position of the pyridine donor groups, in order to obtain insights into the reaction mechanism of mononuclear nonheme iron(III)-dependent catechol dioxygenases, and found that the iron(III)-catecholate complexes undergo the high-spin/low-spin crossover and that electron-withdrawing substituents make the low-spin state more favorable. This counterintuitive result indicated that pyridine ligands with electron-withdrawing substituents stabilize the $d\pi$ orbitals of iron, probably through π back-bonding interactions of iron $d\pi$ orbitals and π^* orbitals of the pyridine ligands. At that time, however, an evaluation of the contribution of π back-bonding interactions was prevented by a significant amount of iron(II)-semiquinonate

character of the iron(III)-catecholate complex. Recently, we prepared a series of iron(II) complexes supported by TPA-type ligands with different number of 4-nitropyridine groups, $[(\text{PyCH}_2)_{3-n}(4\text{-NO}_2\text{PyCH}_2)_n\text{N}]$ ($n = 0\text{--}3$) (**1–4**) shown in Figure 1b, and carried out the catalytic oxidation of cyclohexane with hydrogen peroxide using **1–4** as catalysts.²² UV–Vis and ¹H NMR spectroscopic and electrochemical measurements revealed that the electronic structures of **1–4** changed as the number of 4-nitropyridine groups increases, which explained well the difference in their catalytic activities of **1–4**. Interestingly, the dominant low-spin state became more favorable as the number of 4-nitropyridine donor groups was increased. This result suggests that $d\pi$ orbitals should be stabilized through π back-bonding interactions between iron(II) and 4-nitropyridine donor group(s), as suggested for the iron(III)-catecholate complexes. Herein, we discuss how low-spin state is stabilized through π back-bonding interactions between iron(II) and 4-nitropyridine donor group(s) in light of theoretical calculations.

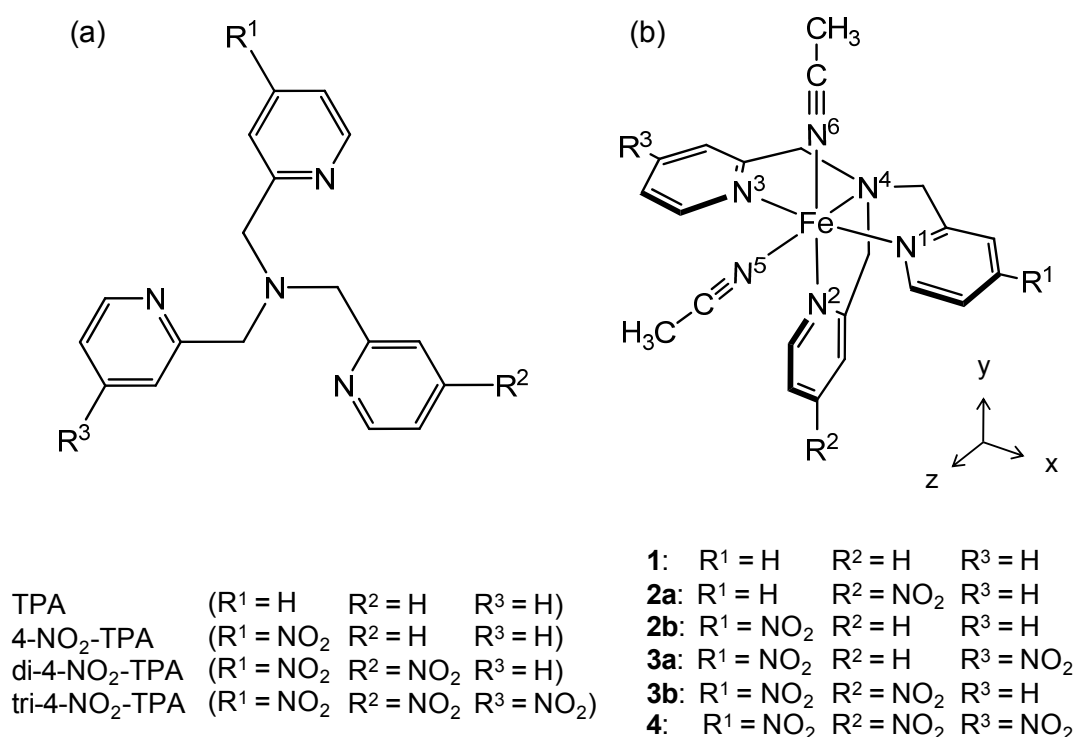


Figure 1. TPA-type ligands used in this study (a) and calculated structures **1–4** (b).

Experimental

Synthesis of a series of iron(II) complexes

[Fe(TPA)(MeCN)₂](ClO₄)₂ (**1**), [Fe(4-NO₂-TPA)(MeCN)₂](ClO₄)₂ (**2**), [Fe(di-4-NO₂-TPA)(MeCN)₂](ClO₄)₂ (**3**), and [Fe(tri-4-NO₂-TPA)(MeCN)₂](ClO₄)₂ (**4**) were prepared according to published procedures (Figure 1a).^{21,22} Variable temperature ¹H NMR spectra of these complexes in MeCN-d₃ were recorded on a JEOL ECX400P spectrometer.

X-ray absorption

The X-ray absorption experiments were carried out on the beam line 7C at Photon Factory (Tsukuba, Japan). The ring energy was 2.5 GeV, and the stored current was 340–370 mA. The Fe K-edge (7.1 keV) XAFS spectra of **1–4** in MeCN (10 mM) were recorded in a fluorescence mode with a Si(111) two-crystal monochromator at room temperature. The EXAFS analysis was performed by a Rigaku REX2000 program. For a curve fitting analysis, the backscattering amplitude and the phase shift functions of an Fe–N pair was obtained from a theoretical reference generated by using the code FEFF 8.²³ A complex consisted of an Fe center and octahedrally coordinated six N atoms with 1.96 Å of Fe–N distances was used as a model for the theoretical reference. The Fe–N distance of 1.96 Å was referenced from the crystal structure of [Fe(bpy)₃]²⁺ (bpy = bipyridine).²⁴ The Fourier transformation and inverse Fourier transformation of the EXAFS signals were performed in the *k*-range of ca 2.5–12 Å⁻¹ and R-range of ca 1–2 Å, respectively.

Computational details

We used computational methods based on density functional theory²⁵ as implemented in the ORCA 2.6 of computer programs.²⁶ Fe(II) complexes **1–4** with two possible stereoisomers of **2** and **3** were calculated (Figure 1b). Spin quantum numbers of *S* = 0 and *S* = 2 were applied for the calculation of low-spin and high-spin configurations, respectively. The calculation made use of BP86 and B3LYP functionals for geometry optimization and single point energy calculations, respectively. All

calculations employed Ahlrichs triple- ζ valence basis set with some sets of first polarization functions; one set for H atom, two sets for C and N atoms and three sets for Fe atom. Tight SCF convergence (10^{-8} au) was used for all calculations. The solvent effect (MeCN) was considered by using the conductor like screening model (COSMO). All reported values for orbital correspond to the B3LYP single point calculations. Vibrational frequency calculations at 298.15 K were performed on Gaussian03²⁷ using BLYP, B3LYP, B3LYP* functionals, and LanL2DZ basis set to estimate thermal energies of the Fe(II) complexes.

Results and Discussion

Variable temperature ¹H NMR study

We already reported the proton NMR spectra of **1–4** in MeCN-*d*₃ at 298 K.²² Here, we report the proton NMR spectral change at a range from 233 to 298 K in order to address the spin-crossover behaviors of **1–4** in solution state (Figure 2). The proton signals appearing at a range of 4–12 ppm were shifted upfield and reached constant values as the temperature decreased to 233 K. This result indicates that a trace fraction of high-spin species exists at 298 K and disappears at 233 K in case of all the complexes **1–4**.²⁸ Spin-crossover behaviors for **1–4** can be clearly seen in the Curie plots of Figure 3. All the signals moved toward diamagnetic values as the temperature was lowered from 298 K to 233 K. The slopes became milder as the number of nitro groups increased. This result clearly indicates that **4** should have the highest fraction of low-spin state among **1–4** at the same temperature. Interestingly, the signals of axial and equatorial pyridine ligands could not be distinguished and appeared as averaged broad signals even at 233 K, which is in sharp contrast to the case of Ru(II)–TPA complex.²⁹ These results indicate the rapid exchange of axial and equatorial pyridine ligands of Fe(II)–TPA complexes at a rate close to but faster than the NMR timescale, probably through a five-coordinated species as proposed by Birtovsek et al.³⁰

Fe K-edge EXAFS studies

Fe K-edge EXAFS spectra of the ferrous complexes **1–4** in MeCN and their Fourier transforms

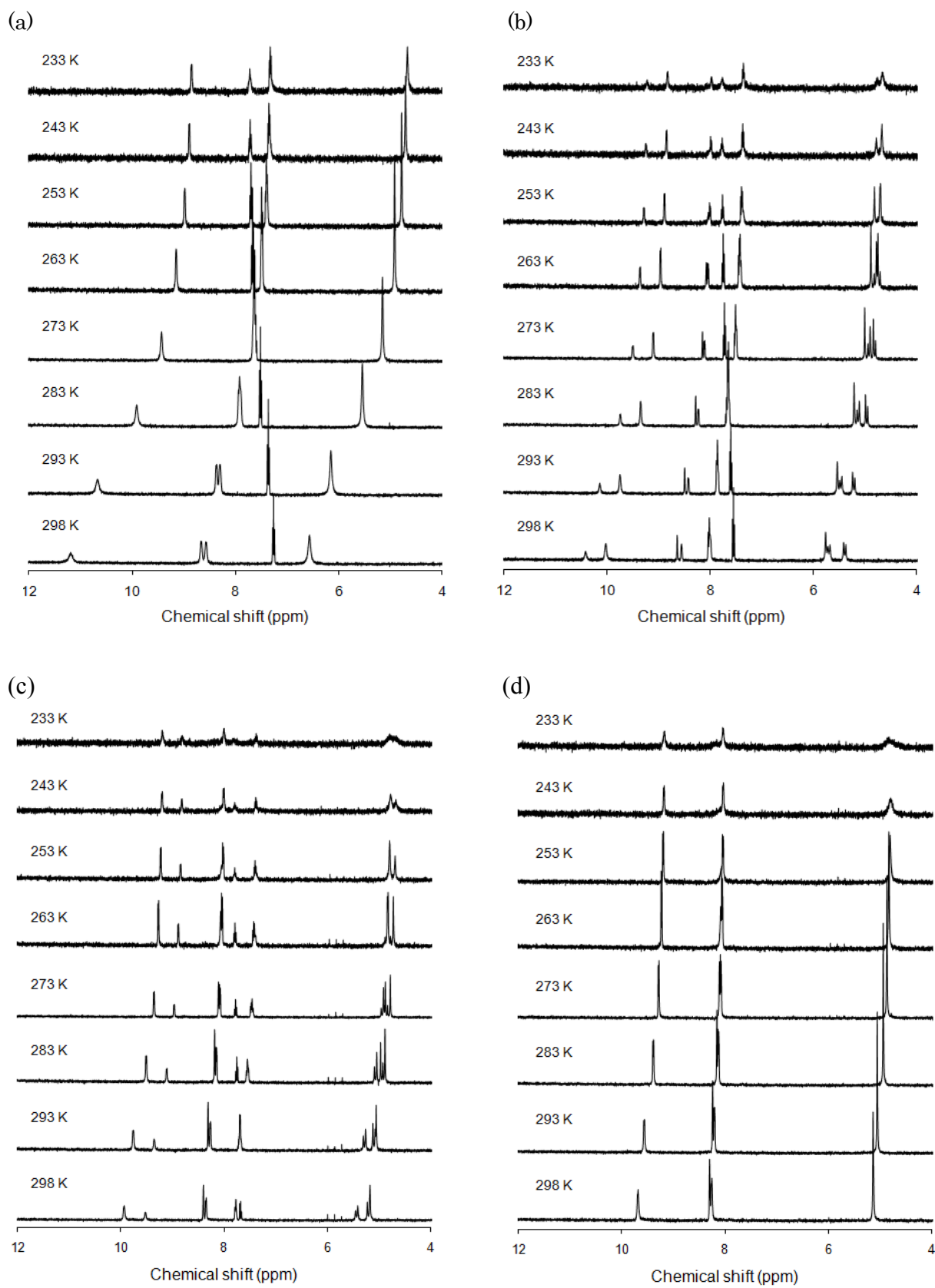


Figure 2. ^1H NMR spectra of (a) **1**, (b) **2**, (c) **3**, and (d) **4** in MeCN-d_3 at various temperatures (298 K to 233 K)

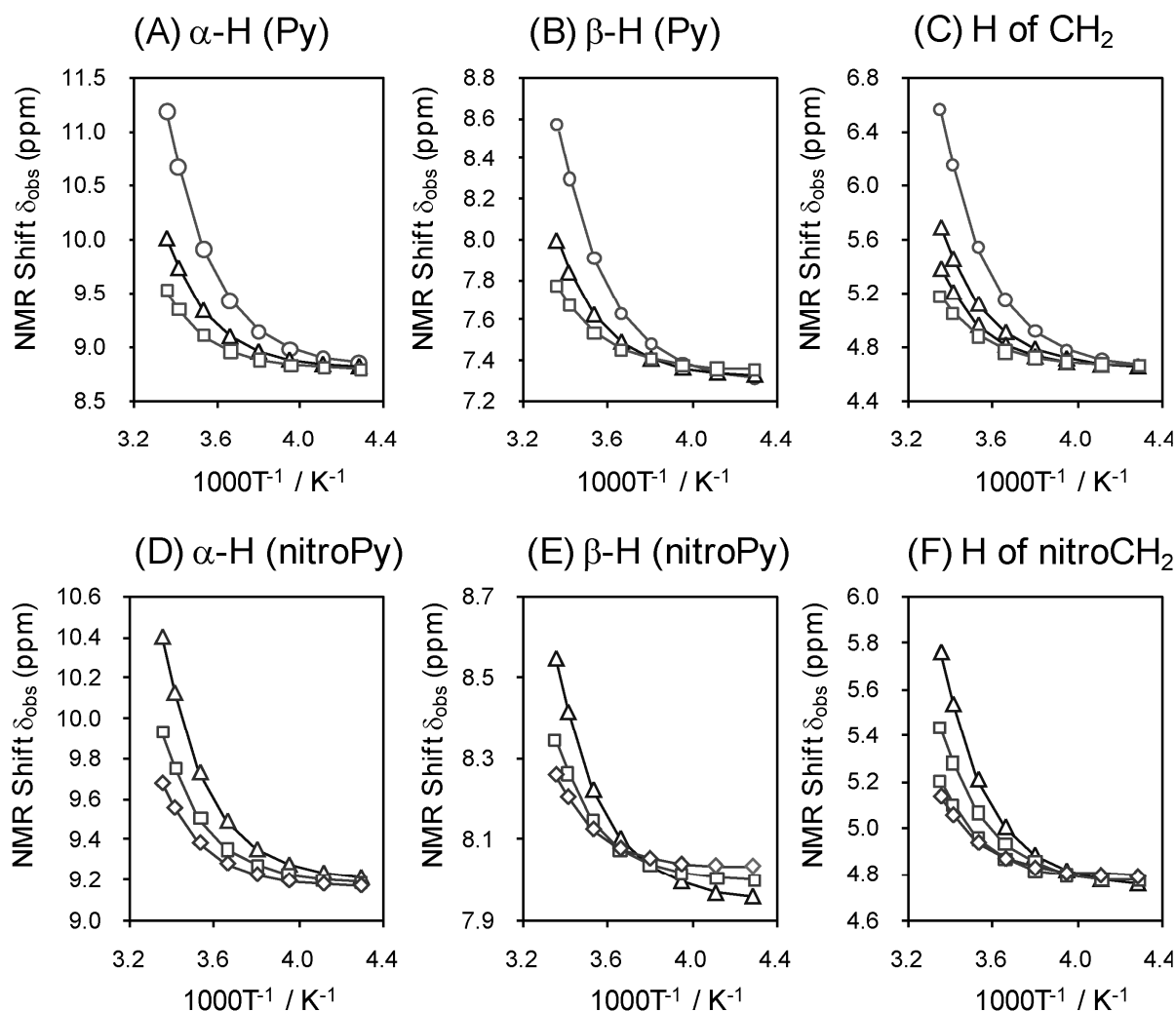


Figure 3. Curie plots for some signals of 1–4: 1 (○), 2 (△), 3 (□), 4 (◇), : (A) α -H (Py), (B) β -H (Py), (C) H of CH₂, (D) α -H (nitroPy), (E) β -H (nitroPy) and (F) H of nitroCH₂.

are shown in Figures 4 and 5, respectively. The peaks at about 1.5 Å in Figure 5 are assigned to Fe–N scatterings. The EXAFS analysis indicated Fe–N distances of 1.940–1.958 Å (Table 1; Fourier filtering and curve fitting were shown in Figure 6), whose values are comparable to those typically found in low-spin Fe(II) complexes such as [Fe(phen)₃]²⁺ (1.97 Å),³¹ [Fe(bpy)₃]²⁺ (1.96 Å),²⁴ and [Fe(bpca)₂]²⁺ (1.94 Å)³² (where phen = 1,10-phenanthroline; bpy = bipyridine; bpca = *N*-(2-pyridinylcarbonyl)-2-pyridinecarboximidate monoanion). The estimated Fe–N bond length decreased by nitro-substitution, even though the standard deviation are rather large (**1**: 1.958(4) Å; **2**: 1.957(6) Å; **3**: 1.950(6) Å; **4**: 1.940(6) Å), indicating stronger ligation to iron(II) by 4-nitropyridine than by 4-unsubstituted pyridine ligand and/or the decrease of a trace fraction of

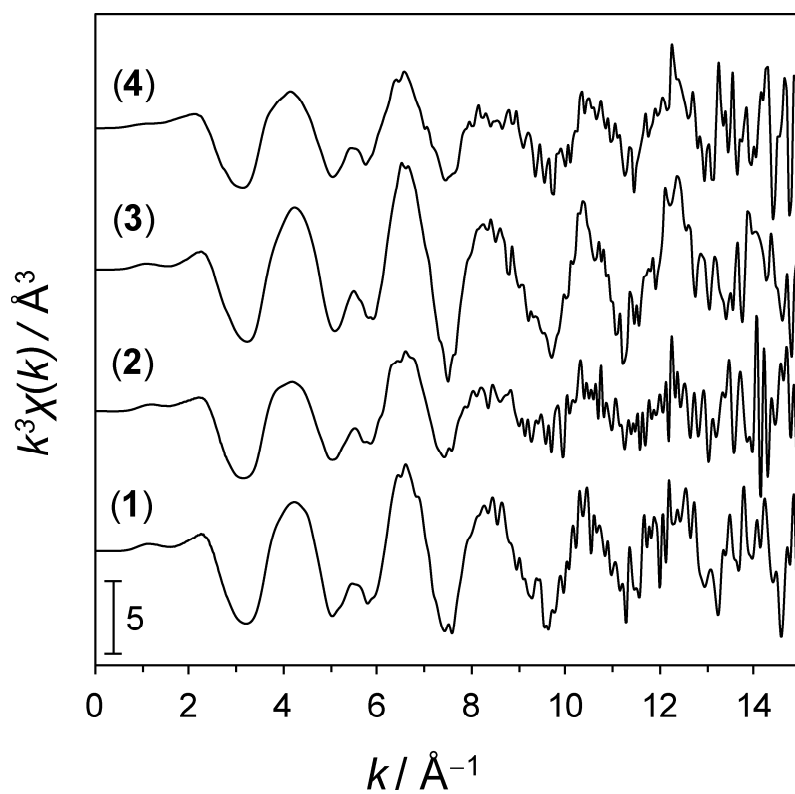


Figure 4. k^3 -Weighted K-edge EXAFS spectra of ferrous complexes 1–4 in MeCN.

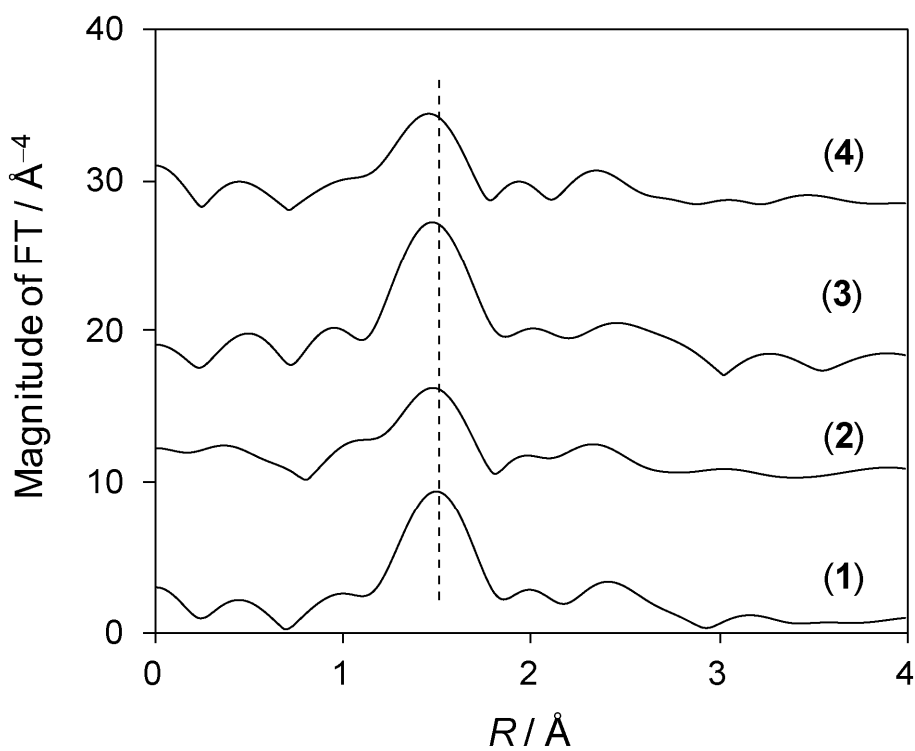


Figure 5. Fourier transformed k^3 -weighted Fe K-edge EXAFS spectra of 1–4 in MeCN.

Table 1. EXAFS curve-fitting results for the Fe–N shells of compounds **1–4**.

complex	r (Å)	σ^2 (Å ²)	R (%)
1	1.958(4)	0.004	1.20
2	1.957(6)	0.004	0.02
3	1.950(6)	0.004	4.31
4	1.940(6)	0.004	1.57

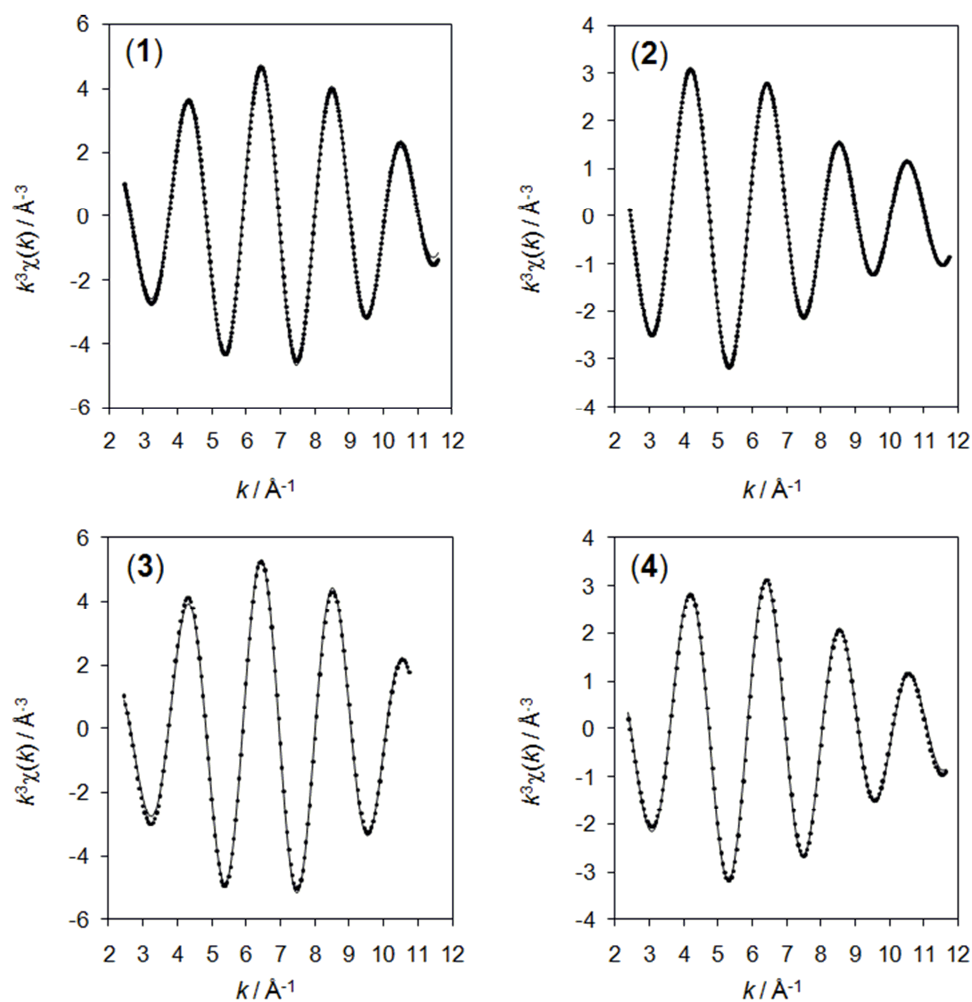


Figure 6. Fourier filtered EXAFS oscillations (solid curve) and the curve fit (circle) for complexes **1–4**.

high-spin species whose Fe–N bond length is ca. 2.10 Å.²⁰ The former reason is more probable because the iron(II) center of **1–4** are predominantly in low-spin state at room temperature.

Calculated orbital energies

A theoretical approach based on DFT calculations is very useful and has been used for investigation of electronic structures of Fe^{33–35} or Ru complexes^{34,36} including π back-bonding interactions. In this study, we performed DFT calculation for low-spin Fe(II) complexes **1–4** with two possible isomers of **2** and **3** (Figure 1b). The so-called frontier orbitals of **1–4** are shown in Figure 7, which includes the two isomers of **2** and **3**, where the frontier orbitals can be seen to stabilize as the number of nitro groups increases. Two $d\sigma$ -like Kohn-Sham orbitals (KSOs) are found at -0.5 to -1.0 eV, and three $d\pi$ -like KSOs are located at -6.4 to -7.2 eV. The stabilization by introduction of nitro groups is ca. 0.1 eV per one nitro group, which is in good agreement with the difference in oxidation potential (**1**: 1.00 V; **2**: 1.12 V; **3**: 1.22 V; **4**: 1.32 V vs. NHE in MeCN).²² Although both $d\sigma$ and $d\pi$ orbitals are incrementally stabilized by introducing one nitro group into the TPA ligand, $d\pi$ orbitals are stabilized more than $d\sigma$ orbitals. For example, $d\sigma$ and $d\pi$ orbitals of **4** are lowered in energy by 0.44 and 0.54 eV, respectively, compared with those of **1** (Table 2). As a result, the energy gap between $d\sigma$ and $d\pi$ orbitals, which correspond to the ligand field strength, is increased by the introduction of nitro groups. These results are in agreement with the observation that a low-spin state became more favorable on going from **1** to **4**. The lower-lying unoccupied π^* -like orbitals of pyridyl ligands are located at -2 to -1 eV, and the lower-lying unoccupied π^* -like orbitals of 4-nitropyridyl ligands were found at around -3.5 eV. Thus, π^* -like orbitals of 4-nitropyridine ligands are located lower in energy by ca. 1.6 eV than those of 4-unsubstituted pyridyl ligands. We already reported that the metal-to-ligand charge transfer (MLCT) transition of **1–4** can be classified in two classes; the MLCT band from $d\pi(\text{Fe})$ to $\pi^*(\text{Py})$ appearing in ca. 3.4 eV and the band from $d\pi(\text{Fe})$ to $\pi^*(\text{NO}_2\text{-Py})$ in ca. 2.5 eV. The energy difference of the two types of MLCT bands should be related to the energy difference of π^* -like orbitals of 4-nitropyridine and 4-unsubstituted pyridyl ligands.²²

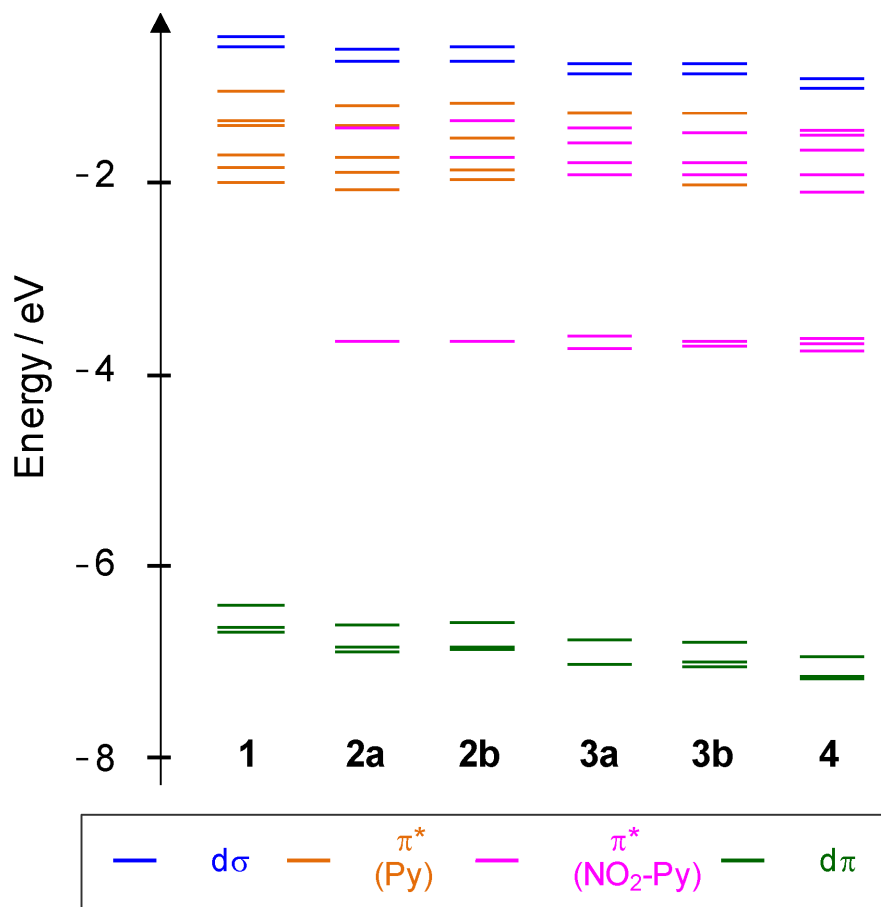


Figure 7. Energy diagrams of frontier orbitals of low-spin ferrous complexes **1–4**.

Table 2. Energy levels of d orbitals of **1–4**.

complex	orbital energy / eV ^a		
	dσ	dπ	dσ – dπ
1	-0.577	-6.414	5.836
2a	-0.740	-6.611	5.871
2b	-0.737	-6.597	5.860
3a	-0.879	-6.772	5.893
3b	-0.879	-6.781	5.902
4	-1.021	-6.952	5.931

^a Energies of the highest dπ orbitals and the lowest dσ ones are listed.

π Back-bonding interactions

The Fe–N distances in the optimized structures of **1–4** ($S = 0$) are listed in Table 3. The averaged Fe–N lengths (N^1 – N^6) of **1–4** (ca. 1.95 Å) agree with those estimated by EXAFS analyses. Clearly, 4-nitropyridine ligands interact with the low-spin iron(II) center than 4-unsubstituted pyridine ligands. For the axial pyridine ligation, the Fe– N^2 bonds of **2a**, **3b** and **4** (1.939–1.952 Å) are shorter than those of **1**, **2b** and **3a** (1.962–1.967 Å). For the equatorial pyridine ligation, the Fe–N bonds involving 4-nitropyridine (1.949–1.970 Å) are shorter than those involving 4-unsubstituted pyridine (1.978–1.986 Å). Interestingly, conformer **2a** has the shortest Fe–N(4-nitropyridine) bond (1.939 Å) and the longest Fe–N(pyridine) bond (1.985 Å). While the average bond length of Fe–N(pyridine) becomes shorter on going from **1** to **4**, the average bond length of Fe–N(MeCN) slightly increases, and the Fe–N(amine) bond distance shows almost no difference among **1–4**. Thus, nitro-substitution shortens corresponding Fe–N(pyridine) length. The averaged Fe–N length (N^1 – N^6) also slightly decreases by introduction of nitro groups, which is consistent with the trend obtained from the EXAFS study.

Table 3. Fe–N distances in the optimized structures of low-spin ferrous complexes **1–4**.

N atom	1	2a	2b	3a	3b	4
N^1	R = H	1.978	1.985			
	R = NO ₂		1.949	1.963	1.964	1.970
N^2	R = H	1.962	1.964	1.967		
	R = NO ₂		1.939		1.947	1.952
N^3	R = H	1.978	1.982	1.983	1.986	
	R = NO ₂			1.964		1.969
Ave. of N^1 – N^3	1.973	1.968	1.965	1.965	1.966	1.963
N^4	2.003	1.999	2.000	2.001	1.998	1.998
N^5	1.895	1.902	1.902	1.904	1.906	1.908
N^6	1.916	1.924	1.922	1.927	1.926	1.928
Ave. of N^1 – N^6	1.956	1.955	1.953	1.955	1.955	1.954

The natural bond order (NBO) analysis also revealed that the bond orders of Fe–N(4-nitropyridine) are higher than those of Fe–N(pyridine) (Table 4). On the other hand, the N–C bond length of the pyridine ring became longer by introducing nitro groups as shown in Table 5. These results strongly indicate the higher π -acceptability of 4-nitropyridine ligand than 4-unsubstituted pyridine ligand.

Table 4. Bond orders of Fe–N bonds of low-spin ferrous complexes **1–4** estimated by natural bond analysis.

N atom		1	2a	2b	3a	3b	4
N ¹	R ¹ = H	0.568	0.566				
	R ¹ = NO ₂			0.581	0.574	0.572	0.569
N ²	R ² = H	0.589		0.592	0.598		
	R ² = NO ₂		0.602			0.599	0.598
N ³	R ³ = H	0.567	0.574	0.564		0.575	
	R ³ = NO ₂				0.574		0.577
N ⁴		0.556	0.563	0.561	0.564	0.566	0.568
N ⁵		0.626	0.619	0.616	0.620	0.617	0.617
N ⁶		0.613	0.606	0.608	0.609	0.608	0.609

Table 5. Selected N–C distances in pyridyl moieties of low-spin ferrous complexes **1–4**. ^a

N atom		1	2a	2b	3a	3b	4
N ¹	R ¹ = H	1.364	1.363				
	R ¹ = NO ₂			1.367	1.365	1.366	1.365
N ²	R ² = H	1.357		1.357	1.356		
	R ² = NO ₂		1.363			1.361	1.360
N ³	R ³ = H	1.364	1.362	1.363		1.362	
	R ³ = NO ₂				1.365		1.364

^a The α -carbon atoms close to amine N atom (N⁴) are selected.

The compositions of the frontier orbitals in terms of contributions from Fe, the pyridyl ligands, the 4-nitropyridyl ligands, and acetonitrile are listed in Table 6. HOKS, HOKS-1, and HOKS-2 have a large contribution of iron (~84%) and also contain some fraction of pyridyl and/or 4-nitropyridyl moieties. The sum of contribution of pyridyl and 4-nitropyridyl moieties reaches ca. 16–17% in HOKS (Fe d_{xy}). On the other hand, HOKS-1 (Fe d_{yz}) and HOKS-2 (Fe d_{zx}) contain the fraction of MeCN, but not the fraction of pyridyl and/or 4-nitropyridyl moieties. Interestingly, the fraction of 4-nitropyridine π^* orbitals in HOKS increases from 0 to 6, 11, and 17 on going from **1** to **4**. In addition, LUKS of **2**, LUKS+1 of **3**, and LUKS+2 of **4** have large fractions of 4-nitropyridyl moieties as well as some contribution of the Fe d_{xy} orbital. In contrast, the total fraction of MeCN π^* orbitals to HOKS-1 and HOKS-2 does not change regardless of the number of nitro groups (**1**: 18.6%, **2a**: 18.4%, **3a**: 18.5%, **4**: 18.6%). Thus, these results demonstrate that π back-bonding interactions between the Fe d_{xy} orbital and the π^* orbitals of the pyridine moiety become stronger in a stepwise manner as the number of nitro groups increases.

Then, we investigated in detail how the nitro-substitution stabilized the orbitals of pyridyl moiety by comparing the KSOs of pyridine and 4-nitropyridine molecules. Figure 5 shows the frontier orbitals of pyridine and 4-nitropyridine. The π and π^* orbitals of 4-nitropyridine are located in lower energy than those of pyridine. Particularly, the LUKS of 4-nitropyridine is located by 2.3 eV lower energy than that of pyridine, which well accounts the enhanced π -acceptability of 4-nitropyridine ligands. In both cases of 4-nitropyridine and pyridine, the phase of the LUKS is allowed to interact with $d_{xy}(\text{Fe})$ orbital (HOKS in the iron complexes) when the pyridine is coordinated to Fe(II). Indeed, the π back-bonding interactions between $d_{xy}(\text{Fe})$ and $\pi^*(\text{NO}_2\text{-Py})$ are clearly observed in LUKS, LUKS+1, and LUKS+2 of **2–4**, as shown in Figure 6.

Ligand field of the complex in high-spin configuration

To understand how the π back-bonding affects the spin-crossover behaviors of **1–4**, the effect of the π back-bonding on the ligand field strength should be investigated not only in the low-spin state ($S = 0$) but also in high-spin state ($S = 2$). In this context, we optimized the structures of **1–4** in high-spin configuration (**1'–4'**) and calculated their KSOs in low-spin configuration ($S = 0$).

Table 6. Orbital energies and atomic orbital contributions for frontier orbitals from HOKS–2 to LUKS+2 of the low-spin ferrous complexes **1–4**.

complex	KSO	E (eV)	%Fe	%Py	%NO ₂ -Py	%MeCN	symmetry ^a
1	LUKS+2	-1.711	1.0	95.0	–	0.9	$\pi^*(\text{Py}) - d_{xy}$
	LUKS+1	-1.828	4.9	94.0	–	0.1	$\pi^*(\text{Py}) - d_{xy}$
	LUKS	-1.987	0.9	93.5	–	0.3	$\pi^*(\text{Py})$
	HOKS	-6.414	79.1	15.8	–	4.7	$d_{xy} - \pi(\text{Py})$
	HOKS–1	-6.647	87.4	4.3	–	7.2	$d_{yz} - \pi(\text{MeCN})$
	HOKS–2	-6.680	85.0	1.8	–	11.4	$d_{zx} - \pi(\text{MeCN})$
2a	LUKS+2	-1.892	2.5	54.9	39.0	0.2	$\pi^*(\text{Py}) - d_{xy}$
	LUKS+1	-2.068	0.8	84.9	7.8	0.3	$\pi^*(\text{Py})$
	LUKS	-3.657	2.3	10.6	86.5	0.2	$\pi^*(\text{NO}_2\text{-Py}) - d_{xy}$
	HOKS	-6.611	78.1	11.2	6.0	4.3	$d_{xy} - \pi(\text{Py}) - \pi(\text{NO}_2\text{-Py})$
	HOKS–1	-6.830	87.2	3.5	0.6	7.4	$d_{yz} - \pi(\text{MeCN})$
	HOKS–2	-6.883	85.2	1.2	1.0	11.0	$d_{zx} - \pi(\text{MeCN})$
3a	LUKS+2	-1.925	1.0	0.0	90.3	0.2	$\pi^*(\text{NO}_2\text{-Py})$
	LUKS+1	-3.605	3.6	0.0	96.0	0.0	$\pi^*(\text{NO}_2\text{-Py}) - d_{xy}$
	LUKS	-3.725	0.2	0.2	98.8	0.1	$\pi^*(\text{NO}_2\text{-Py})$
	HOKS	-6.772	78.0	5.8	11.1	4.8	$d_{xy} - \pi(\text{NO}_2\text{-Py}) - \pi(\text{Py})$
	HOKS–1	-7.008	85.5	1.2	0.9	10.9	$d_{yz} - \pi(\text{MeCN})$
	HOKS–2	-7.008	87.1	0.8	3.2	7.6	$d_{zx} - \pi(\text{MeCN})$
4	LUKS+2	-3.636	3.0	–	96.5	0.0	$\pi^*(\text{NO}_2\text{-Py}) - d_{xy}$
	LUKS+1	-3.685	1.7	–	97.9	0.2	$\pi^*(\text{NO}_2\text{-Py}) - d_{xy}$
	LUKS	-3.761	0.6	–	98.4	0.1	$\pi^*(\text{NO}_2\text{-Py})$
	HOKS	-6.952	78.0	–	16.9	4.6	$d_{xy} - \pi(\text{NO}_2\text{-Py})$
	HOKS–1	-7.158	86.8	–	3.6	8.4	d_{yz}
	HOKS–2	-7.181	85.9	–	2.4	10.2	d_{zx}

^a N_{Py}-Fe-N_{Py} is the x axis, N_{MeCN}-Fe-N_{Py} is the y axis.

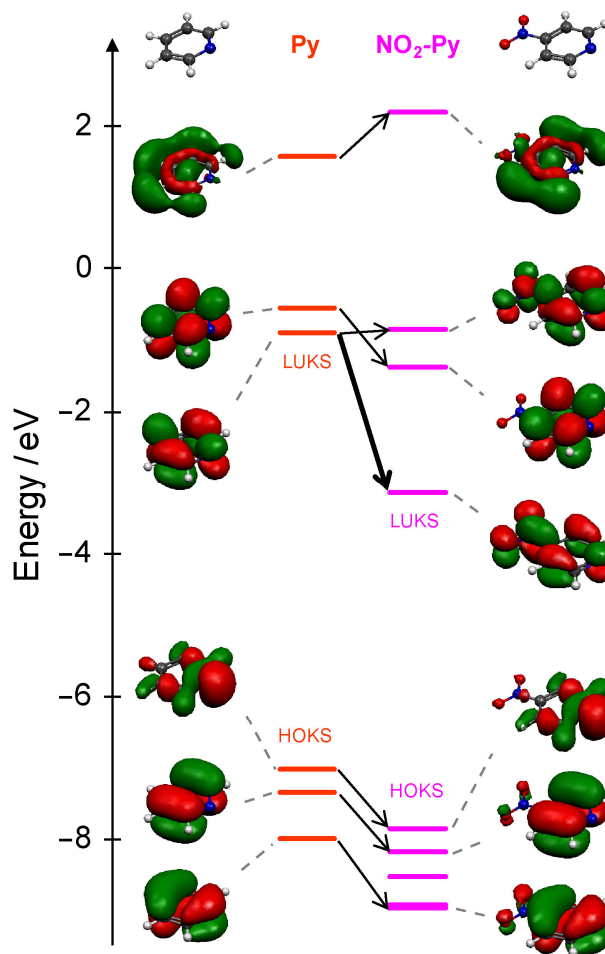


Figure 8. Energy diagrams and schematic illustrations of frontier orbitals of pyridine and 4-nitropyridine molecules. The value of each isocontour surface is 0.03 au.

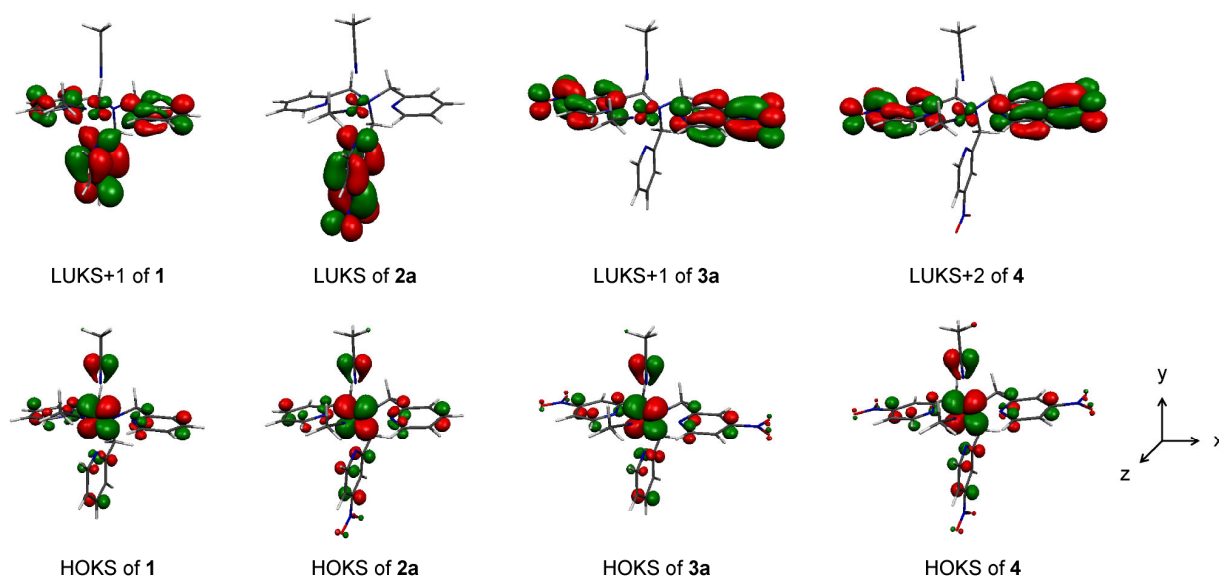


Figure 9. Schematic illustrations of frontier orbitals of low-spin ferrous complexes 1–4. The value of each isocontour surface is 0.03 au.

The Fe–N distances of **1'**–**4'** are about 2.2 Å (Table 7), which show good agreements with those typically found in high-spin Fe(II) complexes such as [Fe(6-Me₃-TPA)(CH₃CN)₂]²⁺ (2.18–2.25 Å),³⁷ [Fe(BQPA)(H₂O)(ClO₄)]⁺ (2.17–2.20 Å)³⁷ and [Fe(5-Me₂-BPMEN)(CH₃CN)₂]²⁺ (2.16–2.23 Å) (where BQPA = bis(2-quinolylmethyl)(2-pyridylmethyl)amine; BPMEN = *N,N'*-dimethyl-*N,N'*-bis(2-pyridylmethyl)-1,2-diamino-ethane).³⁸ Contrary to the low-spin structures, there is no systematic change in Fe–N bond length of the high spin structures on going from **1'** to **4'**. The KSO diagrams of singlet **1'**–**4'** are significantly different from those of singlet **1**–**4** (Figure 7 vs. Figure 10). For examples, dσ like orbitals are located in lower energy than π*(Py) like orbitals. The d-d splittings of **1'**–**4'** are smaller than those of **1**–**4**, which clearly describes that the high-spin structures have weaker ligand fields than the low-spin ones. This result should be caused by the longer Fe–N distances of high-spin structures. The dσ and dπ orbitals of **4'** are stabilized by 0.38 and 0.44 eV than those of **1'**, respectively, which are smaller than the case of the low-spin structures. Moreover, the contribution of π*(Py) orbital to dπ like HOKS in **1'**–**4'** (**1'**; 9.0%, **2a'**; 8.6%, **3a'**; 8.6%, **4'**; 7.3%) is lower than that in **1**–**4** (**1**; 15.8%, **2a**; 17.2%, **3a**; 16.9%, **4**; 16.9%). These results strongly suggest that the π back-bonding interactions of **1'**–**4'** are smaller than those of **1**–**4**. Thus, the high-spin structure has smaller ligand field and is less sensitive toward nitro-substitution than the low-spin one. Stabilization of dπ orbitals (especially d_{xy} orbital) corresponding to the highest occupied KSOs seems to stabilize total electronic energy of the complex and to make the low-spin state more preferable.

Table 7. Fe–N distances in the optimized structures of **1'**–**4'**.

	N atom	1'	2a'	2b'	3a'	3b'	4'
N ¹	R ¹ = H	2.179	2.179				
	R ¹ = NO ₂			2.154	2.185	2.156	2.183
N ²	R ² = H	2.175		2.176	2.174		
	R ² = NO ₂		2.177			2.189	2.172
N ³	R ³ = H	2.180	2.163	2.171		2.178	
	R ³ = NO ₂				2.143		2.155
	N ⁴	2.269	2.247	2.250	2.240	2.253	2.237
	N ⁵	2.090	2.102	2.108	2.105	2.104	2.106
	N ⁶	2.167	2.158	2.159	2.155	2.143	2.145

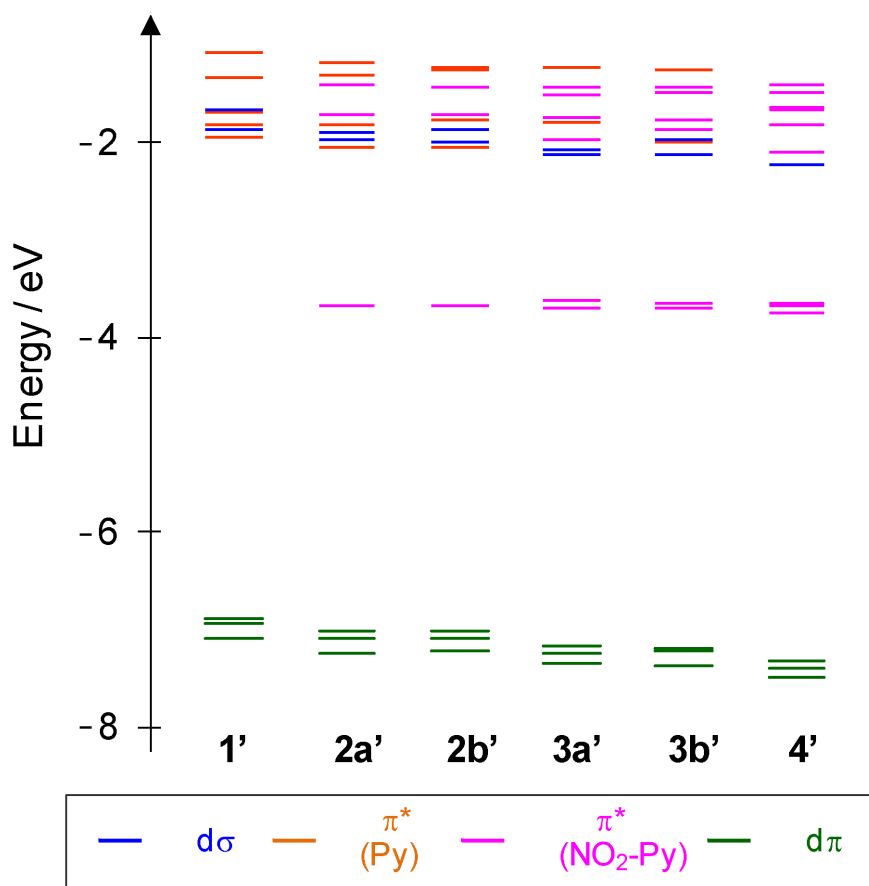


Figure 10. Energy diagrams of frontier orbitals of high-spin ferrous complexes **1'**–**4'**.

Then, in order to estimate the thermal energies, we carried out vibrational frequency calculations with using some functionals such as BLYP, B3LYP, and B3LYP* for **1** and **4** in low-spin configuration ($S = 0$) and **1'** and **4'** in high-spin one ($S = 2$) as listed in Table 8. Reiher et al. reported that B3LYP* functional, B3LYP analogue of which exact exchange admixture parameter was modified from 20% to 15%, could well reproduce low-spin/high-spin energy splittings of Fe(II) complexes.^{39,40} The calculated low-spin/high-spin splittings in enthalpy ($\Delta H_{\text{LS-HS}}$) are negative, and the $\Delta H_{\text{LS-HS}}$ value for trinitro-substituted complex is more negative than that of unsubstituted one, regardless of functionals. This result supports that the low-spin state becomes more thermodynamically preferable by introduction of nitro groups. Although the calculated values based on B3LYP functional are close to zero, BLYP and B3LYP* functionals give values which are consistent with the experimental results that the low-spin species are dominant at 298 K.

Table 8. Calculated gap in enthalpy ($\Delta H_{\text{LS-HS}}$ / kcal·mol⁻¹) between low-spin and high-spin complexes using several functionals. ^a

complex	functional		
	BLPY	B3LYP	B3LYP*
1 (1')	-19.6	-0.08	-5.5
4 (4')	-20.2	-0.12	-6.8

^a $\Delta H_{\text{LS-HS}} = H_{\text{LS}} - H_{\text{HS}}$. LS; low-spin, HS; high-spin.

Conclusions

In this study, we investigated the effect of the nitro groups on the electronic and geometric structures of iron(II) complexes supported by TPA-type ligands. The introduction of nitro groups on the tpa-type ligand stabilizes the low-spin state of the ferrous complex, which is caused by significant π back-bonding interactions between iron(II) and 4-nitropyridine ligand. The DFT calculation revealed that introducing the nitro groups stabilizes $d\pi$ orbitals more than $d\sigma$ orbitals, which is more prominent with the low-spin state than with the high-spin. Thus, our study demonstrates that a 4-nitropyridine donor group can work as a good π -acceptor and favor a low-spin ferrous iron state by stabilizing the iron $d\pi$ orbitals.

References

- (1) Kahn, O.; Martinez, C. J. *Science* **1998**, 279, 44.
- (2) Beattie, J. K. *Adv. Inorg. Chem.* **1988**, 32, 1.
- (3) Toftlund, H. *Coord. Chem. Rev.* **1989**, 94, 67.
- (4) König, E. *Struct. Bond.* **1991**, 76, 51.
- (5) Gutlich, P.; Hauser, A.; Spiering, H. *Angew. Chem. Int. Ed. Engl.* **1994**, 33, 2024.
- (6) Boca, R.; Baran, P.; Dlhán, L.; Fuess, H.; Haase, W.; Renz, F.; Linert, W.; Svoboda, I.; Werner, R. *Inorg. Chim. Acta* **1997**, 260, 129.

- (7) Boca, R.; Baran, P.; Dlhán, L.; Sima, J.; Wiesinger, G.; Renz, F.; ElAyaan, U.; Linert, W. *Polyhedron* **1997**, *16*, 47.
- (8) Toyazaki, S.; Nakanishi, M.; Komatsu, T.; Kojima, N.; Matsumura, D.; Yokoyama, T. *Synth. Met.* **2001**, *121*, 1794.
- (9) Boca, R. *Solid State Chem. V* **2003**, *90-91*, 141.
- (10) Boca, R.; Renz, F.; Boca, M.; Fuess, H.; Haase, W.; Kickelbick, G.; Linert, W.; Vrbova-Schikora, M. *Inorg. Chem. Commun.* **2005**, *8*, 227.
- (11) Nihei, M.; Shiga, T.; Maeda, Y.; Oshio, H. *Coord. Chem. Rev.* **2007**, *251*, 2606.
- (12) Linert, W.; Enamullah, M.; Gutmann, V.; Jameson, R. F. *Monatsh. Chem.* **1994**, *125*, 661.
- (13) Enamullah, M.; Linert, W. *J. Coord. Chem.* **1996**, *40*, 193.
- (14) Constable, E. C.; Baum, G.; Bill, E.; Dyson, R.; van Eldik, R.; Fenske, D.; Kaderli, S.; Morris, D.; Neubrand, A.; Neuburger, M.; Smith, D. R.; Wieghardt, K.; Zehnder, M.; Zuberbuhler, A. *D. Chem. Eur. J.* **1999**, *5*, 498.
- (15) Elhaik, J.; Money, V. A.; Barrett, S. A.; Kilner, C. A.; Evans, I. R.; Halcrow, M. A. *Dalton Trans.* **2003**, 2053.
- (16) Paulsen, H.; Duelund, L.; Zimmermann, A.; Averseng, F.; Gerdan, M.; Winkler, H.; Toftlund, H.; Trautwein, A. X. *Monatsh. Chem.* **2003**, *134*, 295.
- (17) Mukherjee, S.; Weyhermuller, T.; Bill, E.; Wieghardt, K.; Chaudhuri, P. *Inorg. Chem.* **2005**, *44*, 7099.
- (18) Nakano, K.; Suemura, N.; Yoneda, K.; Kawata, S.; Kaizaki, S. *Dalton Trans.* **2005**, 740.
- (19) Kuroiwa, K.; Shibata, T.; Sasaki, S.; Ohba, M.; Takahara, A.; Kunitake, T.; Kimizuka, N. *J. Polym. Sci. Pol. Chem.* **2006**, *44*, 5192.
- (20) Reger, D. L.; Gardinier, J. R.; Elgin, J. D.; Smith, M. D.; Hautot, D.; Long, G. J.; Grandjean, F. *Inorg. Chem.* **2006**, *45*, 8862.
- (21) Higuchi, M.; Hitomi, Y.; Minami, H.; Tanaka, T.; Funabiki, T. *Inorg. Chem.* **2005**, *44*, 8810.
- (22) Hitomi, Y.; Furukawa, S.; Higuchi, M.; Shishido, T.; Tanaka, T. *J. Mol. Catal. A: Chem.* **2008**, *288*, 83.
- (23) Ankudinov, A. L.; Ravel, B.; Rehr, J. J.; Conradson, S. D. *Phys. Rev. B* **1998**, *58*, 7565.

- (24) Posse, M. E. G.; Juri, M. A.; Aymonino, P. J.; Piro, O. E.; Negri, H. A.; Castellano, E. E. *Inorg. Chem.* **1984**, *23*, 948.
- (25) Parr, R. G.; Gadre, S. R.; Bartolotti, L. J. *Proc. Nat. Acad. Sci.* **1979**, *76*, 2522.
- (26) Neese, F. ORCA – an ab initio, Density Functional and Semiempirical program package; 2.6 ed. University of Bonn, 2008.
- (27) Frisch, M. J.; Trucks, G. W.; Schlegel, H. B.; Scuseria, G. E.; Robb, M. A.; Cheeseman, J. R.; Montgomery, J., J. A.; Vreven, T.; Kudin, K. N.; Burant, J. C.; Millam, J. M.; Iyengar, S. S.; Tomasi, J.; Barone, V.; Mennucci, B.; Cossi, M.; Scalmani, G.; Rega, N.; Petersson, G. A.; Nakatsuji, H.; Hada, M.; Ehara, M.; Toyota, K.; Fukuda, R.; Hasegawa, J.; Ishida, M.; Nakajima, T.; Honda, Y.; Kitao, O.; Nakai, H.; Klene, M.; Li, X.; Knox, J. E.; Hratchian, H. P.; Cross, J. B.; Bakken, V.; Adamo, C.; Jaramillo, J.; Gomperts, R.; Stratmann, R. E.; Yazyev, O.; Austin, A. J.; Cammi, R.; Pomelli, C.; Ochterski, J. W.; Ayala, P. Y.; Morokuma, K.; Voth, G. A.; Salvador, P.; Dannenberg, J. J.; Zakrzewski, V. G.; Dapprich, S.; Daniels, A. D.; Strain, M. C.; Farkas, O.; Malick, D. K.; Rabuck, A. D.; Raghavachari, K.; Foresman, J. B.; Ortiz, J. V.; Cui, Q.; Baboul, A. G.; Clifford, S.; Cioslowski, J.; Stefanov, B. B.; Liu, G.; Liashenko, A.; Piskorz, P.; Komaromi, I.; Martin, R. L.; Fox, D. J.; Keith, T.; Al-Laham, M. A.; Peng, C. Y.; Nanayakkara, A.; Challacombe, M.; Gill, P. M. W.; Johnson, B.; Chen, W.; Wong, M. W.; Gonzalez, C.; Pople, J. A. Gaussian 03; Revision C.02 ed.; Gaussian, Inc.: Wallingford CT, 2004.
- (28) Diebold, A.; Hagen, K. S. *Inorg. Chem.* **1998**, *37*, 215.
- (29) Kojima, T.; Amano, T.; Ishii, Y.; Ohba, M.; Okaue, Y.; Matsuda, Y. *Inorg. Chem.* **1998**, *37*, 4076.
- (30) Britovsek, G. J. P.; England, J.; White, A. J. P. *Inorg. Chem.* **2005**, *44*, 8125.
- (31) Zalkin, A.; Templeto, D. H.; Ueki, T. *Inorg. Chem.* **1973**, *12*, 1641.
- (32) Wocadlo, S.; Massa, W.; Folgado, J. V. *Inorg. Chim. Acta* **1993**, *207*, 199.
- (33) Bikiel, D. E.; Bari, S. E.; Doctorovich, F.; Estrin, D. A. *J. Inorg. Biochem.* **2008**, *102*, 70.
- (34) Estrin, D. A.; Hamra, O. Y.; Paglieri, L.; Slep, L. D.; Olabe, J. A. *Inorg. Chem.* **1996**, *35*, 6832.

- (35) Estrin, D. A.; Baraldo, L. M.; Slep, L. D.; Barja, B. C.; Olabe, J. A.; Paglieri, L.; Corongiu, G. *Inorg. Chem.* **1996**, *35*, 3897.
- (36) Rusanova, J.; Rusanov, E.; Gorelsky, S. I.; Christendat, D.; Popescu, R.; Farah, A. A.; Beaulac, R.; Reber, C.; Lever, A. B. P. *Inorg. Chem.* **2006**, *45*, 6246.
- (37) Chen, K.; Que, L. *J. Am. Chem. Soc.* **2001**, *123*, 6327–6337.
- (38) Chen, K.; Costas, M.; Kim, J. H.; Tipton, A. K.; Que, L. *J. Am. Chem. Soc.* **2002**, *124*, 3026.
- (39) Reiher, M.; Salomon, O.; Hess, B. A. *Theor. Chem. Acc.* **2001**, *107*, 48.
- (40) Reiher, M.; Kirchner, B.; Hutter, J.; Sellmann, D.; Hess, B. A. *Chem. Eur. J.* **2004**, *10*, 4443.

Part II

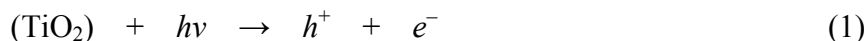
Selective Oxidation Using Heterogeneous Nb₂O₅-Based Photocatalysts

Introduction of Part II

In industrial chemistry, organic molecules including C=O¹ or C=N² moiety (carbonyl compounds or imine derivatives) have been used as important building blocks of higher-valued product such as polymers, fine chemicals, and pharmaceutical compounds. These products are usually synthesized by oxidative dehydrogenation of alcohols and amines or by oxygenation of hydrocarbons. However, non-catalytic methods with stoichiometric, toxic, corrosive, and expensive oxidants such as dichromate and permanganate, which produce a large amount of heavy metal waste, under stringent conditions of high pressure and/or temperature have been widely used.³ Therefore, in the last few years, much attention has been paid to the development of heterogeneous catalytic systems that use clean and atom efficient oxidants like molecular oxygen or H₂O₂.^{4,5} Recently, several heterogeneous catalysts employing transition metals that can function with molecular oxygen were reported. Ru species supported by hydroxyapatite,^{6,7} Al₂O₃,⁸⁻¹⁰ Au nanoparticles supported by CeO₂,¹¹⁻¹³ and graphite^{14,15} are known to be highly active for oxidative dehydrogenation of both of alcohols and amines. Pd-based catalysts such as Pd/hydroxycalcite,^{16,17} Pd/hydroxyapatite,^{18,19} and Pd/Al₂O₃²⁰ are also effective for aerobic oxidation of alcohols. But in these systems, expensive precious metals are employed and relative high temperature (mostly >373 K) is required. In addition, use of solvent such as benzene, trifluorotoluene is necessary in the case of most of these systems.

Aerobic Oxidation Using TiO₂-based Photocatalysts

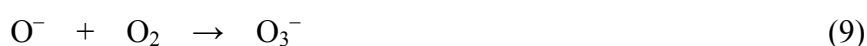
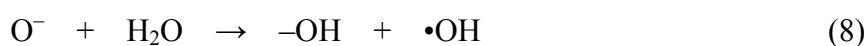
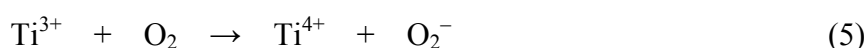
Utilizing semiconductor photocatalysts for aerobic oxidation of organic molecules has practical advantages of economical efficiency, environmental-friendliness, reusability, and durability. Up to now, various semiconductor materials have been tested as oxidation photocatalysts, and it is generally accepted that the anatase TiO₂ is the most reliable material owing to its low cost, high photostability, and high photocatalytic activity. When a semiconductor material is irradiated with photons equal to or greater than the band gap energy (e. g. $h\nu \geq 3.2$ eV for anatase TiO₂), electrons are excited in the conduction band and remaining holes are generated in the valence band (charge separation, eq 1).²¹ The excited electrons and positive holes can recombine on the surface or in the bulk of the particle in a few nano seconds and the energy dissipates as heat (recombination, eq 2).²¹



Since photocatalytic activity strongly depends on the efficiency of charge separation, it is a significant factor to inhibit recombination of the charge carriers. Addition of electron acceptors such as transition metals has been commonly employed in this context.²² Indeed, a series of various transition-metal loaded TiO_2 (M/TiO_2 ; $\text{M} = \text{Pt},^{23-28} \text{Rh},^{29} \text{Ru},^{30} \text{Ni},^{31} \text{Cu},^{32-34}$ and Ag^{35}) shows improved photocatalytic activity. Excited electrons in the conduction band and positive holes in the valence band can be also trapped by Ti^{4+} to form Ti^{3+} (eq 3) and O^{2-} (lattice oxygen) to form O^- (eq 4), respectively.³⁶



The valence band of anatase TiO_2 composed of O 2p orbital has a considerably positive potential (ca. +3.0 V vs. NHE).²¹ The trapped hole (O^-) is, therefore, able to oxidize most organic compounds. However, as partial oxidation products are generally more easily to be oxidized than parent substrate, over-oxidation to CO_2 is essentially associated with photocatalytic oxidation with TiO_2 due to the strong oxidizing ability. Moreover, photocatalytic system of anatase TiO_2 in aerobic condition generally produces various active oxygen species other than O^- as represented in eqs 5–9.^{21,28,36-38}



where $-\text{OH}$ represents surface hydroxyl group of TiO_2 . These active oxygen species are also highly oxidizing and trigger non-selective oxidation. Particularly in aqueous condition, formation of hydroxyl radical becomes dominant. With this background, most researchers have focused on application of TiO_2 to degradation reactions such as mineralization of volatile organic compounds (VOC) and water purification.³⁹ In this context, application of TiO_2 to selective catalytic oxidation

has been challenging.

Recently, a few efforts have been devoted to developing TiO_2 as a selective catalyst in the oxidation of various types of organic molecules such as alkanes,⁴⁰⁻⁴⁴ arenes,⁴⁵ and alcohols.⁴⁶⁻⁴⁸ The strategies employed are based on optimizing the solvent, the reaction conditions, or the preparation method of TiO_2 . However, over-oxidation to CO_2 or non-selective oxidation is inevitably associated even with these systems. To establish a selective photocatalytic oxidation system, one should focus on fundamental approaches to remove the undesired oxidation process caused by the active oxygen species.

Selective Photooxidation of Alcohols over Nb_2O_5

In 2007, Ohuchi et al.⁴⁹ reported that solvent-free aerobic oxidation of alcohol photocatalytically proceeded over niobium oxide (Nb_2O_5), and Nb_2O_5 showed higher selectivity to partial oxidation products than TiO_2 at a comparable conversion level (Figure 1). In this case, the highest photocatalytic activity is obtained when the calcination temperature of niobic acid hydrate as a catalyst precursor is 773 K. The photocatalytic activity correlates to the surface area and crystallinity which are decreases and increases with increase in calcination temperature, respectively.

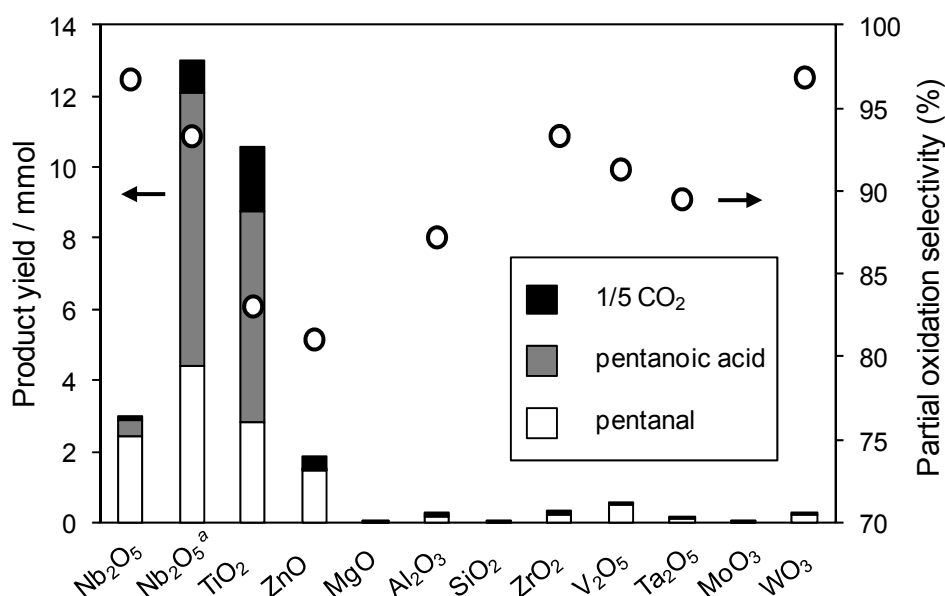
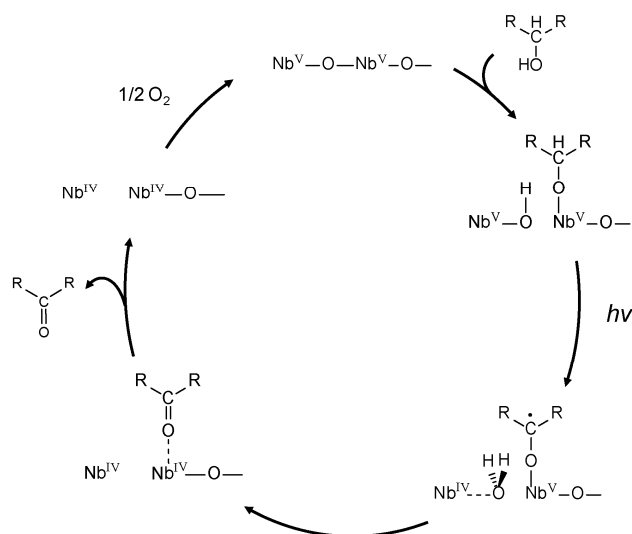


Figure 1. Photooxidation of 1-pentanol over various metal oxides. Reaction condition: pentanal (10 ml), catalyst (100 mg), O_2 flow ($2 \text{ ml} \cdot \text{min}^{-1}$) irradiation time (24 h). ^a irradiation time (84 h).

The mechanistic study⁵⁰ revealed that alcohol photooxidation over Nb₂O₅ was oxidative dehydrogenation via photoactivation of surface complex consisted of dissociatively adsorbed alcohol (alkoxide) and Nb₂O₅ as shown scheme 1: (a) dissociative adsorption of alcohol, (b) photoactivation of Nb₂O₅-alkoxide surface complex, (c) conversion of photogenerated carbon radical to carbonyl compound, (d) desorption of product, and (e) reoxidation of reduced Nb⁴⁺ sites by molecular oxygen. Moreover, although Nb₂O₅ catalyst is not able to absorb light at wavelengths longer than 390 nm, the photooxidation of 1-pentanol proceeds under irradiation up to ca. 480 nm. This phenomenon has been rationalized by generation of donor levels within the forbidden band of Nb₂O₅ due to the formation of alkoxide species. Thus, the mechanism they proposed is entirely different from classical electron transfer mechanism found in semiconductor photocatalysis; the formation of an excited electron in the conduction band and a positive hole in the valence band which trigger reduction and oxidation, respectively.



Scheme 1. Proposed reaction mechanism of alcohol photooxidation over Nb₂O₅

Survey of Part II

As mentioned above, Nb₂O₅ shows selective photocatalysis and unique photoactivation mechanism in the system of alcohol oxidation. But the photocatalytic activity of Nb₂O₅ is much lower than that of TiO₂. One of particular interest is whether the properties of Nb₂O₅ are also observed for substrates other than alcohol. In this context in chapter 4 and 5, the author applied Nb₂O₅ to aerobic photooxidation of amines and hydrocarbons, evaluated the photocatalytic performance, and investigated their reaction mechanisms in detail. The rationale for the higher selectivity observed for Nb₂O₅ than that for TiO₂ was also discussed and clarified.

The other interest is the methodologies to improve the photocatalytic performance of existing materials, in other words, how to increase the photocatalytic activity of Nb₂O₅ or to enhance the selectivity for TiO₂. In chapter 6, the author prepared a variety of metal loaded Nb₂O₅ photocatalysts

(M/Nb₂O₅; M = Pt, Rh, Ru, Ni, Cu, and Ag) for the purpose of increase in the photocatalytic activity in 1-pentanol oxidation due to promotion of charge separation. In addition, the Cu/Nb₂O₅ catalyst which showed much higher activity than bare Nb₂O₅ was applied to a wide scope of alcohols. In this case, however, no promotion effect was observed through the addition of Pt, Rh, Ru, Ni and Ag. This result strongly suggests that the role of Cu cannot be explained by the simple charge promotion mechanism. In chapter 7, the mechanism of alcohol photooxidation over Cu/Nb₂O₅ was investigated in detail to understand the role of Cu in enhancement of the photocatalytic activity in alcohol oxidation. In chapter 8, the author modified the electronic state of Cu on Cu/Nb₂O₅ by pretreatment to optimize the positive role of Cu revealed in the previous chapter. Correlation between photocatalytic activity of the modified Cu/Nb₂O₅ catalysts in alcohol photooxidation and the state of Cu on Cu/Nb₂O₅ was also studied by means of X-ray absorption fine structure (XAFS) spectroscopy. On the other hand, to develop a selective photocatalytic system using TiO₂-based material, one should inhibit non-selective oxidation caused by active oxygen species. In chapter 9, the author demonstrated a selectivity enhancement in alcohol photooxidation using TiO₂ covered with Nb₂O₅. Correlation between the selectivity and amount of photogenerated oxygen anion radical species was also discussed.

References

- (1) Hermans, I.; Spier, E. S.; Neuenschwander, U.; Turra, N.; Baiker, A. *Top. Catal.* **2009**, *52*, 1162.
- (2) Murahashi, S. I. *Angew. Chem. Int. Ed. Engl.* **1995**, *34*, 2443.
- (3) Larock, R. C. *Comprehensive Organic Transformations: A Guide to Functional Group Preparations*; VCH: New York, 1989.
- (4) Mallat, T.; Baiker, A. *Chem. Rev.* **2004**, *104*, 3037.
- (5) Sheldon, R. A.; Arends, I. W. C. E.; Dijkman, A. *Catal. Today* **2000**, *57*, 157.
- (6) Mori, K.; Yamaguchi, K.; Mizugaki, T.; Ebitani, K.; Kaneda, K. *Chem. Commun.* **2001**, 461.
- (7) Kaneda, K.; Yamashita, T.; Matsushita, T.; Ebitani, K. *J. Org. Chem.* **1998**, *63*, 1750.
- (8) Mizuno, N.; Yamaguchi, K. *Catal. Today* **2008**, *132*, 18.
- (9) Yamaguchi, K.; Mizuno, N. *Angew. Chem. Int. Ed.* **2003**, *42*, 1480.

- (10) Yamaguchi, K.; Mizuno, N. *Angew. Chem. Int. Ed.* **2002**, *41*, 4538.
- (11) Aschwanden, L.; Mallat, T.; Maciejewski, M.; Krumeich, F.; Baiker, A. *Chemcatchem* **2010**, *2*, 666.
- (12) Aschwanden, L.; Mallat, T.; Krumeich, F.; Baiker, A. *J. Mol. Catal. A: Chem.* **2009**, *309*, 57.
- (13) Enache, D. I.; Knight, D. W.; Hutchings, G. J. *Catal. Lett.* **2005**, *103*, 43.
- (14) Hutchings, G. J.; Carrettin, S.; Landon, P.; Edwards, J. K.; Enache, D.; Knight, D. W.; Xu, Y. J.; Carley, A. F. *Top. Catal.* **2006**, *38*, 223.
- (15) So, M. H.; Liu, Y. G.; Ho, C. M.; Che, C. M. *Chem. Asian J.* **2009**, *4*, 1551.
- (16) Kakiuchi, N.; Nishimura, T.; Inoue, M.; Uemura, S. *Bull. Chem. Soc. Jpn.* **2001**, *74*, 165.
- (17) Kakiuchi, N.; Maeda, Y.; Nishimura, T.; Uemura, S. *J. Org. Chem.* **2001**, *66*, 6620.
- (18) Mori, K.; Hara, T.; Mizugaki, T.; Ebitani, K.; Kaneda, K. *J. Am. Chem. Soc.* **2004**, *126*, 10657.
- (19) Mori, K.; Yamaguchi, K.; Hara, T.; Mizugaki, T.; Ebitani, K.; Kaneda, K. *J. Am. Chem. Soc.* **2002**, *124*, 11572.
- (20) Wu, H. L.; Zhang, Q. H.; Wang, Y. *Adv. Synth. Catal.* **2005**, *347*, 1356.
- (21) Mills, A.; LeHunte, S. *J. Photochem. Photobiol. A* **1997**, *108*, 1.
- (22) Anpo, M. *Bull. Chem. Soc. Jpn.* **2004**, *77*, 1427.
- (23) Siemon, U.; Bahnemann, D.; Testa, J. J.; Rodriguez, D.; Litter, M. I.; Bruno, N. *J. Photochem. Photobiol. A* **2002**, *148*, 247.
- (24) Hufschmidt, D.; Bahemann, D.; Testa, J. J.; Emilio, C. A.; Litter, M. I. *J. Photochem. Photobiol. A* **2002**, *148*, 223.
- (25) Ohtani, B.; Iwai, K.; Nishimoto, S.; Sato, S. *J. Phys. Chem. B* **1997**, *101*, 3349.
- (26) Sadeghi, M.; Liu, W.; Zhang, T. G.; Stavropoulos, P.; Levy, B. *J. Phys. Chem.* **1996**, *100*, 19466.
- (27) Hussein, F. H.; Pattenden, G.; Rudham, R.; Russell, J. J. *Tetrahedron Lett.* **1984**, *25*, 3363.
- (28) Anpo, M.; Aikawa, N.; Kubokawa, Y. *J. Phys. Chem.* **1984**, *88*, 3998.
- (29) Kohno, Y.; Hayashi, H.; Takenaka, S.; Tanaka, T.; Funabiki, T.; Yoshida, S. *J. Photochem. Photobiol. A* **1999**, *126*, 117.
- (30) Wetchakun, K.; Wetchakun, N.; Phanichphant, S. *Adv. Matel. Res.* **2008**, *55-57*, 853.

- (31) Prahov, L. T.; Disdier, J.; Herrmann, J. M.; Pichat, P. *Int. J. Hydrogen Energy* **1984**, *9*, 397.
- (32) Xin, B. F.; Wang, P.; Ding, D. D.; Liu, J.; Ren, Z. Y.; Fu, H. G. *Appl. Surf. Sci.* **2008**, *254*, 2569.
- (33) Arana, J.; Rodriguez, C. F.; Diaz, O. G.; Melian, J. A. H.; Pena, J. P. *Catal. Today* **2005**, *101*, 261.
- (34) Song, K. Y.; Kwon, Y. T.; Choi, G. J.; Lee, W. I. *Bull. Korean Chem. Soc.* **1999**, *20*, 957.
- (35) Alberici, R. M.; Jardim, W. F. *Water Res.* **1994**, *28*, 1845.
- (36) Berger, T.; Sterrer, M.; Diwald, O.; Knozinger, E.; Panayotov, D.; Thompson, T. L.; Yates, J. T. *J. Phys. Chem. B* **2005**, *109*, 6061.
- (37) Einaga, H.; Ogata, A.; Futamura, S.; Ibusuki, T. *Chem. Phys. Lett.* **2001**, *338*, 303.
- (38) Meriaudeau, P.; Vadrine, J. C. *J Chem Soc Farad T 2* **1976**, *72*, 472.
- (39) Demeestere, K.; Dewulf, J.; Van Langenhove, H. *Crit Rev Env Sci Tec* **2007**, *37*, 489.
- (40) Du, P.; Moulijn, J. A.; Mul, G. *J. Catal.* **2006**, *238*, 342.
- (41) Almquist, C. B.; Biswas, P. *Appl Catal a-Gen* **2001**, *214*, 259.
- (42) Boarini, P.; Carassiti, V.; Maldotti, A.; Amadelli, R. *Langmuir* **1998**, *14*, 2080.
- (43) Mu, W.; Herrmann, J. M.; Pichat, P. *Catal. Lett.* **1989**, *3*, 73.
- (44) Giannotti, C.; Legreneur, S.; Watts, O. *Tetrahedron Lett.* **1983**, *24*, 5071.
- (45) Wittenberg, R.; Pradera, M. A.; Navio, J. A. *Langmuir* **1997**, *13*, 2373.
- (46) Yurdakal, S.; Palmisano, G.; Loddo, V.; Alagoz, O.; Augugliaro, V.; Palmisano, L. *Green Chem* **2009**, *11*, 510.
- (47) Pillai, U. R.; Sahle-Demessie, E. *J. Catal.* **2002**, *211*, 434.
- (48) Muggli, D. S.; Falconer, J. L. *J. Catal.* **1998**, *175*, 213.
- (49) Ohuchi, T.; Miyatake, T.; Hitomi, Y.; Tanaka, T. *Catal. Today* **2007**, *120*, 233.
- (50) Shishido, T.; Miyatake, T.; Teramura, K.; Hitomi, Y.; Yamashita, H.; Tanaka, T. *J. Phys. Chem. C* **2009**, *113*, 18713.

Chapter 4

Selective Photooxidation of Amines Using Nb₂O₅

Abstract

Niobium oxide (Nb₂O₅) can function as a photocatalyst for selective oxidation of benzylamine rather than other semiconductor metal oxides such as TiO₂, ZnO and WO₃. Various amines including primary, secondary and cyclic amines are also photocatalytically converted to corresponding imines in excellent yields by using Nb₂O₅ in atmospheric pressure of O₂. Nb₂O₅ exhibits a catalytic activity with high selectivity even under visible light ($\lambda > 390$ nm) irradiation, although Nb₂O₅ does not absorb visible light. Mechanistic study revealed that the photooxidation of amine over Nb₂O₅ was oxidative dehydrogenation of amine to corresponding imine via photoactivation of surface complex consisted of dissociatively adsorbed amine (amide) and Nb₂O₅. When the substrate is a primary amine, the produced primary imine is immediately hydrolyzed and converted into dimerized imine. DFT calculations revealed that 1) the surface donor level derived from the adsorbed amide species was located in the forbidden band, 2) direct electron excitation from the surface donor level to the conduction band takes place by absorbing a photon, 3) the excitation energy from surface donor level to the Nb 4d conduction band is lower than that from the O 2p valence band to Nb 4d.

Introduction

Oxidation of amine to imine is an important chemical transformation because of the versatile applications of imines as synthetic intermediates of medicines or biologically active nitrogen containing organic compounds.¹ Several oxidation procedures using stoichiometric oxidants such as 2-iodoxybenzoic acid^{2,3} or *N-tert*-butylphenylsulfonimidoyl chloride⁴ have been reported. However, a catalytic system using molecular oxygen as a sole oxidant has been desired in view of green chemistry.^{5,6} In this context, a number of transition-metal catalyzed aerobic oxidation systems have been developed. Ru-based catalysts such as RuCl₃,⁷ [RuCl₂(RCH₂NH₂)₂(PPh₃)₂],^{8,9} Ru-porphyrin,¹⁰ Ru-hydroxyapatite,¹¹ Ru₂(OAc)₄Cl,¹² and Ru/Al₂O₃¹³ are known to be effective for aerobic oxidation of amines. Au nanoparticles supported on Al₂O₃,^{14,15} CeO₂,^{14,15} graphite,¹⁶ and hydroxyapatite¹⁶ are also found to be good catalysts for amine oxidation. But in these systems, expensive precious metals are employed and relative high temperature (mostly > 373 K) is required.

Utilizing semiconductor photocatalysts for aerobic oxidation of organic molecules has practical advantages of economical efficiency, environmental-friendliness, reusability, and durability. In addition, to effectively utilize solar energy, it is necessary to develop a material that will function under visible light.¹⁷ Very recently, Su and co-workers reported that mesoporous graphite carbon nitride (mpg-C₃N₄) can work as effective photocatalyst to activate O₂ for the selective oxidations of benzylic alcohols and amines with visible light^{18,19} Although this material exhibits excellent catalytic performance under visible light irradiation, high oxygen pressure (0.5 MPa) and trifluorotoluene as solvent are necessary to obtain good yields. Zhao et al. reported that photooxidation of amines using TiO₂ with UV light gave a high selectivity to imines under a diluted condition.²⁰ We recently reported that photocatalytic oxidation of various alcohols proceeded selectively over niobium oxide (Nb₂O₅) under a mild condition.^{21,22} Nb₂O₅ showed higher selectivities to partial oxidation products; therefore it can be thought that Nb₂O₅ is more suitable for selective oxidation than TiO₂. Moreover, we found that Nb₂O₅ can catalyze the selective photooxidation of alcohols even under visible light irradiation up to 450 nm, although the band gap of Nb₂O₅ is at 390 nm (3.2 eV).

In the present study, we report that photocatalytic aerobic oxidations of various amines to

imines take place over Nb_2O_5 with high yields at room temperature and atmospheric pressure. Nb_2O_5 exhibits a catalytic activity in high selectivity even under visible light irradiation as well as alcohol oxidation. Mechanistic study was also carried out to understand the catalysis and the mechanism of visible response.

Experimental

Preparation

Niobium oxide hydrate ($\text{Nb}_2\text{O}_5 \cdot n\text{H}_2\text{O}$, HY-340) was kindly supplied from CBMM. Niobium oxide (Nb_2O_5) catalyst was prepared by calcinations of niobium oxide hydrate in a dry air flow at 773 K for 5 h (BET surface area: $48 \text{ m}^2 \cdot \text{g}^{-1}$). BET surface areas of catalysts were determined using N_2 adsorption isotherm at 77 K measured by a BELSORP 28SA (BEL Japan Corp.). TiO_2 , ZrO_2 and CeO_2 samples used in this study were supplied from Japan Catalysis Society and were calcined at 773 K for 5 h (JRC-TIO-4, equivalent to Degussa. P-25; rutile/anatase = 3/7; BET surface area = $49 \text{ m}^2 \cdot \text{g}^{-1}$, JRC-ZRO-1 and JRC-CEO-1). MoO_3 and WO_3 were prepared by calcination (773 K, 5 h) of ammonium paratungstate ($(\text{NH}_4)_{10}(\text{H}_2\text{W}_{12}\text{O}_{42}) \cdot 4\text{H}_2\text{O}$) and molybdic acid (H_2MoO_4), respectively. V_2O_5 , Ta_2O_5 and ZnO were purchased from Wako Pure Chemical Industries, Ltd and were calcined at 773 K for 5 h. All catalysts were ground into powder under 100 mesh (0.15 mm) after calcination. All reagents (substrate and solvent) were of reagent grade and were obtained from Aldrich Chemical Co., Tokyo Kasei Kogyo Co., Ltd and Wako Pure Chemical Industries, Ltd. According to the literature,²³ *N*-deuterated benzylamine (benzylamine-*N*- d_2) was prepared by washing of benzylamine (3 g) in CH_2Cl_2 (5 ml) with D_2O (3 ml) three times, followed by separation, evaporation of CH_2Cl_2 , and distillation. An ^1H NMR spectrum indicated >90% deuterium content at the α positions by comparison of the α signals' integral with that of the benzylic position.

Reaction Conditions of Photooxidation of Amine

The photocatalytic oxidation of amines was carried out in a batch system under atmospheric oxygen. Nb_2O_5 (100 mg), amine (5 mmol), benzene as a solvent (10 ml), and a stirring bar were

introduced to the Pyrex glass reactor. The substrate was used without further purification. The suspension was stirred vigorously at room temperature and irradiated through the flat bottom of the reactor by reflection from a cold mirror with a 500 W ultra-high pressure Hg lamp (USHIO Denki Co.). The organic products were identified by GC-MS (Shimadzu GC-MS QP5050) and $^1\text{H-NMR}$ (JEOL ECX400) and quantified by FID-GC (Shimadzu GC-14B) using chlorobenzene as an internal standard. For kinetic analysis, benzylamine or dibenzylamine was used as a substrate. Substrate concentration and oxygen pressure were balanced by using benzene and nitrogen when required, respectively. The light intensity was controlled using a metal mesh. To measure an action spectrum, the reaction was carried out in a batch reactor with Nb_2O_5 (200 mg) and benzylamine (4 mmol) and benzene as a solvent (5 ml) using a monochromatic irradiator (JASCO CRM-FA Spectro Irradiator) as light source.

UV-Vis spectra

Diffuse reflectance spectra (1 nm resolution) were obtained with a UV-Vis spectrometer (JASCO UV570). A slurry of the mixture of benzylamine (0.8 ml) and Nb_2O_5 (500 mg) was used as the sample of benzylamine adsorbed on Nb_2O_5 .

FT-IR spectra

FT-IR spectra of the sample before and during photo irradiation were recorded with a Perkin-Elmer SPECTRUM ONE Fourier transform infrared spectrometer. The resolution of the spectra was 4 cm^{-1} . A Nb_2O_5 sample was cast into a pellet with diameter 12 mm. The molded sample was introduced into an in situ IR cell equipped with BaF_2 windows. Prior to the measurements, the sample was pretreated with 6.7 kPa of O_2 for 1 h and evacuated at 673 K for 0.5 h. A 200 W Hg-Xe lamp (SAN-EI ELECTRIC SUPERCURE-204S) was used as light source. An L-42 cutoff filter was used for visible light irradiation ($> 390\text{ nm}$). 6.7 kPa of O_2 was introduced onto the Nb_2O_5 with adsorbed amine before photo-irradiation.

ESR spectra

ESR measurements were carried out using an X-band ESR spectrometer (JEOL JES-SRE2X) with in situ quartz cell. Prior to the measurements, the sample was pretreated with 6.7 kPa of O₂ for 1 h and evacuated at 673 K for 0.5 h. The *g* value of the radical species was determined using a Mn(II) marker. The ESR spectra of Nb₂O₅ with adsorbed amine were recorded before and after photo-irradiation. A 500 W ultra-high pressure Hg lamp was used as light source. An L-42 cutoff filter was used for visible light irradiation (> 390 nm). ESR spectral simulations were performed using the Win-EPR SimFonia software package from Bruker, software version 1.25, 1996.

Surface models and DFT calculation method

Quantum chemical calculations using the DFT method as implemented in Gaussian 03²⁴ were carried out to investigate the electronic structure and excitation energy of the Nb₂O₅ and Nb₂O₅-amide complex. We used the neutral Nb₁₂O₄₃H₂₆ cluster (**1**) in this study which was obtained from the structure of H-Nb₂O₅²⁵ by saturating the peripheral oxygen atoms with hydrogen atoms. The Nb₁₂O₄₂H₂₅(NHCH₃) cluster (**2**) as a model of the Nb₂O₅-amide complex was obtained by substitution of one OH group of the Nb₁₂O₄₃H₂₆ cluster. The calculation made use of Becke's three parameter hybrid (B3LYP) method involving Lee et al.'s correlation function^{26,27} and the LanL2DZ basis set for a single point energy calculation. One-electron excitation energies of model clusters were also obtained by time-dependent (TD) calculations²⁸⁻³⁰ with singlet spin multiplicity.

Results and Discussion

Photooxidation of Benzylamine over Various Metal Oxides

Photocatalytic activity and selectivity in the aerobic oxidation of benzylamine over various metal oxides were examined as summarized in Table 1. TiO₂, ZnO, and Nb₂O₅ show much higher yields of *N*-benzylidene benzylamine than other oxides (Table 1, entry 1–3). Nb₂O₅ showed the highest yield per mole of catalyst (Table 1, entry 3). TiO₂, which is an extensively used photocatalyst, also exhibited higher yield than Nb₂O₅ and ZnO. However the selectivity to *N*-benzylidene benzylamine was comparatively low because benzaldehyde was formed as a byproduct (Table 1,

entry 1). The highest selectivity was obtained with Nb₂O₅ among the metal oxides tested. When benzylamine was photoirradiated in the absence of any catalyst, a very low yield was observed (Table 1, entry 11). The evolution of photogenerated products over Nb₂O₅ responded to illumination. Moreover, no product was detected in the dark with the Nb₂O₅ catalyst (Table 1, entry 4). These indicate that that photooxidation over the Nb₂O₅ catalyst was due entirely to a photocatalytic reaction.

Table 1. Oxidation of benzylamine over various metal oxides.^a

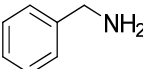
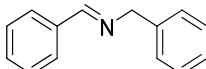
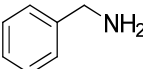
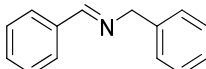
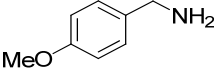
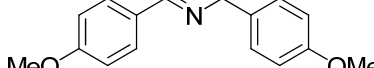
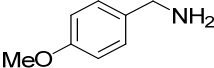
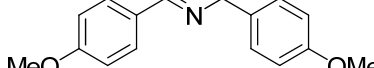
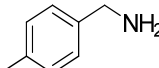
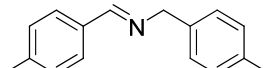
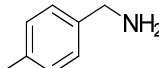
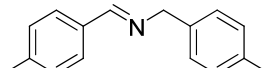
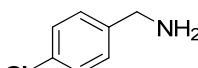
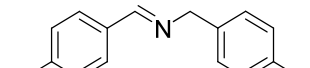
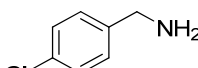
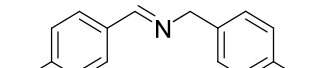
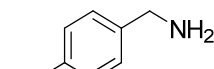
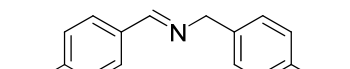
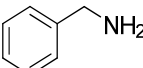
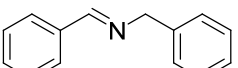
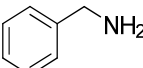
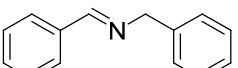
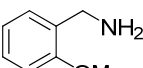
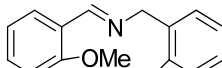
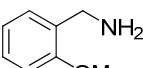
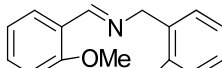
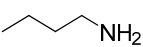
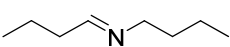
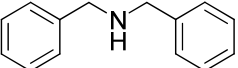
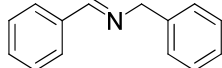
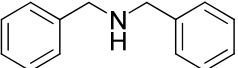
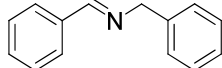
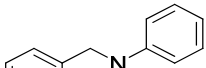
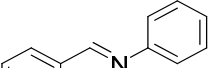
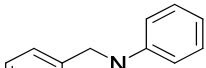
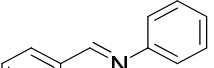
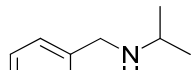
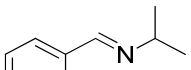
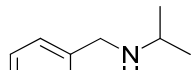
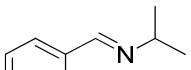
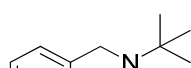
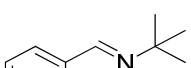
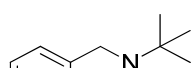
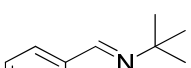
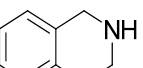
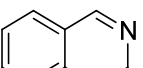
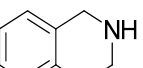
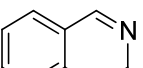
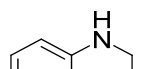
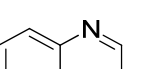
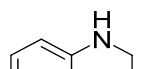
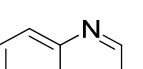
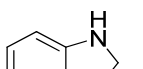
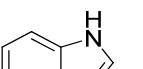
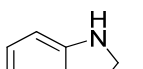
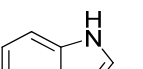
Entry	catalyst	Yield (μmol)	Yield (μmol / mmol cat) ^b	Selectivity (%) ^c
1	TiO ₂	886	708	89
2	ZnO	790	643	94
3	Nb ₂ O ₅	649	915	98
4 ^d	Nb ₂ O ₅	n. d.	–	–
5	MoO ₃	328	472	97
6	CeO ₂	264	497	97
7	Ta ₂ O ₅	201	444	96
8	ZrO ₂	175	216	95
9	WO ₃	143	332	89
10	V ₂ O ₅	322	298	59 ^e
11	none	199	–	81

^a Reaction conditions: catalyst (100 mg), benzylamine (5 mmol), benzene as a solvent (10 ml), irradiation time (5 h), oxygen pressure (1 atm), ^b amount of *N*-benzylidene benzylamine per mole of catalyst. ^c selectivity to *N*-benzylidene benzylamine. Benzaldehyde was yielded as a main by-product except entry 10. ^d In the dark. ^e Benzylamine-*N*-carbaldehyde was formed as a main by-product.

Photooxidation of Various Amines over Nb₂O₅

The oxidation of various amines including primary, secondary and bicycloamine derivatives were examined by using the Nb₂O₅ photocatalyst (Table 2). Primary benzylamine derivatives bearing various functional groups (OMe, Me, H, Cl, and CF₃) were converted to corresponding coupled imines with excellent yields (Table 2, entries 1–7). Electron-rich benzylamines (OMe and Me derivatives) were oxidized faster than electron-deficient ones (Cl and CF₃ derivatives) (Table 2, entries 2–5). The reaction rate of the regioisomer increased in the order of *ortho* < *meta* < *para* isomer, indicating the presence of a steric effect (Table 2, entries 2, 6, and 7). A primary aliphatic amine was also converted to the corresponding coupled imine, but the selectivity was lower than those of benzylic homologues (Table 2, entry 8). Secondary *N*-alkylbenzylamines (alkyl = Bn, Ph, *i*Pr, and *t*Bu) were also oxidized to dehydrogenated imines. (Table 2, entries 9–12). Relative high yields were observed within 20 h in the oxidations of *N*-isopropylbenzylamine and dibenzylamine. On the other hand, *N*-phenyl and *N*-*tert*-butyl derivatives were oxidized very slowly. The order of reaction rates corresponding to the bulkiness of the alkyl moiety (*i*Pr > Bn >> *t*Bu > Ph) indicates that steric hindrance around the nitrogen atom is a key factor for the reaction rate. Benzaldehyde was formed as a byproduct in the oxidations of these secondary benzylic amines. The formation of benzaldehyde is attributed to the oxidative cleavage of the C–N bond. In addition, a small amount of *N*-benzylidene benzylamine was also yielded in these cases. This indicates an involvement of the C–N bond cleavage, followed by coupling of the fragments. 1,2,3,4-Tetrahydroisoquinoline was smoothly converted to mono-dehydrogenated 3,4-dihydroisoquinoline with high yield (Table 2, entry 13). In contrast, the rate of oxidation of 1,2,3,4-tetrahydroquinoline to aromatized quinoline was much slower than the *iso*-isomer (Table 2, entry 14). In this case, a small amount of mono-dehydrogenated 3,4-dihydroquinoline as an intermediate product was also detected. The significant difference of the reaction rate between the tetrahydroquinoline isomers is generally observed in various catalytic systems.^{12,16,19,31} Indole was yielded with moderate selectivity in the oxidation of indoline. The Nb₂O₅ photocatalyst was reusable and showed the same conversion and selectivity without any pretreatment as the catalyst as prepared. The amine oxidations over Nb₂O₅ took place even under visible light (> 390 nm) irradiation (Table 2, entries 1'–15'). Although the reaction rates were lower than that under UV (> 300 nm) irradiation, comparable selectivities were obtained. In the absence of Nb₂O₅, oxidation of benzylamine did not proceed under visible irradiation.

Table 2. Aerobic oxidation of various amines to corresponding imines using Nb₂O₅.^a

Entry	Substrate	Product	T / h	Conv. (%)	Sel. (%)
1			50	>99	97
1'			24	21	97
2			24	>99	99
2'			24	29	94
3			38	>99	95
3'			24	19	94
4			45	>99	98
4'			24	12	94
5			51	>99	96
6			27	>99	95
6'			24	30	95
7			29	>99	94
7'			24	16	95
8			24	>99	61
9			20	97	71
9'			24	16	70
10			48	15	63
10'			24	2.5	86
11			15	82	92
11'			24	47	91
12			24	30	88
12'			24	13	89
13			11	>99	92
13'			24	47	85
14			48	43	70
14'			24	4.2	84
15			24	39	64
15'			24	2.4	87

^a Reaction condition: Nb₂O₅ (100 mg), substrate (5 mmol), benzene as a solvent (10 ml), λ > 300 nm (entries 1–15) or λ > 390 nm (entries 1'–15'), oxygen pressure (1 atm).

FT-IR Measurement for Adsorbed Species

In order to understand the reaction mechanism of amine photooxidation over Nb₂O₅, the adsorbed species on Nb₂O₅ before and during photoirradiation were characterized in detail by FT-IR. Figure 1 shows FT-IR spectra obtained when benzylamine was adsorbed on Nb₂O₅. Although two bands assigned to NH₂ bending vibration (δ_{SNH_2})³² were observed at 1620 and 1583 cm⁻¹ upon the introduction of benzylamine, the band at 1583 cm⁻¹ grew with increase in the introduction time (Figure 1B, form a–e). After evacuation at room temperature, the band at 1620 cm⁻¹ disappeared whereas the band at 1583 cm⁻¹ remained (Figure 1B, e and f). These results indicate that the bands at 1620 and 1583 cm⁻¹ correspond to physisorbed and chemisorbed species, respectively. A similar behavior was also observed for the bands assigned to C–N stretching vibration ($\nu_{\text{C-N}}$)³² at 1129, 1071, and 1035 cm⁻¹ (the former two correspond to chemisorption). In contrast, other bands due to CH₂ bending vibrations (ω_{CH_2} ; 1380 cm⁻¹, δ_{sCH_2} ; 1456 cm⁻¹)³² and C–C stretching vibrations of aromatic ring ($\nu_{\text{C-C}}$; 1499 and 1525 cm⁻¹)³² showed continuous growths. In the region of >3100 cm⁻¹, the band at 3442 and 3245 cm⁻¹ corresponding to $\nu_{\text{O-H}}$ and $\nu_{\text{N-H}}$ developed with time (Figure 1A). The corresponding bands for $\nu_{\text{O-D}}$ and $\nu_{\text{N-D}}$ were observed at 2544 and 2400 cm⁻¹ with use of benzylamine-*N-d*₂ (Figure 2, a–d). The experimental ratios of $\nu_{\text{O-H}}/\nu_{\text{O-D}}$ and $\nu_{\text{N-H}}/\nu_{\text{N-D}}$ are both 1.35, in good agreement with the theoretical ratio of 1.37 expected for H–D isotopic exchange. These strongly suggest that the appearance of O–H(D) bond is due to dissociative adsorption of benzylamine at N–H(D) moiety. The band at 3734 cm⁻¹ assigned to $\nu_{\text{O-H}}$ of surface hydroxyl groups, on the other hand, decreased immediately after the introduction of benzylamine. This band was recovered after evacuation (Figure 1A, e and f), indicating an interaction between the surface hydroxyl groups and physisorbed benzylamine. The corresponding band for $\nu_{\text{O-D}}$ was observed at 2700 cm⁻¹ in addition to the band at 2545 cm⁻¹ upon exposure to D₂O (Figure 2, e–g). The experimental ratio of $\nu_{\text{O-H}}/\nu_{\text{O-D}}$ (1.38; 3734 cm⁻¹ / 2545 cm⁻¹) shows a good agreement with the theoretical ratio of 1.37. On the basis of these results, the adsorption fashion of benzylamine on Nb₂O₅ can be summarized as shown in scheme 1. The introduced benzylamine weakly interacts with an isolated surface hydroxyl group as a physisorbed species at first. Dissociative adsorption of benzylamine occurs to form an amide species as a chemisorbed species and a bridging hydroxyl group. These two hydroxyl groups are also generated by heterolytic adsorption of water.

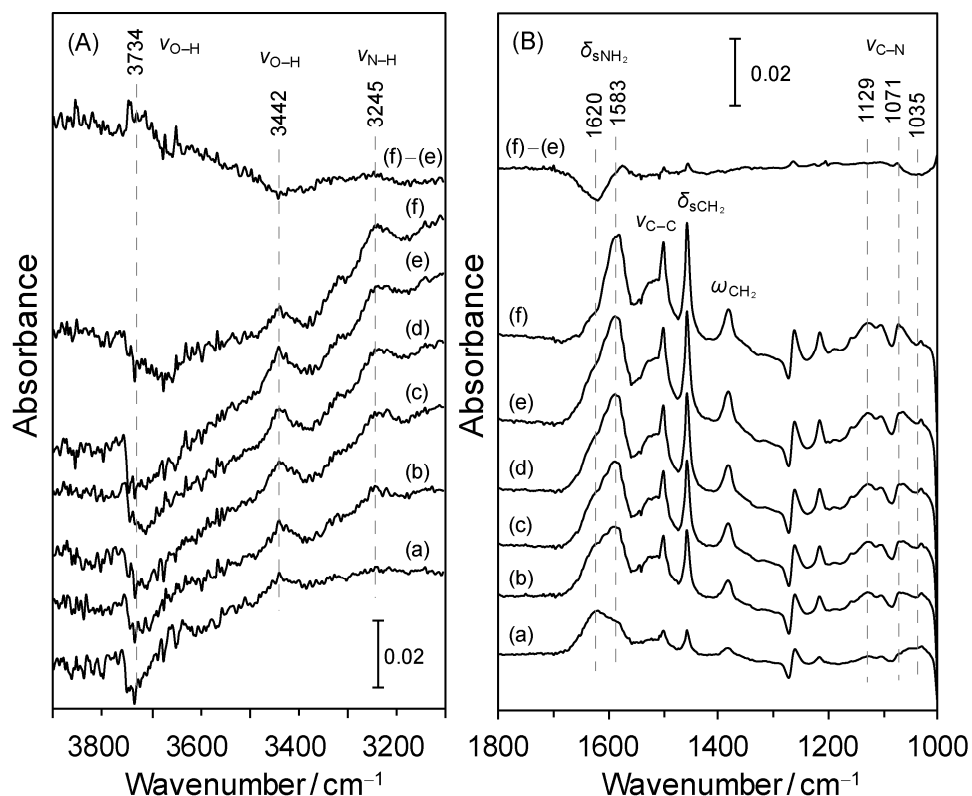


Figure 1. FT-IR spectra obtained when Nb_2O_5 was exposed to $0.6\mu\text{mol}$ of benzylamine for (a) 1, (b) 10, (c) 20, (d) 30, and (e) 40 min, (f) followed by evacuation. The regions of (A) $3100\text{--}3900\text{ cm}^{-1}$ and (B) $1000\text{--}1800\text{ cm}^{-1}$ are shown.

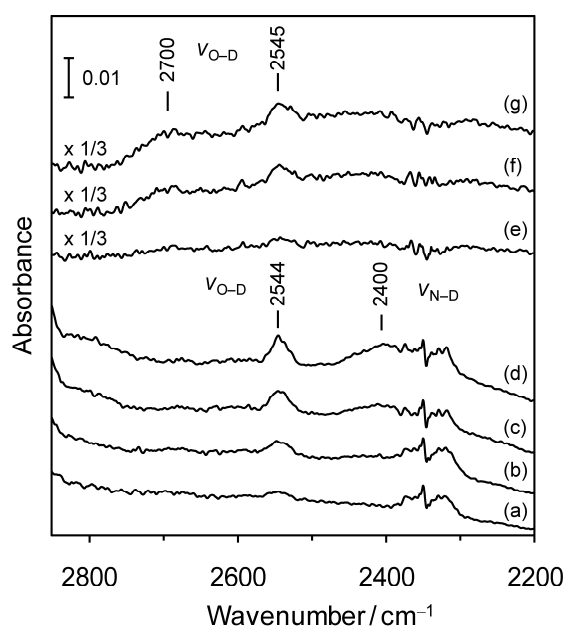
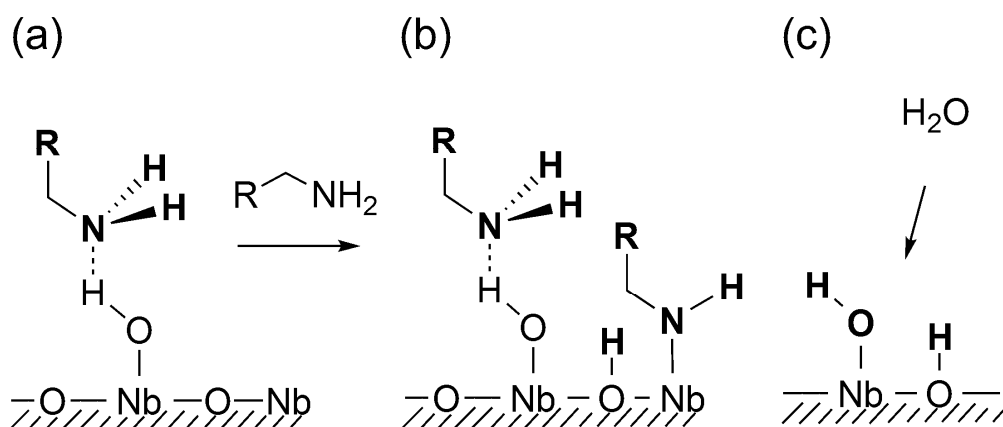


Figure 2. FT-IR spectra obtained when (a) 0.45 , (b) 0.98 , (c) 1.6 , and (d) $2.8\ \mu\text{mol}$ of benzylamine- $N\text{-}d_2$ was introduced or Nb_2O_5 was exposed to (e) 0.04 , (f) 0.17 , and (g) $0.28\ \text{kPa}$ of D_2O , respectively.



Scheme 1. Proposed adsorption fashion of benzylamine on Nb₂O₅ and water: (a) physisorption of benzylamine to an isolated surface hydroxyl group, (b) chemisorption of benzylamine to form an amide species as and a bridging hydroxyl group, and (c) dissociative adsorption of water.

After the evacuation, the sample containing the chemisorbed species was exposed to illumination of visible light ($h\nu > 390$ nm). Figure 3 shows the changes in FT-IR spectra during the irradiation. As irradiation time increased, the bands for ν_{C-N} (1071 and 1129 cm^{-1}), ω_{CH_2} (1363 cm^{-1}), δ_{sCH_2} (1456 cm^{-1}), δ_{sNH_2} (1583 cm^{-1}), and ν_{N-H} (3260 cm^{-1}) which belonged to the amide species decreased (Figure 3, blue arrows). In contrast, several bands were newly observed in the whole region. The peak positions of the developed bands within 1200–1800 cm^{-1} are in good agreements with those of authentic benzaldehyde adsorbed on Nb₂O₅ (Figure 3, red arrows). The prominent bands at 1648, 1547, and 1410 cm^{-1} are assigned to $\nu_{C=O}$, ν_{C-C} (aromatic), and δ_{sCHO} , respectively.³² The band around 1049 cm^{-1} and the broad feature in the region of 2800–3600 cm^{-1} were absent in the spectrum of authentic benzaldehyde. These features are in accordance with those of ammonia adsorbed on Nb₂O₅ (Figure 3, green arrows). The broad feature within 2800–3600 cm^{-1} can be assigned to an ensemble of various modes such as symmetric and asymmetric stretching vibrations (ν_{sN-H} and ν_{asN-H}) or overtone of asymmetric bending of NH₃ (δ_{asNH_3}).^{33–35} Other bands characteristic to the adsorbed ammonia (δ_{sNH_3} ; 1199 and 1431 cm^{-1} , δ_{asNH_3} ; 1602 cm^{-1})^{33–35} seem to be overlapped with those for benzaldehyde in the spectra during irradiation. These results clearly show that the adsorbed amide species was converted into benzaldehyde and ammonia, which was triggered by visible light. In the cases of secondary alcohols, corresponding dehydrogenated imines were yielded

as mentioned above, whereas, no evidence for the dehydrogenated primary imine was obtained by FT-IR at room temperature. This indicates that hydrolysis of the primary imine to aldehyde immediately takes place.

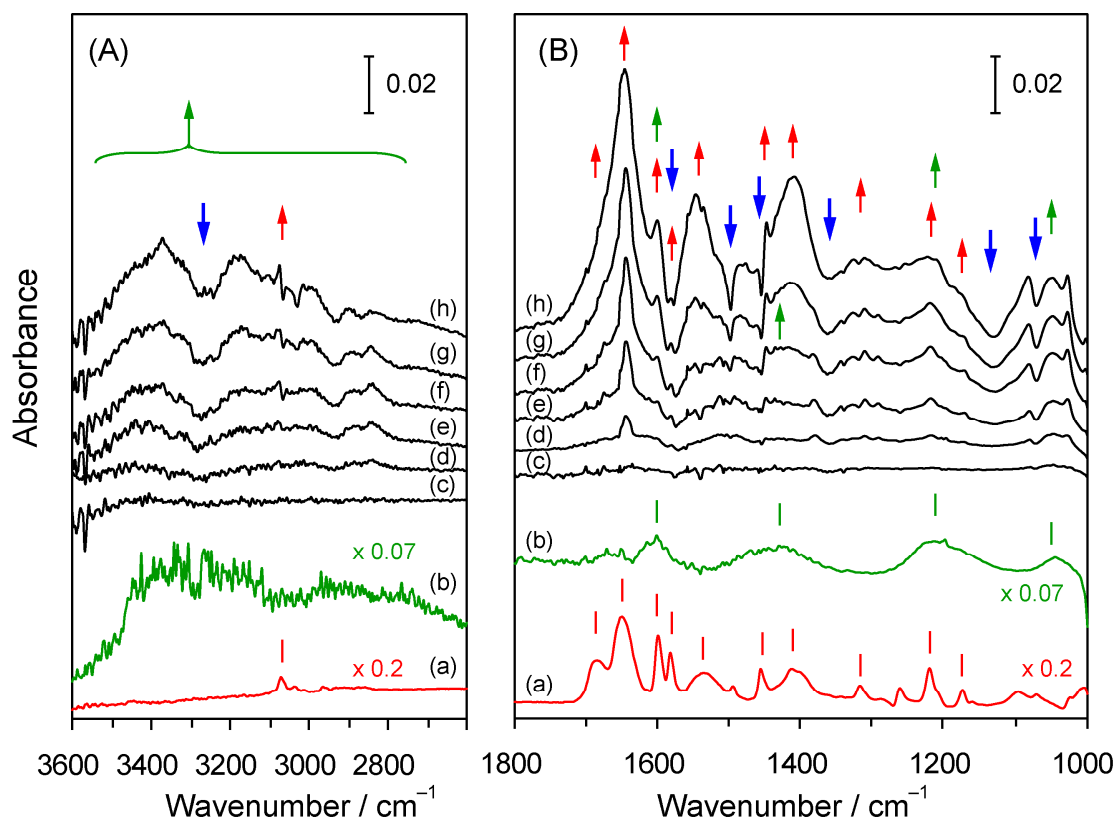


Figure 3. FT-IR spectra of (a) benzaldehyde and (b) ammonia adsorbed on Nb₂O₅ after evacuation and differential FT-IR spectra before and after irradiation of visible light ($h\nu > 390$ nm) to benzylamine chemisorbed on Nb₂O₅ for (b) 1, (c) 10, (d) 30, (e) 60, (f) 120, and (g) 180 min. The regions of (A) 2600–3600 cm⁻¹ and (B) 1000–1800 cm⁻¹ are shown.

Wavelength Dependence on the Apparent Quantum Yield

Figure 4 shows the apparent quantum yield of the benzylamine photooxidation over Nb₂O₅ as a function of the wavelength of the incident light (action spectrum). UV-Vis spectra of Nb₂O₅ before and after the adsorption of benzylamine on Nb₂O₅, and difference spectrum were also described. Nb₂O₅ shows an intense broad band at 300 nm due to band gap excitation, but no absorption in the region of $\lambda > 390$ nm (Figure 4A, trace 1). As mentioned above, oxidation of various amines

proceeded over Nb_2O_5 under visible irradiation ($h\nu > 390 \text{ nm}$). The action spectrum indeed does not agree with the UV-Vis spectrum of Nb_2O_5 , and the reaction is responsive to light up to 460 nm (Figure 4B, plot 4). Figure 4A, trace 2 shows UV-Vis spectrum obtained when benzylamine was added to Nb_2O_5 . The absorption band at 300 nm extended to higher wavelength region and the differential spectrum before and after the adsorption of benzylamine showed a new absorption band at ca. 350 nm which was overlapped with the region of $>390 \text{ nm}$ (Figure 4B, trace 3). Since benzylamine itself exhibits no absorption in the region of $>300 \text{ nm}$, the new absorption can be ascribed to a surface species derived from adsorbed amine. This surface species corresponds to an Nb_2O_5 -amide surface complex according to the results of FT-IR study, as shown in Scheme 2b. Moreover, the differential spectrum shows a good agreement with the action spectrum, which strongly suggest that the amine oxidation is triggered by light absorption by the surface complex. On the basis of these results we proposed a possible rationale for the visible-response photooxidation; generation of surface donor levels within the forbidden band of Nb_2O_5 owing to the formation of the surface complex, and direct electron excitation from the donor level to the conduction band of Nb_2O_5 .

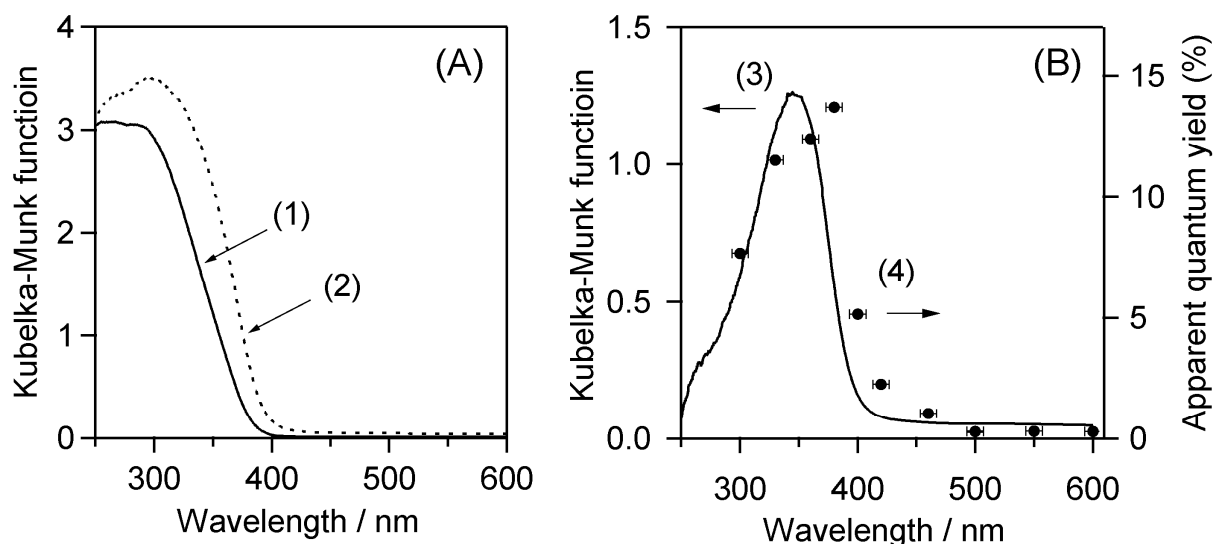


Figure 4. (A) UV-Vis spectra of (1) Nb_2O_5 , and (2) Nb_2O_5 with adsorbed benzylamine. (B) (3) Differential UV-Vis spectrum of (2) – (1) and (4) action spectrum of benzylamine photooxidation over Nb_2O_5 .

DFT Calculations for Excitation Mechanism

To demonstrate theoretically the proposed photoactivation mechanism, the electronic structures of Nb₂O₅ and Nb₂O₅-amide surface complex were estimated and compared by DFT calculations using model clusters. Figure 5a shows the model cluster of Nb₂O₅ (Nb₁₂O₄₃H₂₆; **1**) and that of amide adsorbed on Nb₂O₅ [Nb₁₂O₄₂H₂₅(NHCH₃); **2**]. In the cluster **2**, one of the hydroxyl groups is substituted with a methylamide. The occupied and the unoccupied Kohn-Sham orbitals (KS) of these model clusters dominantly consist of delocalized O 2p orbitals and Nb 4d orbitals, respectively (Figure 6). These compositions are consistent with the band structure of Nb₂O₅.

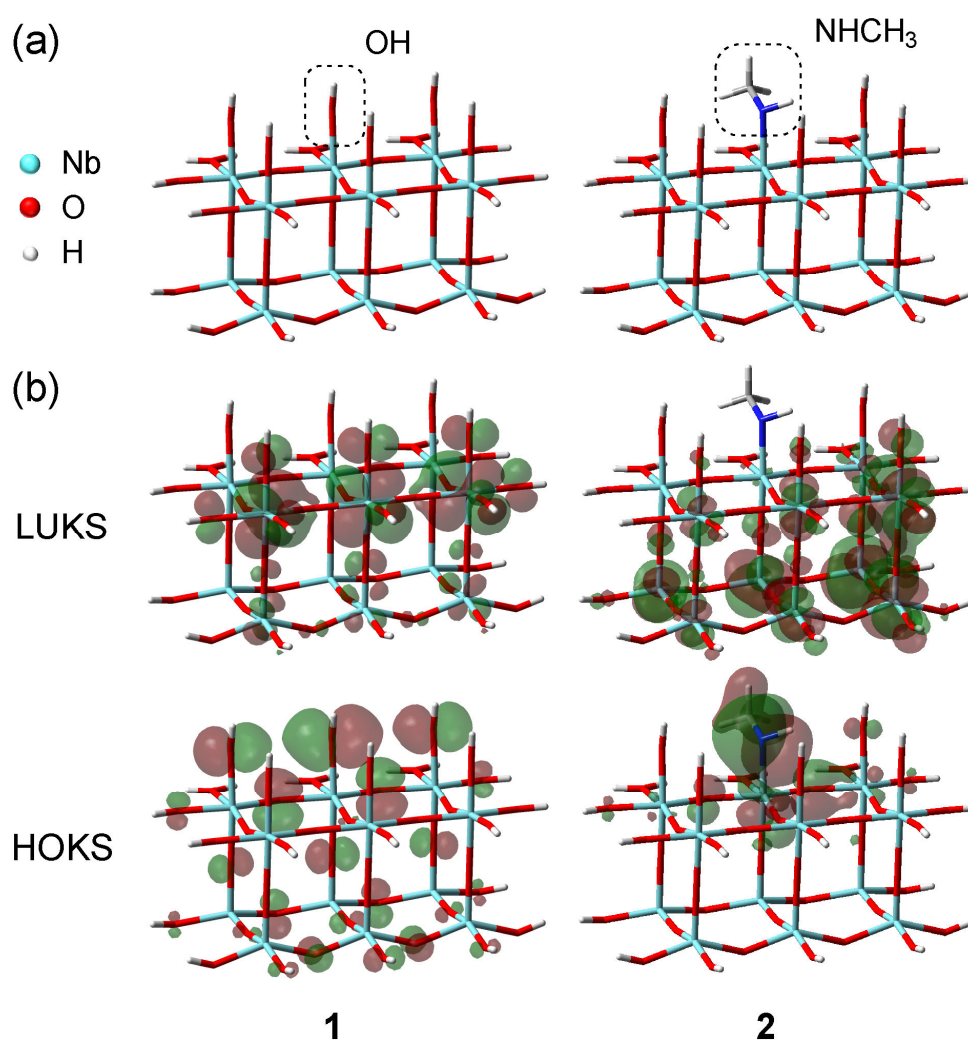


Figure 5. (A) Model cluster of Nb₂O₅ (Nb₁₂O₄₃H₂₆; **1**) and that of amide adsorbed on Nb₂O₅ [Nb₁₂O₄₂H₂₅(NHCH₃); **2**]. (B) Graphical illustrations of LUKS and HOKS of **1** and **2**.

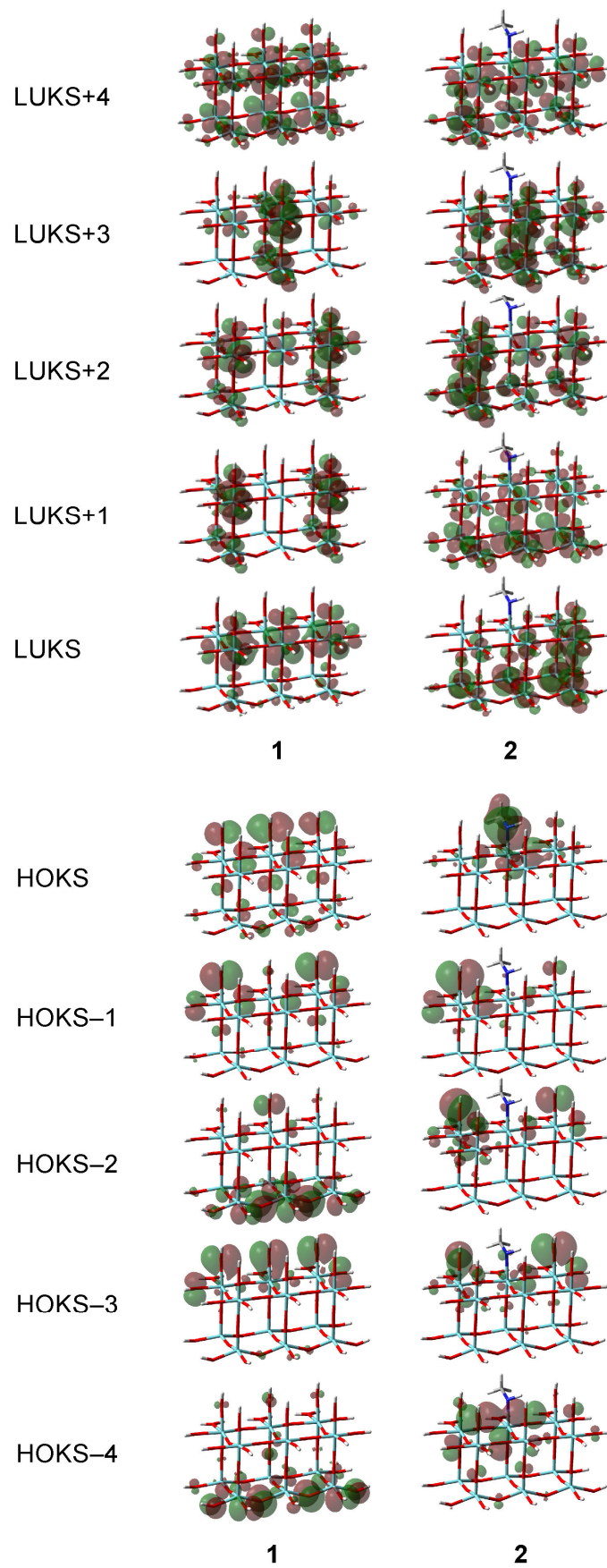


Figure 6. Graphical illustrations of occupied and unoccupied KSOs of **1** and **2**.

Figure 5b shows schematic illustrations of the highest occupied and the lowest unoccupied Kohn-Sham orbitals (HOKS and LUKS) of **1** and **2**. The cluster **2** exhibits quite a different electronic structure of HOKS from the cluster **1**; HOKS of **1** is composed by delocalized O 2p orbitals, whereas that of **2** is made up of N 2p orbital localized on the amide nitrogen atom. Moreover, the energy level of HOKS of **2** is higher than that of HOKS of **1**, while those of LUKS–LUKS+4 are almost same whether **1** or **2** (Figure 7). These results clearly show that a donor level whose population is localized on the amide nitrogen is generated by formation of Nb₂O₅-amide surface complex. Indeed, the electron excitation energies of **1** and **2** calculated by TD-DFT revealed that lower energy transition takes place with **2** than with **1** (Table 3). Thus, the photooxidation of amine led by lower-energy light than the band gap of Nb₂O₅ can be explained by excitation of the surface complex, i.e., direct electron transition from N 2p orbital localized on amide nitrogen to Nb4d orbital composing conduction band of Nb₂O₅ (Scheme 2).

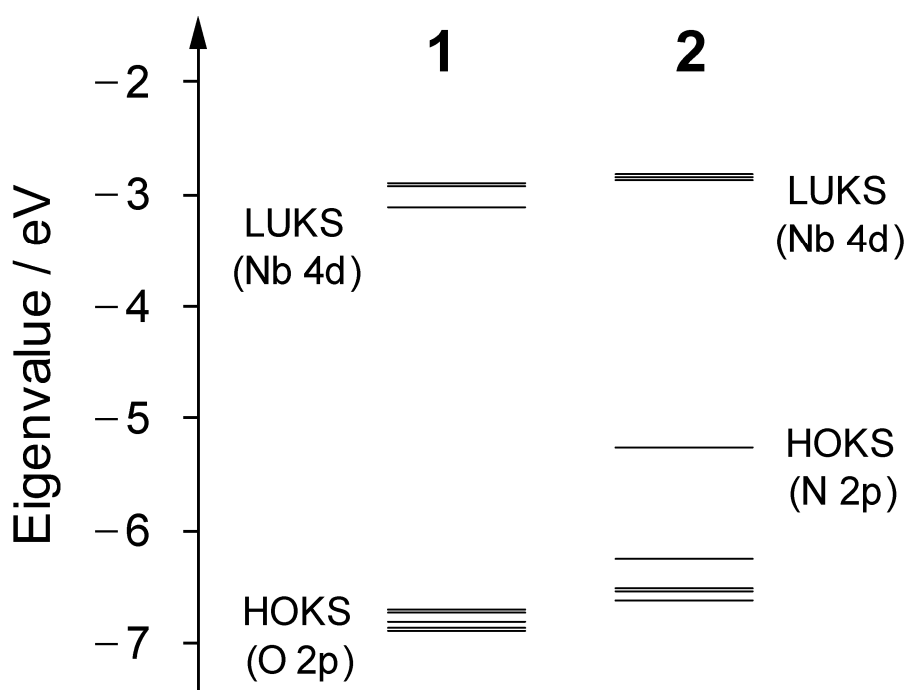
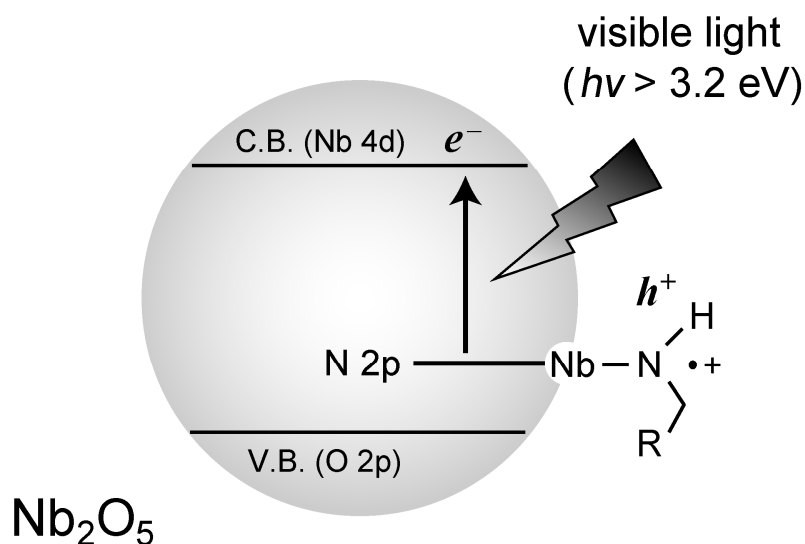


Figure 7. Energy diagram of the frontier KSOs of **1** and **2**.

Table 3. Electron excitation energies of **1** and **2** estimated by TD-DFT calculations.

entry	model	energy / eV	f^a	assignment ^b
1	1	2.82	0.0018	H-6 → L+2 (43%)
2		2.82	0.0001	H-6 → L+1, L+3 (54%)
3		2.84	0.0003	H → L (63%)
4	2	1.92	0.0008	H → L (65%)
5		1.95	0.0010	H → L+2 (51%)
6		2.01	0.0031	H → L+1, L+2 (98%)

^aOscillator strength. ^bOnly the major parent one-electron excitations are reported. Their percentage contributions to wave functions of excited states are given in parentheses. H = HOKS. L = LUKS



Scheme 2. Schematic illustration of visible-light-induced direct electron transition from N 2p orbital localized on amide nitrogen atom to the conduction band of Nb₂O₅. Formation of an excited electron in the conduction band and a hole at amide nitrogen atom (amide radical) are described.

ESR Measurement of Intermediate Species

We then performed ESR measurement of intermediate species to understand the oxidation process in detail. Figure 8a shows ESR spectra of adsorbed amine on Nb₂O₅ under photo irradiation at 77 K. Visible-irradiation (> 390 nm) to butylamine adsorbed on bare Nb₂O₅ at 77 K resulted in the appearance of an ESR signal assigned to organic radical at $g = 2.005$. In addition to this organic radical, a broad feature owing to Nb(IV) was also observed at $g = 1.924$.^{36,37} But visible-irradiation to neat butylamine at 77 K showed no signal. Since Nb₂O₅ does not absorb visible light (> 390 nm), the formation of this organic radical can be attributed to photoactivation of the surface complex above mentioned. The DFT calculation indicated that photoactivation of Nb₂O₅-amide complex induced electron excitation from N 2p orbital localized on amide nitrogen to conduction band of Nb₂O₅ consisted of Nb 4d orbital. Therefore, the observed Nb(IV) and organic radical can be due to

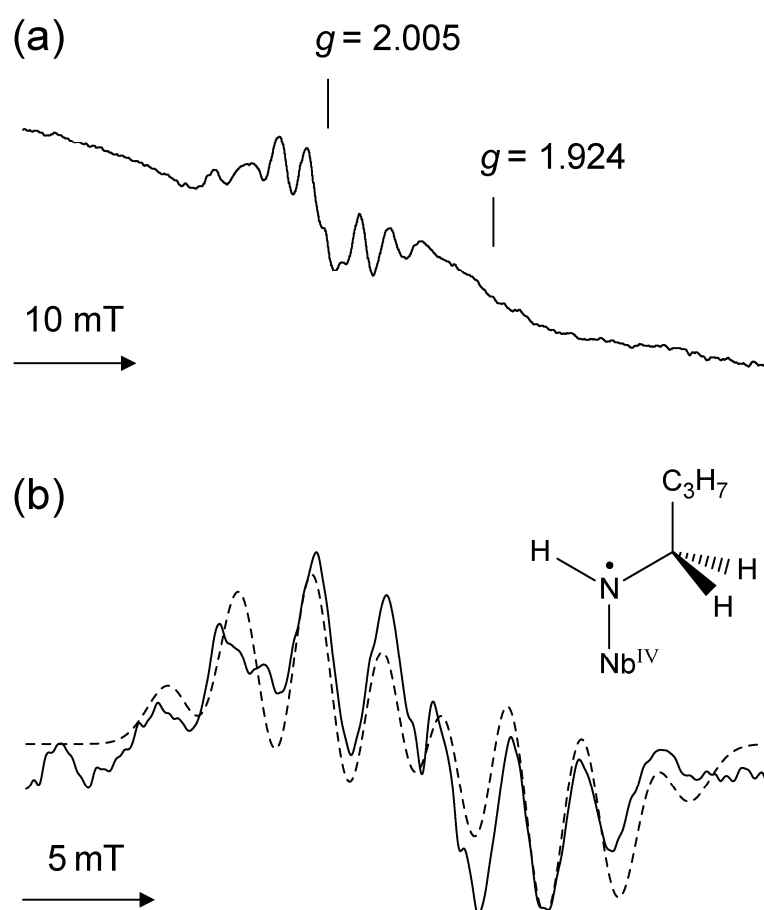
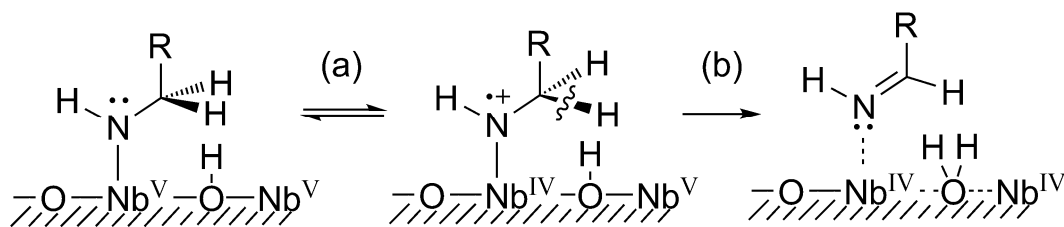


Figure 8. (a) ESR spectrum obtained when butylamine adsorbed on Nb₂O₅ was exposed to illumination of visible light ($h\nu > 390$ nm) at 77 K. (b) Experimental spectrum after background subtraction (solid line) and simulated spectrum of the proposed amide radical (dotted line).

reduction of Nb(V) by excited electrons and resulting amide radical, respectively. Indeed, a simulated ESR spectrum assuming an axially symmetric amide radical with one amino- and two α -protons showed a good agreement with the experimental spectrum (Figure 8b; estimated hyperfine coupling constants are listed in Table 4). This result strongly supports generation of the amide radical and the proposed photoactivation mechanism. In addition, this photoexcitation process does not involve change in the molecular backbone and is consistent with the Franck-Condon principle. On the basis of these results, we proposed a plausible electron transfer mechanism during the photooxidation process as shown in Scheme 3. At first, photo irradiation to the Nb₂O₅-amide surface complex induces excitation from N 2p orbital localized on amide nitrogen to conduction band of Nb₂O₅, followed by reduction of Nb(V) to Nb(IV) by the excited electron and formation of resulting amide radical (Scheme 3, step a). This process can be triggered by lower-energy light (>390 nm) than the band gap of Nb₂O₅ because of the excitation from donor levels derived from amide species. Then, the resulting positive hole on the amide nitrogen corresponding to an amide radical triggers oxidation of α -C–H bond to generate dehydrogenated imine and Nb(IV) (Scheme 3, step b).

Table 4. Condition of the ESR simulation assuming an amide radical.

nuclei	I	number of nuclei	$A_{//}$ / mT	A_{\perp} / mT
¹⁴ N	1	1	1.33	0.20
¹ H	1/2	1	3.30	1.40
¹ H	1/2	2	1.10	0.55



Scheme 3. Proposed electron transfer during photooxidation of amine over Nb₂O₅ based on the results of ESR: (a) electron excitation from amide nitrogen atom and reduction of Nb(V), (b) α -C–H activation by positive hole generated on amide nitrogen atom (amide radical) to form dehydrogenated imine and Nb(IV).

Photocatalytic oxidation of benzylamine under N₂ atmosphere

The photooxidation of benzylamine over Nb₂O₅ was performed under N₂ atmosphere to investigate the role of molecular oxygen. As shown in Figure 9, although the reaction ceased within a few hours, a small amount of *N*-benzylidene benzylamine (36 μmol, 6 h) was evolved despite the absence of O₂. This amount is close to that of chemisorbed NH₃ on Nb₂O₅ (28 μmol / 100 mg·cat) determined in the previous study. In addition, the color of the catalyst turned dark blue during the reaction under N₂, which corresponds to accumulation of excited electrons^{38,39} due to the absence of O₂ as an electron acceptor. These results suggest that complete reduction of the adsorption sites on the catalyst surface (Nb⁵⁺ + e⁻ → Nb⁴⁺) results in catalyst deactivation. After 6 h of the reaction, excess O₂ was flushed into the reactor. The color of the catalyst returned white and continuous evolution of *N*-benzylidene benzylamine was observed. This indicates that reoxidation of the reduced Nb⁴⁺ sites by O₂ is required for catalytic oxidation of benzylamine.

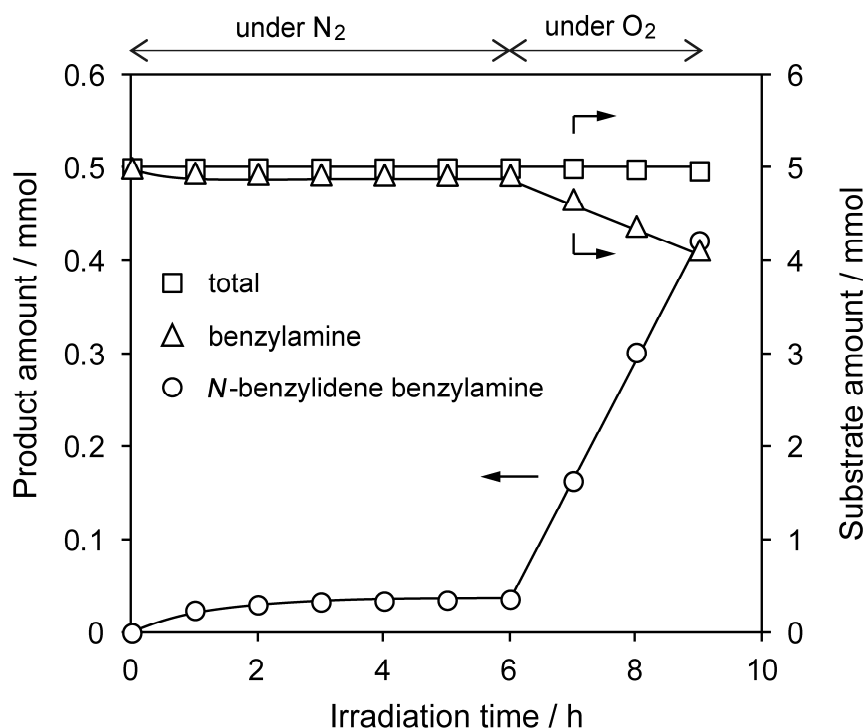


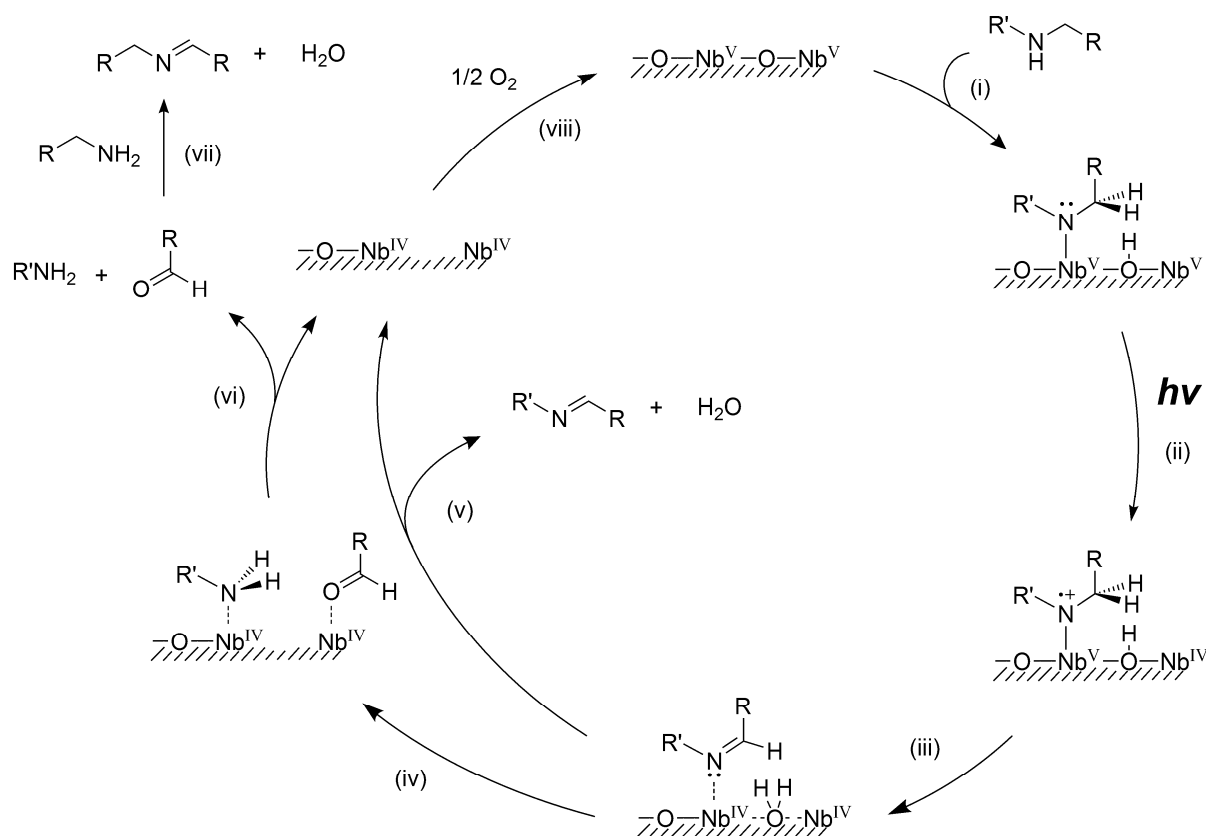
Figure 9. Change in product amount during photooxidation of benzylamine over Nb₂O₅ under 1 atm N₂ (0–6 h) or 1 atm O₂ (6–9 h). Reaction condition: Nb₂O₅ (100 mg), benzylamine (5 mmol), benzene (10 ml), $h\nu > 300$ nm. After 6 h of reaction, the reaction atmosphere was replaced with excess O₂. Total amount of benzylamine and *N*-benzylidene benzylamine is expressed as [(mol of benzylamine) + 2 x (mol of *N*-benzylidene benzylamine)].

Proposed Reaction Mechanism

On the basis of the obtained results, a plausible reaction mechanism of photooxidation of amines over Nb₂O₅ is proposed as shown in Scheme 4. At first, the substrate amine is dissociatively adsorbed on Nb₂O₅ to form an amide species (step i). The Nb₂O₅-amide surface complex absorbs light of lower energy than the band gap of Nb₂O₅ (3.2 eV, 390 nm) and electron at the amide nitrogen atom is excited to the conduction band of Nb₂O₅. The excited electron is trapped by Nb(V) to generate Nb(IV) and a positive hole remains at amide nitrogen (step ii). The remaining hole at amide nitrogen (amide radical) oxidizes α -C-H bond to generate corresponding dehydrogenated imine (step iii). In the case of a primary amine (R' = H), the dehydrogenated primary imine is immediately hydrolyzed into an aldehyde and ammonia by the neighboring water molecule generated due to oxidative dehydrogenation (step iv). Then, the produced aldehyde and ammonia are desorbed (step vi). Condensation of the aldehyde and the substrate primary amine immediately takes place to generate dimerized imine (vii). In the case of a secondary amine (R' \neq H), the dehydrogenated secondary imine and water are desorbed (v). A part of the secondary imine may be hydrolyzed into an aldehyde and a primary amine (R'NH₂). Although this process can be reversible, the aldehyde eventually seems to remain as a by-product due to overoxidation of the fragmented amine. Finally, the reduced Nb(IV) site are reoxidized to Nb(V) by O₂. We have confirmed that the condensation of benzaldehyde and benzylamine to *N*-benzylidene benzylamine immediately and quantitatively proceeds when benzaldehyde is added to benzylamine in benzene solvent in the absence of Nb₂O₅ under the dark. Moreover, gaseous ammonia was indeed detected by TCD-GC in the reaction atmosphere of benzylamine photooxidation.

Kinetic Study to Determine the Rate-determining Step

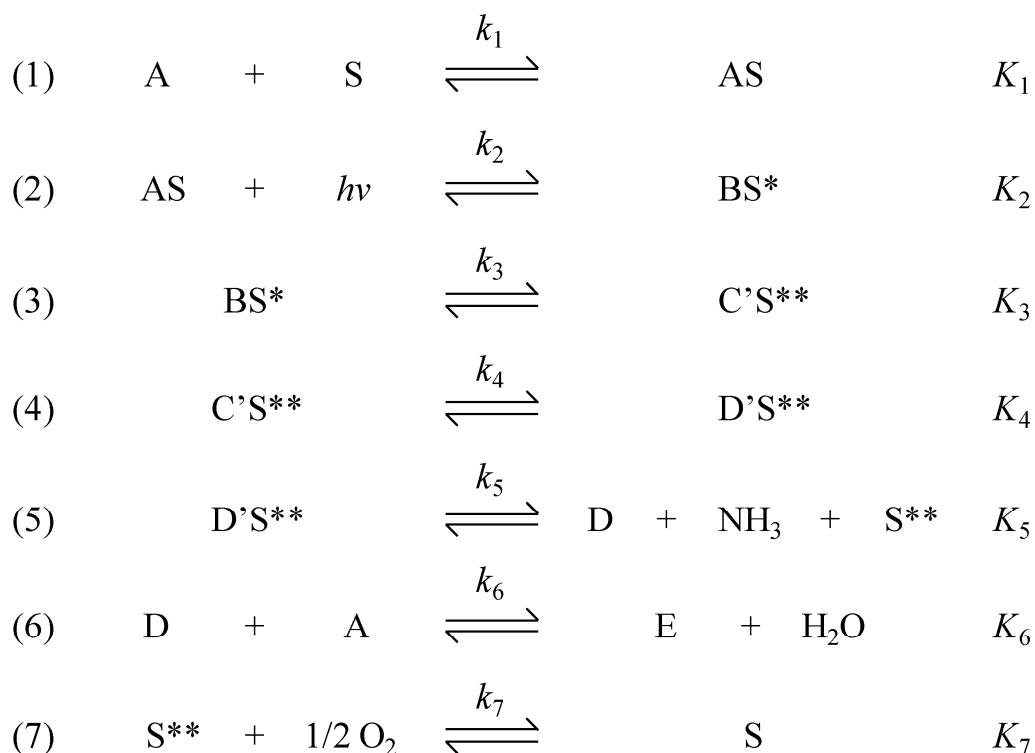
We performed a kinetic analysis to verify the proposed mechanism shown in Scheme 4 and to determine the rate-determining step of the photooxidation of amine over Nb₂O₅. The dependencies of the concentrations of substrate and O₂ and light intensity on the reaction rate (*r*) of benzylamine photooxidation were obtained as expressed in eq 1.



Scheme 4. Proposed reaction mechanism of photooxidation of amines over Nb_2O_5 : (i) dissociative adsorption of amine, (ii) photoactivation of Nb_2O_5 -amide surface complex, (iii) α -C–H activation by hole generated on amide nitrogen atom to form dehydrogenated imine, (iv) hydrolysis of imine, (v) desorption of imine and H_2O , (vi) desorption of aldehyde and $\text{R}'\text{NH}_2$, (vii) condensation of aldehyde and primary amine, and (viii) reoxidation of reduced Nb(IV) sites by O_2 .

$$r = k P_{\text{O}_2}^{0.018} I^{0.76} [\text{A}]^{0.30} \quad (1)$$

Here, the rate constant, the O_2 pressure, the light intensity, and the substrate concentration are abbreviated to k , P_{O_2} , I , and $[\text{A}]$, respectively. The obtained rate equations are compared with those derived from the proposed reaction mechanism employing steady-state approximation. Rate constants and equilibrium constants in each elementary step for the case of a primary amine are defined as shown in Scheme 5. As mentioned above, the condensation of benzaldehyde and



Scheme 5. Elementary steps in photooxidation of a primary amine over Nb₂O₅.S: vacant active site, A: amine, AS: active site adsorbed amine, B : amide radical, S*: reduced site (one electron), C: imine, C': imine and H₂O, S**: reduced site (two electrons), D: aldehyde, D' aldehyde and NH₃, E: dimerized imine.

benzylamine immediately took place without catalyst and only a trace amount of benzaldehyde was yielded as a by-product in the photooxidation of benzylamine. These clearly indicate that the dimerization process (Scheme5, step 6) does not correspond to the rate determining step. The rate equations for other steps were derived by assuming that the total number of adsorption sites is constant (eq 2) and that each step is a rate-determining step as follows (eqs 3–8):

$$[S]_0 = [S] + [AS] + [BS^*] + [C'S^{**}] + [D'S^{**}] + [S^{**}] \quad (2)$$

(step 1)

$$r = \frac{k_1 K_2 K_3 K_4 K_5 K_6 K_7 [S]_0 P_{O_2}^{0.5} I [A]^2}{K_2 K_3 K_4 K_5 K_6 (K_7 P_{O_2}^{0.5} + 1) I [A] + [(K_3 K_4 + K_3 + 1) K_2 I + 1] [NH_3] [H_2O] [E]} \quad (3)$$

(step 2)

$$r = \frac{k_2 K_1 K_3 K_4 K_5 K_6 K_7 [S]_0 P_{O_2}^{0.5} I [A]^2}{K_1 K_3 K_4 K_5 K_6 K_7 P_{O_2}^{0.5} I [A]^2 + K_3 K_4 K_5 K_6 (K_7 P_{O_2}^{0.5} + 1) [A] + (K_3 K_4 + K_3 + 1) [NH_3] [H_2O] [E]} \quad (4)$$

(step 3)

$$r = \frac{k_3 K_1 K_2 K_4 K_5 K_6 K_7 [S]_0 P_{O_2}^{0.5} I [A]^2}{K_1 K_4 K_5 K_6 K_7 (K_2 I + 1) P_{O_2}^{0.5} [A]^2 + K_4 K_5 K_6 (K_7 P_{O_2}^{0.5} + 1) [A] + (K_4 + 1) [NH_3] [H_2O] [E]} \quad (5)$$

(step 4)

$$r = \frac{k_4 K_1 K_2 K_3 K_5 K_6 K_7 [S]_0 P_{O_2}^{0.5} I [A]^2}{K_1 K_5 K_6 K_7 (K_2 I + 1) P_{O_2}^{0.5} [A]^2 + K_4 K_5 K_6 (K_7 P_{O_2}^{0.5} + 1) [A] + (K_4 + 1) [NH_3] [H_2O] [E]} \quad (6)$$

(step 5)

$$r = \frac{k_5 K_1 K_2 K_3 K_4 K_6 K_7 [S]_0 P_{O_2}^{0.5} I [A]}{K_1 K_2 K_7 (K_3 K_4 + K_3 + 1) P_{O_2}^{0.5} I [A] + K_7 (K_1 [A] + 1) P_{O_2}^{0.5} + 1} \quad (7)$$

(step 7)

$$r = \frac{k_7 K_1 K_2 K_3 K_4 K_5 K_6 [S]_0 P_{O_2}^{0.5} I [A]^2}{K_1 K_2 K_3 K_4 K_5 K_6 I [A]^2 + [(K_3 K_4 + K_3 + 1) K_2 I + 1] [NH_3] [H_2O] [E] [A] + [NH_3] [H_2O] [E]} \quad (8)$$

The reaction orders of the substrate concentration, the light intensity, and the pressure of the oxygen in steps 1, 2, and 7 are not compatible with the experimental data. As a consequence, step 3 (conversion of amide radical into primary imine), step 4 (hydrolysis of primary imine to aldehyde), or step 5 (desorption of products) is the rate-determining step of the photooxidation of primary amine over Nb₂O₅. The amide radical species could be observed at 77 K, but was not detected at room temperature. The primary imine was also not observed by FT-IR at room temperature in contrast to the aldehyde. These suggest that step 3 and 4 are much faster than step 5. On the basis of these results, we conclude that the desorption of the aldehyde and ammonia is the rate-determining step of the photooxidation of primary amine over Nb₂O₅.

Conclusion

In this study, the photocatalytic performance of Nb₂O₅ in photooxidation of amine was compared with other metal oxides and the substrate scope was investigated. Nb₂O₅ showed higher selectivity than TiO₂, ZnO, and other metal oxides. Various amines including primary, secondary, and bicycloamine derivatives were selectively oxidized in the presence of Nb₂O₅. Secondary amines were oxidized into corresponding dehydrogenated imines, whereas primary amines were converted into dimerized imines. The mechanistic study revealed that the photooxidation of amine over Nb₂O₅ was oxidative dehydrogenation of amine via photoexcitation of the Nb₂O₅-amide surface complex, which consisted of dissociatively adsorbed amine (amide) and Nb₂O₅. In the case of primary amine, the dehydrogenated primary imine was immediately hydrolyzed into aldehyde and ammonia, followed by condensation of the aldehyde and substrate amine to dimerized imine. The reaction took place not only under UV light (> 300 nm) but also visible light (390 nm), although the band gap of Nb₂O₅ is ca. 3.2 eV (390 nm). DFT calculations revealed that 1) the surface donor level derived from adsorbed amide species is located in the forbidden band, 2) direct electron transition from the surface donor level to the conduction band takes place by absorbing a photon, 3) the excitation energy from surface donor level to Nb 4d is lower than that from O 2p valence band to Nb 4d. The effective wavelength is shifted to a longer wavelength by the formation of a donor level derived from the adsorbed molecule during a chemical reaction, which can be expressed as “in-situ doping” effect.

The photoactivation mechanism and the outline of the photooxidation of amine over Nb₂O₅ is essentially the same as that for alcohol, except that the hydrolysis of primary imine and the subsequent dimerization take place.

References

- (1) Murahashi, S. I. *Angew. Chem. Int. Ed.* **1995**, *34*, 2443.
- (2) Nicolaou, K. C.; Mathison, C. J. N.; Montagnon, T. *Angew. Chem. Int. Ed.* **2003**, *42*, 4077.
- (3) Nicolaou, K. C.; Mathison, C. J. N.; Montagnon, T. *J. Am. Chem. Soc.* **2004**, *126*, 5192.
- (4) Mukaiyama, T.; Kawana, A.; Fukuda, Y.; Matsuo, J. *Chem. Lett.* **2001**, 390.
- (5) Punniyamurthy, T.; Velusamy, S.; Iqbal, J. *Chem. Rev.* **2005**, *105*, 2329.
- (6) Frei, H. *Science* **2006**, *313*, 309.
- (7) Tang, R.; Diamond, S. E.; Neary, N.; Mares, F. *J. Chem. Soc., Chem. Comm.* **1978**, 562.
- (8) Cenini, S.; Porta, F.; Pizzotti, M. *J. Mol. Catal.* **1982**, *15*, 297.
- (9) Porta, F.; Crotti, C.; Cenini, S.; Palmisano, G. *J. Mol. Catal.* **1989**, *50*, 333.
- (10) Bailey, A. J.; James, B. R. *Chem. Commun.* **1997**, 505.
- (11) Mori, K.; Yamaguchi, K.; Mizugaki, T.; Ebitani, K.; Kaneda, K. *Chem. Commun.* **2001**, 461.
- (12) Murahashi, S.; Okano, Y.; Sato, H.; Nakae, T.; Komiya, N. *Synlett* **2007**, *11*, 1675.
- (13) Yamaguchi, K.; Mizuno, N. *Angew. Chem. Int. Ed.* **2003**, *42*, 1480.
- (14) Aschwanden, L.; Mallat, T.; Krumeich, F.; Baiker, A. *J. Mol. Catal. A: Chem.* **2009**, *309*, 57.
- (15) Aschwanden, L.; Mallat, T.; Maciejewski, M.; Krumeich, F.; Baiker, A. *Chemcatchem* **2010**, *2*, 666.
- (16) So, M. H.; Liu, Y. G.; Ho, C. M.; Che, C. M. *Chem. Asian J.* **2009**, *4*, 1551.
- (17) Anpo, M. *Bull. Chem. Soc. Jpn.* **2004**, *77*, 1427.
- (18) Su, F. Z.; Mathew, S. C.; Lipner, G.; Fu, X. Z.; Antonietti, M.; Blechert, S.; Wang, X. C. *J. Am. Ceram. Soc.* **2010**, *132*, 16299.
- (19) Su, F. Z.; Mathew, S. C.; Mohlmann, L.; Antonietti, M.; Wang, X. C.; Blechert, S. *Angew. Chem. Int. Ed.* **2011**, *50*, 657.

- (20) Lang, X. J.; Ji, H. W.; Chen, C. C.; Ma, W. H.; Zhao, J. C. *Angew. Chem. Int. Ed.* **2011**, *50*, 3934.
- (21) Ohuchi, T.; Miyatake, T.; Hitomi, Y.; Tanaka, T. *Catal. Today* **2007**, *120*, 233.
- (22) Shishido, T.; Miyatake, T.; Teramura, K.; Hitomi, Y.; Yamashita, H.; Tanaka, T. *J. Phys. Chem. C* **2009**, *113*, 18713.
- (23) Smith, J. K.; Bergbreiter, D. E.; Newcomb, M. *J. Org. Chem.* **1985**, *50*, 4549.
- (24) Frisch, M. J.; Trucks, G. W.; Schlegel, H. B.; Scuseria, G. E.; Robb, M. A.; Cheeseman, J. R.; Montgomery, J., J. A.; Vreven, T.; Kudin, K. N.; Burant, J. C.; Millam, J. M.; Iyengar, S. S.; Tomasi, J.; Barone, V.; Mennucci, B.; Cossi, M.; Scalmani, G.; Rega, N.; Petersson, G. A.; Nakatsuji, H.; Hada, M.; Ehara, M.; Toyota, K.; Fukuda, R.; Hasegawa, J.; Ishida, M.; Nakajima, T.; Honda, Y.; Kitao, O.; Nakai, H.; Klene, M.; Li, X.; Knox, J. E.; Hratchian, H. P.; Cross, J. B.; Bakken, V.; Adamo, C.; Jaramillo, J.; Gomperts, R.; Stratmann, R. E.; Yazyev, O.; Austin, A. J.; Cammi, R.; Pomelli, C.; Ochterski, J. W.; Ayala, P. Y.; Morokuma, K.; Voth, G. A.; Salvador, P.; Dannenberg, J. J.; Zakrzewski, V. G.; Dapprich, S.; Daniels, A. D.; Strain, M. C.; Farkas, O.; Malick, D. K.; Rabuck, A. D.; Raghavachari, K.; Foresman, J. B.; Ortiz, J. V.; Cui, Q.; Baboul, A. G.; Clifford, S.; Cioslowski, J.; Stefanov, B. B.; Liu, G.; Liashenko, A.; Piskorz, P.; Komaromi, I.; Martin, R. L.; Fox, D. J.; Keith, T.; Al-Laham, M. A.; Peng, C. Y.; Nanayakkara, A.; Challacombe, M.; Gill, P. M. W.; Johnson, B.; Chen, W.; Wong, M. W.; Gonzalez, C.; Pople, J. A. *Gaussian 03; Revision C.02 ed.*; Gaussian, Inc.: Wallingford CT, 2004.
- (25) Nowak, I.; Ziolk, M. *Chem. Rev.* **1999**, *99*, 3603.
- (26) Lee, C. T.; Yang, W. T.; Parr, R. G. *Phys. Rev. B* **1988**, *37*, 785.
- (27) Becke, A. D. *J. Chem. Phys.* **1993**, *98*, 5648.
- (28) Bauernschmitt, R.; Ahlrichs, R. *Chem. Phys. Lett.* **1996**, *256*, 454.
- (29) Casida, M. E.; Jamorski, C.; Casida, K. C.; Salahub, D. R. *J. Chem. Phys.* **1998**, *108*, 4439.
- (30) Gorelsky, S. I.; Lever, A. B. P. *J. Organomet. Chem.* **2001**, *635*, 187.
- (31) Maeda, Y.; Nishimura, T.; Uemura, S. *Bull. Chem. Soc. Jpn.* **2003**, *76*, 2399.
- (32) Silverstein, R. M.; Webster, F. X. *Spectrometric Identification of Organic Compounds*, 6th ed.; Wiley: New York, 1998.

- (33) Ramis, G.; Busca, G.; Bregani, F.; Forzatti, P. *Appl. Catal.* **1990**, *64*, 259.
- (34) Kung, M. C.; Kung, H. H. *Catal. Rev.* **1985**, *27*, 425.
- (35) Chuang, C. C.; Shiu, J. S.; Lin, J. L. *PCCP* **2000**, *2*, 2629.
- (36) Sugantha, M.; Varadaraju, U. V.; Rao, G. V. S. *J. Solid State Chem.* **1994**, *111*, 33.
- (37) Verissimo, C.; Garrido, F. M. S.; Alves, O. L.; Calle, P.; MartinezJuarez, A.; Iglesias, J. E.; Rojo, J. M. *Solid State Ionics* **1997**, *100*, 127.
- (38) Hiskia, A.; Mylonas, A.; Papaconstantinou, E. *Chem. Soc. Rev.* **2001**, *30*, 62.
- (39) Miyaoka, H.; Mizutani, G.; Sano, H.; Omote, M.; Nakatsuji, K.; Komori, F. *Solid State Commun.* **2002**, *123*, 399.

Chapter 5

Mechanism of Photooxidation of Hydrocarbons over Nb₂O₅

Abstract

Selective aerobic photooxidation of hydrocarbons to oxidized products, mainly ketones, was conducted over Nb₂O₅ in the absence of solvent. For the oxidation of cyclohexane and ethylbenzene, Nb₂O₅ shows significantly higher selectivity to partial oxidation products than does TiO₂. In the oxidation of cyclohexane, Nb₂O₅ gave a much higher ketone/alcohol ratio than TiO₂. On the basis of spectroscopic and kinetic studies, the following mechanism is proposed. Both hydrocarbon and dioxygen adsorb on Nb₂O₅. The C–H bond of the hydrocarbon is activated to produce an alkyl radical by a photogenerated positive hole, and adsorbed oxygen is reduced by a photogenerated electron. The alkyl radical reacts with superoxide to produce a hydroperoxide. Then, the hydroperoxide is converted to a ketone, which subsequently desorbs from Nb₂O₅. This proposed mechanism is a typical Langmuir–Hinshelwood mechanism, including the formation of the hydroperoxide species as an intermediate. A linear correlation between logarithms of the reaction rates and bond dissociation enthalpies of several hydrocarbons indicates that the rate-determining step is C–H bond activation. ESR study suggests that the higher selectivity of Nb₂O₅ for partial oxidation products than TiO₂ is due to the absence of O₃[–], which is highly active for the complete oxidation of hydrocarbons.

Introduction

Heterogeneous photocatalysts have potential application in the aerobic oxidation of organic molecules.¹⁻³ Up to now, various semiconductor materials have been tested as oxidation photocatalysts, and it is generally accepted that the anatase TiO₂ is the most reliable material, owing to its low cost and high photostability. Significant effort has been devoted to developing TiO₂ as a selective catalyst in the oxidation of various types of organic molecules such as alkanes,⁴⁻⁹ arenes,¹⁰ and alcohols.¹¹⁻¹³ However, the undesired over-oxidation to CO_x (CO and CO₂) is essentially associated with photocatalytic oxidation using TiO₂ owing to the strong oxidation ability of a hole generated in the valence band of TiO₂.¹⁴ To achieve selective oxidation, a variety of catalytic systems based on TiO₂ have been devised with a view of optimizing the solvent,^{7,8} the reaction conditions,¹¹ or the preparation method of TiO₂.¹³ On the other hand, we have developed a series of selective photocatalytic systems as alternatives to TiO₂, e.g., hydrocarbon oxidation over alumina-supported vanadium oxide (V₂O₅/Al₂O₃)¹⁵⁻¹⁸ and alcohol oxidation over niobium oxide (Nb₂O₅).¹⁹⁻²¹ The mechanisms of photoactivation of these systems are entirely different from those of classical photoactivation, which involves the formation of an excited electron in the conduction band and a positive hole in the valence band, followed by the activation of the substrate by the positive hole or the excited electron. In the case of V₂O₅/Al₂O₃, orthovanadate-like (V=O) O₃ species in the triplet excited state activate adsorbed alkanes.^{17,18} In the case of Nb₂O₅, an alcohol is dehydrogenated to the corresponding carbonyl compound via photoexcitation of a surface complex consisting of adsorbed alkoxide species and Nb₂O₅.^{20,21} Moreover, these photocatalysts show high selectivities to partial oxidation products.

In this study, the photocatalytic activity of Nb₂O₅ and its selectivity to partial oxidation products in hydrocarbon oxidation are investigated and compared with those of anatase TiO₂. Herein, we report that Nb₂O₅ shows higher selectivities in the aerobic oxidation of various hydrocarbons than TiO₂. We also carried out a mechanistic study by FT-IR, ESR spectroscopy, and a kinetic study to understand the reaction mechanism and rationalize the observed difference in the selectivities of Nb₂O₅ and TiO₂.

Experimental Section

Catalyst Preparation

Niobic acid, niobium oxide hydrate ($\text{Nb}_2\text{O}_5 \cdot n\text{H}_2\text{O}$, AD/2872, HY-340) was kindly supplied from CBMM. Niobium oxide catalyst was prepared by calcination of niobic acid in a dry air flow at 773 K for 5 h. A TT- Nb_2O_5 phase with a pseudo-hexagonal structure was obtained from the XRD pattern and Raman spectral data.¹⁹ The specific surface area of this Nb_2O_5 sample, which was evaluated by the Brunauer–Emmett–Teller (BET) method using the N_2 adsorption isotherm at 77 K, was $48 \text{ m}^2 \cdot \text{g}^{-1}$.¹⁹ TiO_2 used in this research was JRC-TIO-11, supplied by the Catalysis Society of Japan as a standard TiO_2 sample. This TiO_2 sample was hydrated in distilled water at 353 K for 2 h, followed by evaporation, drying, and calcination at 773 K for 5 h in a dry air flow. JRC-TIO-11 consists of anatase (91%) and rutile (9%) phases, and its specific surface area was evaluated to be $78 \text{ m}^2 \cdot \text{g}^{-1}$. After calcinations, the catalysts were ground into powders under 100 mesh (0.15 mm).

Reaction Conditions

The photocatalytic oxidation of the hydrocarbon was carried out in a quasi-flowing batch system (Figure 1) under atmospheric oxygen at room temperature. The substrate was used without further purification. The catalyst (100 mg), hydrocarbon substrate (10 mL), and a stirring bar were added into a Pyrex glass reactor in the absence of solvent. The suspension was vigorously stirred at room temperature and irradiated from the flat bottom of the reactor using a 500 W ultrahigh-pressure Hg lamp via reflection through a cold mirror (USHIO Denki Co.). Oxygen was introduced into the reactor at $2 \text{ mL} \cdot \text{min}^{-1}$. The organic oxidation products were analyzed by GC-FID (Shimadzu GC-14B) and GC-MS (Shimadzu GC-MS QP5050). At the downstream of the flow reactor, a saturated barium hydroxide solution ($\text{Ba}(\text{OH})_2$) was used to determine the quantity of carbon dioxide by the formation of barium carbonate (BaCO_3). The total amount of the products formed in the reaction is used to define the reaction rate (r) in units of $\text{mmol} \cdot \text{h}^{-1}$. The relative reaction rate (r_{rel}) considering the frequency factor is further defined by dividing r by the number of C–H bonds involved in the reaction ($n_{\text{C-H}}$: cyclooctene, 16; toluene, 3; ethylbenzene, 2; diphenylmethane, 2). In the kinetic study, benzene and nitrogen were used as diluents to modify the concentration of the substrate and oxygen pressure, respectively. Light intensity was controlled using a metal mesh.

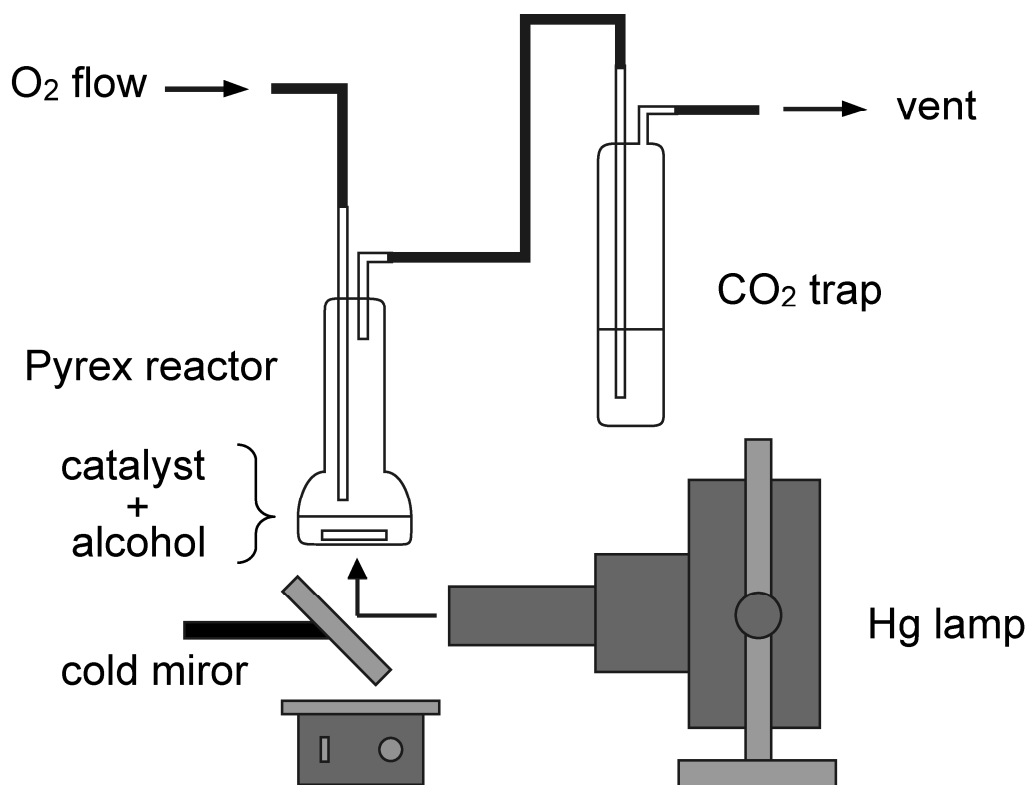


Figure 1. Setup of the quasi-flowing batch system for the liquid phase photocatalytic oxidation of hydrocarbons.

ESR Spectra

ESR measurements were conducted using an X-band ESR spectrometer (JEOL JES-SRE2X) with an in situ quartz cell. Prior to ESR measurements, the sample (Nb_2O_5 or TiO_2) was pretreated with 6.7 kPa of O_2 at 673 K for 1 h, followed by evacuation for 0.5 h at 673 K. After pretreatment, the sample was exposed to 0.5 kPa of $^{16}\text{O}_2$ or degassed ethylbenzene at room temperature. Subsequently, the sample was cooled to 77 K and irradiated. ESR spectra were recorded before and after photoirradiation. When isotopically enriched oxygen (20% ^{17}O) was used, 4.0 kPa of oxygen was introduced. The g values of the radical species were determined using a Mn marker. A 500 W ultrahigh-pressure mercury lamp was used as the light source.

FT-IR Spectra

FT-IR spectra of the samples after photoirradiation were recorded with a Perkin-Elmer SPECTRUM ONE Fourier transform infrared spectrometer. The spectral resolution was 4 cm^{-1} . The Nb_2O_5 sample was pressed into a pellet (diameter: 12 mm). The molded sample was introduced into an in situ IR cell equipped with BaF_2 windows. Prior to measurements, the sample was pretreated with 6.7 kPa of O_2 for 1 h at 673 K, followed by evacuation for 0.5 h at 673 K. The pretreated sample was exposed to 16.1 kPa of degassed cyclohexane for 15 min, followed by evacuation for an additional 10 min. Before photoirradiation, 1.6 kPa of O_2 was introduced to the sample cell. A 200 W Hg–Xe lamp (SUN-EI ELECTRIC SUPERCURE-204S) was used as a light source.

Results

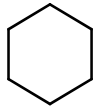
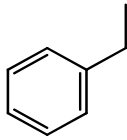
Photocatalytic Oxidation of Alkanes over Nb_2O_5 and TiO_2

Table 1 shows the yields of the partial oxidation products and carbon dioxide (CO_2) in liquid-phase photooxidations of ethylbenzene and cyclohexane over Nb_2O_5 and TiO_2 . Acetophenone and a small amount of 1-phenylethanol were obtained as partial oxidation products in the ethylbenzene oxidation. In addition, cyclohexanone was mainly produced as a partial oxidation product in the cyclohexane oxidation. Oxidation of cyclohexane is an important chemical process for the production of caprolactam, which is a monomer used for the synthesis of nylon-6. A higher ketone/alcohol ratio (K/A ratio) is preferred for caprolactam production because the following step of cyclohexanol overoxidation to cyclohexanone requires additional cost and energy. It is therefore noteworthy that a much higher K/A ratio was obtained in the cyclohexane photooxidation over Nb_2O_5 (>999) than that obtained over TiO_2 (47). The photocatalytic activity of Nb_2O_5 is lower than TiO_2 in the oxidation of cyclohexane but is higher in the oxidation of ethylbenzene. In both cases, Nb_2O_5 exhibited higher selectivities to partial oxidation products than TiO_2 .

We previously reported that alcohol oxidation over Nb_2O_5 occurred even under irradiation by visible light ($\lambda > 390\text{ nm}$).²⁰ A mechanistic study using UV–Vis, action spectra, and DFT calculation revealed that this is caused by direct electron transition from a donor level derived from adsorbed alkoxide species. However, oxidation of cyclohexane over Nb_2O_5 did not proceed under visible light

irradiation ($\lambda > 390$ nm) or in the dark. Oxidation of ethylbenzene also barely occurred under the same conditions. These results are different from those obtained from alcohol oxidation and indicate that the oxidation of the hydrocarbon is triggered by band gap excitation of Nb₂O₅ (<390 nm),²⁰ as is the case for oxidation over TiO₂ (< 390 nm).

Table 1. Evolutions of partial oxidation products and carbon dioxide in photooxidation of cyclohexane and ethylbenzene.^a

substrate	catalyst	products / μmol^b				Conv. (%)	Sel. (%) ^c	K/A ratio
		alcohol	ketone	dimer	1/n CO ₂			
cyclo hexane 	Nb ₂ O ₅	n. d.	572	n. d.	160	0.76	78	> 999
	Nb ₂ O ₅ ^d	n. d.	n. d.	n. d.	n. d.	0	–	–
	Nb ₂ O ₅ ^e	n. d.	n. d.	n. d.	n. d.	0	–	–
	TiO ₂ ^f	17	796	n. d.	714.6	1.39	57	47
	TiO ₂	54	1828	n. d.	1711	3.7	52	34
ethyl benzene 	Nb ₂ O ₅	1469	7831	n. d.	272	11.7	98	5.3
	Nb ₂ O ₅ ^e	n. d.	287	n. d.	n. d.	0.35	> 99	> 999
	Nb ₂ O ₅ ^g	2	3	65	n. d.	0.09	> 99	-
	TiO ₂	905	5044	n. d.	562	7.9	91	5.6

^a Reaction conditions: catalyst; 100 mg, substrate 10 ml, O₂ flow; 2 ml·min⁻¹, photo irradiation time; 24 h. ^b For cyclohexane, cyclohexanol (alcohol) and cyclohexanone (ketone); for ethylbenzene, 1-phenylethanol (alcohol), acetophenone (ketone), and 2,3-diphenylbutane (dimer); *n* represents the number of carbon atoms included in the substrate. ^c Selectivity to partial oxidation products. ^d Under the dark. ^e $\lambda > 390$ nm. ^f Photo irradiation time; 6 h. ^g Photo irradiation time; 12 h, under 1 atm N₂.

The photooxidation of ethylbenzene over Nb_2O_5 under 1 atm N_2 resulted in the formation of 2,3-diphenylbutane, a dimer coupled at the benzylic position of ethylbenzene, almost as the sole product. Likewise, a similar coupled dimer, 1,2-diphenylethane, was exclusively formed in the photooxidation of toluene under an N_2 atmosphere. The formation of such dimers strongly suggests the generation of a radical with an unpaired electron at the benzylic position, followed by radical coupling. Moreover, the absence of oxygenated products (1-phenylethanol and/or acetophenone for ethylbenzene, benzaldehyde, and/or benzoic acid for toluene) suggests that molecular oxygen participates in oxygenation of the substrate. Figure 2 shows the time course of the product yield and K/A ratio in the oxidation of ethylbenzene. Although the ketone was predominantly produced, the K/A ratio decreased as the reaction proceeded. If the ketone is produced via overoxidation of the alcohol as a primary product, the K/A ratio should increase with reaction time. Therefore, this change in K/A ratios indicates that the ketone was not formed by the overoxidation of the alcohol but directly from the hydrocarbon.

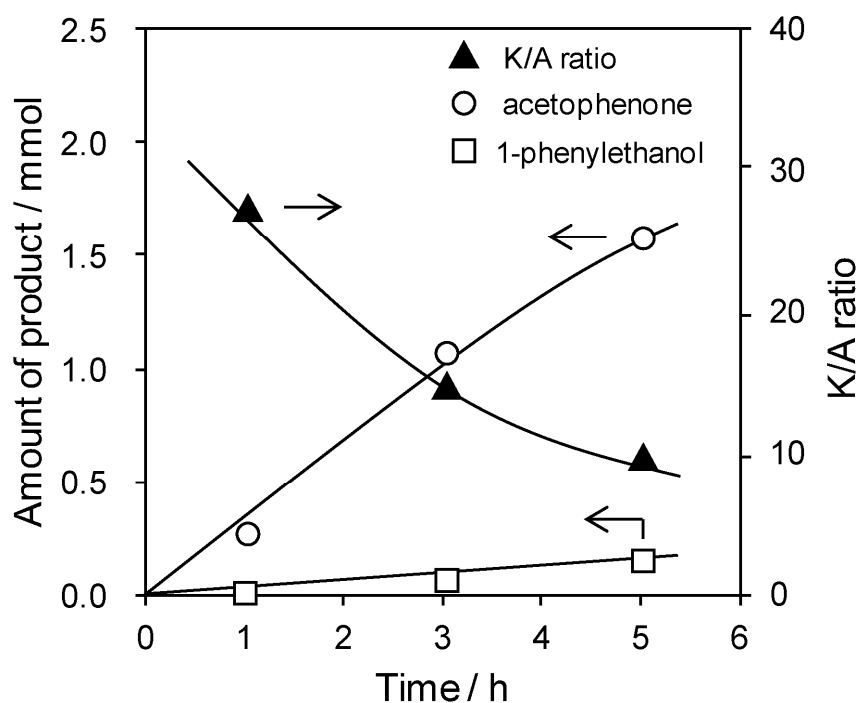


Figure 2. Time course of the product yields and K/A ratio of photooxidation of ethylbenzene over Nb_2O_5 .

The oxidation of hydrocarbons with various C–H bond dissociation energies (C–H BDE), such as cyclooctane ($92.0 \text{ kcal}\cdot\text{mol}^{-1}$),²² toluene ($87.5 \text{ kcal}\cdot\text{mol}^{-1}$),²³ ethylbenzene ($84.5 \text{ kcal}\cdot\text{mol}^{-1}$)²³, and diphenylmethane ($82.0 \text{ kcal}\cdot\text{mol}^{-1}$)²⁴ were also carried out. Figure 3 shows the correlation between the relative reaction rates (r_{rel}) and C–H BDE. The logarithm of r_{rel} linearly correlated with C–H BDE values of the substrates, giving a slope of approximately -0.3 . Thus, the reaction rates of the photocatalytic oxidations of hydrocarbons over Nb_2O_5 decreased with the increase of the C–H BDE of substrates. This linear relationship clearly shows that C–H activation of the hydrocarbon is the rate-determining step of the reaction.^{25–29}

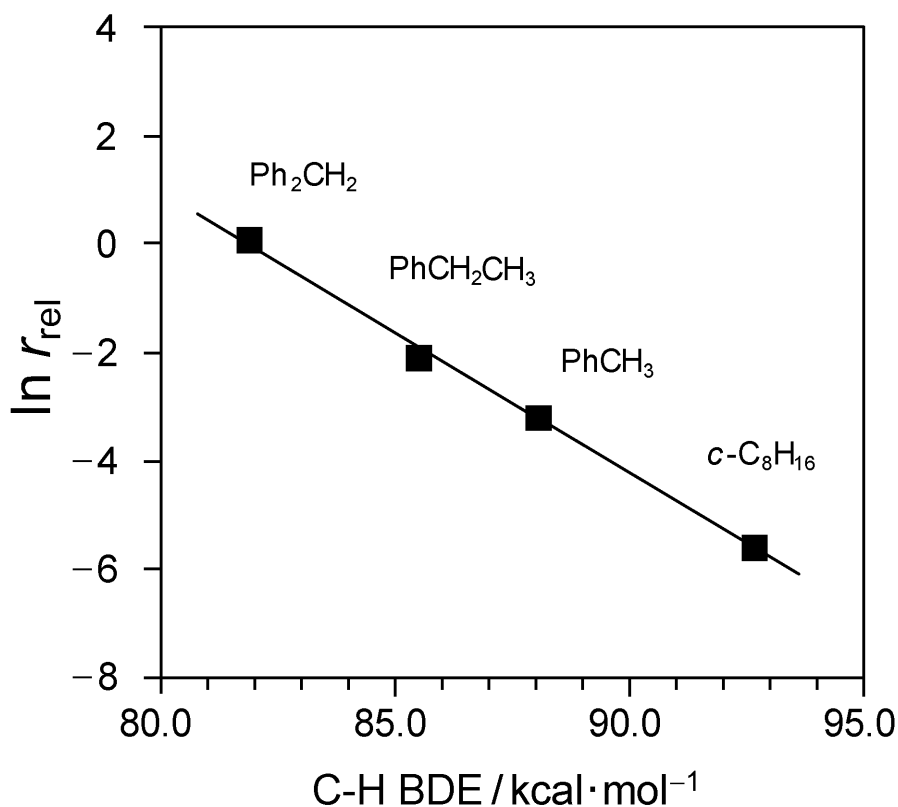


Figure 3. Plot of logarithm of r_{rel} against C–H BDE of substrates (Ph₂CH₂, diphenylmethane; PhCH₂CH₃, ethylbenzene; PhCH₃, toluene; c-C₈H₁₆, cyclooctane).

ESR Study of Oxygen Anion Radicals and Alkyl Radical

We conducted ESR measurements to characterize the photogenerated reaction intermediate species. Figure 4 shows the ESR spectra observed when TiO_2 or Nb_2O_5 was irradiated under an O_2 atmosphere at 77 K. Photoirradiation of TiO_2 gave intense signals consisting of two sets of rhombic g values assigned to O_2^- ($g_{1a} = 2.018$, $g_{2a} = 2.010$, and $g_{3a} = 2.003$)^{30,31} and O_3^- ($g_{1b} = 2.013$, $g_{2b} = 2.007$, and $g_{3b} = 2.001$).^{32,33} The generation of O_2^- and O_3^- is attributed to the reduction of adsorbed O_2 by excited electrons and the combination of positive holes trapped on surface lattice oxygen (equivalent to O^-) and adsorbed O_2 , respectively. On the other hand, only a tiny signal consisting of one set of rhombic g values ($g_1 = 2.036$, $g_2 = 2.003$, and $g_3 = 1.986$) was observed when Nb_2O_5 was irradiated.

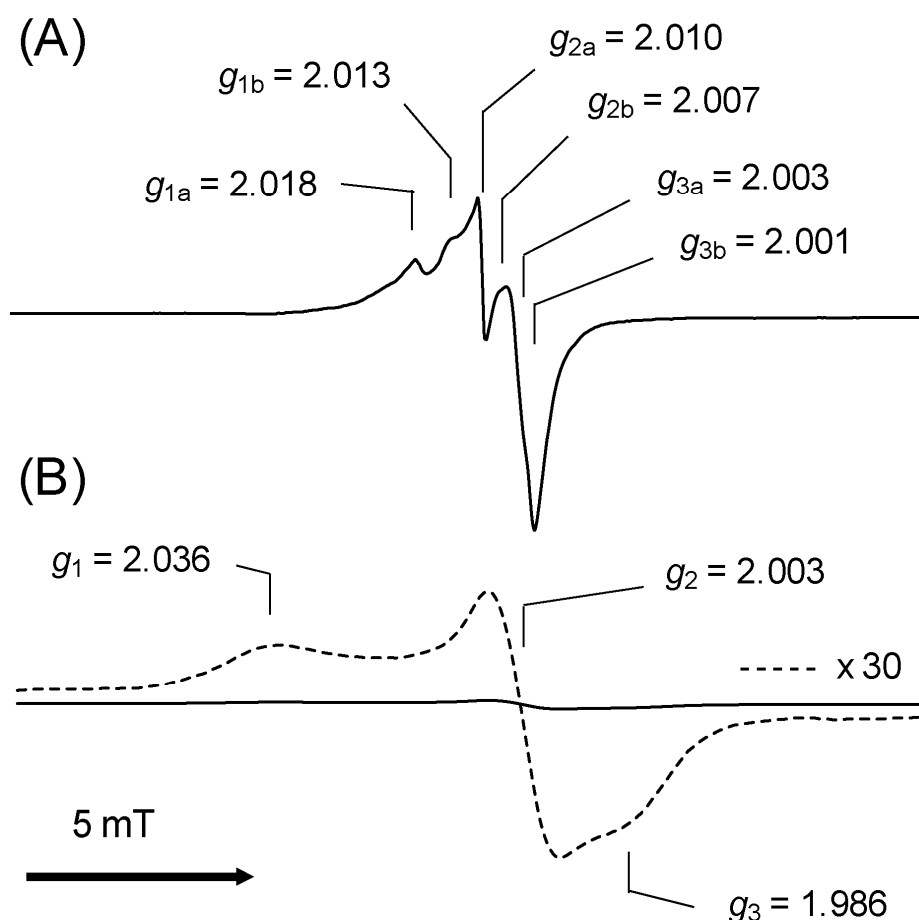


Figure 4. ESR spectra of (A) anatase- TiO_2 and (B) Nb_2O_5 irradiated in the presence of $^{16}\text{O}_2$ (0.5 kPa) at 77 K.

To obtain further information about this species,³⁴ a similar experiment with ^{17}O -enriched oxygen was performed. As shown in Figure 5, six lines due to hyperfine interaction with one ^{17}O nuclei ($I = 5/2$) along the g_2 direction were confirmed. This hyperfine structure strongly suggests the generation of $^{16}\text{O}^{17}\text{O}^-$ and that the two oxygen nuclei are equivalent. The equivalent hyperfine interactions also suggest that the O_2^- ion is adsorbed in a side-on fashion on the Nb_2O_5 surface, with its internuclear axis parallel to the plane of the surface, as commonly observed in other metal oxides.³¹ Eleven lines corresponding to two ^{17}O nuclei ($^{17}\text{O}^{17}\text{O}^-$, $I = 5$) that were expected were not apparently observed, probably because of inadequate enrichment of ^{17}O (20%).

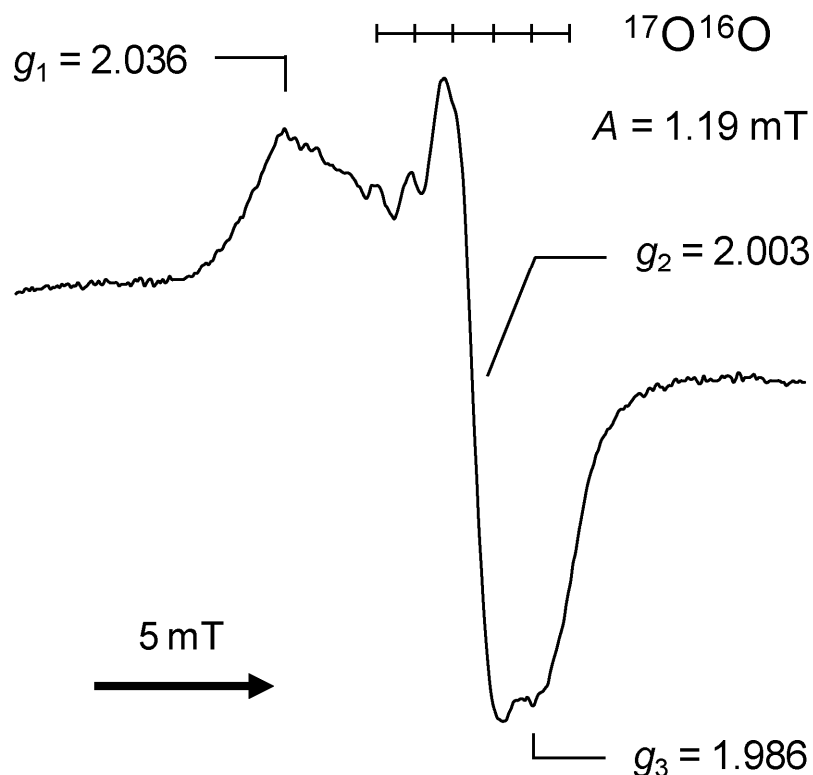


Figure 5. ESR spectrum of Nb_2O_5 irradiated in the presence of ^{17}O -enriched oxygen (4.0 kPa) at 77 K. A refers to the ^{17}O hyperfine structures.

Figure 6 shows the ESR spectrum obtained when ethylbenzene adsorbed on Nb₂O₅ was exposed to irradiation at 77 K. Irradiation of this sample resulted in the appearance of an intense signal with fine structure around $g = 2.0$. This fine structure can be assigned to the ethylbenzyl radical ($g = 2.003$, $A_{H1} = 6.0$ mT, $A_{H2} = 2.0$ mT) overlapped with the signal of electrons trapped at an oxygen vacancy (F center).³⁵⁻³⁷ In addition, a broad signal assigned to Nb(IV) ($g = 1.933$)^{38,39} was concomitantly observed with the ethylbenzyl radical. These results strongly support the oxidation of the benzylic C–H bond of ethylbenzene by the photogenerated hole and the reduction of Nb(V) to Nb(IV) by the excited electron. Subsequently, this sample was exposed to O₂ under photoirradiation at 77 K. A signal assigned to O₂⁻ appeared and the fine structure of the ethylbenzyl radical vanished (Figure 7). This suggests that the ethylbenzyl radical reacted with excess O₂⁻ to form a diamagnetic alkyl peroxide anion (ROO⁻) or hydroperoxide (ROOH).

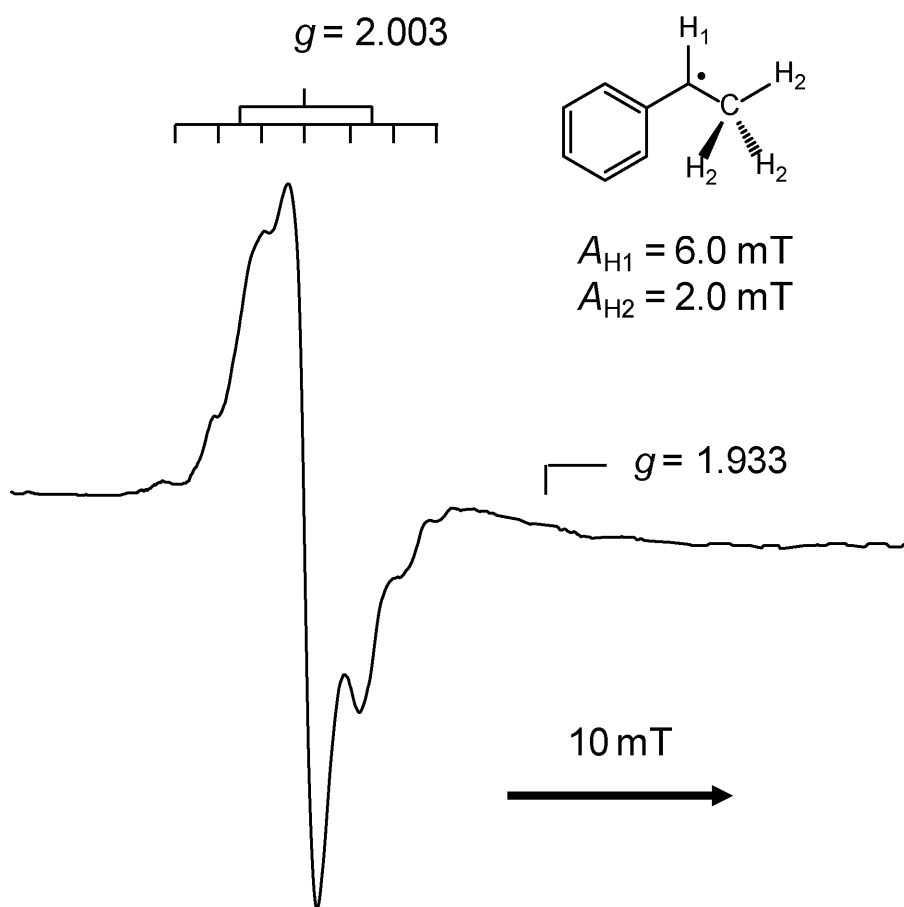


Figure 6. ESR spectrum of ethylbenzene adsorbed on Nb₂O₅ irradiated at 77 K.

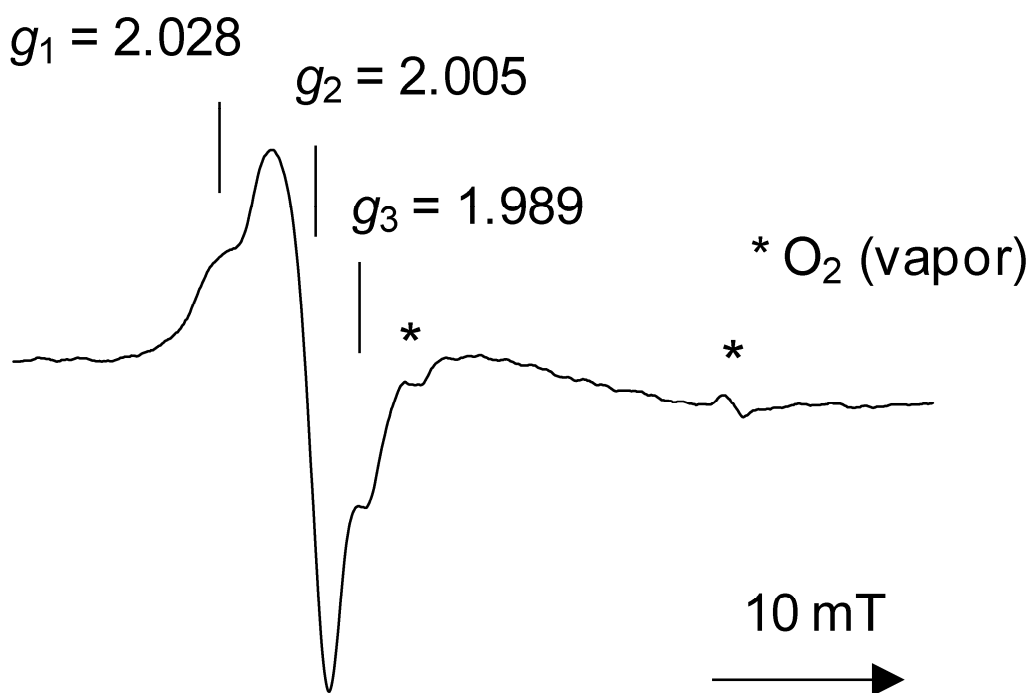


Figure 7. ESR spectrum obtained when ethylbenzene adsorbed on Nb₂O₅ was irradiated at 77 K, followed by being exposed to O₂.

FT-IR Measurement for Adsorbed Species

Figure 8 shows the FT-IR spectrum obtained after 10 min of photoirradiation of cyclohexane adsorbed on Nb₂O₅ in the presence of O₂. After photoirradiation, the bands assigned to $\nu(\text{C}=\text{O})$ (1666 cm⁻¹) and $\nu(\text{carbonate})$ (1567 cm⁻¹) appeared. These changes indicate generation of cyclohexanone and the subsequent photodecomposition of cyclohexanone into carbonate species. This photodecomposition is due to the $n \rightarrow \pi^*$ transition at the carbonyl moiety of cyclohexanone, known as the Norrish I type reaction.^{40,41} In the $\nu(\text{O}-\text{H})$ region, a negative peak at 3673 cm⁻¹ and a broad feature in the 3200–3500 cm⁻¹ range were observed. These bands are assigned to isolated surface hydroxyl groups and hydrogen-bonded surface hydroxyl groups and/or water molecules, respectively. The negative peak may be due to the loss of isolated surface hydroxyl groups by hydrogen bonding or oxidative consumption by photogenerated holes, producing hydroxyl radicals.

A small band assigned to $\nu(\text{C}-\text{O})$ appeared at 1192 cm⁻¹. We previously reported that the IR spectra of cyclohexanol adsorbed on Nb₂O₅ exhibited characteristic peaks at 1068 cm⁻¹ (nondissociative adsorption) and 1091 cm⁻¹ (dissociative adsorption).²⁰ The position of the peak

observed at 1192 cm^{-1} is significantly different from those of the adsorbed cyclohexanol species. Therefore, this suggests that a certain species containing the C–O bond, which can be distinguished from cyclohexanol, is formed to some extent on the Nb_2O_5 surface. According to the literature, alkyl hydroperoxide species exhibit absorption due to $\nu(\text{CCO})$ in the range of $1198\text{--}1176\text{ cm}^{-1}$.⁴² Moreover, it has been reported that authentic cyclohexyl hydroperoxide introduced on TiO_2 exhibits characteristic bands at 1367 cm^{-1} corresponding to $\omega(\text{CH}_2)$.⁴³ Similar peaks are also observed in this study (1192 cm^{-1} and 1367 cm^{-1}). On this basis, we can consider that cyclohexyl hydroperoxide is generated in the photooxidation of cyclohexane over Nb_2O_5 . The evolution of water molecules could be rationalized by decomposition of this hydroperoxide to ketone and water and/or C–H activation by hydroxyl radicals.

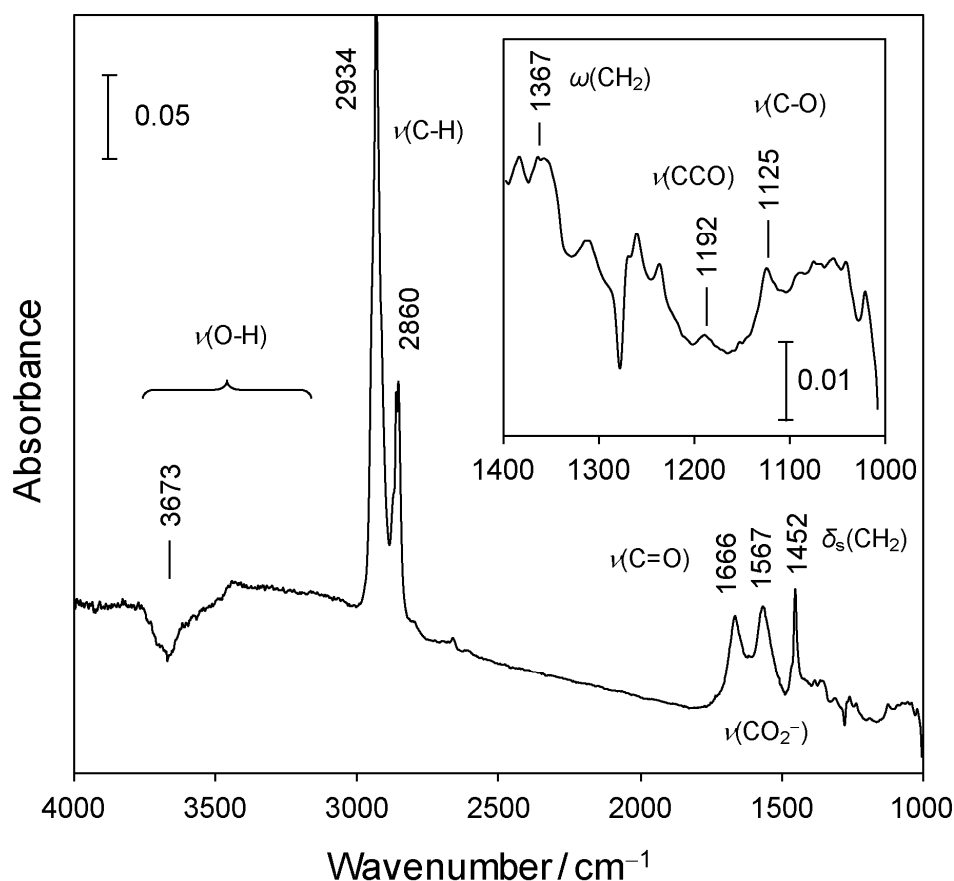


Figure 8. FT-IR spectrum after 10 min of photo irradiation to cyclohexane adsorbed on Nb_2O_5 in the presence of O_2 . Differential spectrum between before and after irradiation is shown. Inset shows a close-up of the $1400\text{--}1000\text{ cm}^{-1}$ region.

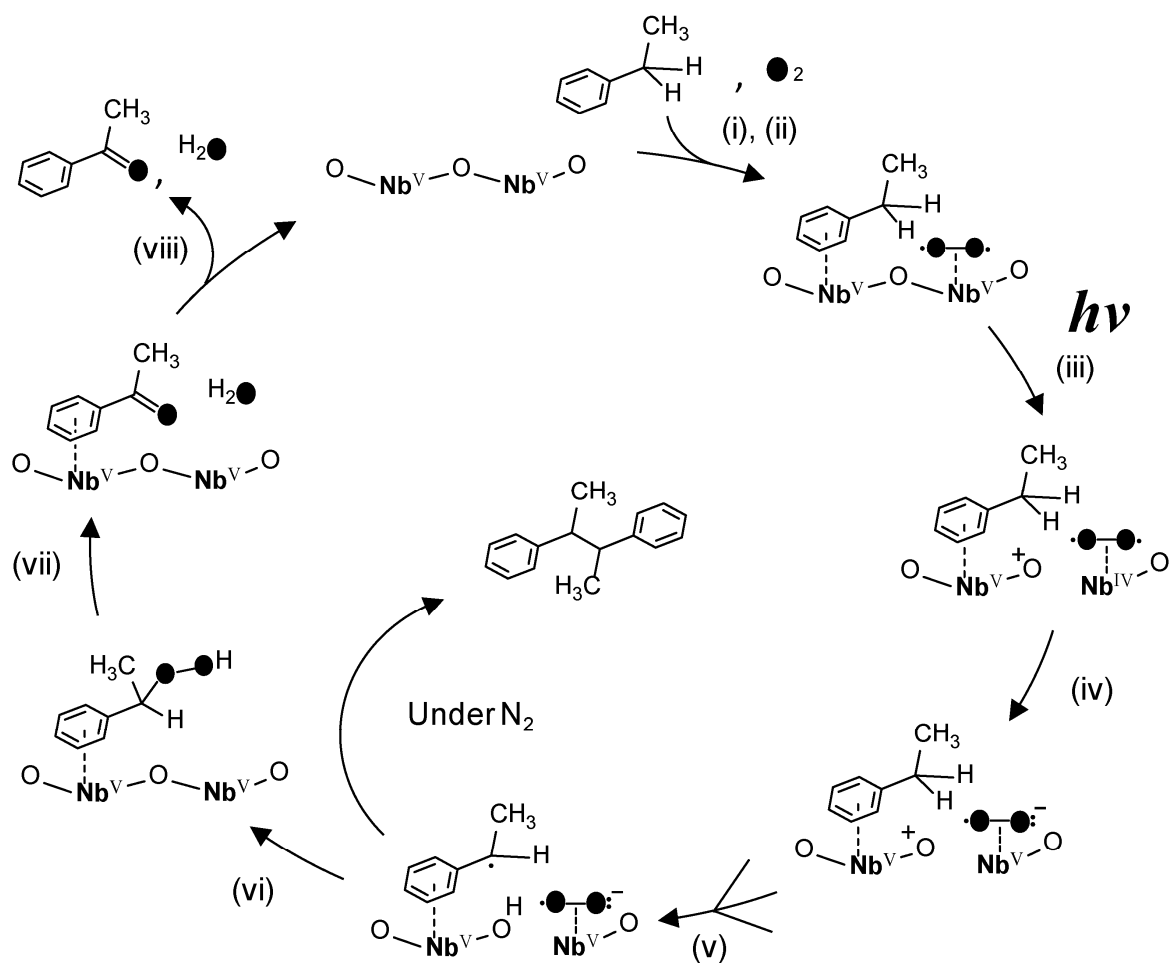
Discussion

On the basis of these results, the reaction mechanism is proposed as shown in Scheme 1. The hydrocarbon and molecular oxygen are competitively adsorbed on the Nb₂O₅ surface (steps i and ii, respectively). Photoirradiation of Nb₂O₅ results in the reduction of Nb(V) to Nb(IV) by an excited electron and the formation of a positive hole on lattice oxygen (step iii). Molecular oxygen is reduced to superoxide by an excited electron (step iv), and a C–H bond of the substrate is oxidized to produce an alkyl radical by a positive hole (step v, rate-determining step). Furthermore, C–H activation is possibly caused by a hydroxyl radical as commonly suggested. However, the generation of a hydroxyl radical should result in the formation of oxygenated products even under N₂ atmosphere, as shown in eqs 1 and 2.



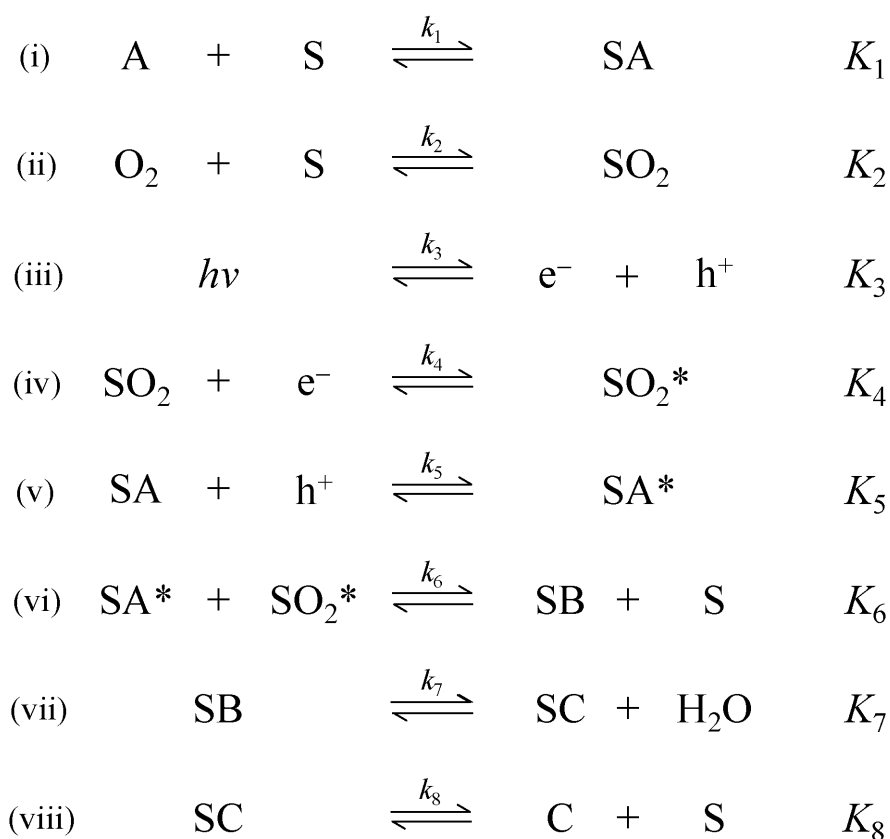
In fact, the oxygenated products (1-phenylethanol and acetophenone) did not form in the photooxidation of ethylbenzene under N₂. Subsequently, the alkyl radical is oxidized to alkyl hydroperoxide by the reaction with superoxide, followed by protonation (step vi). The alkyl hydroperoxide is decomposed to ketone and water (step vii), followed by desorption (step viii). Such decomposition of alkyl hydroperoxide to ketone or alcohol has frequently been proposed in various systems where the aerobic oxidation of cyclohexane is performed using materials such as metal-containing molecular sieves,⁴⁴ O₂-loaded Na–Y zeolite⁴⁵, and TiO₂ photocatalyst.⁴⁶ It has also been proposed that the ketone is formed by heterolytic decomposition, whereas the alcohol is formed by homolytic decomposition.⁴⁴ The proposed mechanism is essentially similar to that of the photooxidation of cyclohexane over TiO₂ reported by Mul and co-workers.⁴⁶ However, in the present study, a principal difference was observed in the amount and type of oxygen anion radical species (O₂⁻ or O₃⁻) formed in the reaction over TiO₂ and in that formed in the reaction over Nb₂O₅. The amount of oxygen anion radical formed on Nb₂O₅ was much lower than that formed on TiO₂.

Moreover, in contrast to the reaction over TiO_2 , O_3^- was not generated in that over Nb_2O_5 . Such surface oxygen species are known to be active for the complete oxidation of various hydrocarbons.⁴⁷⁻⁵¹ However, Lunsford et al. reported that O_2^- was stable up to ca. 423 K.⁵⁰ In contrast, O_3^- was active even at room temperature.^{49,51} On this basis, the higher selectivity to partial oxidation products that was observed for Nb_2O_5 than for TiO_2 may be due to the lack of O_3^- .



Scheme 1. Proposed mechanism of photooxidation of hydrocarbon over Nb_2O_5 : (i) adsorption of hydrocarbon, (ii) adsorption of O_2 , (iii) charge separation, (iv) reduction of O_2 , (v) C-H activation, (vi) oxygenation of alkyl radical, (vii) heterolytic decomposition of hydroperoxide and (viii) desorption of ketone.

On the basis of the proposed mechanism, kinetic analysis was then carried out. The rate constants and equilibrium constants of these elemental steps are defined as shown in Scheme 2. The overall reaction rate r is represented as the rate of step v (eq 3). This rate equation is converted to a function of substrate concentration ($[A]$), oxygen pressure (P_{O_2}), and light intensity (I) (eq 4) by considering the following conditions: steady-state approximation, charge conservation (eq 5), and by the total number of adsorption sites being constant (eq 6). Equation 4 can be simplified into a single function of $[A]$, P_{O_2} , or I , (eqs 7–9, respectively).



Scheme 2. Elementary steps in photooxidation of hydrocarbon over Nb_2O_5 . A: hydrocarbon. S: vacant adsorption site. AS: adsorbed hydrocarbon. SO_2 : adsorbed oxygen. SO_2^* : reduced oxygen. SA^* : oxidized hydrocarbon. SB: adsorbed hydroperoxide. SC: adsorbed product. C: product.

$$r = k_5[\text{SA}][h^+] \quad (3)$$

$$r = \frac{k_5 K_1 K_2 K_3 K_4 K_6 K_7 K_8 [\text{S}]_0 [\text{A}] \text{P}_{\text{O}_2} \text{I}}{K_2^2 K_3 K_4^2 K_6 K_7 K_8 \text{P}_{\text{O}_2}^2 \text{I} + K_2 K_3^{0.5} K_4 K_6 \text{P}_{\text{O}_2} (K_1 K_7 K_8 [\text{A}] + K_2 K_7 K_8 \text{P}_{\text{O}_2} + K_7 K_8 + K_7 [\text{C}] + [\text{C}][\text{H}_2\text{O}]) \text{I}^{0.5} + [\text{C}][\text{H}_2\text{O}]} \quad (4)$$

$$[e^-] = [h^+] \quad (5)$$

$$[\text{S}]_0 = [\text{S}] + [\text{SA}] + [\text{SA}^*] + [\text{SO}_2] + [\text{SO}_2^*] + [\text{SB}] + [\text{SC}] \quad (6)$$

$$\frac{1}{r} = a_1 \frac{1}{[\text{A}]} + b_1 \quad (7)$$

$$\frac{\text{P}_{\text{O}_2}}{r} = a_2 \text{P}_{\text{O}_2}^2 + b_2 \text{P}_{\text{O}_2} + c_2 \quad (8)$$

$$\frac{\text{I}}{r} = a_3 (\text{I}^{0.5})^2 + b_3 (\text{I}^{0.5}) + c_3 \quad (9)$$

The experimental reaction rate of the photooxidation of ethylbenzene over Nb_2O_5 ($r / \text{mmol} \cdot \text{h}^{-1}$) was obtained as a function of $[\text{A}]$, P_{O_2} , and I (Figure 9). A positive correlation was observed in the r vs. $[\text{A}]$ and r vs. I plots, whereas a negative correlation was observed in the r vs. P_{O_2} plot, suggesting competitive adsorption of the substrate and molecular oxygen. We then plotted reciprocals of the reaction rates ($1/r$) versus the reciprocal of the substrate concentration ($1/[\text{A}]$), as shown in Figure 10a. A linear correlation was obtained between $1/r$ and $1/[\text{A}]$. This correlation can be expressed as eq 10, corresponding with eq 7. Likewise, a good quadratic correlation was found in the P_{O_2}/r vs. P_{O_2} , and I/r vs. $r^{0.5}$ plots (Figure 10b and c, respectively). These correlations are described as eqs 11 and 12, corresponding with eqs 8 and 9, respectively. Thus, the kinetic model derived from the proposed mechanism is satisfactorily consistent with the experimental data.

$$\frac{1}{r} = 14.2 \frac{1}{[A]} + 2.41 \quad (10)$$

$$\frac{P_{O_2}}{r} = 2.05 P_{O_2}^2 + 0.770 P_{O_2} + 0.0365 \quad (11)$$

$$\frac{I}{r} = -15.5(I^{0.5})^2 + 29.6(I^{0.5}) - 9.7 \quad (12)$$

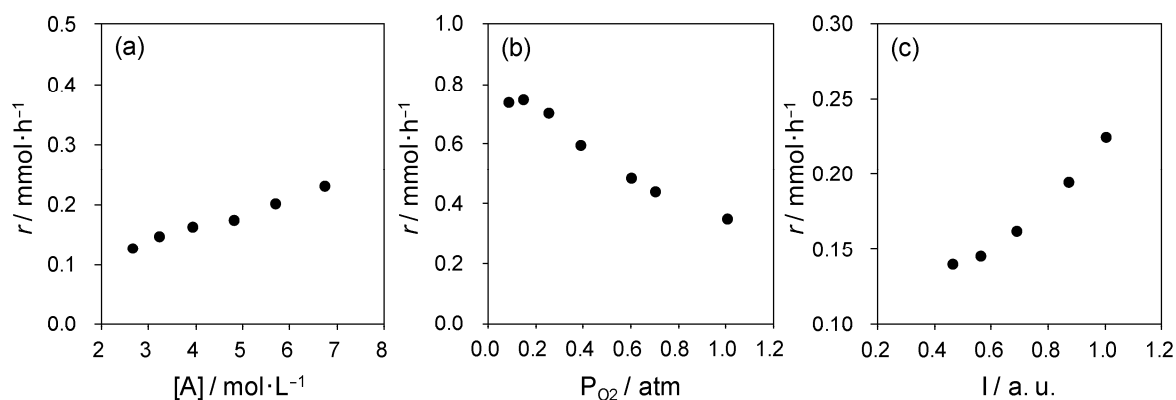


Figure 9. Reaction rates of ethylbenzene photooxidation over Nb_2O_5 under conditions of (a) various concentrations of ethylbenzene in benzene as a solvent; $[A]$, (b) O_2 diluted by N_2 in the gas phase; P_{O_2} and (c) different light intensity; I .

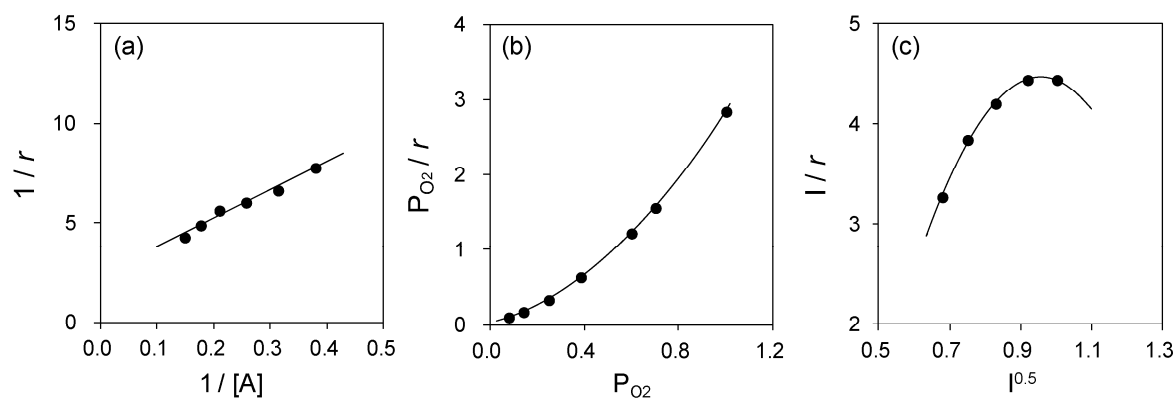


Figure 10. Plots of (a) $1/r$ against $1/[A]$, (b) P_{O_2}/r against P_{O_2} and (c) I/r against $r^{0.5}$.

Conclusions

The photooxidation of various undiluted hydrocarbons in liquid phase was conducted over Nb₂O₅ at room temperature. Nb₂O₅ exhibited higher selectivities to partial oxidation products than did TiO₂. A much higher K/A ratio was obtained in the photooxidation of cyclohexane over Nb₂O₅ than in that over TiO₂. The mechanistic study revealed that the photooxidation of hydrocarbon over Nb₂O₅ proceeds via a typical Langmuir–Hinshelwood mechanism as follows. Substrate and dioxygen are adsorbed on the Nb₂O₅ surface. Photoirradiation of Nb₂O₅ resulted in the reduction of Nb(V) to Nb(IV) by an excited electron and the formation of a positive hole on lattice oxygen. Dioxygen is reduced to superoxide by an excited electron, and a C–H bond of the substrate is oxidized by a positive hole to produce an alkyl radical. The alkyl radical is oxygenated to alkyl hydroperoxide by reaction with superoxide, followed by protonation. Finally, the alkyl hydroperoxide is decomposed to ketone and water. This mechanism is essentially the same as that of the photooxidation of cyclohexane over TiO₂. However, ESR measurements revealed that the strongly oxidizing species O₃[−] was not formed in the reaction over Nb₂O₅, in contrast to that conducted over TiO₂. These results lead us to the conclusion that the absence of O₃[−] is the key factor for the high selectivity to partial oxidation that is achieved in the photooxidation of hydrocarbon over Nb₂O₅. Moreover, this reaction mechanism does not involve the photoactivation of an adsorbed species, as is found in the alcohol photooxidation over Nb₂O₅; that is, excitation from an O 2p orbital localized on adsorbed alkoxide species to a conduction band consisting of Nb 4d orbital. This implies that the strong interaction between a substrate and surface (e.g., dissociative adsorption) is a key factor in the photoactivation of the adsorbed species.

References

- (1) Fox, M. A.; Dulay, M. T. *Chem. Rev.* **1993**, *93*, 341–357.
- (2) Mills, A.; LeHunte, S. J. *Photochem. Photobiol. A* **1997**, *108*, 1.
- (3) Maldotti, A.; Molinari, A.; Amadelli, R. *Chem. Rev.* **2002**, *102*, 3811.
- (4) Giannotti, C.; Legreneur, S.; Watts, O. *Tetrahedron Lett.* **1983**, *24*, 5071.
- (5) Mu, W.; Herrmann, J. M.; Pichat, P. *Catal. Lett.* **1989**, *3*, 73.

- (6) Beaune, O.; Finiels, A.; Geneste, P.; Graffin, P.; Guida, A.; Olive, J. L.; Saeedan, A. *Heterogeneous Catalysis and Fine Chemicals III* **1993**, 78, 401.
- (7) Boarini, P.; Carassiti, V.; Maldotti, A.; Amadelli, R. *Langmuir* **1998**, 14, 2080.
- (8) Almquist, C. B.; Biswas, P. *Appl. Catal., A* **2001**, 214, 259.
- (9) Du, P.; Moulijn, J. A.; Mul, G. *J. Catal.* **2006**, 238, 342.
- (10) Wittenberg, R.; Pradera, M. A.; Navio, J. A. *Langmuir* **1997**, 13, 23739.
- (11) Pillai, U. R.; Sahle-Demessie, E. *J. Catal.* **2002**, 211, 434.
- (12) Muggli, D. S.; Falconer, J. L. *J. Catal.* **1998**, 175, 213.
- (13) Yurdakal, S.; Palmisano, G.; Loddo, V.; Alagoz, O.; Augugliaro, V.; Palmisano, L. *Green Chem.* **2009**, 11, 510.
- (14) Scaife, D. E. *Sol. Energy* **1980**, 25, 41.
- (15) Teramura, K.; Tanaka, T.; Hosokawa, T.; Ohuchi, T.; Kani, M.; Funabiki, T. *Catal. Today* **2004**, 96, 205.
- (16) Teramura, K.; Tanaka, T.; Kani, M.; Hosokawa, T.; Funabiki, T. *J. Mol. Catal. A: Chem.* **2004**, 208, 299.
- (17) Teramura, K.; Hosokawa, T.; Ohuchi, T.; Shishido, T.; Tanaka, T. *Chem. Phys. Lett.* **2008**, 460, 478.
- (18) Teramura, K.; Ohuchi, T.; Shishido, T.; Tanaka, T. *J. Phys. Chem. C* **2009**, 113, 17018.
- (19) Ohuchi, T.; Miyatake, T.; Hitomi, Y.; Tanaka, T. *Catal. Today* **2007**, 120, 233.
- (20) Shishido, T.; Miyatake, T.; Teramura, K.; Hitomi, Y.; Yamashita, H.; Tanaka, T. *J. Phys. Chem. C* **2009**, 113, 18713.
- (21) Shishido, T.; Teramura, K.; Tanaka, T. *Catal. Sci. Technol.* **2011**, 1, 541.
- (22) Luo, Y.-R. *Handbook of Bond Dissociation Energies in Organic Compounds*; CRC Press: Boca Raton, 2003.
- (23) Baciocchi, E.; D'Acunzo, F.; Galli, C.; Lanzalunga, O. *J. Chem. Soc., Perkin Trans. 2* **1996**, 133.
- (24) Bordwell, F. G.; Zhang, X. M.; Cheng, J. P. *J. Org. Chem.* **1991**, 56, 3216.
- (25) Mayer, J. M. *Acc. Chem. Res.* **1998**, 31, 441.

- (26) Kaizer, J.; Klinker, E. J.; Oh, N. Y.; Rohde, J. U.; Song, W. J.; Stubna, A.; Kim, J.; Munck, E.; Nam, W.; Que, L. *J. Am. Chem. Soc.* **2004**, *126*, 472.
- (27) Lam, W. W. Y.; Yiu, S. M.; Lee, J. M. N.; Yau, S. K. Y.; Kwong, H. K.; Lau, T. C.; Liu, D.; Lin, Z. Y. *J. Am. Chem. Soc.* **2006**, *128*, 2851.
- (28) Sastri, C. V.; Lee, J.; Oh, K.; Lee, Y. J.; Lee, J.; Jackson, T. A.; Ray, K.; Hirao, H.; Shin, W.; Halfen, J. A.; Kim, J.; Que, L.; Shaik, S.; Nam, W. *Proc. Nat. Acad. Sci.* **2007**, *104*, 19181.
- (29) Seo, M. S.; Kim, N. H.; Cho, K. B.; So, J. E.; Park, S. K.; Clemancey, M.; Garcia-Serres, R.; Latour, J. M.; Shaik, S.; Nam, W. *Chem. Sci.* **2011**, *2*, 1039.
- (30) Vanhoof, J. H. C. *J. Catal.* **1968**, *11*, 277.
- (31) Lunsford, J. H. *Catal. Rev.* **1973**, *8*, 135.
- (32) Tench, A. J. *J. Chem. Soc. Faraday Trans. 1* **1972**, *68*, 1181.
- (33) Che, M.; Giamello, E.; Tench, A. J. *Colloids Surf.* **1985**, *13*, 231.
- (34) To the best of our knowledge, there has been no literature that characterizes surface oxygen species on Nb₂O₅.
- (35) Okumura, M.; Coronado, J. M.; Soria, J.; Haruta, M.; Conesa, J. C. *J. Catal.* **2001**, *203*, 168.
- (36) Teramura, K.; Tanaka, T.; Funabiki, T. *Chem. Lett.* **2003**, *32*, 1184.
- (37) Yamazoe, S.; Okumura, T.; Tanaka, T. *Catal. Today* **2007**, *120*, 220.
- (38) Sugantha, M.; Varadaraju, U. V.; Rao, G. V. S. *J. Solid State Chem.* **1994**, *111*, 33.
- (39) Verissimo, C.; Garrido, F. M. S.; Alves, O. L.; Calle, P.; MartinezJuarez, A.; Iglesias, J. E.; Rojo, J. M. *Solid State Ionics* **1997**, *100*, 127.
- (40) Norrish, R. G. W.; Bamford, C. H. *Nature* **1936**, *138*, 1016.
- (41) Norrish, R. G. W.; Bamford, C. H. *Nature* **1937**, *140*, 195.
- (42) Silverstein, R. M.; Webster, F. X. *Spectrometric Identification of Organic Compounds*, 6th ed.; Wiley: New York, 1998.
- (43) Almeida, A. R.; Moulijn, J. A.; Mul, G. *J. Phys. Chem. C* **2011**, *115*, 1330.
- (44) Tian, P.; Liu, Z. M.; Wu, Z. B.; Xu, L.; He, Y. L. *Catal. Today* **2004**, *93-95*, 735.
- (45) Sun, H.; Blatter, F.; Frei, H. *J. Am. Chem. Soc.* **1996**, *118*, 6873.
- (46) Almeida, A. R.; Moulijn, J. A.; Mul, G. *J. Phys. Chem. C* **2008**, *112*, 1552.
- (47) Aika, K. I.; Lunsford, J. H. *J. Phys. Chem.* **1977**, *81*, 1393.

- (48) Aika, K. I.; Lunsford, J. H. *J. Phys. Chem.* **1978**, *82*, 1794.
- (49) Takita, Y.; Lunsford, J. H. *J. Phys. Chem.* **1979**, *83*, 683.
- (50) Iwamoto, M.; Lunsford, J. H. *J. Phys. Chem.* **1980**, *84*, 3079.
- (51) Takita, Y.; Iwamoto, M.; Lunsford, J. H. *J. Phys. Chem.* **1980**, *84*, 1710.

Chapter 6

Solvent-free aerobic alcohol oxidation using Cu/Nb₂O₅: Green and highly selective photocatalytic system

Abstract

Photooxidation of alcohols without organic solvents in the presence of O₂ took place at the atmospheric pressure and room temperature over Nb₂O₅ and Cu/Nb₂O₅, avoiding the cost, toxicity, and purification problems associated with transition-metal systems. Loading of a small amount of copper on Nb₂O₅ significantly enhanced activity without lowering selectivity. On the other hand, loading of Pt, Ni, Rh, Ru, and Ag showed no promotion effect. The selectivities of the photooxidation of aliphatic, aromatic and heteroatom-containing alcohols over Cu/Nb₂O₅ were in the range of 80–99%. Cu/Nb₂O₅ was easily separated from the reaction mixture and was reusable without reducing the catalytic performance.

Introduction

Alcohol oxidation to corresponding carbonyl compounds is one of the most useful and the simplest transformations in organic and industrial chemistry. Non-catalytic methods with stoichiometric, toxic, corrosive and expensive oxidants such as ClO^- , dichromate, permanganate, and peroxy acids under stringent conditions of high pressure and/or temperature have been widely used for alcohol oxidations.¹⁻⁴ In addition, these reactions are often carried out with high concentration of bases and environmentally unfriendly organic solvents. Therefore, much attention has been paid to the development of heterogeneous catalytic systems that use clean and atom efficient oxidants like molecular oxygen or H_2O_2 without organic solvents.⁵⁻¹⁶ Therefore, the development of catalytic systems for alcohol oxidation has been one of the most pursued targets in last decade, due to substituting them with heterogeneous catalytic oxidation using clean and atom-efficient oxidants such as molecular oxygen without organic solvents.

Recently, the aerobic alcohol oxidation was successfully carried out by using heterogeneous catalysts such as tetrapropylammonium perruthenate (TPAP)/MCM-41,⁸ Ru/CeO₂,⁹ Ru-hydroxalcite,¹⁰ Ru/hydroxyapatite (Ru-HAP),^{11,12} [RuCl₂(*p*-cymene)]/activated carbon,¹³ Ru/Al₂O₃,¹⁴ Pd-hydroxalcite which requires the addition of pyridine,¹⁵ and Pt on activated carbon.¹⁶ These systems require the use of organic solvents like toluene and trifluorotoluene. Solvent-free aerobic oxidation of alcohols by Pd/Al₂O₃ was also reported,¹⁷ however, the use of the noble metal Pd is essentially required.

In this respect, photoreactions are promising processes and the development of photocatalysts is a subject that is now receiving noticeable attention. TiO₂ has been identified as one example of a practical and useful photocatalysts,¹⁸⁻²² and widely used in degradation of organic pollutants in air and water. In the most part of these reports, TiO₂ is used in vapor phase oxidations at high temperatures,¹⁸ oxidation of only lower alcohols,¹⁹⁻²¹ oxidation using solvents such as benzene²² and a low selectivity to partial oxidized products due to excess photo-activation of target products which leads to deep oxidation. Zhao et al^{23,24} reported that the photooxidation of alcohols on TiO₂ could be dramatically accelerated without any loss of selectivity by adsorption of Brønsted acid and this effect by Brønsted acid results from the

decomposition of the relatively stable side-on peroxide promoted by the protons, which effectively clean the catalytic Ti–OH₂ sites. Recently, Su and co-workers reported that mesoporous graphite carbon nitride (mpg-C₃N₄) can work as effective photocatalyst for the selective oxidations of benzylic alcohols with visible light. However, these systems require the use of benzotrifluoride as a solvent.

Here, we report that Nb₂O₅ and Cu/Nb₂O₅ catalyze photooxidation of various aliphatic and aromatic alcohols without solvents in the presence of O₂ at the atmospheric pressure and room temperature. We found that loading of a small amount of copper on Nb₂O₅ significantly enhanced activity without lowering selectivity, whereas loading of Pt, Ni, Rh, Ru, and Ag showed no promotion effect. This strongly suggests that the role of Cu on Nb₂O₅ is different from those of precious metals such as Pt and Rh on TiO₂ photocatalyst, in other words, the promotion of charge separation.

Experimental

Preparation

Niobic acid, niobium oxide hydrate (Nb₂O₅ · nH₂O, AD/2872, HY-340) was kindly supplied from CBMM. Other chemicals used were of reagent grade and were obtained from Aldrich Chemical Co., Tokyo Kasei Kogyo Co., Ltd and Wako Pure Chemical Industries, Ltd. All reagents were used without further purification.

Niobium oxide (Nb₂O₅) catalyst was prepared by calcination of niobic acid in a dry air flow at 773 K for 5 h (BET surface area: 48 m²g⁻¹). A series of niobium oxide supported metal catalysts (M/Nb₂O₅; M = Ru, Rh, Ni, Pt, Cu, and Ag) was prepared by impregnation of niobic acid with an aqueous solutions of metal salts (RuCl₂, RhCl₃, Ni(NO₃)₂, H₂PtCl₄, Cu(NO₃)₂ and Ag(NO₃)) at 353 K, followed by evaporation, drying and calcination at 773 K in a stream of dry air for 5 h. After calcination, the catalysts were ground into powder under 100 mesh (0.15 mm). M/Nb₂O₅ catalysts were reduced under 5% H₂/N₂ flow at 20 cm³min⁻¹ for 0.5 h at 673 K prior to use.

Characterization

BET surface areas of catalysts were determined using N₂ adsorption isotherm at 77 K measured by a BELSORP 28SA (BEL Japan Corp.). Crystal phase of each catalyst was determined by X-ray diffraction technique (XRD) under ambient conditions at room temperature using a Shimadzu XD-D1 X-ray diffractometer with Cu K α radiation ($\lambda = 1.5418 \text{ \AA}$).

Photooxidation of alcohols

The photocatalytic oxidation of alcohol was carried out in a quasi-flowing batch system (see Chapter 5, Figure 1). Catalyst (100 mg) and a stirring bar were introduced to the Pyrex glass reactor (cut-off light below 300 nm). An alcohol as a substrate (10 ml) without solvent was introduced into the reactor. The suspension was vigorously stirred at room temperature and irradiated from the flat bottom of the reactor through a reflection by a cold mirror with a 500 W ultra-high-pressure Hg lamp (USHIO Denki Co.). Oxygen was flowed into the reactor at 2 cm³min⁻¹ (0.1 MPa). At the down stream of the flow reactor, a saturated barium hydroxide solution (Ba(OH)₂) was equipped to determine the quantity of carbon dioxide (CO₂) as barium carbonate (BaCO₃). Products were analyzed and quantified by FID–GC (Shimadzu GC14B) and GC–MS (Shimadzu QP-5050).

Results and Discussion

Solvent-Free Photooxidation of 1-Pentanol over M/Nb₂O₅

Table 1 shows the results of photooxidation of 1-pentanol over Nb₂O₅ and M/Nb₂O₅ (M = Ru, Rh, Ni, Pt, Cu, and Ag) with molecular oxygen under irradiation at 323 K. The photogenerated products were pentanal (RCHO) as a main product, and a small amount of pentanoic acid (RCOOH) and carbon dioxide (CO₂). Control experiments revealed that catalyst, oxygen and photo irradiation are necessary for the reaction (entries 12–14). The evolution of photogenerated products occurred in response to illumination. These results indicate that photooxidation of 1-pentanol over Nb₂O₅ and M/Nb₂O₅ was due entirely to a photocatalytic reaction. We have already reported that Nb₂O₅ shows higher selectivity to pentanal than TiO₂ at

the same conversion level although TiO₂ shows higher activity than Nb₂O₅.²⁵ Cu/Nb₂O₅ showed much higher activity than that of bare Nb₂O₅ (entries 1 and 7–11). On the other hand, when Ru, Rh, Ni, Pt, and Ag were supported on Nb₂O₅, the yields were almost similar to or slightly lower than that of bare Nb₂O₅ (entries 1–6).

Table 1. Photocatalytic activities of M/Nb₂O₅ (M = Ru, Rh, Ni, Pt, Cu, and Ag) in solvent-free photooxidation of 1-pentanol. ^a

Entry	Catalyst	Loading (mol%)	Yield / μmol^b
1	Nb ₂ O ₅	–	355
2	Ru/Nb ₂ O ₅	2.6	315
3	Rh/Nb ₂ O ₅	2.6	305
4	Ni/Nb ₂ O ₅	2.6	220
5	Pt/Nb ₂ O ₅	2.6	340
6	Ag/Nb ₂ O ₅	2.6	445
7	Cu/Nb ₂ O ₅	0.65	780
8	Cu/Nb ₂ O ₅	1.3	1145
9	Cu/Nb ₂ O ₅	1.9	1285
10	Cu/Nb ₂ O ₅	2.6	1125
11	Cu/Nb ₂ O ₅	5.2	880
12 ^c	Cu/Nb ₂ O ₅	1.9	36
13 ^d	Cu/Nb ₂ O ₅	1.9	n. d.
14	none	–	n. d.

^a Reaction condition: catalyst (100 mg), 1-pentanol (10 ml), oxygen flow (2 cm³ min⁻¹), $\lambda > 300$ nm, irradiation time, 5 h. ^b Amount of pentanal produced. ^c Under 1 atm N₂. ^d In the dark.

XRD patterns of Nb_2O_5 and $\text{M}/\text{Nb}_2\text{O}_5$ showed diffraction lines assignable to TT-phase Nb_2O_5 with a pseudohexagonal structure (Figure 1). No diffraction line due to these metal species was detected, indicating that these metal species were highly dispersed or with amorphous. It has been reported that modification with a small amount of highly dispersed metal species like Pt^{20,22,26}, Rh²⁷ and Ni²⁸ improves the photocatalytic activity of TiO_2 .

Usually, it is thought that these metal species supported on TiO_2 act as an electron acceptor, resulting in inhibiting the recombination of photoactivated electrons and positive holes (charge separation mechanism). Therefore, above results of photooxidation over Nb_2O_5 and $\text{M}/\text{Nb}_2\text{O}_5$ suggest that the role of Cu supported on Nb_2O_5 is different from that of metal species on TiO_2 , i.e., electron acceptor in charge separation mechanism. Hashimoto and co-workers reported that Cu(II) species grafted on TiO_2 promotes the oxidative decomposition of 2-propanol even under visible light (>450 nm) irradiation.^{29,30} They also proposed that visible light initiates interfacial charge transfer (IFCT),³¹⁻³³ in other words, electron in the valence band of TiO_2 are directly transferred to Cu(II) and form Cu(I). In the IFCT mechanism, Cu(II) acts as an electron acceptor.

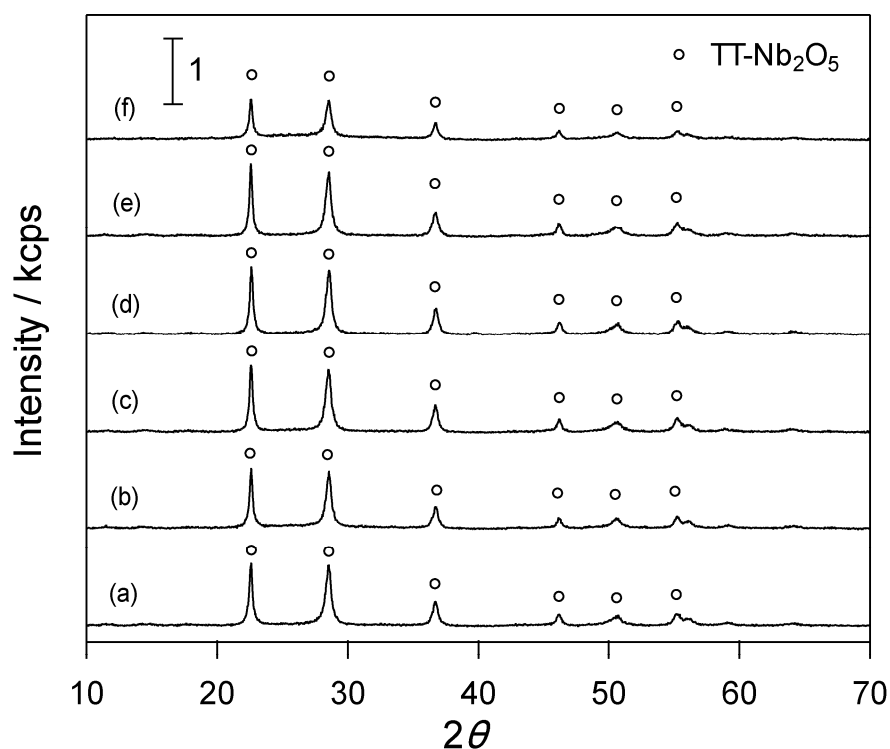


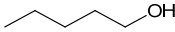
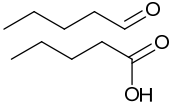
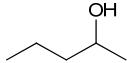
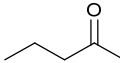
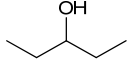
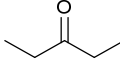
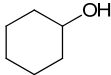
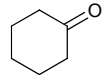
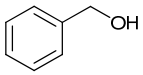
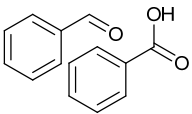
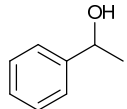
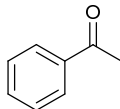
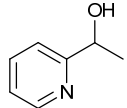
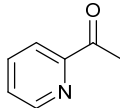
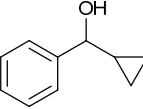
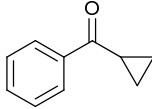
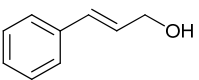
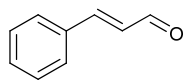
Figure 1. XRD patterns of $\text{M}/\text{Nb}_2\text{O}_5$: M = (a) Ru, (b) Rh, (c) Ni, (d) Pt, (e) Cu and (f)

Recently, we found that the photooxidation of 1-pentanol over Nb₂O₅ took place under visible light irradiation up to 480 nm, although the band gap of Nb₂O₅ is 390 nm (3.2 eV).^{34,35} This observation indicates that the photo-activation mechanism of alcohol over Nb₂O₅ is different from the classical electron transfer mechanism found in semiconductor photocatalysis (the formation of an excited electron in the conduction band and the positive hole in the valence band). By means of UV–Vis, ESR, FT-IR with the aid of DFT calculations, the detailed reaction mechanism of photooxidation of alcohol over revealed and unique photo-activation mechanism by “*in situ doping*” (the direct electron transfer from the O 2p orbital derived from adsorbed alcoholate species to the conduction band consisting of Nb 4d orbitals) was proposed.^{34–37} Moreover, kinetic analysis revealed that the rate-determining step of the photooxidation of alcohol over Nb₂O₅ is desorption of products. These results suggest that copper on Nb₂O₅ acts as an accelerator of the product desorption in addition to the promoter of charge separation. The detailed reaction mechanism and the role of copper of Cu/Nb₂O₅ are now under investigation and will be reported in the near future.^{36,37}

Photooxidation of Alcohols over Cu/Nb₂O₅

The catalytic activities and selectivities for the solvent-free photooxidation of several aliphatic and aromatic alcohols over Nb₂O₅ and Cu/Nb₂O₅ with molecular oxygen at atmospheric pressure are summarized in Table 2 (entries 1–6). These aliphatic and aromatic alcohols were selectively oxidized to corresponding carbonyl compounds. The selectivity to cyclohexanone was slightly low (entry 4) among aliphatic alcohols tested. This may be due to autooxidation by the formation of radical species by the photo-activation (Norrish Type I reaction)^{38,39} of the produced cyclohexanone. In the case of aliphatic primary and secondary alcohols except for cyclohexanol (entry 4), the catalytic activities were significantly increased by loading of Cu. The conversions and selectivities in oxidation of aromatic alcohols were higher than those of aliphatic alcohols (entries 5 and 6). This tendency is similar to the conventional thermal catalyst. Primary alcohols were easier to be oxidized than secondary ones in the case of both of aliphatic and aromatic ones. This result is in contrast to the photooxidation of alcohol over TiO₂ film.¹⁸

Table 2. Photooxidations of various alcohols catalyzed by Cu/Nb₂O₅ and Nb₂O₅.^a

Entry	Substrate	Products	Time / h	Cu/Nb ₂ O ₅		Nb ₂ O ₅	
				C (%)	S (%)	C (%)	S (%)
1			48	33	80	16	71
2			48	26	86	12	87
3			48	23	82	8	93
4			48	30	81	37	81
5			24	36	99	37	99
6			24	24	98	19	93
			192	99	96	88	92
7 ^b			48	94	91	93	90
8a ^b			48	97	59	99	50
8b ^{b,c}			48	40	64	42	61
9a ^b			48	96	21	99	11
9b ^{b,c}			48 ^c	51	49	76	30

^a Reaction condition: catalyst (100 mg), alcohol (10 ml), oxygen flow (2 cm³ min⁻¹), $h\nu > 300$ nm, C; conversion of alcohol, S; selectivity to partial oxidation products. ^b Catalyst (100 mg), alcohol (1 mmol), benzene (10 ml), oxygen pressure (0.1 MPa), $h\nu > 300$ nm. To avoid solvent evaporation, the oxidation was carried out in a closed system. ^c $h\nu > 390$ nm (using L42 cut-filter). BET surface areas of Nb₂O₅ and Cu/Nb₂O₅ are 48 and 59 m²g⁻¹.

Figure 2 shows the time course of photooxidation of 1-phenylethanol over Nb_2O_5 and $\text{Cu}/\text{Nb}_2\text{O}_5$. The conversion increased with irradiation time. On the other hand, the selectivity to acetophenone was almost constant. The formation rate of acetophenone over $\text{Cu}/\text{Nb}_2\text{O}_5$ was higher than that of Nb_2O_5 . Furthermore, in the case of $\text{Cu}/\text{Nb}_2\text{O}_5$, 1-phenylethanol was almost stoichiometrically oxidized after 192 h of photo irradiation even under solvent-free condition (96% yield; entry 6). Up to now, attempts to use photocatalyst for selective solvent-free aerobic oxidation of alcohols have met with very limited success. Fukuzumi et al. reported that 9-phenyl-10-methylacridium acts as an effective photocatalyst for solvent-free selective photocatalytic oxidation of benzyl alcohol under visible light irradiation via efficient photoinduced electron transfer from benzyl alcohol to the singlet excited state of the acridium ion.⁴⁰ However, turnover number (TON) of their system is quite small. To the best of our knowledge, our system ($\text{Cu}/\text{Nb}_2\text{O}_5$) is the first example that aerobic photooxidation of alcohol proceeded quantitatively even under solvent-free condition.

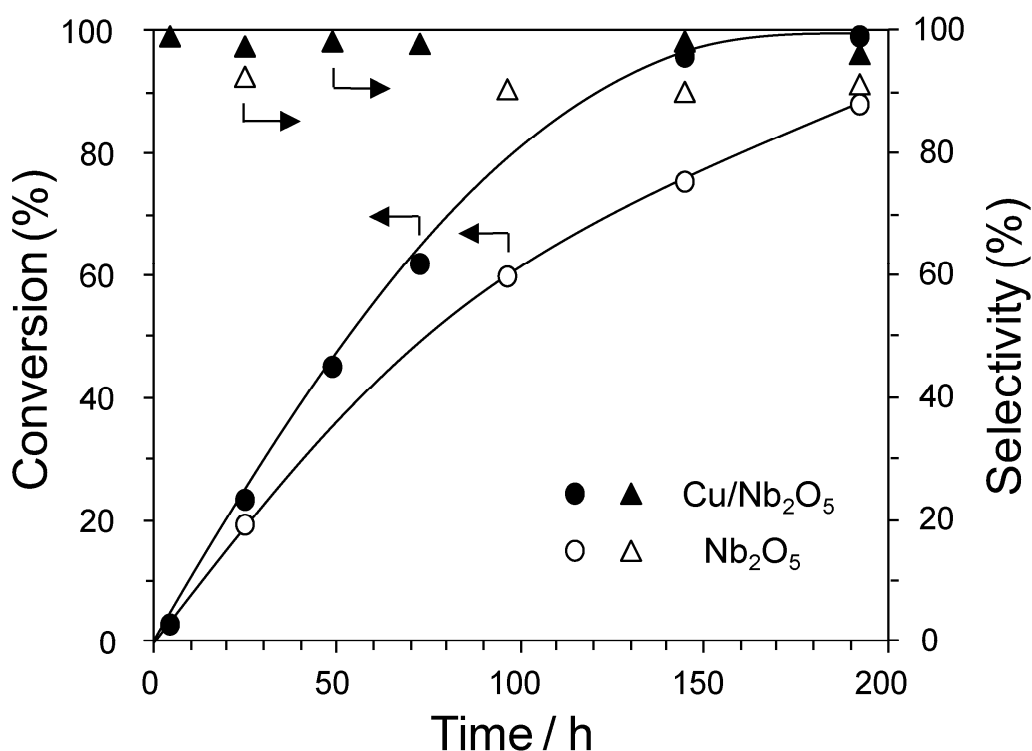


Figure 2. Time course of conversions and selectivities in photooxidation of 1-phenylethanol over $\text{Cu}/\text{Nb}_2\text{O}_5$ and Nb_2O_5 . Filled circle and triangle are the conversion and selectivity over $\text{Cu}/\text{Nb}_2\text{O}_5$ and unfilled circle and triangle are those over Nb_2O_5 .

Leaching of active metal species into solution is important point to consider the stability of catalyst. After 5 h of photooxidation of 1-pentanol, Cu/Nb₂O₅ catalysts could be easily separated by filtration. Further irradiation to the solid-free solution did not give any products. Moreover, the separated Cu/Nb₂O₅ was successfully reused with no reduction in the activity and selectivity as well as the separated Nb₂O₅. These results strongly suggest that the photooxidation takes place on the surface of the Cu/Nb₂O₅ catalyst.

In the cases of photooxidations of α -methyl-2-pyridine methanol, α -cyclopropylbenzyl alcohol, and cinnamyl alcohol, benzene was used as a solvent (Table 2, entries 7–9). In the case of Pd catalysts, alcohols having heteroatom, such as (3-pyridyl)methanol, (2-aminophenyl)methanol and (3-thiophenyl)methanol did not proceed due to the complexation of Pd with the heteroatom.¹⁵ However, by using Cu/Nb₂O₅, α -methyl-2-pyridine methanol was converted to the corresponding ketone in high yield. On the other hand, the photooxidations of α -cyclopropylbenzyl alcohol, and cinnamyl alcohol did not give the corresponding ketone and α,β -unsaturated aldehyde in high yields. In these cases, benzaldehyde was mainly produced as by-product, indicating that C–C or C=C bond was cleaved at α -position in each case. Interestingly, the selectivities to corresponding ketone and α,β -unsaturated aldehyde moderately increased by the addition of Cu to Nb₂O₅. To confirm the contribution of photoreaction of α -cyclopropylbenzyl alcohol and cinnamyl alcohol, these alcohols were irradiated in the absence of catalyst. The conversions of α -cyclopropylbenzyl alcohol and cinnamyl alcohol were 71 and 99 % after 48 h of irradiation, respectively. This result indicates that a part of benzaldehyde formation was due to the photoreaction of these alcohols independently of the photo-activation by photocatalyst. On the other hand, the photoreaction of these alcohols in the absence of catalyst did not take place under visible light irradiation (> 390 nm). The photooxidation of these alcohols with Nb₂O₅ or Cu/Nb₂O₅ catalysts were tested under visible light irradiation. Although the band gap of Nb₂O₅ is 390 nm, the photooxidations proceeded over Nb₂O₅ and Cu/Nb₂O₅, and the selectivities to corresponding ketone and α,β -unsaturated aldehyde improved (entries 8b and 9b). Moreover, Cu/Nb₂O₅ showed higher selectivities than those over Nb₂O₅. However, these selectivities are not still sufficiently high and admit of improvement. In our previous work, we proposed unique photo-activation mechanism by “*in situ doping*” (the direct electron transfer from the electron

donor level derived from adsorbed alcoholate species to the conduction band of photocatalyst).^{34,35} The fact that the photooxidation of α -cyclopropylbenzyl alcohol and cinnamyl alcohol proceeded even under visible light irradiation supports that the photooxidation of alcohols over Nb₂O₅ and Cu/Nb₂O₅ took place by this “*in situ doping*” mechanism. In our proposed mechanism, the radical species was formed by the direct electron transfer from the electron donor level to the conduction band under photo-irradiation, and then radical species was converted to corresponding carbonyl compound. We already confirmed that a radical intermediate with an unpaired electron located on α -carbon is generated by photoexcitation of the chemisorbed alcohol.^{34,36,37} It is well known that a radical adjacent to the cyclopropyl or allyl moiety is unstable to easily rearrange. Therefore, it is likely that C–C and C=C bonds cleavage accompanied with the radical rearrangement occurs in the cases of photooxidation of α -cyclopropylbenzyl alcohol and cinnamyl alcohol. This undesired radical rearrangement probably results in the decrease of the selectivity to the desired product.

Conclusions

Solvent-free aerobic photooxidations of various alcohols over Cu/Nb₂O₅ and Nb₂O₅ were examined. Several alcohols were selectively oxidized into corresponding carbonyl compounds at room temperature under atmospheric pressure. The photocatalytic activities were remarkably enhanced by addition of a small amount of Cu to Nb₂O₅ without lowering selectivities. 1-penylethanol was quantitatively oxidized to acetophenone by using Cu/Nb₂O₅ even under solvent-free condition. A heteroatom-containing alcohol, α -methyl-2-pyridine methanol was selectively oxidized by using Cu/Nb₂O₅ and Nb₂O₅. On the other hand, Nb₂O₅ and Cu/Nb₂O₅ gave moderate selectivities in the photooxidation of an allylic alcohol (cinnamyl alcohol) or α -cyclopropylbenzyl alcohol. By the addition of a small amount of Cu to Nb₂O₅, the selectivities to the corresponding carbonyl compounds improved. Cu/Nb₂O₅ was easily separated from the reaction mixture and was reusable without reducing the catalytic performance.

References

- (1) Sheldon, R. A.; Kochi, J. K. *Metal-Catalyzed Oxidations of Organic Compounds*; Academic Press: New York, 1981.
- (2) Hudlicky, M. *Oxidations in Organic Chemistry*; American Chemical Society: Washington, DC, 1990.
- (3) Hill, C. L. *Advance in Oxygenated Process*; JAI: London, 1998.
- (4) Larock, R. C. *Comprehensive Organic Transformations*; VCH: New York, 1989.
- (5) Sheldon, R. A.; Arends, I. W. C. E.; Dijkstra, A. *Catal. Today* **2000**, *57*, 157.
- (6) Mallat, T.; Baiker, A. *Chem. Rev.* **2004**, *104*, 3037.
- (7) Srinivas, N.; Rani, V. R.; Kishan, M. R.; Kulkarni, S. J.; Raghavan, K. V. *J. Mol. Catal. A: Chem.* **2001**, *172*, 187.
- (8) Bleloch, A.; Johnson, B. F. G.; Ley, S. V.; Price, A. J.; Shephard, D. S.; Thomas, A. W. *Chem. Commun.* **1999**, 1907.
- (9) Vocanson, F.; Guo, Y. P.; Namy, J. L.; Kagan, H. B. *Synth. Commun.* **1998**, *28*, 2577.
- (10) Matsushita, T.; Ebitani, K.; Kaneda, K. *Chem. Commun.* **1999**, 265.
- (11) Yamaguchi, K.; Mori, K.; Mizugaki, T.; Ebitani, K.; Kaneda, K. *J. Am. Chem. Soc.* **2000**, *122*, 7144.
- (12) Mori, K.; Kanai, S.; Hara, T.; Mizugaki, T.; Ebitani, K.; Jitsukawa, K.; Kaneda, K. *Chem. Mater.* **2007**, *19*, 1249.
- (13) Choi, E.; Lee, C.; Na, Y.; Chang, S. *Org. Lett.* **2002**, *4*, 2369.
- (14) Yamaguchi, K.; Mizuno, N. *Angew. Chem. Int. Ed.* **2002**, *41*, 4538.
- (15) Kakiuchi, N.; Maeda, Y.; Nishimura, T.; Uemura, S. *J. Org. Chem.* **2001**, *66*, 6620.
- (16) Mallat, T.; Baiker, A. *Catal. Today* **1994**, *19*, 247.
- (17) Wu, H. L.; Zhang, Q. H.; Wang, Y. *Adv. Synth. Catal.* **2005**, *347*, 1356.
- (18) Pillai, U. R.; Sahle-Demessie, E. *J. Catal.* **2002**, *211*, 434.
- (19) Muggli, D. S.; McCue, J. T.; Falconer, J. L. *J. Catal.* **1998**, *173*, 470.
- (20) Falconer, J. L.; Magrini-Bair, K. A. *J. Catal.* **1998**, *179*, 171.
- (21) Chen, J.; Ollis, D. F.; Rulkens, W. H.; Bruning, H. *Water Res.* **1999**, *33*, 661.

- (22) Hussein, F. H.; Pattenden, G.; Rudham, R.; Russell, J. J. *Tetrahedron Lett.* **1984**, *25*, 3363.
- (23) Zhang, M.; Wang, Q.; Chen, C. C.; Zang, L.; Ma, W. H.; Zhao, J. C. *Angew. Chem. Int. Ed.* **2009**, *48*, 6081.
- (24) Wang, Q.; Zhang, M.; Chen, C.; Ma, W.; Zhao, J. *Angew. Chem. Int. Ed.* **2010**, *49*, 7976.
- (25) Ohuchi, T.; Miyatake, T.; Hitomi, Y.; Tanaka, T. *Catal. Today* **2007**, *120*, 233.
- (26) Driessen, M. D.; Grassian, V. H. *J. Phys. Chem. B* **1998**, *102*, 1418.
- (27) Kohno, Y.; Hayashi, H.; Takenaka, S.; Tanaka, T.; Funabiki, T.; Yoshida, S. *J Photochem. Photobiol. A* **1999**, *126*, 117.
- (28) Prahov, L. T.; Disdier, J.; Herrmann, J. M.; Pichat, P. *Int. J. Hydrogen Energy* **1984**, *9*, 397.
- (29) Irie, H.; Miura, S.; Kamiya, K.; Hashimoto, K. *Chem. Phys. Lett.* **2008**, *457*, 202.
- (30) Irie, H.; Kamiya, K.; Shibanuma, T.; Miura, S.; Tryk, D. A.; Yokoyama, T.; Hashimoto, K. *J. Phys. Chem. C* **2009**, *113*, 10761.
- (31) Creutz, C.; Brunschwig, B. S.; Sutin, N. *J. Phys. Chem. B* **2005**, *109*, 10251.
- (32) Creutz, C.; Brunschwig, B. S.; Sutin, N. *J. Phys. Chem. B* **2006**, *110*, 25181.
- (33) Nakamura, R.; Okamoto, A.; Osawa, H.; Irie, H.; Hashimoto, K. *J. Am. Chem. Soc.* **2007**, *129*, 9596.
- (34) Shishido, T.; Miyatake, T.; Teramura, K.; Hitomi, Y.; Yamashita, H.; Tanaka, T. *J. Phys. Chem. C* **2009**, *113*, 18713.
- (35) Shishido, T.; Teramura, K.; Tanaka, T. *Catal. Sci. Technol.* **2011**, *1*, 541.
- (36) Furukawa, S.; Ohno, Y.; Shishido, T.; Teramura, K.; Tanaka, T. *Shokubai* **2011**, *53*, 132-134.
- (37) Furukawa, S.; Ohno, Y.; Shishido, T.; Teramura, K.; Tanaka, T. *ChemPhysChem* **2011**, *12*, 2823.
- (38) Norrish, R. G. W.; Bamford, C. H. *Nature* **1936**, *138*, 1016.
- (39) Norrish, R. G. W.; Bamford, C. H. *Nature* **1937**, *140*, 195.
- (40) Ohkubo, K.; Suga, K.; Fukuzumi, S. *Chem. Commun.* **2006**, 2018.

Chapter 7

Reaction Mechanism of Alcohol Photooxidation over Cu/Nb₂O₅:

Roles of Cu in Enhancement of Photocatalytic Activity

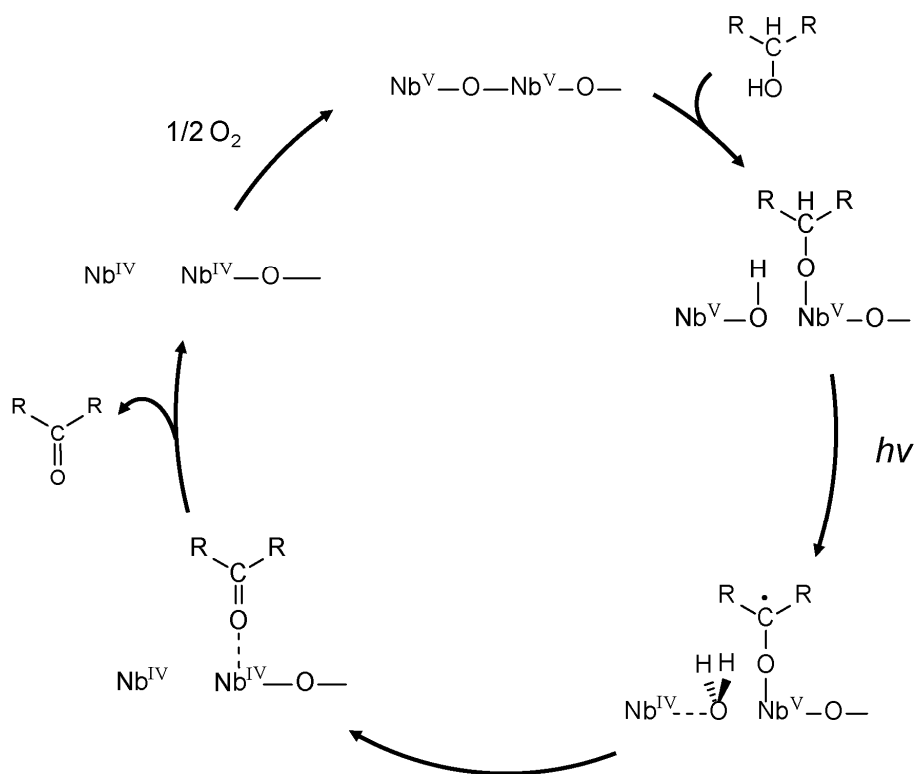
Abstract

Reaction mechanism of photooxidation of alcohol over Cu/Nb₂O₅ and the role of Cu in enhancement of photocatalytic activity was elucidated. Alcohol was adsorbed on the Lewis acid site (Nb(V)) to form an alkoxide species. Photo-generated holes and electrons on Cu/Nb₂O₅ were trapped by the adsorbed alkoxide and Cu(II) species to form the alkoxide carbon radical and Cu(I) species. The formed alkoxide carbon radical was converted to a carbonyl compound and then desorbed. Finally, the reduced Cu(I) sites were re-oxidized by reaction with O₂. The alcohol photooxidation over Nb₂O₅ takes place under not only UV-irradiation but also visible light irradiation up to 450 nm, although the band gap of Nb₂O₅ is 390 nm (3.2 eV). DFT calculations revealed that 1) the surface donor level derived from the adsorbed alkoxide species is located in the forbidden band, 2) direct electron transition from the surface donor level to the conduction band takes place by absorbing a photon, 3) the excitation energy from surface donor level to the Nb 4d conduction band is lower than that from the O 2p valence band to Nb 4d. The kinetic study and FT-IR spectra suggest that Cu(I) acts as an effective desorption site for the products. Based on these results, we conclude that copper functions as an effective redox promoter and desorption site for the product.

Introduction

We have reported that the aerobic photooxidation of alcohols without organic solvents in the presence of O₂ under mild conditions (at atmospheric pressure and room temperature) proceeded over niobium oxide (Nb₂O₅) with excellent selectivity to carbonyl compounds.¹⁻² In the previous study, we proposed the reaction mechanism of the photooxidation of alcohols over Nb₂O₅ as follows (Scheme 1): alcohol adsorbed on a Lewis acid site (Nb(V)) over Nb₂O₅ surface. The adsorbed alcohol was excited under photo-irradiation to generate an alkoxide carbon radical by trapping a photo-formed hole. At the same time, Nb(V) was reduced to Nb(IV) by trapping an excited electron. The formed alkoxide carbon radical was converted to a carbonyl compound. The product desorbed and the reduced Nb(IV) sites were re-oxidized by reaction with molecular oxygen. A kinetic study revealed that the rate-determining step of the photooxidation of alcohol over Nb₂O₅ is desorption of the formed carbonyl compounds. In this mechanism, the direct electron transition from the donor level derived from the adsorbed molecule to the conduction band of the photocatalyst plays an important role in the photo-activation step.

It is well known that the photocatalytic activity of TiO₂ is enhanced by the addition of a small amount of metal species such as Pt,³⁻⁷ Rh,⁸ Ru,⁹ Ni,¹⁰ Cu¹¹⁻¹³ and Ag.¹⁴ Many researchers claimed that this enhancement of activity by metal species was based on the promotion of charge separation, that is, inhibition of recombination of excited electrons and positive holes generated by photo-irradiation.⁴⁻⁶ Recently, we investigated the effect of various metals on the activity of the photooxidation of alcohols over Nb₂O₅. No promotion effect was observed through the addition of Pt, Rh, Ru, Ni and Ag. On the other hand, we found that loading of a small amount of copper significantly enhanced the catalytic activities of the photooxidation of various alcohols.¹⁵ Although this result strongly suggests that the role of copper can not be explained by the simple charge separation mechanism, the role of copper over Nb₂O₅ in the photooxidation of alcohols still remains unclear. In this study, to clarify the role of copper, we investigated the reaction mechanism of the photooxidation of alcohol over Cu/Nb₂O₅ in detail through the action spectrum, kinetic analysis, DFT calculations, and several spectroscopic techniques (Cu K-edge XAFS, FT-IR, UV-Vis, and ESR).



Scheme 1. Proposed reaction mechanism of alcohol photooxidation over Nb_2O_5

Experimental

Preparation

Niobic acid, niobium oxide hydrate ($\text{Nb}_2\text{O}_5 \cdot n\text{H}_2\text{O}$, AD/2872, HY-340) were kindly supplied by CBMM. The niobium oxide catalyst was prepared by calcination of niobic acid in dry air flow at 773 K for 5 h. After calcination, the catalyst was ground into powder below 100 mesh (0.15 mm). The TT- Nb_2O_5 phase with pseudo-hexagonal structure¹⁶ was obtained according to the XRD pattern and Raman spectral data.¹ A niobium oxide-supported copper catalyst ($\text{Cu}/\text{Nb}_2\text{O}_5$) was prepared by impregnation of niobic acid with an aqueous solution of $\text{Cu}(\text{NO}_3)_2$ at 353 K, followed by evaporation, drying and calcination in dry air flow at 773 K for 5 h. The amount of Cu loaded was fixed at 1.9 mol%. After calcination, the catalysts were ground into powder below 100 mesh (0.15 mm).

Photocatalytic Activity Measurements

The photocatalytic oxidation of alcohols was carried out in a quasi-flowing batch system under atmospheric oxygen. Catalyst (100 mg), 1-pentanol (10 ml), and a stirring bar were introduced

to the Pyrex glass reactor. The substrate was used without further purification. The suspension was stirred vigorously at RT and irradiated through the flat bottom of the reactor by reflection from a cold mirror with a 500 W ultra-high pressure Hg lamp (USHIO Denki Co.). Oxygen was passed into the reactor at $2 \text{ cm}^3\text{min}^{-1}$. The organic products were analyzed by FID–GC (Shimadzu GC-14B) and GC–MS (Shimadzu GC–MS QP5050). The quantity of carbon dioxide (CO_2) was determined as barium carbonate (BaCO_3) using a saturated barium hydroxide solution ($\text{Ba}(\text{OH})_2$) trap placed downstream of the flow reactor. For kinetic analysis, 1-pentanol was used as a substrate. We confirmed that no product was detected in the dark with a $\text{Cu}/\text{Nb}_2\text{O}_5$ catalyst and the evolution of photogenerated products responded to illumination. Substrate concentration and oxygen pressure were balanced by using benzene and nitrogen when required, respectively. The light intensity was controlled using a metal mesh.

To measure an action spectrum, the reaction was carried out in a batch reactor with $\text{Cu}/\text{Nb}_2\text{O}_5$ (200 mg) and 1-pentanol (4 ml) and using a monochromatic irradiator (JASCO CRM-FA Spectro Irradiator) as light source.

Cu K-edge X-ray absorption spectra

Cu K-edge X-ray absorption spectra were measured on the beam line BL01B1 at SPring-8 of the Japan Synchrotron Radiation Research Institute (Proposal No. 2007B1123 and 2008A1147), Japan in transmission mode at RT using two ion chambers. The storage ring was operated at 8 GeV with injection currents of 100 mA. An Si (111) two crystal monochromator was used to obtain a monochromatic X-ray beam. The photon energy was calibrated with Cu foil. The samples were sealed in polyethylene bags under dry nitrogen atmosphere. Data were analyzed using the REX2000 program (Version: 2.5.9; Rigaku Corp.). The oscillation was normalized using the edge height around 70–100 eV higher than the threshold.

UV-Vis spectra

Diffuse reflectance spectra (1 nm resolution) were obtained with a UV-Vis spectrometer (JASCO UV570). A slurry of the mixture of 1-pentanol (0.2 ml) and $\text{Cu}/\text{Nb}_2\text{O}_5$ (100 mg) was used as the sample of 1-pentanol adsorbed on $\text{Cu}/\text{Nb}_2\text{O}_5$.

FT-IR spectra

FT-IR spectra of the sample before and during photo irradiation were recorded with a Perkin-Elmer SPECTRUM ONE Fourier transform infrared spectrometer. The resolution of the spectra was 4 cm^{-1} . A Cu/Nb₂O₅ sample was cast into a pellet with diameter 12 mm. The molded sample was introduced into an in situ IR cell equipped with BaF₂ windows. Prior to the measurements, the sample was pretreated with 15.6 kPa of O₂ for 1 h and evacuated at 773 K for 0.5 h. A 300 W Xe lamp (Perkin-Elmer CERAMAX PE300BF) was used as light source. An L-42 cutoff filter was used for visible light irradiation ($> 390\text{ nm}$). 13.3 kPa of O₂ was introduced onto the Cu/Nb₂O₅ with adsorbed alcohol before photo-irradiation.

ESR spectra

ESR measurements were carried out using an X-band ESR spectrometer (JEOL JES-SRE2X) with in situ quartz cell. The *g* value of the radical species was determined using a Mn(II) marker. The ESR spectra of Nb₂O₅ or 1.9 mol% Cu/Nb₂O₅ with adsorbed alcohols were recorded before and after photo-irradiation. A 500 W ultra-high pressure mercury lamp was used as light source.

Surface models and DFT calculation method

Quantum chemical calculations using the DFT method as implemented in Gaussian 03¹⁷ were carried out to investigate the electronic structure and excitation energy of the Nb₂O₅ and Nb₂O₅-alkoxide complex. We used the neutral Nb₁₂O₄₃H₂₆ cluster in this study which was obtained from the structure of H-Nb₂O₅¹⁶ by saturating the peripheral oxygen atoms with hydrogen atoms. The Nb₁₂O₄₂H₂₅(OCH₃) cluster as a model of the Nb₂O₅-alkoxide complex was obtained by substitution of one OH group of the Nb₁₂O₄₃H₂₆ cluster.

The calculation made use of Becke's three parameter hybrid (B3LYP) method involving Lee et al.'s correlation function¹⁸⁻¹⁹ and the LanL2DZ basis set for a single point energy calculation. One-electron excitation energies of model clusters were also obtained by time-dependent (TD)²⁰⁻²² calculations with singlet spin multiplicity.

Results

Redox Behavior and Local Structure of Cu over Nb₂O₅

Cu K-edge XANES spectra were measured to investigate the change in copper valency under the photooxidation of alcohol. Figure 1 shows the Cu K-edge XANES spectra and first derivatives of several reference compounds (Cu foil, Cu₂O, CuO and Cu(OH)₂) and Cu/Nb₂O₅. It is well known that Cu K-edge XANES spectra strongly reflect the chemical state and local symmetry of Cu species.²³⁻³⁰ The XANES spectrum of Cu₂O exhibited a single strong peak owing to the 1s → 4p π transition around 8982 eV, characteristic of Cu(I).²³⁻²⁵ A small pre-edge peak around 8977.5 eV owing to Cu(II) 1s → 3d transition appeared in the XANES spectrum of Cu(II) (d⁹). This transition is formally dipole-forbidden, however, the dipole forbidden transition partially allows for distortion of the octahedral environment, which brings about the absence of a centre of inversion symmetry and the mixing of p orbitals with d orbitals.³¹ Therefore, it becomes more intense as the symmetry distorts from that of a regular octahedron. The coordination of copper in CuO: 4 atoms O at 1.94 Å + 2 atoms O at 2.78 Å and in Cu(OH)₂: 4 atoms O at 1.96 Å + 2 atoms O at 2.63 Å, is similar but the CuO₆ unit is much more distorted in Cu(OH)₂. As a result, the peak intensity owing to the Cu(II) 1s → 3d transition of Cu(OH)₂ (distorted O_h) is more intense than that of CuO (D_{4h}). The absorption edge varied with copper oxidation state in the following order: Cu(0) < Cu(I) < Cu(II) (D_{4h}) < Cu(II) (O_h). The peak position of Cu/Nb₂O₅ oxidized at 298 K was similar to that of Cu(OH)₂, and higher than that of CuO. A small pre-edge peak appeared around 8977.5 eV. These results indicate that Cu(II) is present in the octahedral symmetry. In the case of Cu/Nb₂O₅ reduced at 673 K, the Cu K-edge XANES spectrum clearly showed that copper had a zero valence. After photooxidation, a similar XANES spectrum was obtained in spite of the pretreatment (Figure 1, c and d). A small pre-edge peak owing to the Cu(II) 1s → 3d transition was observed; the intensity of the pre-edge peak was similar to that of CuO. Peaks owing to the Cu(II) 1s → 4p_z and the Cu(II) 1s → 4p_x transitions were also observed at 8987 and 8997 eV, respectively. The first derivatives of XANES spectra gave a shoulder peak at 8981 eV assigned to the 1s → 4p π^* transition. This peak is assigned to Cu(I). On the basis of these results, we conclude that the copper forms oxide species and the state of copper during photo-irradiation was a mixture of the dominant divalent cation with a small

amount of the monovalent cation. This result suggests that redox of copper (between Cu(II) and Cu(I)) was involved in the catalytic cycle of photooxidation of 1-pentanol over Cu/Nb₂O₅.

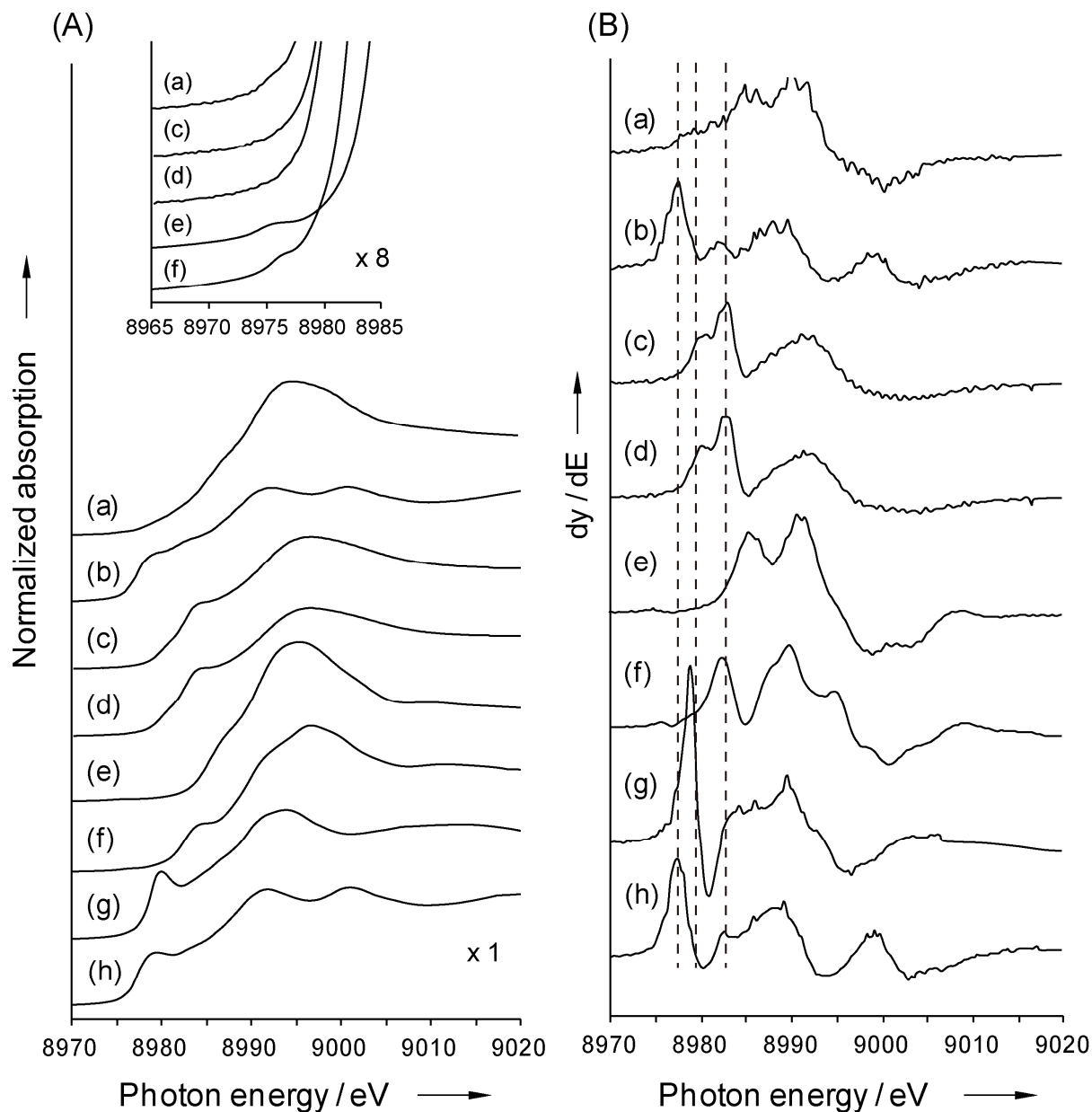


Figure 1. (A) Cu K-edge XANES spectra and (B) their first derivatives of Cu/Nb₂O₅ catalyst and the reference compounds: (a) oxidized at 298 K for 24 h, (b) reduced at 673 K for 2 h, (c) oxidized at 298 K for 24 h followed by 6 h of photooxidation, (d) reduced at 673 K for 2 h followed by 6 h of photooxidation, (e) Cu(OH)₂, (f) CuO, (g) Cu₂O and (h) Cu foil. The inset shows a magnified view of the pre-edge region.

FT-IR measurement for adsorbed species

Figure 2 shows FT-IR spectra of adsorbed cyclohexanol on Cu/Nb₂O₅. The bands at 1467 and 1452 cm⁻¹ were assigned to $\delta_s(\text{CH}_2)$. The peaks at 1364 cm⁻¹ were assigned to $\omega(\text{CH}_2)$. Formation of the alkoxide species by the chemisorption of alcohol is usually accompanied by a shift of the stretching mode of the C–O bond to a higher wavenumber. Pure cyclohexanol had a band at 1068 cm⁻¹, which is assignable to the stretching mode of a C–O bond. This band was similar to that of the physisorbed cyclohexanol (Figure 2, c). After adsorption on Cu/Nb₂O₅, the bands at 1093 and 1130 cm⁻¹ appeared, and these were assigned to the stretching mode of a C–O bond in the alkoxide species on Cu/Nb₂O₅. These results correspond to FT-IR spectra of adsorbed cyclohexanol on bare Nb₂O₅.² Furthermore, the positions of these bands were consistent with those of the niobium alkoxide complex Nb(OC₆H₁₁)₅.³² This result indicates that the alkoxide species was generated on an Nb(V) site.

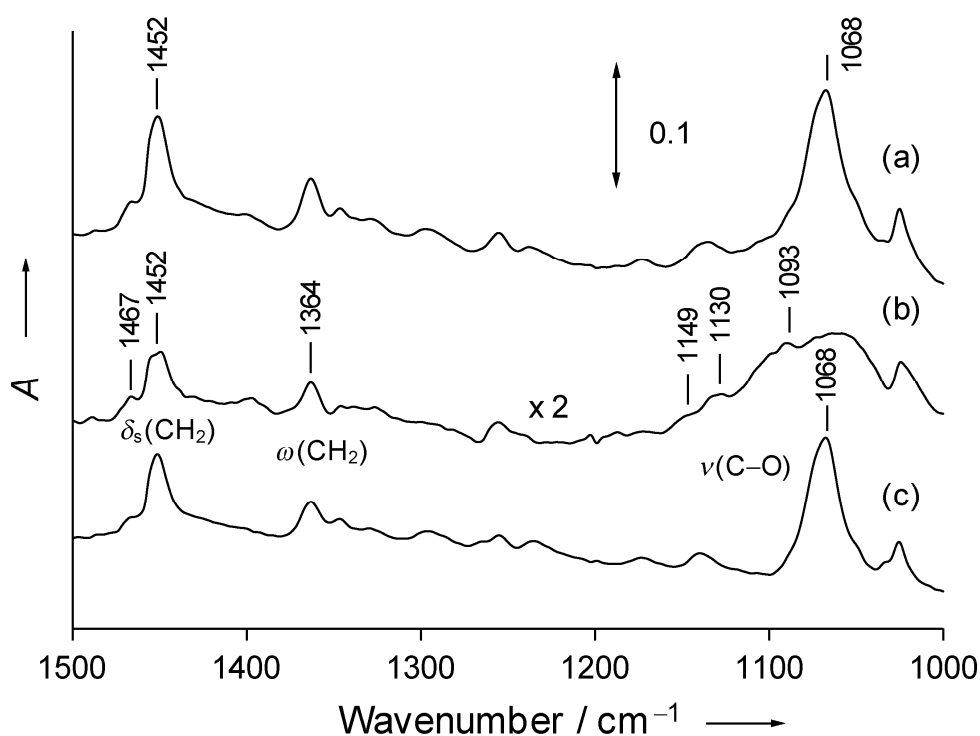


Figure 2. FT-IR spectra of cyclohexanol adsorbed on Cu/Nb₂O₅: (a) cyclohexanol exposed to Nb₂O₅ for 1.0 h (physisorption + chemisorption), (b) evacuated for 0.2 h (chemisorption), (c) difference spectrum (a-b: physisorption). Cu/Nb₂O₅ was oxidized at 673 K with 10.7 kPa of O₂ then evacuated at 298 K for 0.5 h before FT-IR measurements.

Figure 3A shows the change in FT-IR spectra during visible light irradiation (> 400 nm) of the alkoxide species adsorbed on $\text{Cu}/\text{Nb}_2\text{O}_5$. The intensity of the bands assigned to $\nu(\text{C}-\text{O})$ (around 1090 cm^{-1}), $\delta_s(\text{CH}_2)$ (1467 cm^{-1}) and $\omega(\text{CH}_2)$ (1364 cm^{-1}) decreased as the light irradiation time increased, whereas the bands assigned to $\nu(\text{C}=\text{O})$ (1705 and 1721 cm^{-1}) and the asymmetric and symmetric stretches of the carboxylic acid anion (1551 and 1412 cm^{-1}) grew gradually. This result clearly indicates that the surface complex consisting of adsorbed cyclohexanol (i.e. alkoxide species)

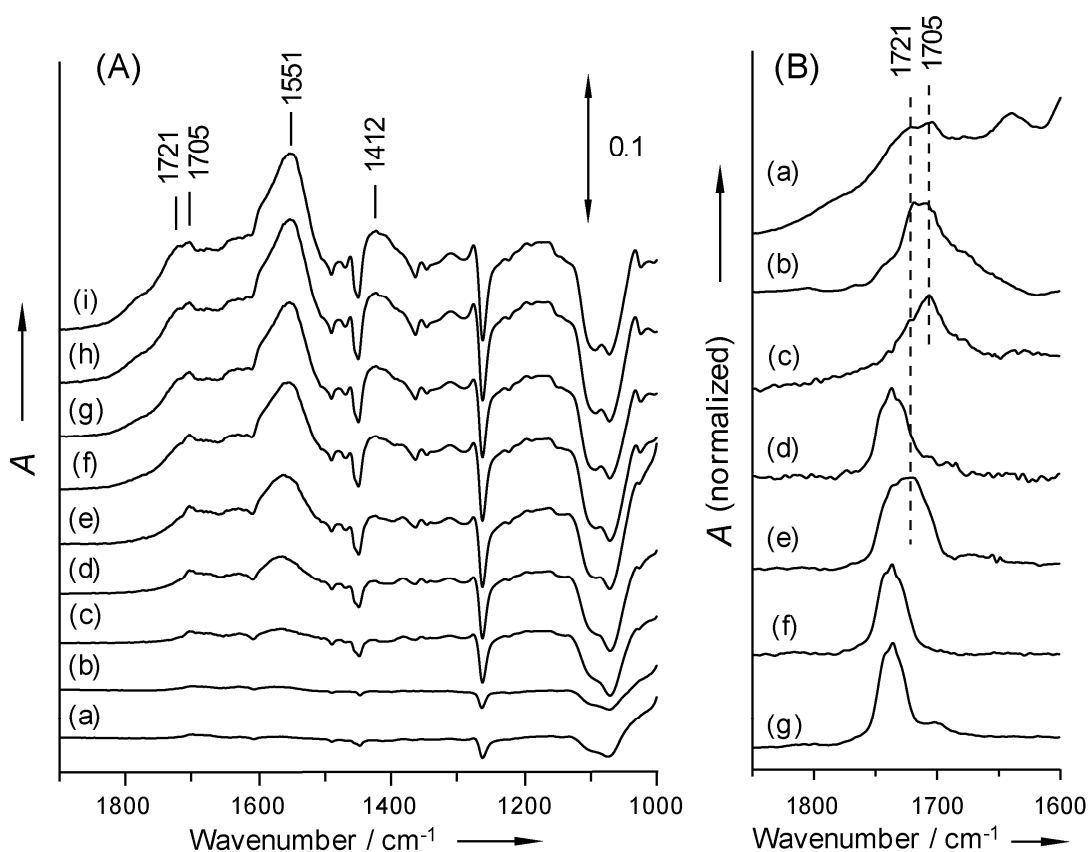


Figure 3. (A) FT-IR spectra of (A) cyclohexanol adsorbed $\text{Cu}/\text{Nb}_2\text{O}_5$ under visible light irradiation. Differential spectra between before and after photo irradiation are shown (irradiation time; (a) 5 min, (b) 10 min, (c) 15 min, (d) 30 min, (e) 60 min, (f) 120 min, (g) 180 min and (h) 240 min). (B) FT-IR spectra in the region of $\text{C}=\text{O}$ stretching vibrations; (a) after 240 min of photo irradiation to the adsorbed cyclohexanol on $\text{Cu}/\text{Nb}_2\text{O}_5$, (b) cyclohexanone introduced on $\text{Cu}/\text{Nb}_2\text{O}_5$, (c) after photo irradiation to the adsorbed cyclohexanol on Nb_2O_5 , (d) cyclohexanone introduced on CuO , (e) Cu_2O , (f) Cu metal and (g) gaseous cyclohexanone.

and metal oxide was excited by photons and oxidized to carbonyl compounds by visible light irradiation. In the region of the C=O stretching vibration (around 1710 cm^{-1}), first the band at 1705 cm^{-1} grew, then the band at 1721 cm^{-1} appeared.

When cyclohexanone was introduced onto Cu/Nb₂O₅, these two bands were observed (Figure 3B, b). On the other hand, the band at 1705 cm^{-1} appeared after photo-irradiation of the adsorbed cyclohexanol on bare Nb₂O₅, whereas the band at 1721 cm^{-1} was not observed (Figure 3B, c). This suggests that the band at 1721 cm^{-1} arises from cyclohexanone adsorbed on a Cu site. The band at 1721 cm^{-1} was also observed when Cu₂O was exposed to cyclohexanone (Figure 4B, e). In addition, the band at 1721 cm^{-1} was not observed when Cu metal and CuO were exposed to cyclohexanone (Figure 3B, d and f), indicating that both CuO (Cu(II)) and Cu metal (Cu(0)) have no interaction with cyclohexanone. These results suggest that the photogenerated carbonyl compounds adsorbed on the Nb sites and Cu(I) sites over Cu/Nb₂O₅. The position of the band owing to $\nu(\text{C}=\text{O})$ of the photogenerated cyclohexanone on the Cu(I) site was lower than that for pure cyclohexanone, but higher than on the Nb site (Figure 3B, g). This indicates that the photogenerated cyclohexanone on the Cu(I) sites has a weaker interaction with the Cu(I) sites than the Nb(V) site.

Wavelength dependence on the apparent quantum yield

Figure 4 shows the apparent quantum yield of the 1-pentanol photooxidation over Cu/Nb₂O₅ as a function of the wavelength of the incident light (action spectrum). UV-Vis spectra of Cu/Nb₂O₅ before and after the adsorption of 1-pentanol on Cu/Nb₂O₅, and difference spectrum were also described. Cu/Nb₂O₅ exhibited an intense absorption band around 275 nm corresponding to the interband transition of the Nb₂O₅ support. The band gap energy of Cu/Nb₂O₅ was estimated as 3.2 eV (the photoexcitation wavelength was 390 nm) and was similar to bare Nb₂O₅ (390 nm). When 1-pentanol was adsorbed on Cu/Nb₂O₅, a slight increase in absorption around 300–350 nm was observed. The difference spectrum showed an absorption band at 340 nm. Since 1-pentanol has no absorption at wavelengths longer than 300 nm,³³ it seems that the band around 340 nm is attributed to absorption by a surface complex consisting of adsorbed species and Nb₂O₅.

In the case of typical semiconductor photocatalysis, an interband transition takes place by photo-irradiation and forms an excited electron in the conduction band and a positive hole in the

valence band.³⁴ Then the excited electron or hole triggers the reaction. In this case, the action spectrum agrees with the absorption band corresponding to the interband transition. However, the photooxidation of 1-pentanol over Cu/Nb₂O₅ proceeded under irradiation up to ca. 460 nm, although the band gap of Cu/Nb₂O₅ is at 390 nm (3.2 eV). This indicates that the photo-activation mechanism of alcohol over Cu/Nb₂O₅ is different from the interband transition in typical semiconductor photocatalysis. The action spectrum of 1-pentanol photooxidation over Cu/Nb₂O₅ shows agreement with the difference spectrum. These results suggest strongly that the absorption by a surface complex consisting of adsorbed species and Nb₂O₅ support would be involved in the photo-activation process.

Interestingly, the apparent quantum yield was improved remarkably by addition of a small amount of copper to Nb₂O₅ (from 7%² to 30% at 340 nm). This value (30%) is much higher than those for general semiconductor photocatalysts.³⁵⁻³⁶

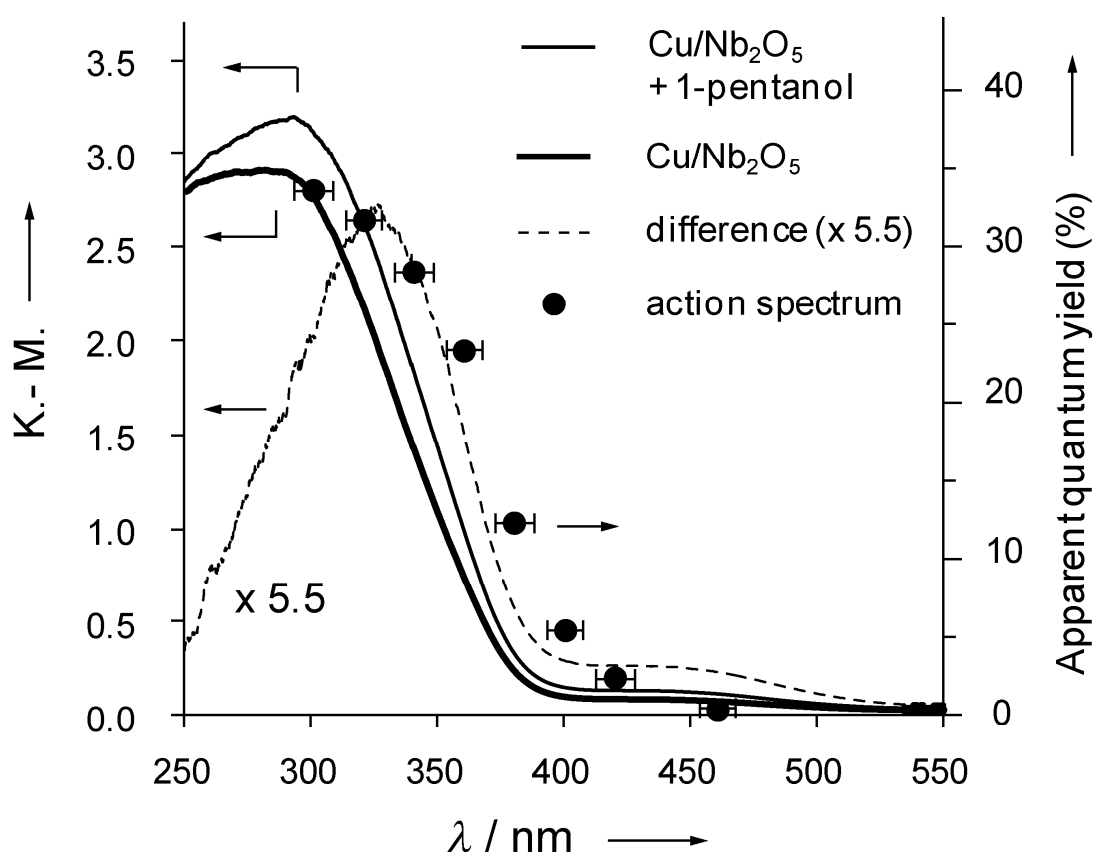


Figure 4. Action spectrum of 1-pentanol photooxidation over Cu/Nb₂O₅, UV-Vis spectra of Cu/Nb₂O₅ and 1-pentanol adsorbed on Cu/Nb₂O₅, and difference spectrum between them.

Investigation of excitation mechanism by DFT calculations

The electronic structure of the model of the Nb₂O₅-alkoxide complex was compared to that of Nb₂O₅ by DFT calculations. Figure 5A shows the model cluster of the H-phase Nb₂O₅ (**1**; Nb₁₂O₄₃H₂₆) and that of the dissociative adsorption of methanol onto the H-phase Nb₂O₅ (100) surface (**2**; Nb₁₂O₄₂H₂₅(OCH₃)). In cluster **2**, one terminal hydroxyl group was substituted with methoxy one. The occupied and virtual Kohn-Sham orbitals (KSOs) of these model clusters consisted of O 2p orbitals and Nb 4d orbitals, respectively (Figure 6). Figure 5B shows selected frontier orbitals of **1** and **2**. Cluster **2** exhibits a different electronic state from cluster **1**. Particularly with HOKS and HOKS-1 of **2**, O 2p orbitals localize on the oxygen atom of the methoxy group.

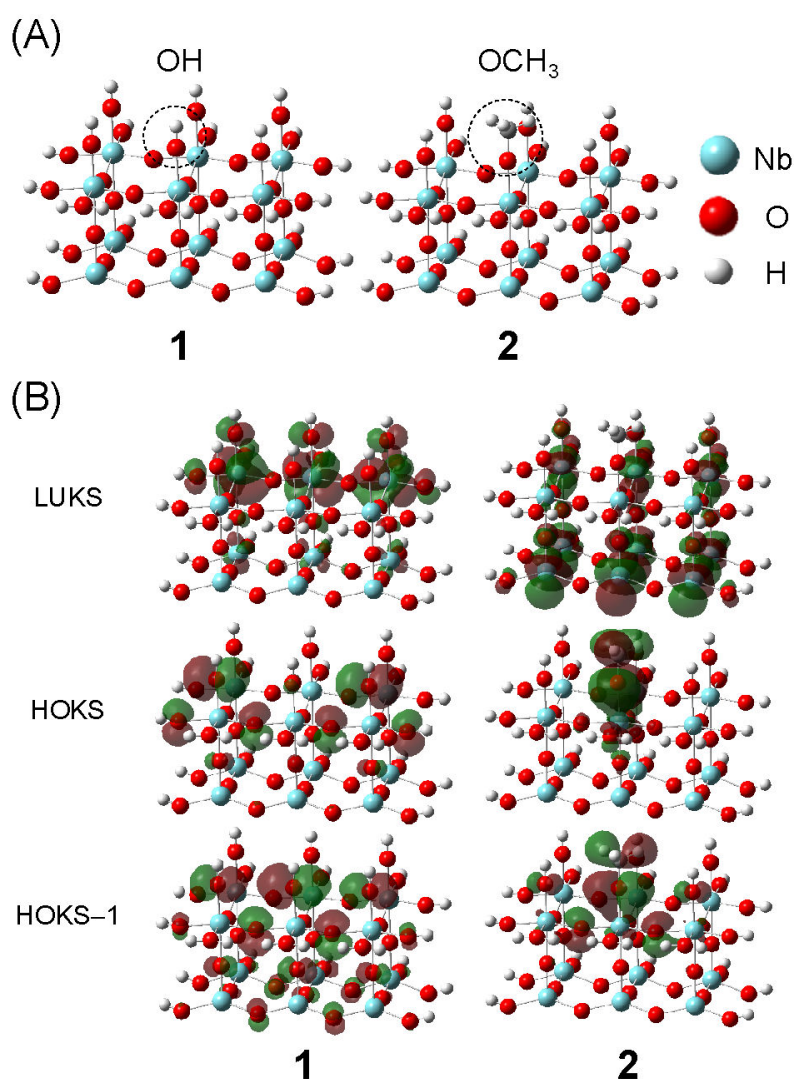


Figure 5. (A) Model clusters of H-Nb₂O₅; Nb₁₂O₄₃H₂₆ (**1**) and alkoxide adsorbed on H-Nb₂O₅; Nb₁₂O₄₂H₂₅(OCH₃) (**2**). (B) Graphical illustrations of LUKS, HOKS, and HOKS-1 of **1** and **2**.

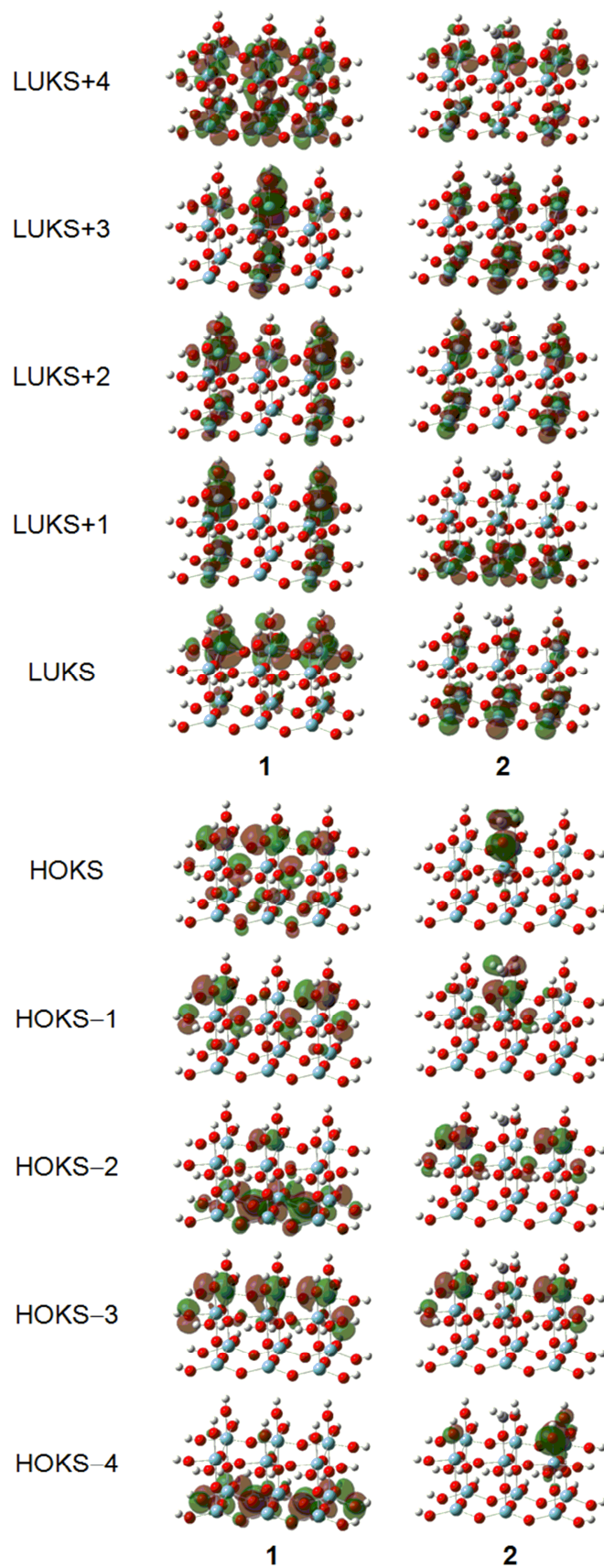


Figure 6. Graphical illustrations of occupied and unoccupied KSOs of **1** and **2**.

As shown in Figure 7, the energy levels of HOKS and HOKS-1 are higher than that of the HOKS of **1**, whereas the energy levels of LUKS and other unoccupied orbitals of **1** and **2** are almost the same. These results clearly show that donor levels whose populations are localized on the alkoxide oxygen are generated by the formation of a surface complex (Nb_2O_5 -alkoxide). Indeed, the electron excitation energies of **1** and **2** calculated by TD-DFT revealed that a lower energy transition takes place with **2** than with **1** (Table 1). Thus, the photooxidation of alcohols proceeding by lower-energy light than the band gap of Nb_2O_5 can be explained by excitation of the surface complex, i.e., direct electron excitation from the O 2p orbital localized on the alkoxide oxygen to the conduction band of Nb_2O_5 consisting of a Nb 4d orbital (Scheme 2a).

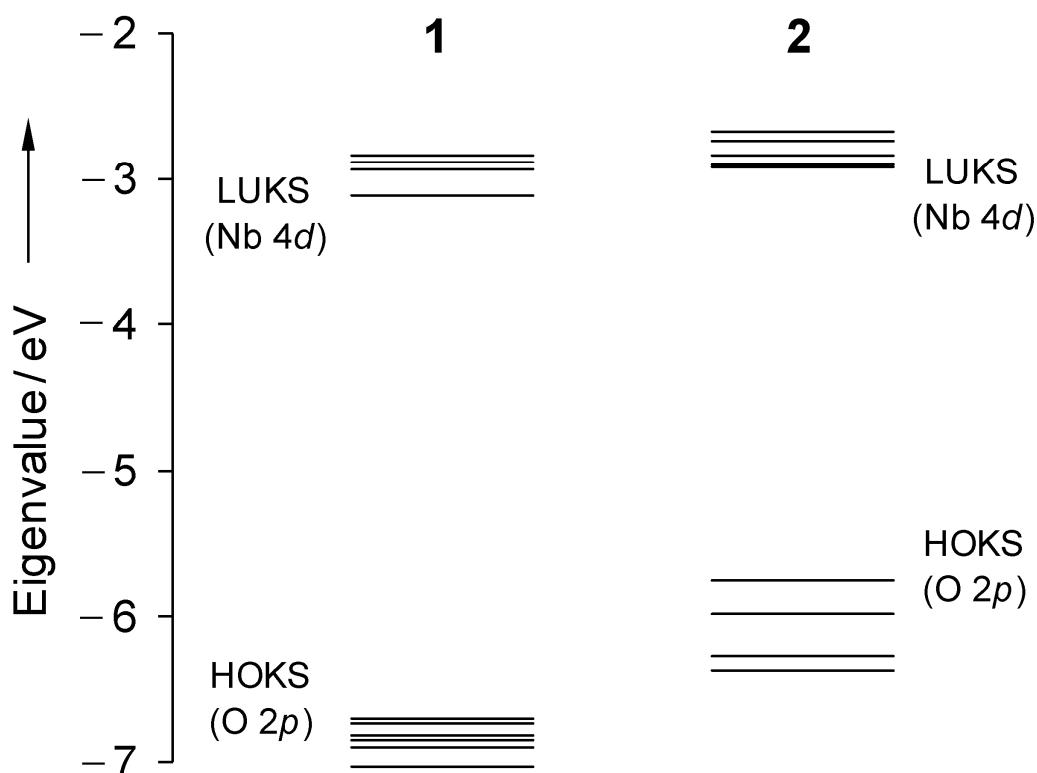
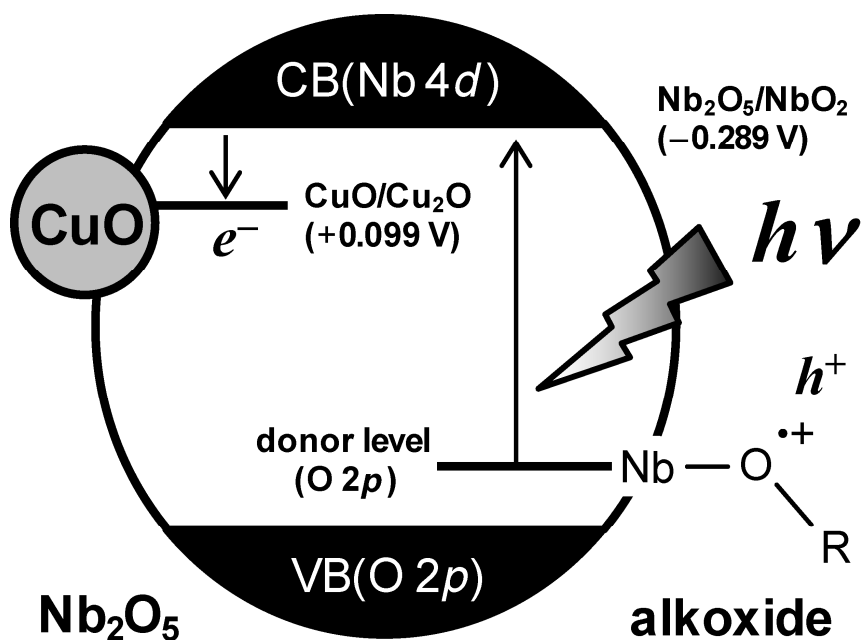


Figure 7. Energy diagram of the frontier KSOs of **1** and **2**.

Table 1. Electron excitation energies of **1** and **2** estimated by TD-DFT calculations.

entry	model	energy / eV	f^a	assignment ^b
1	1	2.82	0.0018	H-6 → L+2 (43%)
2		2.82	0.0001	H-6 → L+1, L+3 (54%)
3		2.84	0.0003	H → L (63%)
4	2	2.38	0.0002	H → L, L+3 (87%)
5		2.43	0.0016	H → L+1, L+2 (95%)
6		2.46	0.0010	H → L+1, L+2 (97%)

^aOscillator strength. ^b Only the major parent one-electron excitations are reported. Their percentage contributions to wave functions of excited states are given in parentheses. H = HOKS. L = LUKS



Scheme 2. Schematic illustration of (a) photo excitation from O 2p orbital localized on alkoxy oxygen atom to Nb 4d orbital and (b) reduction of Cu(II) oxide by excited electron. Applied potentials are vs. NHE.

ESR Measurement for Intermediate Species

Figure 8 shows the ESR spectra of adsorbed alcohols on Nb₂O₅ or Cu/Nb₂O₅ under photo-irradiation at 77 K. UV-irradiation to 1-pentanol adsorbed on bare Nb₂O₅ resulted in the appearance of an ESR signal assigned to the corresponding alkoxide carbon radical² at 77 K (Figure 8a). In the case of 1-pentanol adsorbed on Cu/Nb₂O₅, however, a broad signal assigned to the Cu(II) ion³⁷ appeared, whereas no signal assignable to an organic radical was detected. On the other hand, when tertiary butyl alcohol adsorbed on Nb₂O₅ or Cu/Nb₂O₅ under UV-irradiation at 77K, an intense signal ($g = 2.003$, $A_H = 2.0$ mT) assigned to the methyl radical³⁸ was found predominantly regardless of the presence of copper (Figure 8c, d). As mentioned above, it is suggested that a direct electron transition takes place from the O 2p orbital localized on the oxygen atom of the alkoxide to a conduction band consisting of the Nb 4d orbital by light absorption regardless of the presence of copper. This transfer enables the remaining hole to be located on the oxygen atom of the alkoxide thereby forming an alkoxide radical (Scheme 2a). It seems that the observed methyl radicals are generated via C–C bond cleavage of the adsorbed tertiary butoxide by the hole as shown in Scheme 3a. Moreover, a weak signal was also observed, and this signal may be an alkoxide carbon radical³⁹ formed by C–H bond cleavage of the adsorbed tertiary butoxide. These results suggest that the photoexcitation mechanism of adsorbed alcohol over Cu/Nb₂O₅ is almost similar to that over Nb₂O₅.

In the case of Nb₂O₅, the ESR signal owing to Nb(IV) was observed by exposure to excess alcohol under photo-irradiation.² This indicates that a part of Nb(V) was reduced by excitation of an electron to Nb 4d orbitals (the conduction band of Nb₂O₅). On the other hand, when 1-pentanol adsorbed on Cu/Nb₂O₅ under photo-irradiation, no signal owing to Nb(IV) appeared as shown in Figure 7b. However, the intensity of the ESR signals owing to Cu(II) decreased by photo-irradiation. XANES and FT-IR analyses indicated the generation of Cu(I) oxide species during the photooxidation. Accordingly, the decrease of Cu(II) and increase of Cu(I) may be attributed to reduction of Cu(II) to Cu(I) by a photoexcited electron. This suggests that the photoexcited electron at the conduction band of Nb₂O₅ is trapped by Cu(II) to produce Cu(I) (Scheme 2b). The reduction potential of CuO to Cu₂O can be estimated as +0.099 V vs. NHE from reported values ($\text{CuO} + 2\text{H}^+ + 2\text{e}^- = \text{Cu} + \text{H}_2\text{O}$; $E^\circ/\text{V} = +0.570$ vs. NHE, $\text{Cu}_2\text{O} + 2\text{H}^+ + 2\text{e}^- = 2\text{Cu} + \text{H}_2\text{O}$; $E^\circ/\text{V} = +0.471$ vs.

NHE).⁴⁰ This value is more positive than that of Nb₂O₅ to NbO₂ (Nb₂O₅ + 2H⁺ + 2e⁻ = 2NbO₂ + H₂O; E°/V = -0.289 vs. NHE)⁴⁰, which supports our model.

Scheme 3b shows the proposed electron transfer mechanism in the photooxidation of a primary or secondary alcohol. The photogenerated radical intermediate seems to be oxidized to the product by transferring an electron to Nb(V) or Cu(II). This radical intermediate appeared on Nb₂O₅ whereas it disappeared on Cu/Nb₂O₅, suggesting that the intermediate was immediately converted to the product in the presence of copper, because Cu(II) may work as an electron acceptor.

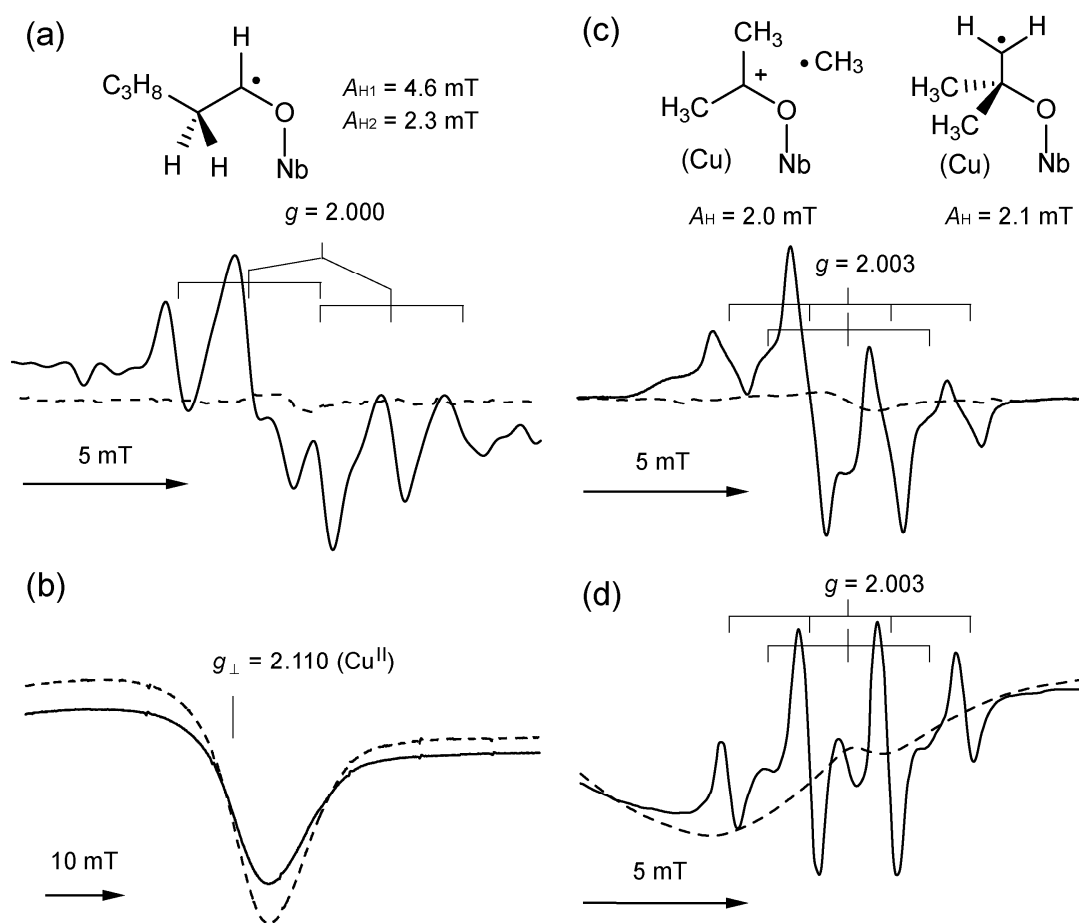
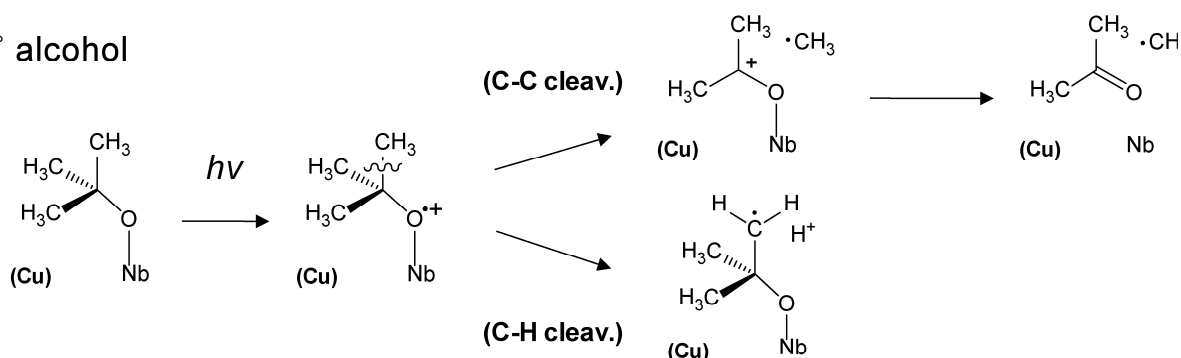
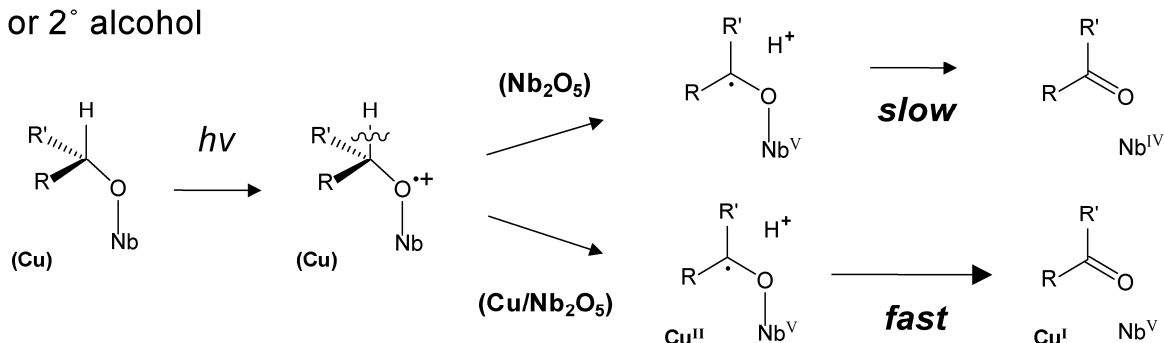


Figure 8. ESR spectra of adsorbed alcohol species under photo irradiation at 77 K (solid line); 1-pentanol adsorbed on (a) Nb₂O₅, (b) Cu/Nb₂O₅, *tert*-butylalcohol adsorbed on (c) Nb₂O₅ and (d) Cu/Nb₂O₅. Dotted lines show spectra under the dark.

(a) 3° alcohol



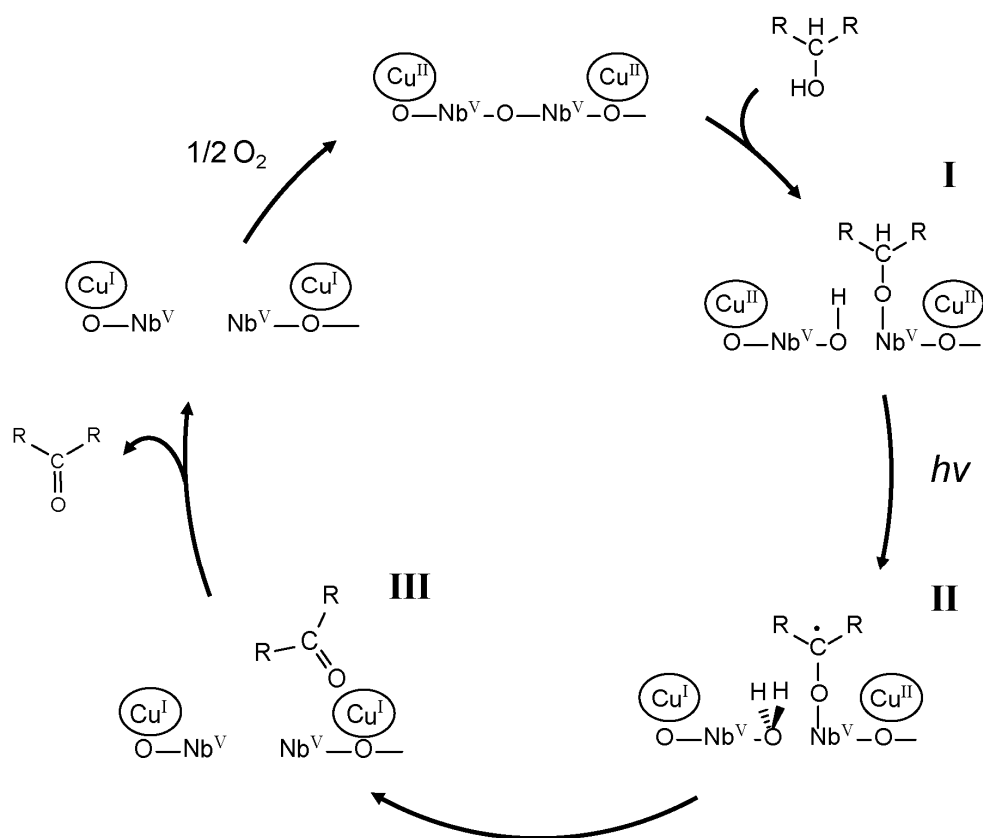
(b) 1° or 2° alcohol



Scheme 3. Plausible electron-transfer mechanism of alkoxide species with (a) tertiary butyl alcohol and (b) primary or secondary alcohol.

Discussion

Based on these results, the reaction mechanism shown in Scheme 4 is proposed. Alcohol is adsorbed on the Cu/Nb₂O₅ surface to generate an alkoxide species **I** (step i). The alkoxide adsorbed on Cu/Nb₂O₅ is excited under photo-irradiation by transferring an electron to copper thus reducing Cu(II) to Cu(I), and leaving a hole on the alkoxide (step ii). The radical intermediate **II** is oxidized and transferred to carbonyl compound **III** (step iii). A part of the carbonyl compound produced on Nb(V) migrates onto the Cu(I) site and then desorbs (step iv). Finally, the reduced Cu(I) sites are reoxidized by reaction with molecular oxygen (step v). The rate of photooxidation of alcohol may depend on the concentrations of alcohol and O₂, and light intensity. Figure 9 shows the formation rate of pentanal in the photooxidation of 1-pentanol over Cu/Nb₂O₅ under various concentrations of 1-pentanol and oxygen, and various light intensities. A slightly positive-correlation was observed for



Scheme 4. The reaction mechanism of alcohol photooxidation over Cu/Nb₂O₅.

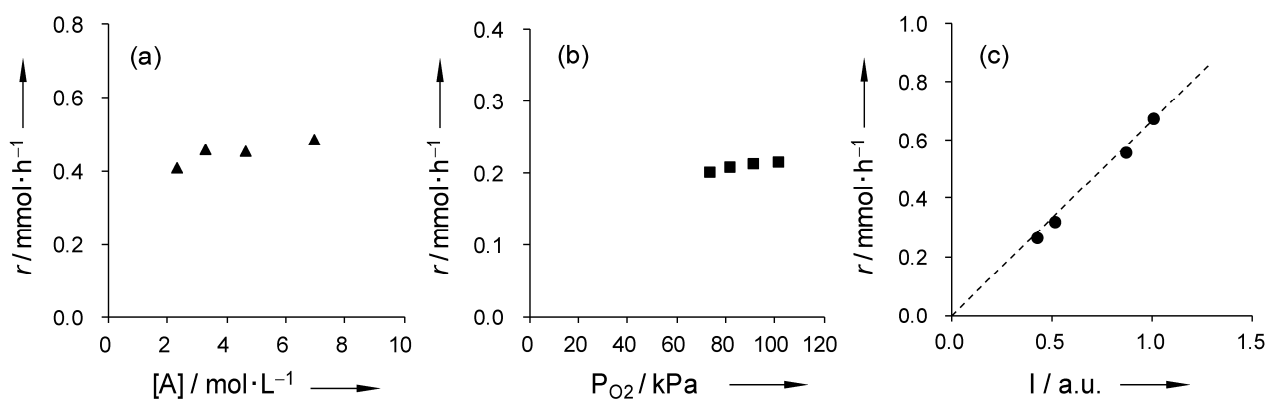
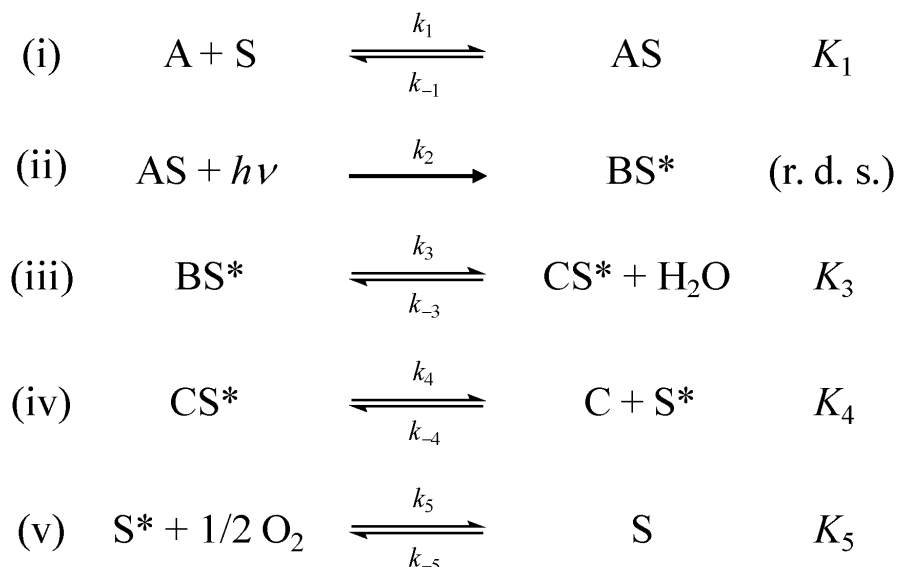


Figure 9. Formation rate of 1-pentanal in the photooxidation of 1-pentanol (r) under various condition of (a) 1-pentanol concentrations; [A], (b) oxygen pressures; P_{O_2} and (c) relative light intensities; I .

the r -[A] and r - P_{O_2} plots. The r -I plot was linear from the origin and the reaction order of light intensity was estimated to be first order. Thus, the rate-determining step of the photooxidation of 1-pentanol over Cu/Nb₂O₅ seems to be one photon absorption process, in other words, photoexcitation of the surface complex. Considering that the rate-determining step of the photooxidation of alcohol over Nb₂O₅ was desorption of the product,² a kinetic analysis of the photooxidation of 1-pentanol over Cu/Nb₂O₅ and FT-IR spectra of adsorbed cyclohexanol on Cu/Nb₂O₅ suggests that the Cu(I) site worked as an effective desorption site and accelerated desorption of the product. Based on the reaction mechanism shown in Scheme 4, elemental steps are described in the rate equation as shown in Scheme 5.



Scheme 5. Rate equations of the elementary steps in 1-pentanol photooxidation. S: vacant active site. AS: active site adsorbed 1-pentanol. B: alkoxide carbon radical. S*: reduced site. C: pentanal.

We derived the following rate equation by assuming that photoexcitation of the surface complex (step ii) is the rate-determining step (eq 1) using a steady-state approximation.

$$r = \frac{k_2 K_1 K_3 K_4 K_5 S_0 [A] P_{O_2}^{0.5} I}{(K_1 + 1) K_3 K_4 K_5 [A] P_{O_2}^{0.5} + K_3 K_4 + K_3 [C] + 1} \quad (1)$$

To verify our proposed reaction mechanism (Scheme 4), the obtained rate equation is compared with the rate equation derived from our proposed reaction mechanism (eq 1). Figure 10 shows plots of the reciprocals of the reaction rates (r^{-1}) against the reciprocal of the substrate concentration ($[A]^{-1}$) and square root of oxygen pressure ($P_{O_2}^{-0.5}$) and these plots shows a linear correlation. This linear correlation indicates that the reaction mechanism is consistent with experimental kinetic data.

This mechanism is essentially the same as the case of Nb_2O_5 , whereas 1) redox of copper (Cu(II)/Cu(I)) takes place instead of the redox of niobium (Nb(V)/Nb(IV)), and 2) desorption of the product from Cu(I) sites is involved. On the basis of the results above, we conclude that Cu(II) acts as a promoter to accelerate step (iii), and Cu(I) promotes desorption of the product (step iv). This mechanism is different from the simple charge separation mechanism.

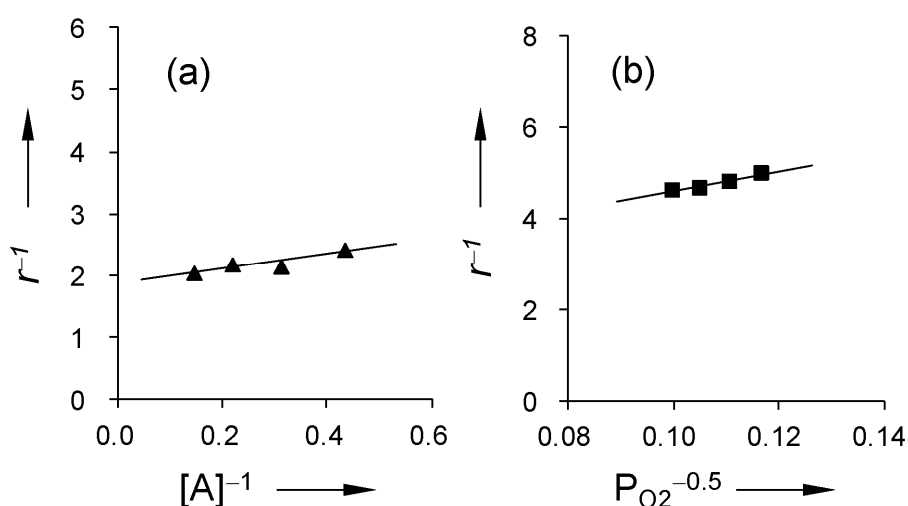


Figure 10. Reciprocals of the reaction rates of 1-pentanol photooxidation (r^{-1}) against the reciprocal of (a) 1-pentanol concentration; $[A]^{-1}$ and (b) square root of oxygen pressure; $P_{O_2}^{-0.5}$.

Conclusion

Loading of a small amount of copper on Nb_2O_5 significantly enhanced the activity of the photooxidation of alcohols without organic solvents in the presence of O_2 at atmospheric pressure and room temperature. A mechanistic study revealed that the photooxidation of alcohols over Cu/ Nb_2O_5 proceeds as follows: alcohol was adsorbed on a Lewis acid site (Nb(V)) to form an

alkoxide species. Photo-generated holes and electrons on Cu/Nb₂O₅ were trapped by the adsorbed alkoxide and Cu(II) species, respectively, to form the alkoxide carbon radical and Cu(I) species. The formed alkoxide carbon radical was converted to a carbonyl compound and desorbed. Finally, the reduced Cu(I) sites are re-oxidized by reaction with molecular oxygen. It was concluded that the rate-determining step is the photoexcitation step, and that the role of copper are 1) as redox promoter and 2) to act as effective desorption site for the product.

DFT calculations revealed that 1) the surface donor level derived from adsorbed alkoxide species is located in the forbidden band, 2) direct electron transition from the surface donor level to the conduction band takes place by absorbing a photon, 3) the excitation energy from surface donor level to Nb 4d is lower than that from O 2p valence band to Nb 4d. The effective wavelength is shifted to a longer wavelength by the formation of a donor level derived from the adsorbed molecule during a chemical reaction, which can be expressed as “in-situ doping” effect. This unique photo-activation mechanism by direct electron transition from the surface donor level to the conduction band gives us attractive ways for removing the limit of band gap energy, and utilization of the visible light.

Reference

- (1) Ohuchi, T.; Miyatake, T.; Hitomi, Y.; Tanaka, T. *Catal. Today* **2007**, *120*, 233.
- (2) Shishido, T.; Miyatake, T.; Teramura, K.; Hitomi, Y.; Yamashita, H.; Tanaka, T. *J. Phys. Chem. C* **2009**, *113*, 18713.
- (3) Hussein, F. H.; Pattenden, G.; Rudham, R.; Russell, J. J. *Tetrahedron Lett.* **1984**, *25*, 3363.
- (4) Sadeghi, M.; Liu, W.; Zhang, T. G.; Stavropoulos, P.; Levy, B. *J. Phys. Chem.* **1996**, *100*, 19466.
- (5) Ohtani, B.; Iwai, K.; Nishimoto, S.; Sato, S. *J. Phys. Chem. B* **1997**, *101*, 3349.
- (6) Hufschmidt, D.; Bahemann, D.; Testa, J. J.; Emilio, C. A.; Litter, M. I. *J. Photochem. Photobiol. A* **2002**, *148*, 223.

- (7) Siemon, U.; Bahnemann, D.; Testa, J. J.; Rodriguez, D.; Litter, M. I.; Bruno, N. *J. Photochem. Photobiol. A* **2002**, *148*, 247.
- (8) Kohno, Y.; Hayashi, H.; Takenaka, S.; Tanaka, T.; Funabiki, T.; Yoshida, S. *J. Photochem. Photobiol. A* **1999**, *126*, 117.
- (9) Wetchakun, K.; Wetchakun, N.; Phanichphant, S. *Adv. Mater. Res.* **2008**, *55-57*, 853.
- (10) Prahov, L. T.; Disdier, J.; Herrmann, J. M.; Pichat, P. *Int. J. Hydrogen Energy* **1984**, *9*, 397.
- (11) Song, K. Y.; Kwon, Y. T.; Choi, G. J.; Lee, W. I. *Bull. Korean Chem. Soc.* **1999**, *20*, 957.
- (12) Arana, J.; Rodriguez, C. F.; Diaz, O. G.; Melian, J. A. H.; Pena, J. P. *Catal. Today* **2005**, *101*, 261.
- (13) Xin, B. F.; Wang, P.; Ding, D. D.; Liu, J.; Ren, Z. Y.; Fu, H. G. *Appl. Surf. Sci.* **2008**, *254*, 2569.
- (14) Alberici, R. M.; Jardim, W. F. *Water Res.* **1994**, *28*, 1845.
- (15) Furukawa, S.; Tamura, A.; Shishido, T.; Teramura, K.; Tanaka, T. *Appl. Catal. B: Environ.* **2011**, *110*, 216.
- (16) Nowak, I.; Ziolk, M. *Chem. Rev.* **1999**, *99*, 3603.
- (17) Frisch, M. J.; Trucks, G. W.; Schlegel, H. B.; Scuseria, G. E.; Robb, M. A.; Cheeseman, J. R.; Montgomery, J., J. A.; Vreven, T.; Kudin, K. N.; Burant, J. C.; Millam, J. M.; Iyengar, S. S.; Tomasi, J.; Barone, V.; Mennucci, B.; Cossi, M.; Scalmani, G.; Rega, N.; Petersson, G. A.; Nakatsuji, H.; Hada, M.; Ehara, M.; Toyota, K.; Fukuda, R.; Hasegawa, J.; Ishida, M.; Nakajima, T.; Honda, Y.; Kitao, O.; Nakai, H.; Klene, M.; Li, X.; Knox, J. E.; Hratchian, H. P.; Cross, J. B.; Bakken, V.; Adamo, C.; Jaramillo, J.; Gomperts, R.; Stratmann, R. E.; Yazyev, O.; Austin, A. J.; Cammi, R.; Pomelli, C.; Ochterski, J. W.; Ayala, P. Y.; Morokuma, K.; Voth, G. A.; Salvador, P.; Dannenberg, J. J.; Zakrzewski, V. G.; Dapprich, S.; Daniels, A. D.; Strain, M. C.; Farkas, O.; Malick, D. K.; Rabuck, A. D.; Raghavachari, K.; Foresman, J. B.; Ortiz, J. V.; Cui, Q.; Baboul, A. G.; Clifford, S.; Cioslowski, J.; Stefanov, B. B.; Liu, G.; Liashenko, A.; Piskorz, P.; Komaromi, I.; Martin, R. L.; Fox, D. J.; Keith, T.; Al-Laham, M.

A.; Peng, C. Y.; Nanayakkara, A.; Challacombe, M.; Gill, P. M. W.; Johnson, B.; Chen, W.; Wong, M. W.; Gonzalez, C.; Pople, J. A. Gaussian 03; Revision C.02 ed.; Gaussian, Inc.: Wallingford CT, 2004.

- (18) Becke, A. D. *J. Chem. Phys.* **1993**, *98*, 5648.
- (19) Lee, C. T.; Yang, W. T.; Parr, R. G. *Phys. Rev. B* **1988**, *37*, 785.
- (20) Bauernschmitt, R.; Ahlrichs, R. *Chem. Phys. Lett.* **1996**, *256*, 454.
- (21) Casida, M. E.; Jamorski, C.; Casida, K. C.; Salahub, D. R. *J. Chem. Phys.* **1998**, *108*, 4439.
- (22) Gorelsky, S. I.; Lever, A. B. P. *J. Organomet. Chem.* **2001**, *635*, 187.
- (23) Kau, L. S.; Spirasolomon, D. J.; Pennerhahn, J. E.; Hodgson, K. O.; Solomon, E. I. *J. Am. Chem. Soc.* **1987**, *109*, 6433.
- (24) Kosugi, N.; Kondoh, H.; Tajima, H.; Kuroda, H. *Chem. Phys.* **1989**, *135*, 149.
- (25) Kosugi, N.; Tokura, Y.; Takagi, H.; Uchida, S. *Phys. Rev. B* **1990**, *41*, 131.
- (26) Grunert, W.; Hayes, N. W.; Joyner, R. W.; Shpiro, E. S.; Siddiqui, M. R. H.; Baeva, G. N. *J. Phys. Chem.* **1994**, *98*, 10832.
- (27) Kuroda, Y.; Yoshikawa, Y.; Konno, S.; Hamano, H.; Maeda, H.; Kumashiro, R.; Nagao, M. *J. Phys. Chem.* **1995**, *99*, 10621.
- (28) Yamashita, H.; Matsuoka, M.; Tsuji, K.; Shioya, Y.; Anpo, M.; Che, M. *J. Phys. Chem.* **1996**, *100*, 397.
- (29) Okamoto, Y.; Kubota, T.; Gotoh, H.; Ohto, Y.; Aritani, H.; Tanaka, T.; Yoshida, S. *J. Chem. Soc., Faraday Trans.* **1998**, *94*, 3743.
- (30) Yamamoto, T.; Tanaka, T.; Kuma, R.; Suzuki, S.; Amano, F.; Shimooka, Y.; Kohno, Y.; Funabiki, T.; Yoshida, S. *PCCP* **2002**, *4*, 2449.
- (31) Yamamoto, T. *X-Ray Spectrom.* **2008**, *37*, 572.
- (32) Aresta, M.; Dibenedetto, A.; Pastore, C. *Inorg. Chem.* **2003**, *42*, 3256.
- (33) Ramirez, B.; Escudero, R.; Tavera, F. J.; Ruiz, G. *Sohn International Symposium Advanced Processing of Metals and Materials, Vol. 3* **2006**, 547.

- (34) Litter, M. I. *Appl. Catal. B: Environ.* **1999**, *23*, 89.
- (35) Del Giacco, T.; Ranchella, M.; Rol, C.; Sebastiani, G. V. *J. Phys. Org. Chem.* **2000**, *13*, 745.
- (36) Wang, C. Y.; Pagel, R.; Bahnemann, D. W.; Dohrmann, J. K. *J. Phys. Chem. B* **2004**, *108*, 14082.
- (37) Cordoba, G.; Viniegra, M.; Fierro, J. L. G.; Padilla, J.; Arroyo, R. *J. Solid State Chem.* **1998**, *138*, 1.
- (38) Fessenden, R. W.; Schuler, R. H. *J. Chem. Phys.* **1963**, *39*, 2147.
- (39) Powell, W. H. *Pure Appl. Chem.* **1993**, *65*, 1357.
- (40) Hata, K. *Chemical Handbook, Japan*; Maruzen: Tokyo, 1966.

Chapter 8

XAFS Study of Cu/Nb₂O₅: Effects of Electronic States of Cu on Photocatalytic Activity in Alcohol photooxidation

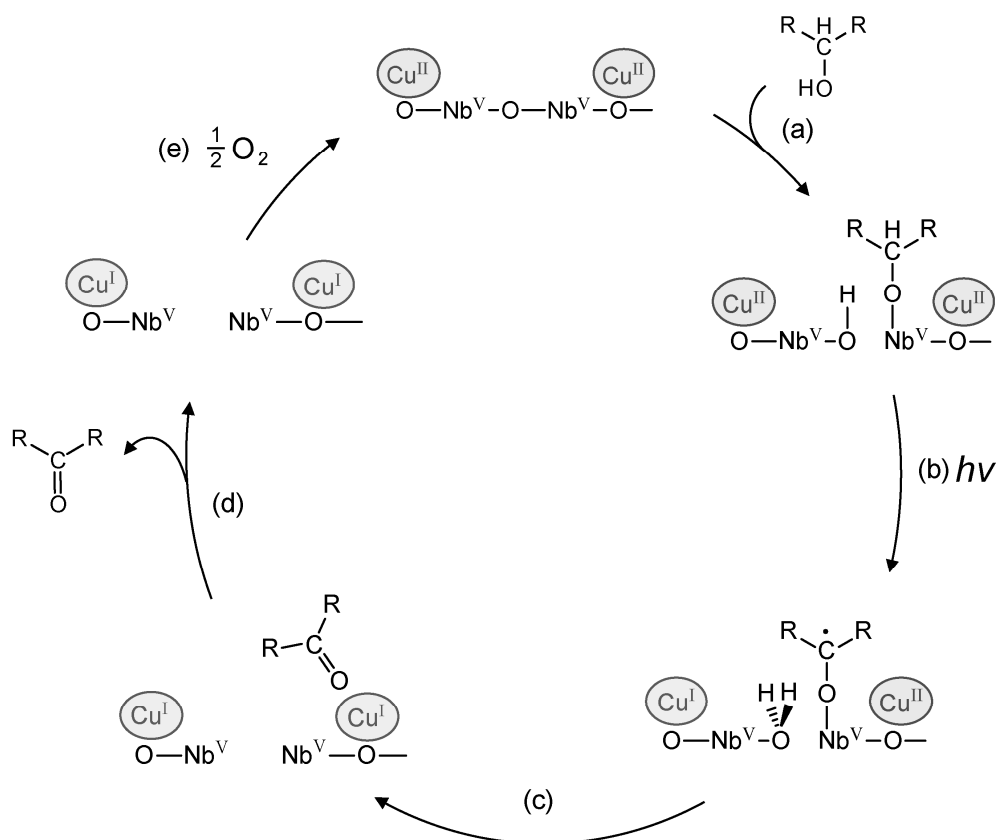
Abstract

Correlation between photocatalytic activity of a series of Cu/Nb₂O₅ catalysts pretreated under various conditions in alcohol photooxidation and state of Cu on Cu/Nb₂O₅ is shown. Reduction of as-prepared Cu/Nb₂O₅ at 673 K enhances its photocatalytic activity. Subsequent oxidation of the reduced Cu/Nb₂O₅ at 348–393 K further improves the activity. But the catalysts oxidized above 393 K show lower activities than the reduced one. The highest activity observed for the catalyst oxidized at 393 K after the reduction is twice as high as the as-prepared catalyst. XANES study reveals that the change in photocatalytic activity corresponds to the fraction of Cu₂O which promotes the rate-determining step, desorption. EXAFS study indicates that Cu metal particles with ca. 4 nm diameter are oxidized to Cu₂O and CuO in a stepwise manner from outer layer of the particles with increase in the oxidation temperature.

Introduction

Heterogeneous photocatalysts have potential application in the aerobic oxidation of organic molecules.¹⁻³ To the present, various semiconductor materials have been tested as oxidation photocatalysts, and it is generally accepted that the anatase TiO₂ is the most versatile and reliable material in view of cost, stability, and photocatalytic activity. Since photocatalytic oxidation of organic molecule over TiO₂ is caused by positive holes and/or hydroxyl radicals derived from band gap excitation of TiO₂, the photocatalytic activity depends on efficiency of charge separation. In this context, various metal species such as Pt,⁴⁻⁸ Rh,⁹ Ru,¹⁰ Ni,¹¹ Cu,¹²⁻¹⁴ and Ag¹⁵ have been often used as effective electron acceptors to promote charge separation in TiO₂-based photocatalytic systems. On the other hand, we previously reported a photocatalytic system of alcohol photooxidation using niobium oxide (Nb₂O₅) of which photoactivation mechanism was different from that of TiO₂:¹⁶⁻¹⁸ reduction by excited electron in the conduction band and oxidation by positive hole in valence band. The alcohol photooxidation over Nb₂O₅ proceeds via photoactivation of surface complex consist of dissociatively adsorbed alcohol (alkoxide) and Nb₂O₅, followed by conversion of photogenerated radical intermediate to carbonyl compound.^{17,18} In this system, the photocatalytic activity is significantly enhanced by loading of Cu, although addition of various metals such as Pt, Rh, Ru, Ni, or Ag to Nb₂O₅ shows no increase in the activity.¹⁹ This suggest that the positive effect of Cu is not promotion of charge separation. Recently, our mechanistic study indeed revealed that the roles of Cu were to accelerate the conversion of photogenerated radical intermediate to product by Cu(II) and to facilitate desorption of the product by Cu(I) (Scheme 1).²⁰ In the former case, Cu(II) acts as an electron acceptor to promote electron transfer from the radical (Scheme 1c), and in the latter case, Cu(I) works as an effective desorption site (Scheme 1d). Thus, the concerted effect provided by two Cu species functions in this system, and they are constantly supplied due to the redox cycle of Cu(II)–Cu(I) couple. However, a XAFS (X-ray absorption fine structure) study showed that Cu on as-prepared Cu/Nb₂O₅ catalyst was entirely Cu(II), and that large portion of Cu remained Cu(II) even during the reaction.²⁰ This implies that some increase in Cu(I) fraction brings about further enhancement in the photocatalytic activity, hence there may be room for optimization of

the initial state of Cu on Cu/Nb₂O₅. In this study, the state of Cu on Cu/Nb₂O₅ was modified by reduction and subsequent oxidation treatment at various temperatures, and the photocatalytic activities of the pretreated catalysts in alcohol photooxidation were evaluated. We also investigated the correlation between the photocatalytic activity and the state of Cu on Cu/Nb₂O₅ which was closely characterized by XAFS analyses.



Scheme 1. Reaction mechanism of alcohol photooxidation over Cu/Nb₂O₅: (a) adsorption of alcohol, (b) photoactivation of adsorbed alcohol and reduction of Cu(II) by excited electron, (c) electron transfer from photogenerated radical intermediated to Cu(I) to form product, (d) desorption of the product, and (e) reoxidation of reduced Cu(I) to Cu(II) by molecular oxygen.

Experimental

Catalyst Preparation

Niobic acid, niobium oxide hydrate ($\text{Nb}_2\text{O}_5 \cdot n\text{H}_2\text{O}$, AD/2872, HY-340) was kindly supplied from CBMM. Other chemicals used were of reagent grade and were obtained from Aldrich Chemical Co., Tokyo Kasei Kogyo Co., Ltd and Wako Pure Chemical Industries, Ltd. All reagents were used without further purification.

Niobium oxide supported Cu catalyst ($\text{Cu}/\text{Nb}_2\text{O}_5$) was prepared by impregnation of niobic acid with an aqueous solutions of $\text{Cu}(\text{NO}_3)_2$ at 353 K, followed by evaporation, drying and calcination at 773 K in a stream of dry air for 5 h. After calcination, the catalysts were ground into powder under 100 mesh (0.15 mm). Loading amount of Cu was fixed to 1.9 mol% (0.46 wt%) which was optimized in the previous study.¹⁹ Unfortunately, TEM images of as-prepared $\text{Cu}/\text{Nb}_2\text{O}_5$ catalyst gave no information about Cu species probably due to low contrast between Nb and Cu.

Reaction Condition

The photocatalytic oxidation of alcohol was carried out in a quasi-flowing batch system^{19,21} under atmospheric oxygen. $\text{Cu}/\text{Nb}_2\text{O}_5$ catalyst (100 mg) and a stirring bar were introduced to the Pyrex glass reactor (cut-off light below 300 nm). The $\text{Cu}/\text{Nb}_2\text{O}_5$ catalyst was pretreated in the reactor under the following conditions: reduction under 5% H_2/N_2 flow at 20 mLmin^{-1} for 0.5 h at 673 K followed by oxidation under O_2 flow at 20 mLmin^{-1} for 0.5 h at various temperatures as appropriate (348 K, 373 K, 393 K, 423 K, and 473 K). Reduced $\text{Cu}/\text{Nb}_2\text{O}_5$ and oxidized $\text{Cu}/\text{Nb}_2\text{O}_5$ after reduction are described as R673 and ROT, respectively; *T* indicates the oxidation temperature. After this pretreatment, 1-pentanol as a substrate (10 mL) without solvent was introduced into the reactor. The suspension was vigorously stirred at room temperature and irradiated from the flat bottom of the reactor through a reflection by a cold mirror with a 500 W ultra-high-pressure Hg lamp (USHIO Denki Co.). Oxygen was flowed into the reactor at 2 mLmin^{-1} (0.1 MPa). Products were analyzed and quantified by FID-GC (Shimadzu GC14B) and GC-MS (Shimadzu QP-5050).

XAFS Study

X-ray adsorption experiments were carried out on the beam line BL12C at Photon Factory, of the High Energy Accelerator Research Organization (Tsukuba, Japan). The ring energy was 2.5 GeV, and the stored current was 450 mA. Cu/Nb₂O₅ catalysts were pretreated prior to measurement under the following conditions: reduction under 7.0 kPa of H₂ for 0.5 h at 673 K followed by oxidation under 7.0 kPa of O₂ for 0.5 h at various temperatures as appropriate (348 K, 373 K, 393 K, 423 K, and 473 K). The pretreated samples were then sealed into polyethylene bags under dry N₂ atmosphere. The Cu K-edge (8.98 keV) XAFS spectra of Cu/Nb₂O₅ were recorded in a fluorescence mode with a Si(111) two-crystal monochromator at room temperature. The XANES and EXAFS analyses were performed by a Rigaku REX2000 program. Pattern fittings of XANES spectra of Cu/Nb₂O₅ oxidized at 473 K were implemented using the spectra of reduced Cu/Nb₂O₅, Cu₂O, CuO, and Cu(OH)₂ in the energy range of 8950–9010 eV. Fittings for other samples were carried out without using the spectra of reduced Cu/Nb₂O₅, Cu₂O, and CuO, because the fitting with that of Cu(OH)₂ showed some negative fractions and worse R factors. The Fourier transformation and inverse Fourier transformation of the EXAFS signals were carried out in the *k*-range of 3.0–12.0 Å⁻¹ and R-range of 1.78–2.70 Å (Cu–Cu) or 1.14–1.81 Å (Cu–O), respectively. Curve-fitting analysis of the EXAFS spectra was performed for the inverse Fourier transforms on the Cu–Cu or Cu–O shells. Empirical parameters for Cu–Cu and Cu–O shells in the analysis were obtained from Cu foil and CuO, respectively.

Results

Photocatalytic Activity of Cu/Nb₂O₅ as a Function of Pretreatment Temperature

Figure 1 shows the results of photooxidation of 1-pentanol over Cu/Nb₂O₅ photocatalysts pretreated under various conditions. In each case, pentanal was evolved as a main oxidized product and the amount was almost linearly increased as the reaction time increased. But a small induction period was observed in the first 1 h for reduced Cu/Nb₂O₅ (R673) (Figure 2). Only a trace amount of pentanoic acid was observed in this conversion level. Figure 3 shows pentanal yield after 5 h as a function of oxidation temperature. Photocatalytic activity of R673 was 1.5

times as high as that of as-prepared catalyst. Cu/Nb₂O₅ catalyst oxidized at 348 K after the reduction (RO348) showed similar activity to R673. The photocatalytic activity increased as oxidation temperature elevated up to 393 K, however it drastically declined over 393 K. Finally, the activity decreased to the same level as untreated one when oxidation temperature reached to 393 K. The highest activity was obtained at 393 K of oxidation temperature (RO393). The photocatalytic activity of RO393 is 2- and 6.5-fold as high as those of as-prepared Cu/Nb₂O₅ and bare Nb₂O₅ catalysts, respectively. Thus, appropriate treatment to Cu/Nb₂O₅ provides further enhancement in photocatalytic activity in alcohol photooxidation.

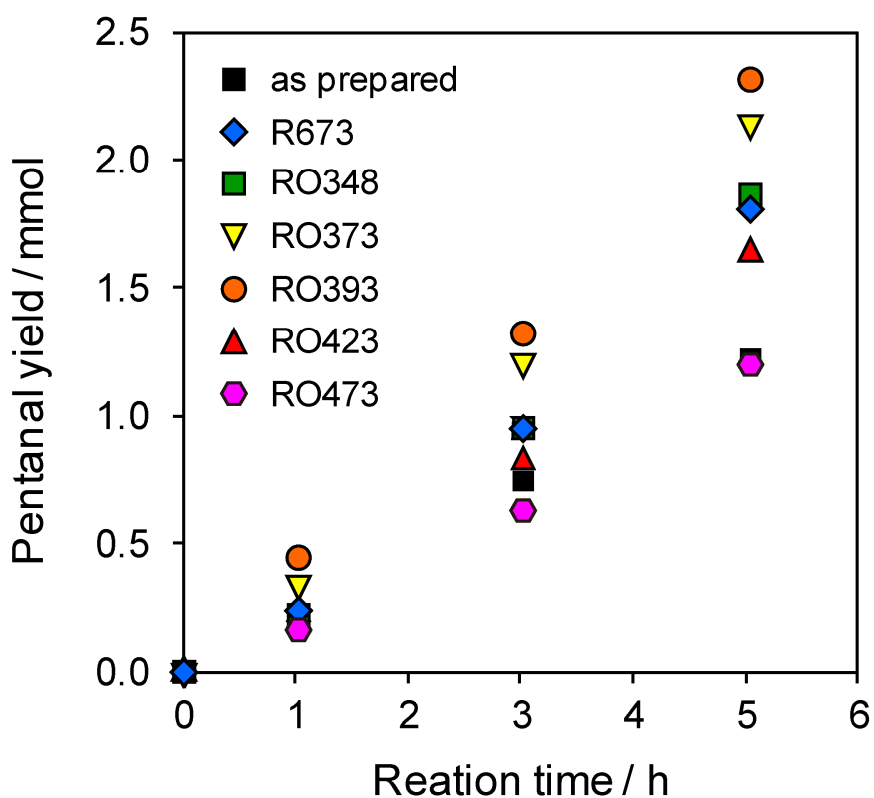


Figure 1. Time course of produced pentanal in photooxidation of 1-pentanol over Cu/Nb₂O₅ catalysts pretreated under various conditions.

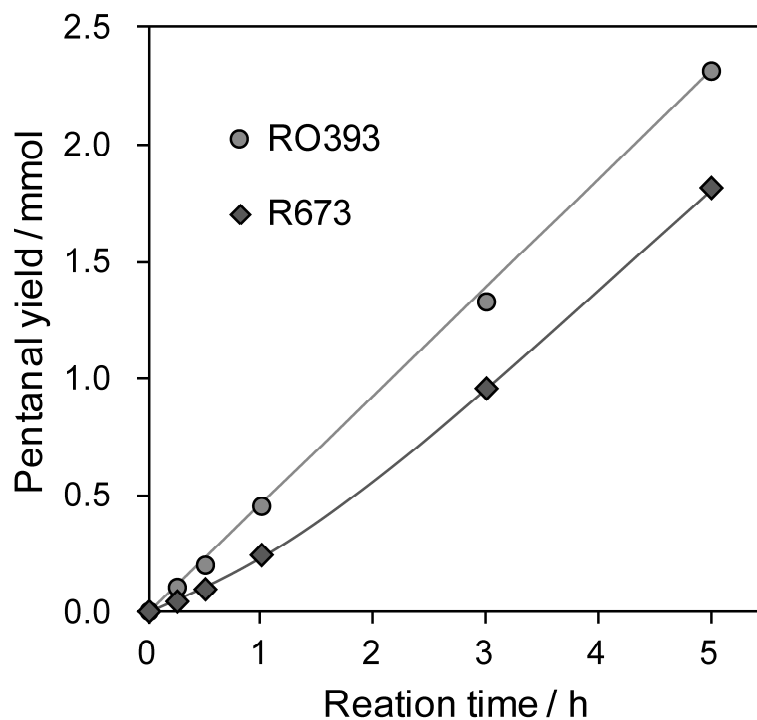


Figure 2. Time course of pentanal yield in photooxidation of 1-pentanol over R673 and RO393.

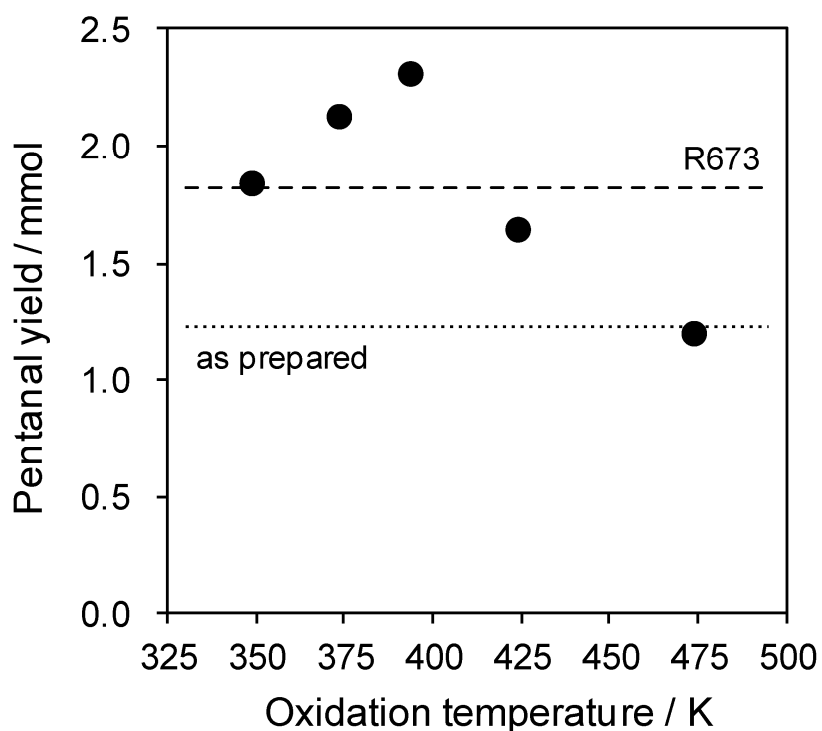


Figure 3. Pentanal yield in 5 h of photooxidation of 1-pentanol over the pretreated catalysts as a function of oxidation temperature. Pentanal yields for R673 and as-prepared $\text{Cu/Nb}_2\text{O}_5$ are represented as a dashed and a dotted lines, respectively.

XANES study of Cu/Nb₂O₅ for Cu valence

Figure 4a shows Cu K-edge XANES spectra of Cu/Nb₂O₅ catalysts pretreated under various conditions and reference compounds. The XANES spectrum of the reduced Cu/Nb₂O₅ (R673) is similar to that of Cu foil, showing that the loaded Cu is reduced to Cu(0). The XANES feature of the oxidized Cu/Nb₂O₅ gradually changed to that characteristic of CuO as oxidation temperature was elevated. This simply describes that oxidation of Cu(0) to Cu(II) proceeds more deeply at higher oxidation temperature. The XANES spectrum of Cu₂O exhibits an intense pre-edge peak due to the 1s → 4pπ transition around 8980 eV, characteristic of Cu(I).²²⁻²⁴ This feature is also observed in the spectrum of Cu/Nb₂O₅ oxidized at 393 K or 423 K after reduction (RO393 or RO423), indicating the presence of Cu(I) species in these samples as an intermediate to Cu(II) species. As shown in Figure 4b, change in composition of Cu species are observed more clearly in the first derivatives of XANES spectra: 1) the peak at 8977.5 eV assignable to Cu(0) decreases with increasing of oxidation temperature; 2) the peak feature characteristic of Cu(I) at 8979 eV increases as oxidation temperature elevated up to 393 K, then it gradually decreases; 3) small features assigned to Cu(II) species grow over 393 K. These trends show stepwise oxidation of Cu(0) to Cu(I) and Cu(II) corresponding to the oxidation temperature. When the oxidation temperature was 473 K, formation of a small portion of Cu(II) species with Cu(OH)₂ like structure was observed. The fractions of Cu species in Cu/Nb₂O₅ were then estimated by pattern fittings of XANES spectra of them (Figure 5). Oxidation of metallic Cu to Cu₂O drastically occurred when oxidation temperature was elevated from 373 K to 393 K. The maximum fraction of Cu₂O in Cu/Nb₂O₅ reached 45% at 393 K of oxidation temperature. With increasing oxidation temperature over 393 K up to 473 K, the fraction of Cu₂O turned to decrease and that of CuO rose to 59%. Thus, the change in the fractions as a function of oxidation temperature well represents the stepwise oxidation of Cu species. The variation of the Cu₂O fraction with RO393 at the top agrees with the change in photocatalytic activity, indicating that the formation of Cu₂O is important to increase the photocatalytic activity, but not of CuO. As mentioned above, we have proposed that the roles of Cu in enhancement of photocatalytic activity are to accelerate conversion of radical intermediate to product by Cu(II) and to facilitate desorption of the product by Cu(I). The results in this study therefore clearly show that the second role of Cu, that is Cu(I),

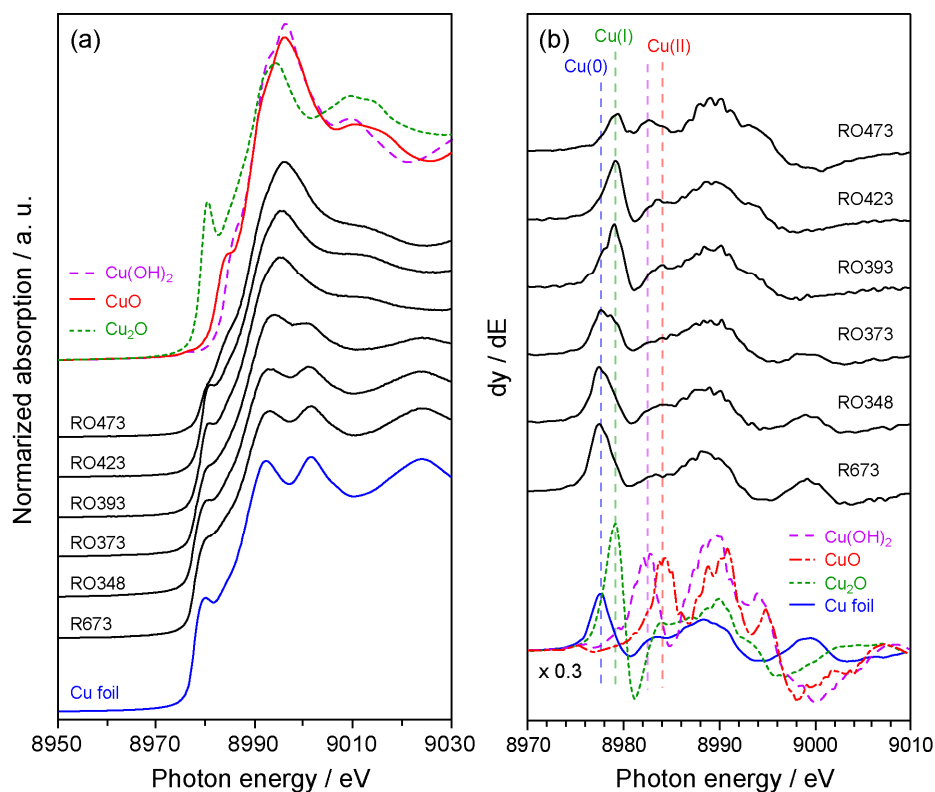


Figure 4. Cu K-edge XANES spectra (a) and their first derivatives (b) of Cu/Nb₂O₅ catalysts pretreated under various conditions and reference compounds.

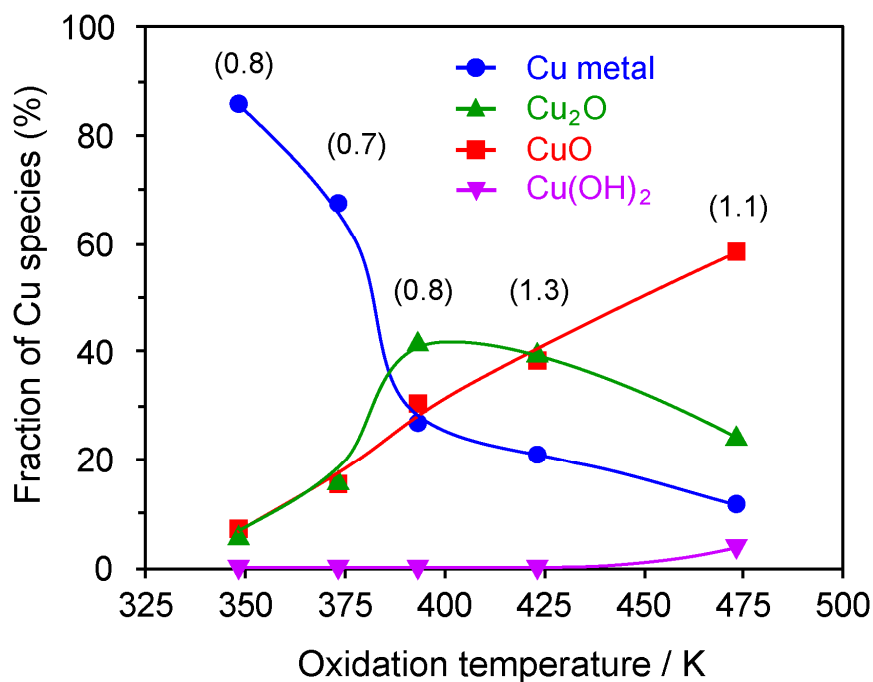


Figure 5. Fractions of Cu species in oxidized Cu/Nb₂O₅ estimated by pattern fittings of XANES spectra as a function of oxidation temperature. Figure in parenthesis shows factors (%) for fitting.

dominantly contribute to improving the photocatalytic activity, and are consistent with the fact that desorption is the rate-determining step in alcohol oxidation over Nb_2O_5 . However, there are some unreasonable behavior: RO423 and RO473 exhibit lower activities than R673 despite higher fractions of Cu_2O , and R673 which does not contain Cu_2O shows higher activity than as-prepared $\text{Cu}/\text{Nb}_2\text{O}_5$. These suggest an involvement of another factor in the photocatalytic activity, such as structure of Cu species.

EXAFS study for structure of Cu species on $\text{Cu}/\text{Nb}_2\text{O}_5$

The structures of Cu species on $\text{Cu}/\text{Nb}_2\text{O}_5$ were then investigated on the basis of EXAFS analyses of them. Figure 6a shows k^3 -weighted Cu K-edge EXAFS spectra of the pretreated $\text{Cu}/\text{Nb}_2\text{O}_5$ catalysts and reference compounds. The EXAFS spectra of R673, RO348, and RO373 show similar oscillation phases to that observed for Cu foil, while the spectra of RO393, RO423, and RO473 resemble that of CuO. As clearly shown in Fourier-transformed EXAFS (FT-EXAFS, Figure 6b), the height of band at 2.2 Å, assigned to the Cu–Cu scatterings of Metallic Cu, decreased with the oxidation temperature increased. In particular, a prominent fall of the height was observed between R373 and R393, and the Cu–Cu scattering almost disappeared with RO473. These changes are in accordance with the drawdown of the Cu(0) fraction represented in Figure 5. The band at 1.5 Å assigned to Cu–O scattering, on the other hand, grew upon increase of the oxidation temperature above 393 K. In addition to the amplitude, the distance of the Cu–O bond slightly increased on going from RO393 to RO473. The FT-EXAFS of reference compounds evidence that CuO or $\text{Cu}(\text{OH})_2$ has larger amplitude and longer distance of Cu–O scattering than that of Cu_2O . Therefore, the increase in Cu–O bond length from RO393 to RO473 can be attributed to formation of CuO and/or $\text{Cu}(\text{OH})_2$. On the basis of these results, a series of the changes in FT-EXAFS corresponds to participation of oxygen atoms into Cu metal particles to form Cu_2O and CuO. A Curve-fittings analysis was then performed for the Cu–Cu and Cu–O shells in the FT-EXAFS (Table 1). For RO423, the low amplitude of Cu-Cu scattering did not allow determination of appropriate structural parameters for the Cu-Cu shell by curve fitting. The coordination number (CN) of the Cu-Cu pair for R673 is 10.8, although the foil have a CN of 12. This suggests that the reduced Cu metal particles have ca. 4 nm diameter, assuming the

cubooctahedral structure. The CN of the Cu-Cu pair decreased along with increase of the oxidation temperature, implying that metallic moiety became reduced in size. But the estimated CN of the Cu-Cu pair of the sample containing Cu oxide species does not correctly indicate coordination number for metallic moiety, as the amplitude of EXAFS oscillation is normalized by total amount of Cu. We therefore defined $\langle \text{CN} \rangle$, namely CN divided by the fraction of metallic Cu, as an alternative which represents coordination number of the Cu-Cu pair just in metallic moiety (Table 1). The $\langle \text{CN} \rangle$ still became smaller on going from R673 to RO393, which supports the shrinkage of the metallic moiety upon increase in the oxidation temperature.

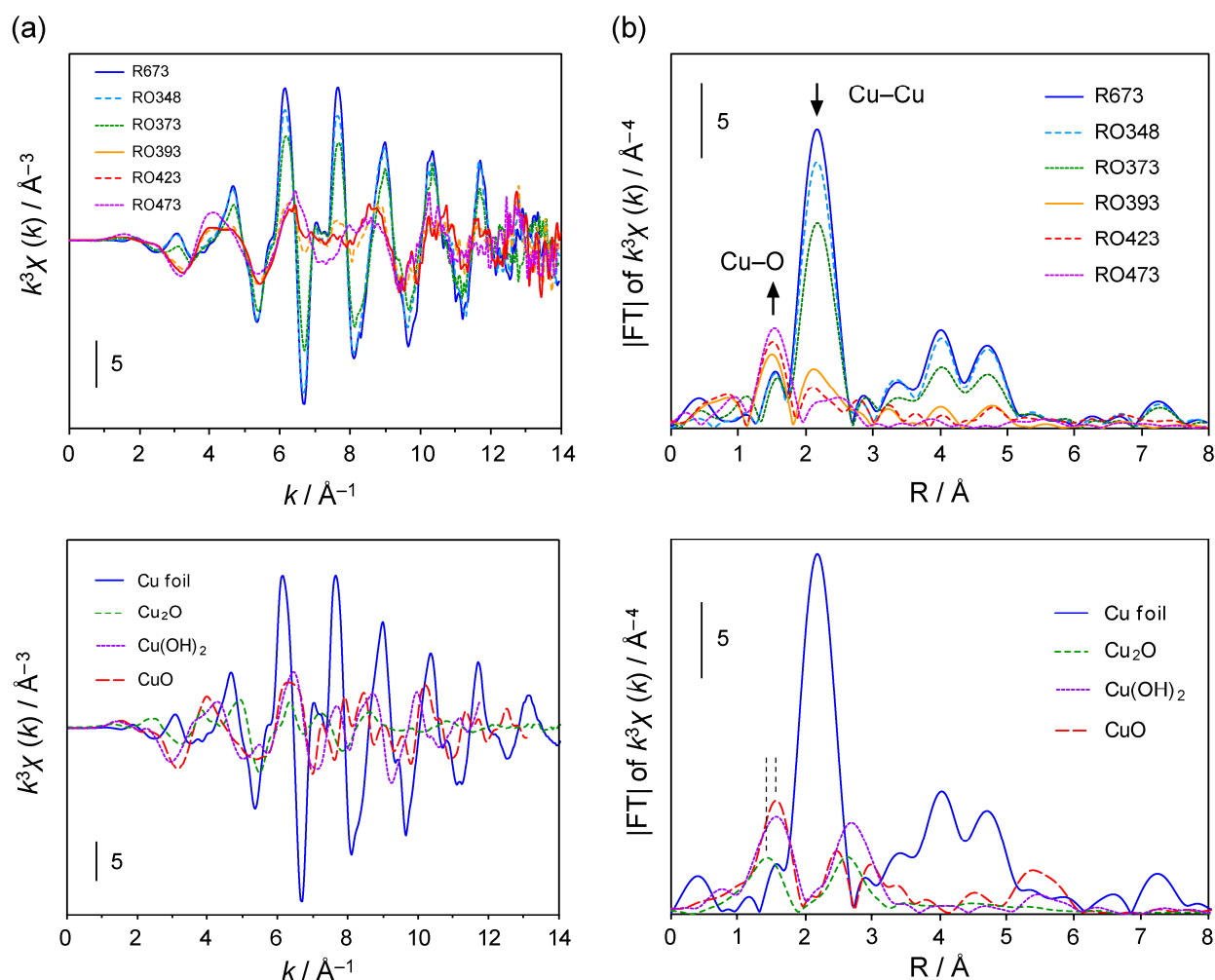


Figure 6. (a) Cu K-edge EXAFS spectra and (b) their Fourier-transformation of Cu/Nb₂O₅ catalysts pretreated under various conditions (top) and reference compounds (bottom), respectively.

Table 1. Curve-fitting results of Cu–Cu or Cu–O scattering of the Cu K-edge FT-EXAFS spectra. ^a

sample	shell	CN ^b	<CN> ^c	<i>r</i> / Å ^d	σ / Å ^e	<i>R_f</i> (%) ^f
R673	Cu–Cu	10.8(23)	10.8(23)	2.55(1)	0.06(3)	10
RO348	Cu–Cu	8.4(17)	9.7(19)	2.56(1)	0.06(3)	22
RO373	Cu–Cu	6.1(13)	9.0(18)	2.56(1)	0.05(3)	23
RO393	Cu–Cu	1.5(3)	5.5(10)	2.56(1)	0.04(3)	27
	Cu–O	1.9(3)	–	1.91(1)	0.05(3)	28
RO423	Cu–O	3.3(5)	–	1.91(1)	0.07(2)	33
RO473	Cu–O	3.6(7)	–	1.94(1)	0.06(3)	30

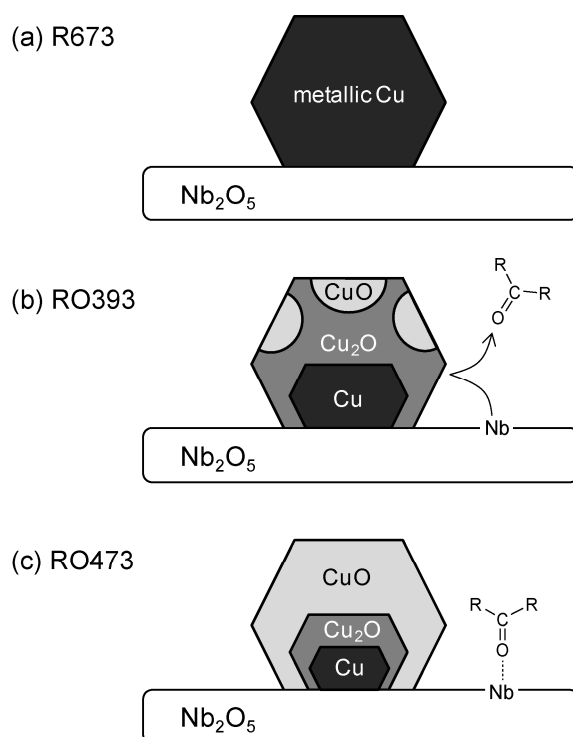
^a Inverse Fourier range $\Delta R = 1.78\text{--}2.70$ Å for Cu–Cu shell, $\Delta R = 1.14\text{--}1.81$ Å for Cu–O shell, fitting range $\Delta k = 3.0\text{--}12.0$ Å. ^b CN: coordination number. ^c <CN>: coordination number of the Cu–Cu pair in metallic moiety. ^d *r*: interatomic distance. ^e σ : Debye-Waller factor. ^f So-called R factor.

Discussion

On the basis of the results from photocatalytic reaction and XAFS study of Cu/Nb₂O₅, we discuss the correlation between the state of Cu species on Cu/Nb₂O₅ and the photocatalytic activity. At first, metallic Cu particles on Cu/Nb₂O₅ are formed with ca. 4 nm diameters (Scheme 2a) by reduction of as-prepared Cu/Nb₂O₅ at 673 K. Cu₂O and CuO moieties are formed at outer layer of the Cu particles by oxidation treatment with the reduced Cu/Nb₂O₅. The Cu₂O moiety formed at the outermost layer acts as an effective desorption site of the product, enhancing the photocatalytic activity (Scheme 2b). When the fraction of Cu₂O reaches the maximum at 393 K of oxidation temperature, the highest activity is accordingly obtained. The Cu₂O fraction in the overall Cu species gradually decreases above 393 K. However, the outermost Cu₂O moiety, that is an effective desorption site, decreases more rapidly than inner one because oxidation proceeds from outside. Therefore, the activity drastically falls above 393 K. Finally, Cu₂O at the outermost layer is wholly converted to CuO at 473 K and in consequence, the activity of R473 becomes identical to that of as-prepared Cu/Nb₂O₅ (Scheme 2c).

We have already confirmed that metallic Cu on Cu/Nb₂O₅ was converted to CuO within 24 h upon exposure to 1 atm O₂ even at room temperature.²⁰ In the case of R673, therefore, Cu₂O and/or CuO moieties may be formed in the reaction atmosphere by molecular oxygen, which results in the higher activity of R673 than that of as-prepared Cu/Nb₂O₅. Indeed, the induction period observed for R673 (Figure 2) can be attributed to such an *in-situ* generation of Cu₂O.

Through a series of stepwise oxidation, metallic Cu core decreases in size by oxidation from outer layer. The shrinkage of metallic moiety is reflected in the change in <CN> estimated by XAFS study as mentioned above. But the number of <CN> for RO393, 5.5 is too small to assume the cubocathedral structure, because the diameter of ca. 1 nm derived from the <CN> is too small to be consistent with the fraction of remaining metallic Cu, 27% (decrease in diameter of metallic Cu from 4 nm to 1 nm corresponds to ca. 95% of metallic Cu being oxidized). For such a small number of <CN>, it may be plausible to further assume that the metallic core has a flattened shape and/or that the particles are split into pieces upon the oxidation treatment.



Scheme 2. States of Cu particle on Cu/Nb₂O₅ after pretreatment in various conditions: (a) reduction at 673 K (R673), oxidation at (b) 393 K (RO393) and (c) 473 K (RO473) after the reduction.

Conclusions

In this study, we investigated the correlation between photocatalytic activity of alcohol photooxidation over Cu/Nb₂O₅ and the state of Cu on Cu/Nb₂O₅. Reduction of as-prepared Cu/Nb₂O₅ at 673 K enhanced its photocatalytic activity. Subsequent oxidation of the reduced Cu/Nb₂O₅ at 348–393 K further improved the activity. But the catalysts oxidized above 393 K showed lower activities than the reduced one. As a consequence, oxidation at 393 K after the reduction exhibited the highest activity which was twice as high as the as-prepared catalyst. Moreover, the highest activity is 6.5-fold as high as the activity of bare Nb₂O₅ photocatalyst. Cu K edge XANES study revealed that the change in photocatalytic activity corresponded to the fraction of Cu₂O which promoted the rate-determining step, desorption. EXAFS study indicated that Cu metal particles with ca. 4 nm diameter were oxidized to Cu₂O and CuO in a stepwise manner from outer layer of the particles with increase in the oxidation temperature. The obtained results also pointed that the presence of Cu₂O at the outermost layer of the Cu particle as an efficient desorption site was indispensable for the enhancement of the photocatalytic activity. Thus, appropriate modification of the state of Cu particle on Cu/Nb₂O₅ provides further enhancement in photocatalytic activity in alcohol photooxidation.

References

- (1) Fox, M. A.; Dulay, M. T. *Chem. Rev.* **1993**, *93*, 341.
- (2) Mills, A.; LeHunte, S. *J. Photochem. Photobiol. A* **1997**, *108*, 1.
- (3) Maldotti, A.; Molinari, A.; Amadelli, R. *Chem. Rev.* **2002**, *102*, 3811.
- (4) Hussein, F. H.; Pattenden, G.; Rudham, R.; Russell, J. J. *Tetrahedron Lett.* **1984**, *25*, 3363.
- (5) Sadeghi, M.; Liu, W.; Zhang, T. G.; Stavropoulos, P.; Levy, B. *J. Phys. Chem.* **1996**, *100*, 19466.
- (6) Ohtani, B.; Iwai, K.; Nishimoto, S.; Sato, S. *J. Phys. Chem. B* **1997**, *101*, 3349.
- (7) Siemon, U.; Bahnemann, D.; Testa, J. J.; Rodriguez, D.; Litter, M. I.; Bruno, N. *J. Photochem. Photobiol. A* **2002**, *148*, 247.
- (8) Hufschmidt, D.; Bahemann, D.; Testa, J. J.; Emilio, C. A.; Litter, M. I. *J. Photochem.*

Photobiol. A **2002**, *148*, 223.

- (9) Kohno, Y.; Hayashi, H.; Takenaka, S.; Tanaka, T.; Funabiki, T.; Yoshida, S. *J. Photochem. Photobiol. A* **1999**, *126*, 117.
- (10) Wetchakun, K.; Wetchakun, N.; Phanichphant, S. *Adv. Matel. Res.* **2008**, *55–57*, 853.
- (11) Prahov, L. T.; Disdier, J.; Herrmann, J. M.; Pichat, P. *Int. J. Hydrogen Energy* **1984**, *9*, 397.
- (12) Song, K. Y.; Kwon, Y. T.; Choi, G. J.; Lee, W. I. *Bull. Korean Chem. Soc.* **1999**, *20*, 957.
- (13) Arana, J.; Rodriguez, C. F.; Diaz, O. G.; Melian, J. A. H.; Pena, J. P. *Catal. Today* **2005**, *101*, 261.
- (14) Xin, B. F.; Wang, P.; Ding, D. D.; Liu, J.; Ren, Z. Y.; Fu, H. G. *Appl. Surf. Sci.* **2008**, *254*, 2569.
- (15) Alberici, R. M.; Jardim, W. F. *Water Res.* **1994**, *28*, 1845.
- (16) Ohuchi, T.; Miyatake, T.; Hitomi, Y.; Tanaka, T. *Catal. Today* **2007**, *120*, 233.
- (17) Shishido, T.; Miyatake, T.; Teramura, K.; Hitomi, Y.; Yamashita, H.; Tanaka, T. *J. Phys. Chem. C* **2009**, *113*, 18713.
- (18) Shishido, T.; Teramura, K.; Tanaka, T. *Catal. Sci. Technol.* **2011**, *1*, 541.
- (19) Furukawa, S.; Tamura, A.; Shishido, T.; Teramura, K.; Tanaka, T. *Appl. Catal. B: Environ.* **2011**, *110*, 216.
- (20) Furukawa, S.; Ohno, Y.; Shishido, T.; Teramura, K.; Tanaka, T. *Chemphyschem* **2011**, *12*, 2823.
- (21) Furukawa, S.; Shishido, T.; Teramura, K.; Tanaka, T. *J. Phys. Chem. C* **2011**, *115*, 19320.
- (22) Kau, L. S.; Spirasolomon, D. J.; Pennerhahn, J. E.; Hodgson, K. O.; Solomon, E. I. *J. Am. Chem. Soc.* **1987**, *109*, 6433.
- (23) Kosugi, N.; Kondoh, H.; Tajima, H.; Kuroda, H. *Chem. Phys.* **1989**, *135*, 149.
- (24) Kosugi, N.; Tokura, Y.; Takagi, H.; Uchida, S. *Phys. Rev. B* **1990**, *41*, 131.

Chapter 9

Selective Photooxidation of Alcohol over TiO₂ Covered with Nb₂O₅

Abstract

A selectivity enhancement in alcohol photooxidation using TiO₂ covered with Nb₂O₅ is demonstrated. A series of TiO₂ covered with Nb₂O₅ catalysts (Nb₂O₅/TiO₂, loading of Nb₂O₅; 0–5 mol%) were prepared and characterized. XPS studies suggest that the TiO₂ surface was completely covered with Nb₂O₅ at a 3.5 mol% loading. UV-Vis spectra of TiO₂ and the Nb₂O₅/TiO₂ series revealed that the band gap energy of the catalyst was not changed upon addition of Nb₂O₅. The amounts of photogenerated oxygen anion radical species (O₂⁻ and O₃⁻) over the catalyst, as estimated by ESR, drastically decreased with increased loadings of Nb₂O₅. The O₃⁻ anion, in particular, which can be formed on anatase TiO₂, completely disappeared at Nb₂O₅ loadings over 4 mol%. In the oxidations of several alcohols (1-pentanol, 2-pentanol, 3-pentanol and cyclohexanol), the Nb₂O₅/TiO₂ catalysts exhibited higher selectivities than TiO₂ with comparable conversion levels. Furthermore, the Nb₂O₅/TiO₂ system gave a higher photocatalytic activity compared to Nb₂O₅ without lowering the selectivity.

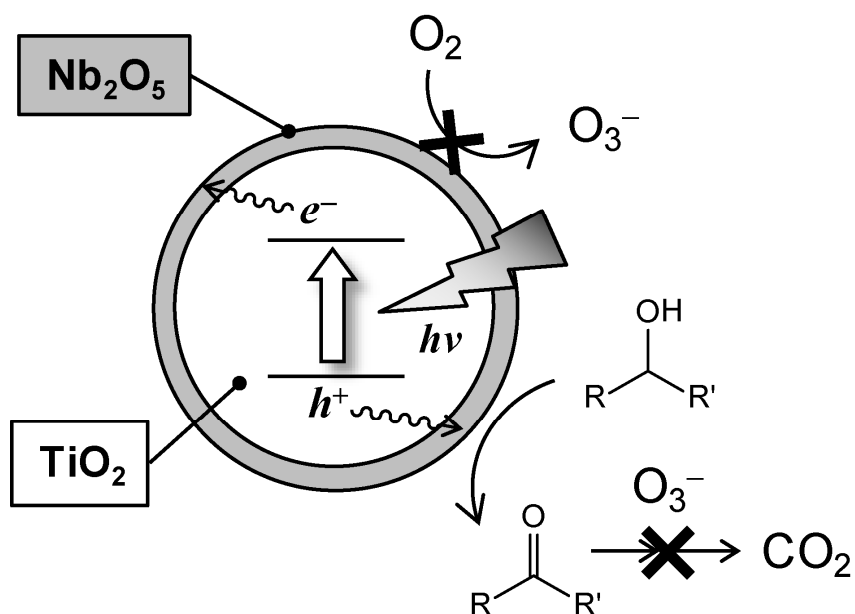
Introduction

Heterogeneous photocatalysis have a potential application in the aerobic oxidation of organic molecules.¹⁻³ Numerous semiconductor-type metal oxides have been tested as photocatalysts for oxidation, but it is generally accepted that anatase TiO₂ is the most reliable material due to its low cost, high photostability and photocatalytic activity. Recently, a lot of effort has been devoted to the application of TiO₂ to the selective catalytic oxidation of various organic molecules, such as alkanes,⁴⁻⁹ arenes¹⁰ and alcohols.¹¹⁻¹³ However, undesired over-oxidation to carbon dioxide (CO₂) is essentially associated with the photocatalytic oxidation over TiO₂,^{14,15} due to the presence of highly oxidizing radical species; positive holes trapped by surface lattice oxygen (O⁻),^{16,17} ozonide ion (O₃⁻)^{18,19} or hydroxyl radical (HO·).^{2,15} It is generally accepted that O₃⁻ is formed upon the combination of O⁻ and O₂,¹⁸⁻²⁰ and that HO· is released via the oxidation of a surface hydroxyl group by a hole.^{2,21} Tsukamoto et al. reported that TiO₂ partially coated with WO₃ showed higher activity and selectivity in the photooxidation of benzylic alcohols to aldehydes than TiO₂ under diluted conditions (5 mg of catalyst, 0.1 mmol of alcohol, and 5 mL of water as a solvent).²² They interpret that the phenomena that TiO₂ surface of the catalyst, which is active for oxidation, is partially coated with WO₃ layer (WO₃ loading: 7.6 wt%), which leads to a decrease in the amount of aldehyde adsorbed on TiO₂ surface. It appeared that the area of TiO₂ surface was decreased by WO₃ addition. However, not only the selectivity to aldehyde but also the rate of alcohol conversion increased. Therefore, it seems that WO₃ layer has another role in addition to adsorption site of photogenerated aldehyde.

We reported that the selective photooxidation of alcohols proceeded over niobium oxide (Nb₂O₅) and showed a higher selectivity than TiO₂ with a comparable conversion level.²³ ESR studies suggested that this high selectivity was due to the absence of O₃⁻ over Nb₂O₅, in contrast to TiO₂ under photo irradiation.²⁴ However, the photocatalytic activity of Nb₂O₅ in the oxidation of alcohols was much lower than that of TiO₂. To develop an effective photocatalyst that exhibits both high activity and selectivity in the aerobic oxidation of alcohols, there are two primary strategies: improve the photocatalytic activity of Nb₂O₅ or enhance the selectivity of TiO₂. In the first strategy, we have already achieved a remarkable increase in photocatalytic activity by addition of Cu to

Nb_2O_5 .²⁵ In the oxidation of alcohols over $\text{Cu}/\text{Nb}_2\text{O}_5$, the $\text{Cu}(\text{I})$ site operates as a desorption site and successfully promotes the desorption of the produced carbonyl compound which is the rate-determining step.²⁶ In the latter, attention should be focused on how the formation of the highly oxidizing species above mentioned is inhibited. In this context, a promising approach is to cover the surface of TiO_2 with Nb_2O_5 which inhibits the production of highly oxidizing O_3^- (Scheme 1).

In this study, we have prepared a series of TiO_2 covered with Nb_2O_5 photocatalysts and their photocatalytic activities and selectivities have been compared with those of bare TiO_2 or Nb_2O_5 in the oxidation of alcohols. The correlation between the amount of photogenerated oxygen anion radicals and selectivity has also been investigated.



Scheme 1. Strategy for the selective photocatalytic oxidation of alcohols over $\text{Nb}_2\text{O}_5/\text{TiO}_2$.

The inhibition of O_3^- generation by surface coverage of TiO_2 with Nb_2O_5 is shown.

Experimental

Catalyst preparation

Ammonium niobium oxalate ($\text{NH}_4[\text{NbO}(\text{C}_2\text{O}_4)_2(\text{H}_2\text{O})]\cdot n\text{H}_2\text{O}$), as a precursor of niobium oxide, and niobium oxide hydrate ($\text{Nb}_2\text{O}_5\cdot n\text{H}_2\text{O}$, HY-340) were kindly supplied by CBMM. The

TiO₂ sample used in this study, JRC-TIO-4 (equivalent to Degussa. P-25; rutile/anatase = 3/7; BET surface area = 49 m²·g⁻¹) was supplied by the Japan Catalysis Society. After the hydration of TiO₂ in distilled water for 2 h at 353 K and evaporation at 368 K, the sample was dried at 353 K overnight. The TiO₂ catalyst was then calcined in dry air at 773 K for 5 h. A series of TiO₂ supported niobium oxide catalysts (*n* mol% Nb₂O₅/TiO₂; *n* = 1–5) were prepared by impregnation of the TiO₂ sample with aqueous solutions of ammonium niobium oxalate followed by calcination at 773 K for 5 h. Nb₂O₅ catalyst (BET surface area = 48 m²·g⁻¹)²³ was prepared by calcination of niobium oxide hydrate in a dry air flow at 773 K for 5 h. All catalysts were ground into powders under a 100 mesh (0.15 mm) after calcination.

Characterization

A Rigaku MultiFlex DR Powder X-ray diffractometer (XRD) was used for the identification of compounds formed on the catalyst samples. Specific surface areas were evaluated using the BET method using liquid nitrogen with a BEL Japan BELSORP28 28A. UV-Vis diffuse reflectance spectra (1 nm resolution) were obtained with a JASCO UV570 spectrometer. X-ray photoelectron spectra (XPS) were acquired using an ULVAC PHI 5500MT. XPS samples were mounted on an indium foil and the spectra were measured using Mg K α radiation (15 kV, 400 W) in a chamber with the base pressure of ca. 10⁻⁹ Torr. The take-off angle was set at 45°. Binding energies were referenced to the O 1s level at 530.2 eV.

ESR measurement of oxygen anion radicals

ESR measurements were carried out using an X-band ESR spectrometer (JEOL JES-SRE2X) with an *in situ* quartz cell. Prior to ESR measurement, the sample was pretreated with 6.7 kPa O₂ at 673 K for 1 h, followed by evacuation for 0.5 h at 673 K. After pre-treatment, the sample was exposed to 0.5 kPa O₂ at room temperature. The sample was then cooled to 123 K and irradiated. ESR spectra were recorded before and after photoirradiation at 123 K. The *g* values and the amounts of yielded radical species were determined using a certain amount of Mn/MgO marker. The radical amounts of the Mn/MgO marker were determined using 4-Hydroxy-2,2,6,6-tetramethylpiperidine-

1-oxyl (TEMPOL; radical density 97%, purchased from Wako). A 500 W ultra-high-pressure mercury lamp was used as a light source.

Reaction conditions

The photocatalytic oxidations of alcohols were carried out in a quasi-flowing batch system²⁵ under atmospheric oxygen. Catalyst (100 mg), alcohol (10 mL) and a stirrer bar were introduced to a Pyrex glass reactor. No solvent was used. Substrate was used without further purification. The suspension was vigorously stirred at room temperature and irradiated from the flat bottom of the reactor via reflection using a cold mirror with a 500 W ultra-high-pressure Hg lamp (USHIO Denki Co.). Oxygen was flowed into the reactor at $2 \text{ cm}^3 \cdot \text{min}^{-1}$. Organic products were analyzed by FID-GC (Shimadzu GC-14B) and GC-MS (Shimadzu GC-MS QP5050). At the down stream of the flow reactor, a saturated barium hydroxide solution ($\text{Ba}(\text{OH})_2$) was set-up to determine the quantities of carbon dioxide (CO_2) formed as barium carbonate (BaCO_3). The partial oxidation product selectivities are defined as yields (mmol) of aldehyde and acid (partial oxidation products) per yield (mmol) of aldehyde, acid and $1/n \text{ CO}_2$ (n = the number of carbon atoms of the substrate).

Results and Discussion

Characterization of catalysts

The valences of niobium and titanium cations on $\text{Nb}_2\text{O}_5/\text{TiO}_2$ catalyst surface were evaluated using XPS. The binding energies of the Nb 3d and Ti 2p peaks of $\text{Nb}_2\text{O}_5/\text{TiO}_2$ did not change regardless of Nb_2O_5 loading (Figure 1). These Nb 3d (207.1 eV for $3d_{5/2}$ and 209.8 eV for $3d_{3/2}$) and Ti 2p (464.5 eV for $2p_{3/2}$ and 458.8 eV for $2p_{1/2}$) peaks can be assigned to Nb^{5+} and Ti^{4+} , respectively. The surface Nb/Ti ratios for the $\text{Nb}_2\text{O}_5/\text{TiO}_2$ catalysts were estimated from the areas of Nb 3d and Ti 2p XPS, as shown in Figure 2. The surface Nb/Ti ratio increases linearly with increasing Nb_2O_5 loading up to 3.5 mol% (equivalent to 10 wt%). It then becomes more gradual. The linear relationship indicates the formation of a two-dimensional niobium oxide overlayer, and the change in the slope can be attributed to the transition from a two-dimensional overlayer to three dimensional particles (monolayer coverage) at loadings over 3.5 mol% Nb_2O_5 .²⁷

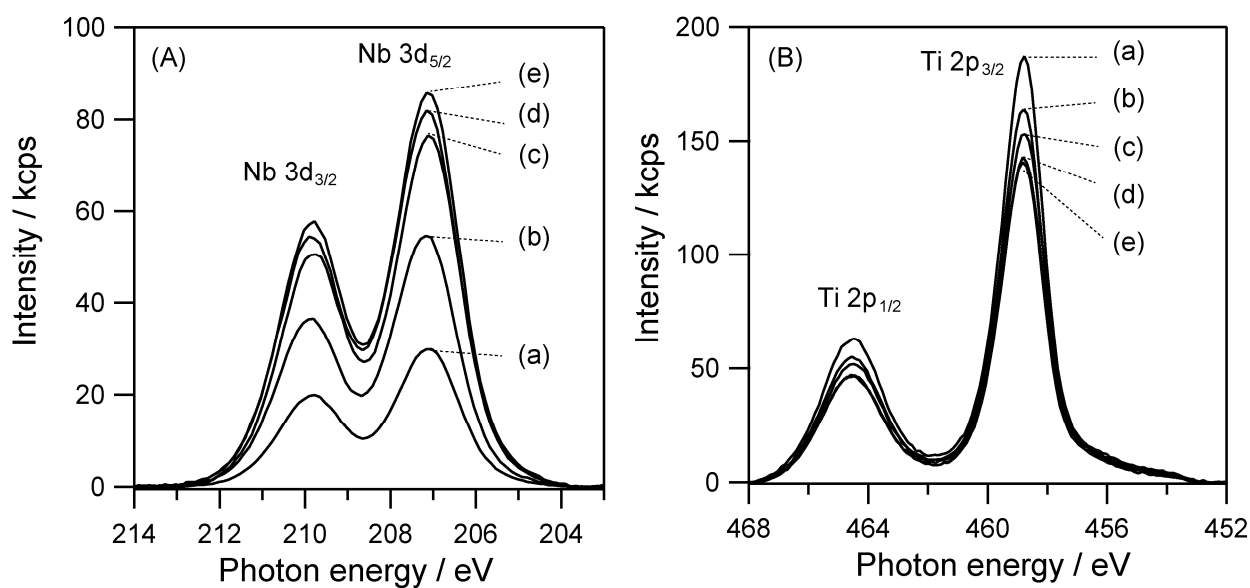


Figure 1. XPS of (A) Nb 3d and (B) Ti 2p regions of Nb₂O₅/TiO₂ catalysts with various loadings; (a) 1 mol%, (b) 2 mol% , (c) 3 mol%, (d) 4 mol% and (e) 5 mol%.

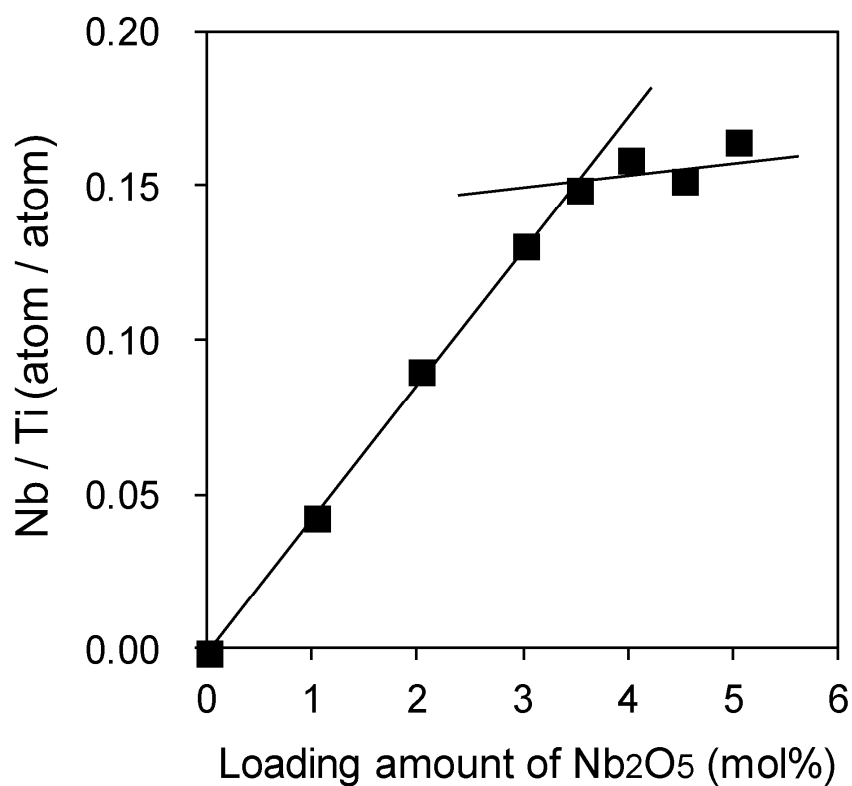


Figure 2. Changes in surface Nb/Ti ratio with Nb₂O₅ loading.

The XRD patterns of a series of Nb₂O₅/TiO₂ catalysts were compared with those of TiO₂ and Nb₂O₅, as shown in Figure 2. The patterns for 1–4 mol% Nb₂O₅/TiO₂ samples indicate no changes in the crystallinity of the TiO₂ support (anatase and rutile) and no formation of a niobium oxide crystallite. On the other hand, the 5 mol% Nb₂O₅/TiO₂ exhibits a small feature assignable to TT-Nb₂O₅^{28–31}, which is associated with TiO₂. Similar diffraction patterns have also been reported for 7.7³² or 11³³ mol% Nb₂O₅/TiO₂ samples. The formation of a niobium oxide crystallite at loadings over 3.5 mol% is consistent with the results from the XPS study.

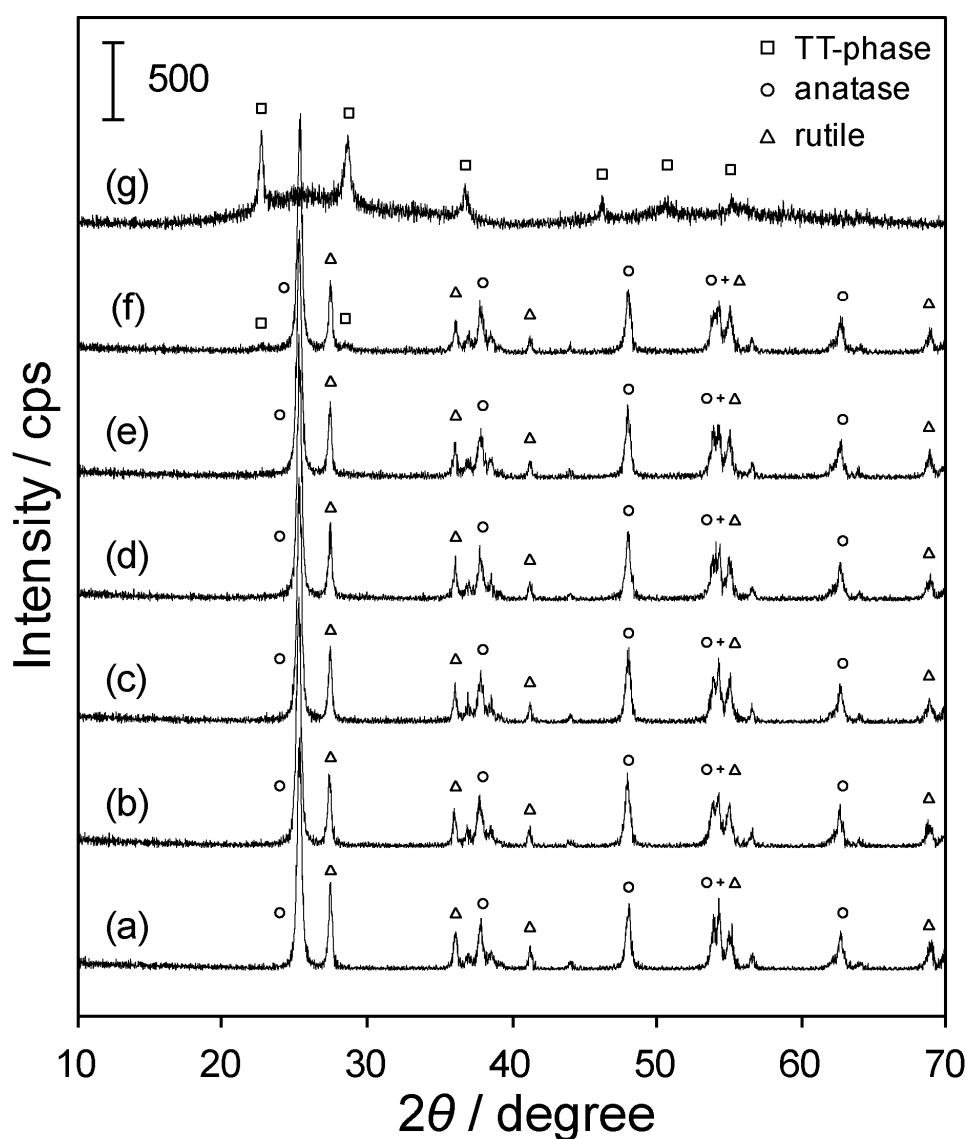


Figure 3. XRD patterns of (a) TiO₂, (b) 1 mol%, (c) 2 mol%, (d) 3 mol%, (e) 4 mol%, (f) 5 mol% Nb₂O₅/TiO₂ and (g) Nb₂O₅.

UV-Vis spectra of the 1–5 mol% Nb₂O₅/TiO₂ catalysts were also identical to that of TiO₂ (Figure 4), whose band gap energy was estimated as 3.10 eV. The Nb₂O₅ catalyst possesses similar spectral features to TiO₂ and the band gap energy was estimated as 3.16 eV. Thus, the surface coverage of TiO₂ with Nb₂O₅ does not influence the crystallinity of the TiO₂ support and does not change the optical properties of the catalysts. The BET surface area measurements revealed that the surface area of TiO₂ (49 m²·g⁻¹) was maintained after the addition of Nb₂O₅ (*S*_{BET} of 1, 2, 3, 4, and 5 mol% Nb₂O₅/TiO₂ are 54, 47, 47, 51, 40 m²·g⁻¹, respectively).

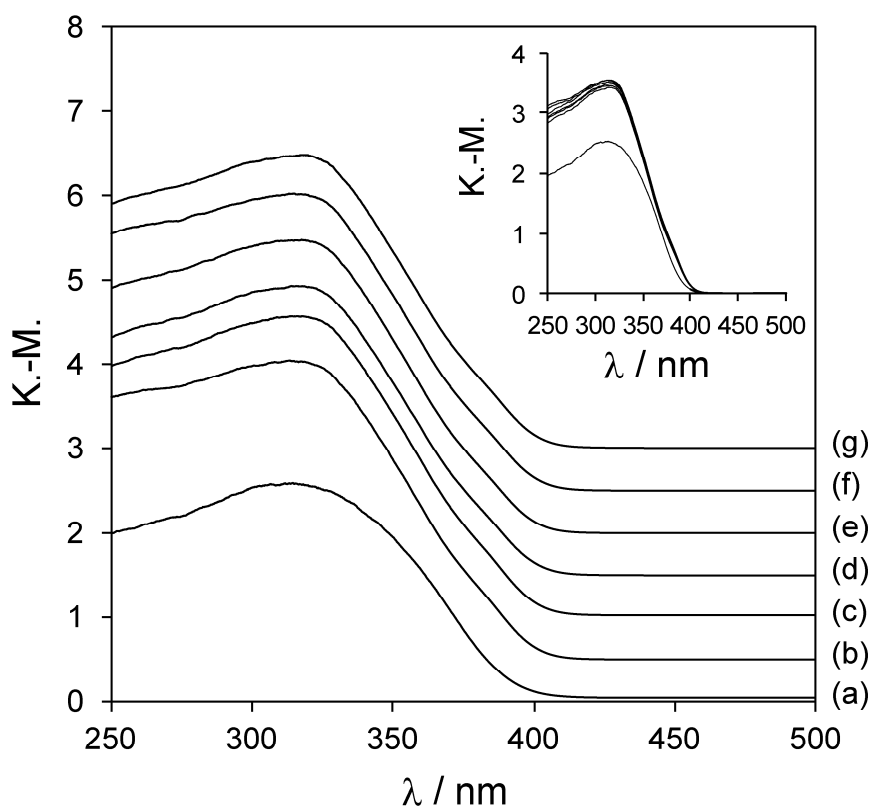


Figure 4. UV-Vis spectra of (a) Nb₂O₅, (b) TiO₂ and Nb₂O₅/TiO₂ catalysts with various loadings; (c) 1 mol%, (d) 2 mol% , (e) 3 mol%, (f) 4 mol% and (g) 5 mol%. The spectra are vertically offset for clarity. Inset shows spectra without offset.

ESR measurements of photogenerated oxygen anion radicals

We characterized the photogenerated oxygen anion radical species over TiO_2 , $\text{Nb}_2\text{O}_5/\text{TiO}_2$ and Nb_2O_5 using ESR and estimated the amounts of the radical species. Figure 5 shows the ESR spectra obtained when the catalysts were irradiated in the presence of oxygen at 123 K. An intense signal consisting of two sets of rhombic g values were observed over TiO_2 , which can be assigned to superoxide (O_2^- : $g_1 = 2.024$, $g_2 = 2.009$, $g_3 = 2.003$)³⁴⁻³⁶ and ozonide (O_3^- : $g_1 = 2.019$, $g_2 = 2.006$, $g_3 = 2.000$).³⁵⁻³⁸ Such radical species over TiO_2 are well known and have been widely characterized. Generally, it is proposed that the O_2^- is generated via the reduction of adsorbed O_2 by excited electrons. The O_3^- is formed from the combination of a positive hole captured by surface lattice oxygen (equivalent to O^-) and O_2 .^{20,35,39,40} In contrast, only a small broad signal was observed over Nb_2O_5 . In this case, using ^{17}O -enriched O_2 (20%) instead of $^{16}\text{O}_2$, a signal appeared with hyperfine splitting, as derived from the ^{17}O nuclei ($I = 5/2$) (Figure 6). This hyperfine structure indicates the generation of $^{16}\text{O}^{17}\text{O}^-$ and suggests that the two oxygen nuclei are equivalent. The equivalent hyperfine interactions are also consistent with the O_2^- ion being adsorbed in a side-on fashion onto the Nb_2O_5 surface, with its internuclear axis parallel to the plane of the surface. This type of adsorption is commonly observed with other metal oxides.²⁰ Eleven lines corresponding to the two ^{17}O nuclei ($^{17}\text{O}^{17}\text{O}^-$, $I = 5$) were expected, but not observed apparently, which is likely due to an inadequate enrichment of ^{17}O (20%).

The intensities of the ESR signals for the oxygen anion radicals were dramatically decreased with increasing of Nb_2O_5 loading. Although the signals assigned to O_2^- remained at a 5 mol% loading, the signal assigned to O_3^- completely disappeared at loadings over 4 mol%. This result strongly indicates that the TiO_2 surface, which can produce O_3^- , is completely covered at loadings over 4 mol%. It is also consistent with a monolayer coverage at 3.5 mol% loading, as estimated from the XPS study. The amounts of photogenerated oxygen anion radical species are shown in Figure 7. The amount of the radical species drastically decreases on going from 0 to 4 mol% Nb_2O_5 loading. This change becomes gradual at loadings over 4 mol%. Thus, these results demonstrate that the surface coverage of TiO_2 with Nb_2O_5 effectively inhibits the formation of oxygen anion radicals. In particular, the generation of O_3^- was completely inhibited by full coverage (Scheme 2). The g values

of the ESR signal assigned to O_2^- , as generated on 5 mol% Nb_2O_5/TiO_2 , are different from those on TT- Nb_2O_5 . This may be due to the differences in crystallinity of Nb_2O_5 (amorphous or TT-phase). The ESR spectrum of the oxygen anion radicals formed on 5 mol% Nb_2O_5/TiO_2 has a shoulder feature in the region of $g = 2.003-2.008$. This is in good agreement with the peak features of O_2^- , formed on TT- Nb_2O_5 in the same region (Figure 6), which implies the formation of O_2^- on TT- Nb_2O_5 (Scheme 2).

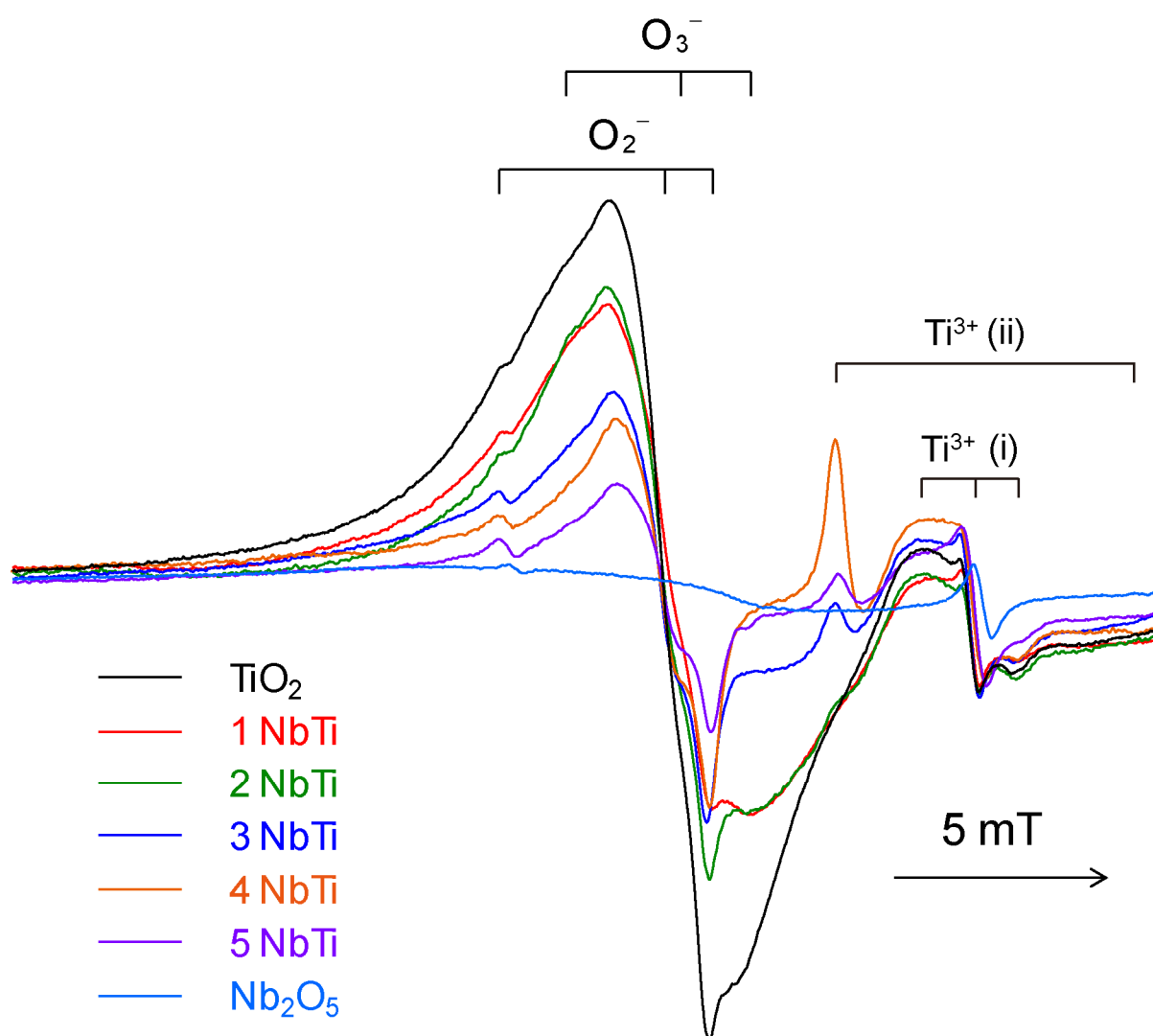


Figure 5. ESR spectra of the photogenerated oxygen anion radical at 77 K over TiO_2 , n mol% Nb_2O_5/TiO_2 (abbreviated as $nNbTi$; $n = 1, 3, 5$) and Nb_2O_5 .

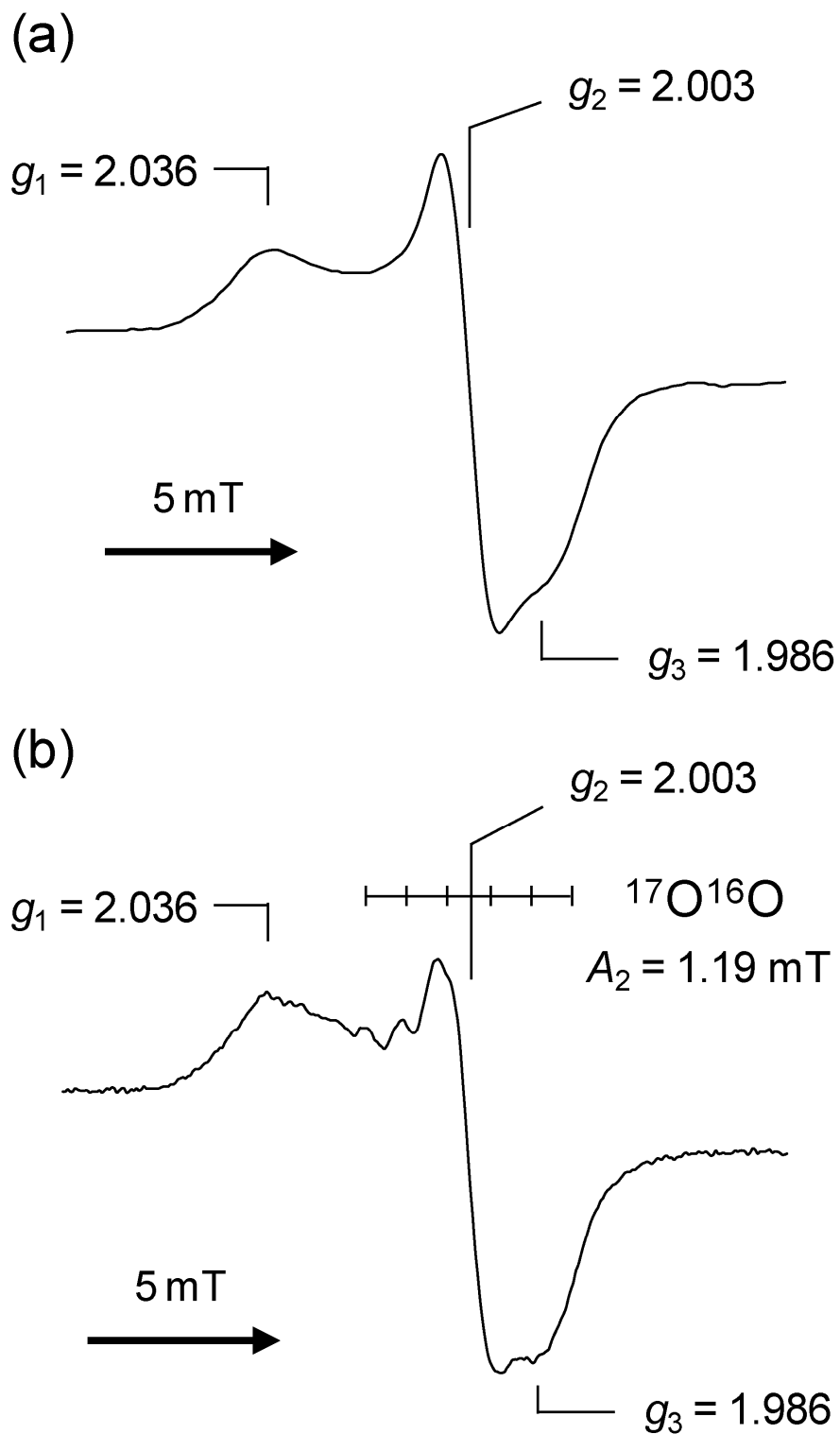


Figure 6. ESR spectra obtained when Nb_2O_5 was irradiated in the presence of 4.0 kPa of (a) oxygen and (b) isotopically enriched oxygen (20% ^{17}O). Hyper fine derived from $^{17}\text{O}^{17}\text{O}$ was not apparently observed due to low ^{17}O concentration.

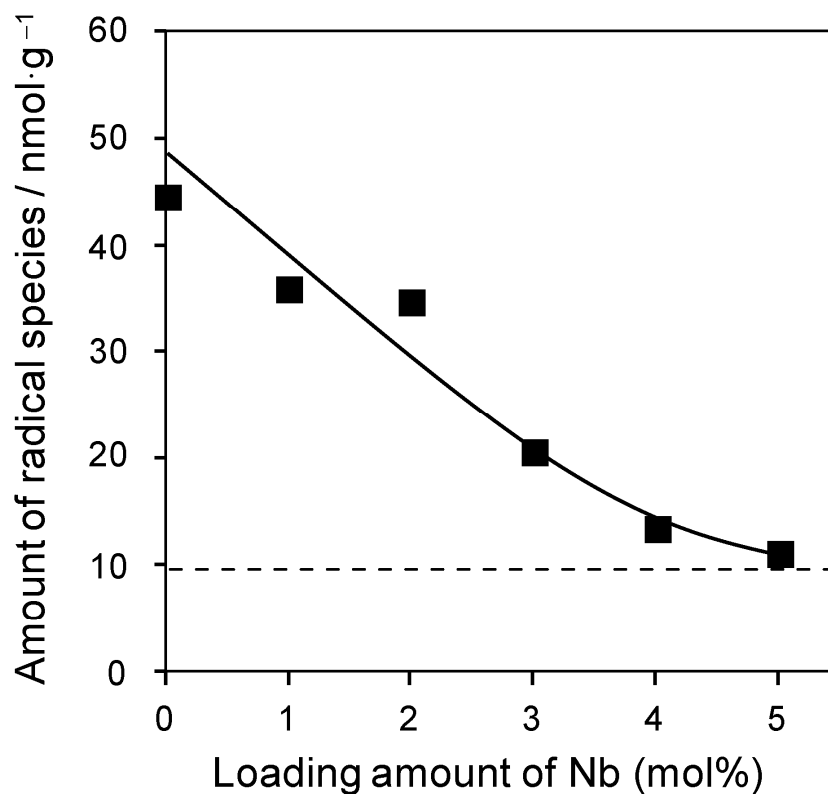
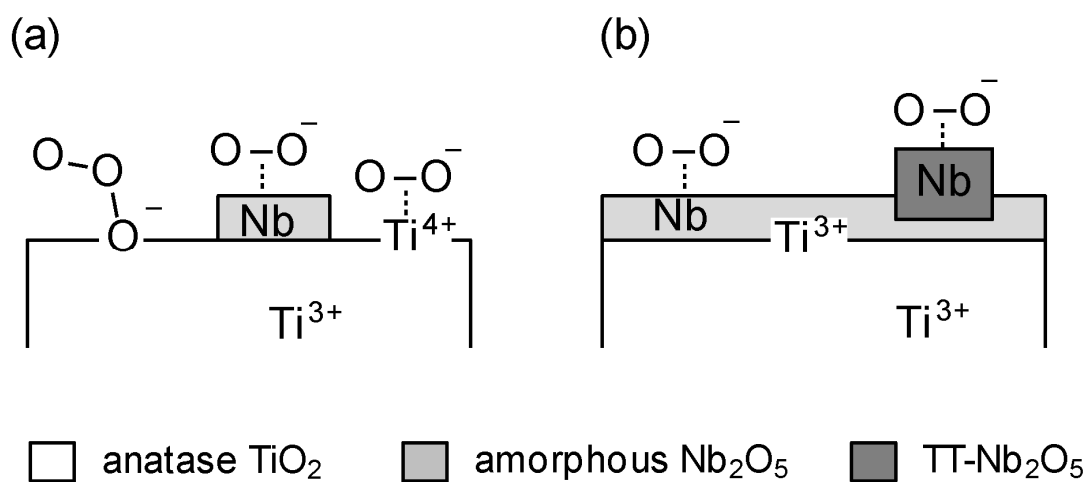


Figure 7. Changes in the amount of photogenerated oxygen anion radical species ($\text{O}_2^- + \text{O}_3^-$) over $\text{Nb}_2\text{O}_5/\text{TiO}_2$ catalyst with Nb_2O_5 loading. The dotted line shows the radical amount over Nb_2O_5 .



Scheme 2. Plausible surface species on the $\text{Nb}_2\text{O}_5/\text{TiO}_2$: (a) below 3 mol% Nb_2O_5 loading and (b) over the monolayer.

In addition to the signals of the oxygen anion radicals, small signals were also observed in the region of $g < 2.000$. These can be assigned to excited electrons trapped by the Ti^{4+} sites (equivalent to Ti^{3+}) and are composed of two distinct signals (Ti^{3+} (i) and (ii)). The g values of Ti^{3+} (i) ($g_1 = 1.982$, $g_2 = 1.977$, $g_3 = 1.971$) are similar to those for bulk and surface Ti^{3+} in TiO_2 .⁴¹ The g values and the signal intensity do not depend on the loading amount of Nb_2O_5 . These suggest that the Ti^{3+} (i) corresponds to the bulk Ti^{3+} site. On the other hand, the signals assigned to Ti^{3+} (ii) are only observed with a large surface coverage of TiO_2 (> 3 mol%). The g values of Ti^{3+} (ii) ($g_{\perp} = 1.990$, $g_{\parallel} = 1.962$) are almost identical to those obtained from Nb-doped anatase TiO_2 , and are attributed to the interstitial Ti^{3+} ion.^{42,43} Based on this, the Ti^{3+} (ii) is assignable to the interfacial Ti^{3+} sites adjacent to loaded Nb_2O_5 (Scheme 2).

Photocatalytic activity and selectivity

The photocatalytic activities and selectivities of the TiO_2 , Nb_2O_5/TiO_2 and Nb_2O_5 catalysts were evaluated using the photooxidation of 1-pentanol as shown in Figure 8. Although the photocatalytic activity gradually decreases as the loading of Nb_2O_5 is increased, 5mol% Nb_2O_5/TiO_2 , which seems to be fully covered with Nb_2O_5 , still exhibits a higher activity than Nb_2O_5 . The selectivity to partial oxidation products became higher on going from 1 to 5mol% loading, and reached 97%, which is as high as that obtained with Nb_2O_5 (Figure 8a). The higher selectivities of the Nb_2O_5/TiO_2 catalysts, as compared to the TiO_2 are maintained at a same conversion level (Figure 8b). Thus, the surface coverage of TiO_2 with Nb_2O_5 effectively enhances the selectivity of the photooxidation of 1-pentanol. The selectivity at comparable conversion levels increased with increasing Nb_2O_5 loading up to 3 mol%. As mentioned above, the ESR study revealed that coverage of the TiO_2 surface with Nb_2O_5 inhibits the generation of O_3^- , which is highly active towards the complete oxidation of organic molecules. In fact, O_3^- is known to be active even at room temperature, while O_2^- is stable up to ca. 423 K. Based on this, the change in selectivity on going from 0 to 3 mol% Nb_2O_5 loading agrees with the results from the ESR study. However, 5 mol% Nb_2O_5/TiO_2 and Nb_2O_5 showed lower selectivities compared to 3 mol%. In this case, higher yields of pentanoic acid are obtained than the lower loading homologues. This indicates that over-oxidation of the products to CO_2 takes place more severely for 5 mol% Nb_2O_5/TiO_2 and Nb_2O_5 , due to the much longer reaction

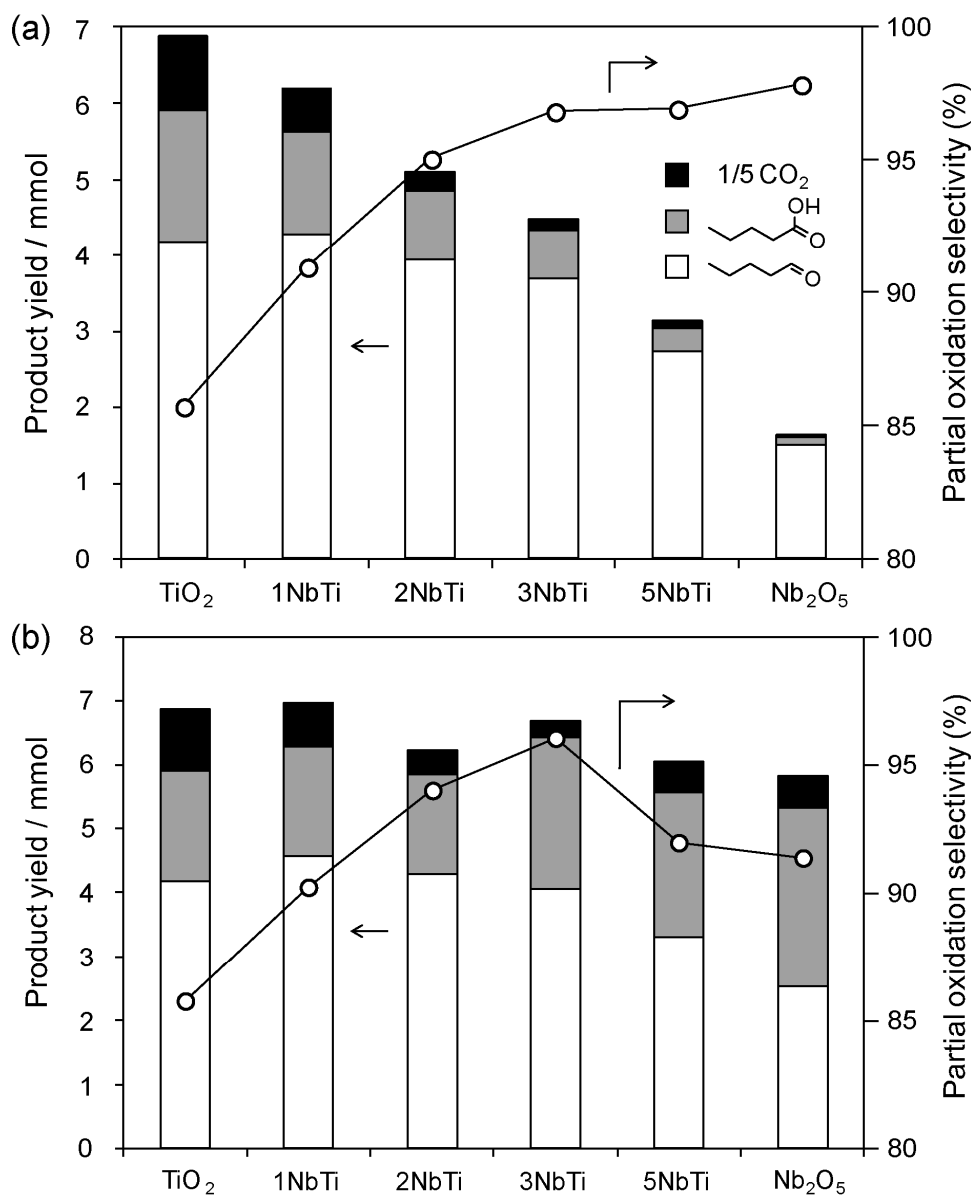


Figure 8. Product yields in the photooxidation of 1-pentanol over TiO₂, *n* mol% Nb₂O₅/TiO₂ (abbreviated as *n*NbTi; *n* = 1, 2, 3 and 5) and Nb₂O₅; (a) after 5 h of photo irradiation, (b) at a comparable conversion level (TiO₂; 5h, 1NbTi; 5.5 h, 2NbTi; 6 h, 3NbTi; 7.5 h, 5NbTi; 13 h and Nb₂O₅; 20 h).

times. Figure 9 shows the relationship between selectivity and conversion in the photooxidation of 1-pentanol over 3 mol% Nb₂O₅/TiO₂ and TiO₂. At the higher the conversion level, 3 mol% Nb₂O₅/TiO₂ catalyst exhibited a much higher selectivity than TiO₂. The 3 mol% Nb₂O₅/TiO₂ catalyst maintained more than 85% selectivity, even at 20% conversion. However, the selectivity fell below 75% at 15% conversion when TiO₂ was used.

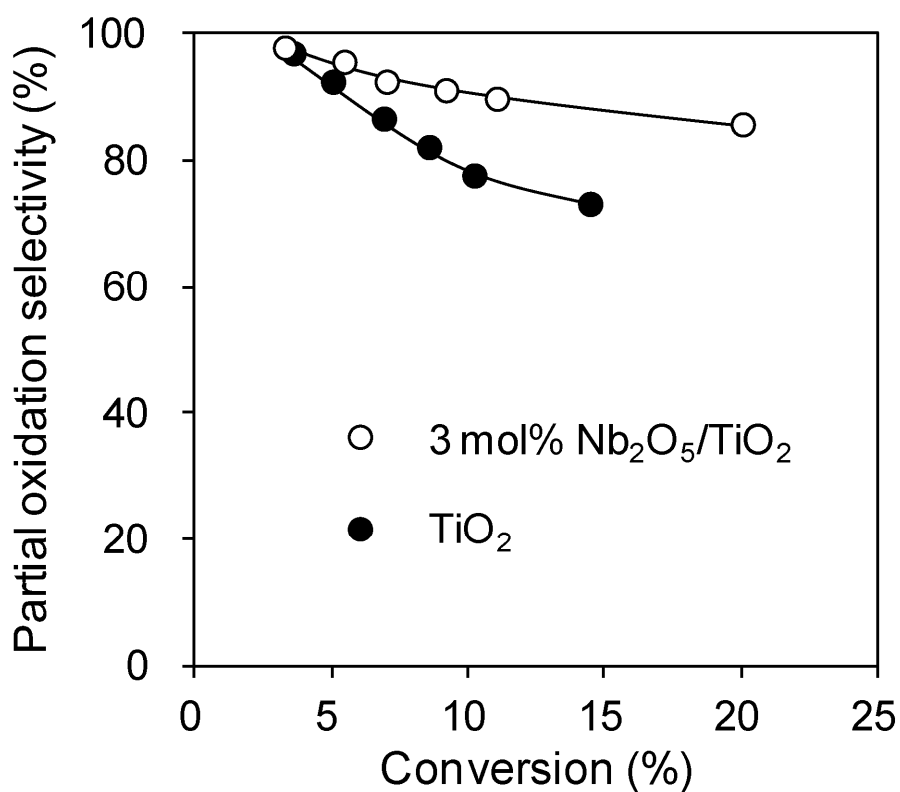


Figure 9. Selectivity-conversion plots for the photooxidation of 1-pentanol over 3 mol% Nb₂O₅/TiO₂ and TiO₂.

We went on to apply 3 mol% Nb₂O₅/TiO₂ to the oxidation of various alcohols. The activities and selectivities were compared with those of TiO₂ and Nb₂O₅ (Figure 10). The oxidation of several secondary alcohols (2-pentanol, 3-pentanol, cyclohexanol) gave the corresponding ketones and certain amounts of CO₂. In each case, the 3 mol% Nb₂O₅/TiO₂ catalyst showed not only a much higher activity than Nb₂O₅ without lowering selectivity, but also a higher selectivity than TiO₂ at a comparable conversion level. Thus, the surface coverage of TiO₂ with Nb₂O₅ enhanced the selective partial oxidation of various alcohols, including primary and secondary alcohols.

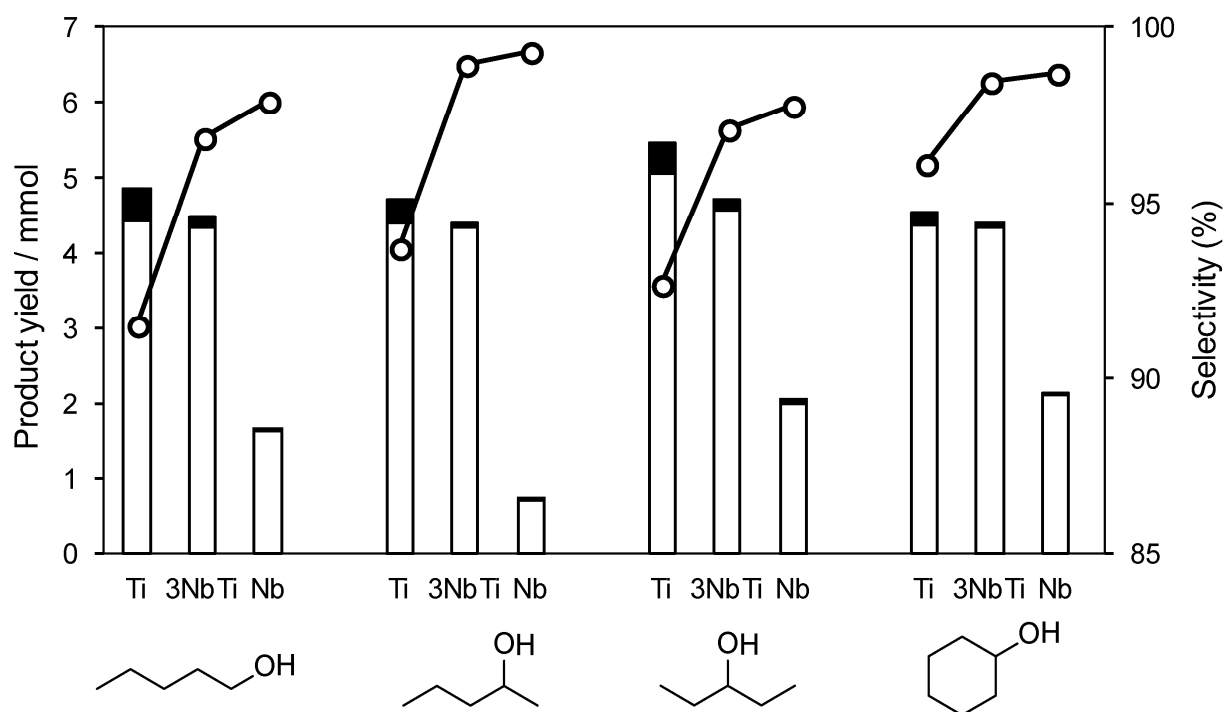


Figure 10. Product yields and Selectivities to partial oxidation product(s) in photocatalytic oxidation of various alcohols over TiO₂ (Ti), 3 mol% Nb₂O₅/TiO₂ (3NbTi) and Nb₂O₅ (Nb). Reaction condition: catalyst (100 mg), alcohol (10 ml), O₂ flow (2 ml·min⁻¹), *hν* (> 300 nm), reaction time (3 h for TiO₂, 5 h for 3NbTi and Nb). □: partial oxidation product(s); aldehyde + acid for primary alcohol or ketone for secondary one, ■: 1/n CO₂ (n indicates the number of carbon atoms of substrate).

Conclusions

In this study, we prepared a series of TiO₂ supported Nb₂O₅ catalysts (Nb₂O₅/TiO₂, with loadings of Nb₂O₅ between 0–5 mol%) for the selective photooxidation of alcohols. XPS studies suggested that the TiO₂ surface was completely covered with Nb₂O₅ at loadings over 3.5 mol%. UV-Vis spectra of TiO₂ and a series of Nb₂O₅/TiO₂ samples revealed that the absorption band of the catalyst remained unchanged by the addition of Nb₂O₅. However, the amounts of photogenerated O₂⁻ and O₃⁻ over the catalyst were estimated by ESR to be drastically decreased with increased loadings of Nb₂O₅. In particular, O₃⁻ which can be formed on anatase TiO₂ completely disappeared at loadings over 4 mol%. We also investigated the photocatalytic activities and selectivities of these catalysts in the oxidation of 1-pentanol. Although the photocatalytic activity gradually decreased with increasing of Nb₂O₅ loading, the selectivity was enhanced. At a comparable conversion level, the maximum selectivity was obtained with a 3 mol% Nb₂O₅ loading. Similarly, 3 mol% Nb₂O₅/TiO₂ exhibited higher selectivities than TiO₂ in the oxidation of secondary alcohols (2-pentanol, 3-pentanol and cyclohexanol). Thus, the surface coverage of TiO₂ with Nb₂O₅ effectively enhanced the selectivity to partial oxidation product(s) in alcohol photooxidation, due to inhibition of O₃⁻ formation.

References

- (1) Fox, M. A.; Dulay, M. T. *Chem. Rev.* **1993**, *93*, 341.
- (2) Mills, A.; LeHunte, S. *J. Photochem. Photobiol. A* **1997**, *108*, 1.
- (3) Maldotti, A.; Molinari, A.; Amadelli, R. *Chem. Rev.* **2002**, *102*, 3811.
- (4) Giannotti, C.; Legreneur, S.; Watts, O. *Tetrahedron Lett.* **1983**, *24*, 5071.
- (5) Mu, W.; Herrmann, J. M.; Pichat, P. *Catal. Lett.* **1989**, *3*, 73.
- (6) Beaune, O.; Finiels, A.; Geneste, P.; Graffin, P.; Guida, A.; Olive, J. L.; Saeedan, A. *Heterogeneous Catalysis and Fine Chemicals III* **1993**, *78*, 401.
- (7) Boarini, P.; Carassiti, V.; Maldotti, A.; Amadelli, R. *Langmuir* **1998**, *14*, 2080.
- (8) Almquist, C. B.; Biswas, P. *Appl. Catal. A: Gen.* **2001**, *214*, 259.
- (9) Du, P.; Moulijn, J. A.; Mul, G. *J. Catal.* **2006**, *238*, 342.

- (10) Wittenberg, R.; Pradera, M. A.; Navio, J. A. *Langmuir* **1997**, *13*, 2373.
- (11) Pillai, U. R.; Sahle-Demessie, E. *J. Catal.* **2002**, *211*, 434.
- (12) Molinari, A.; Montoncello, M.; Rezala, H.; Maldotti, A. *Photochem. Photobiol. Sci.* **2009**, *8*, 613.
- (13) Yurdakal, S.; Palmisano, G.; Loddo, V.; Alagoz, O.; Augugliaro, V.; Palmisano, L. *Green Chem.* **2009**, *11*, 510.
- (14) Larson, S. A.; Falconer, J. L. *Catal. Lett.* **1997**, *44*, 57.
- (15) Pichat, P. *Catal. Today* **1994**, *19*, 313.
- (16) Aika, K. I.; Lunsford, J. H. *J. Phys. Chem.* **1978**, *82*, 1794.
- (17) Furube, A.; Tamaki, Y.; Murai, M.; Hara, K.; Katoh, R.; Tachiya, M. *J. Am. Chem. Soc.* **2006**, *128*, 416.
- (18) Takita, Y.; Lunsford, J. H. *J. Phys. Chem.* **1979**, *83*, 683.
- (19) Takita, Y.; Iwamoto, M.; Lunsford, J. H. *J. Phys. Chem.* **1980**, *84*, 1710.
- (20) Lunsford, J. H. *Catal. Rev.* **1973**, *8*, 135.
- (21) Anpo, M. *Bull. Chem. Soc. Jpn.* **2004**, *77*, 1427.
- (22) Tsukamoto, D.; Ikeda, M.; Shiraishi, Y.; Hara, T.; Ichikuni, N.; Tanaka, S.; Hirai, T. *Chem. Eur. J.* **2011**, *17*, 9816.
- (23) Ohuchi, T.; Miyatake, T.; Hitomi, Y.; Tanaka, T. *Catal. Today* **2007**, *120*, 233.
- (24) Shishido, T.; Miyatake, T.; Teramura, K.; Hitomi, Y.; Yamashita, H.; Tanaka, T. *J. Phys. Chem. C* **2009**, *113*, 18713.
- (25) Furukawa, S.; Tamura, A.; Shishido, T.; Teramura, K.; Tanaka, T. *Appl. Catal. B: Environ.* **2011**, *110*, 216.
- (26) Furukawa, S.; Ohno, Y.; Shishido, T.; Teramura, K.; Tanaka, T. *Chemphyschem* **2011**, *12*, 2823.
- (27) Jehng, J. M.; Wachs, I. E. *J. Mol. Catal.* **1991**, *67*, 369.
- (28) Ko, E. I.; Weissman, J. G. *Catal. Today* **1990**, *8*, 27.
- (29) Tamura, S.; Kato, K.; Goto, M. *Z. Anorg. Allg. Chem.* **1974**, *410*, 313.
- (30) Tamura, S. *J. Mater. Sci.* **1972**, *7*, 298.
- (31) Frevel, L. K.; Rinn, H. W. *Anal. Chem.* **1955**, *27*, 1329.

- (32) Pittman, R. M.; Bell, A. T. *J. Phys. Chem.* **1993**, *97*, 12178.
- (33) Tsur, Y.; Simakov, D. S. A. *J. Nanopart. Res.* **2008**, *10*, 77.
- (34) Okumura, M.; Coronado, J. M.; Soria, J.; Haruta, M.; Conesa, J. C. *J. Catal.* **2001**, *203*, 168.
- (35) Meriaudeau, P.; Vedrine, J. C. *J. Chem. Soc., Faraday Trans. 2* **1976**, *72*, 472.
- (36) Yamazoe, S.; Okumura, T.; Tanaka, T. *Catal. Today* **2007**, *120*, 220.
- (37) Tench, A. J. *J. Chem. Soc., Faraday Trans. 1* **1972**, *68*, 1181.
- (38) Wong, N. B.; Lunsford, J. H. *J. Chem. Phys.* **1972**, *56*, 2664.
- (39) Einaga, H.; Ogata, A.; Futamura, S.; Ibusuki, T. *Chem. Phys. Lett.* **2001**, *338*, 303.
- (40) Gonzalez-Eliphe, A. R.; Munuera, G.; Soria, J. *J. Chem. Soc., Faraday Trans. 1* **1979**, *75*, 748.
- (41) Murphy, D. M.; Attwood, A. L.; Edwards, J. L.; Egerton, T. A.; Harrison, R. W. *Res. Chem. Intermed.* **2003**, *29*, 449.
- (42) Kiwi, J.; Suss, J. T.; Szapiro, S. *Chem. Phys. Lett.* **1984**, *106*, 135.
- (43) Nosaka, Y.; Nakaoka, Y. *J. Photochem. Photobiol. A* **1997**, *110*, 299.

Summary

The author developed two different types of effective aerobic oxidation system in this thesis; one is the homogeneous system using mononuclear non-heme Fe complexes and the other is the heterogeneous system based on Nb₂O₅ photocatalyst.

In Part I, aerobic oxidation of hydrocarbon using Fe(II)–TPA complexes was established by controlling of spin state and coordination environment. Moreover, effects of nitro-substitution to the Fe(II)–TPA complex on its catalytic activity in oxidation of hydrocarbon and detailed electronic structure were investigated and discussed.

In Chapter 1, aerobic oxidation of hydrocarbons without any reductant using Fe(II)–TPA complexes was achieved by modifying spin state and coordination environment of the complex. The author found that aerobic oxidation of hydrocarbons was efficiently promoted by the Fe(II)–TPA complex, when the Fe center was in the high-spin state. It is noteworthy that the aerobic oxidation proceeded without any reductant, since most of the aerobic oxidation systems catalyzed by heme or nonheme iron complexes require stoichiometric co-reductants. The essential factor in the reaction is the presence of labile coordination sites that provides stable coordination of dioxygen, giving Fe(III)-superoxo species active for the H-atom abstraction; the strong interaction of MeCN with the low-spin iron(II) center would prevent the formation of the Fe(III)-superoxo species, and chloride ion may shorten the life-time of the Fe(III)-superoxo species probably through nucleophilic attack.

In Chapter 2, the author synthesized a series of Fe(II)–TPA complex and its derivatives that have one to three nitro-groups at 4-position of the pyridine ligand, and evaluated the effect of the nitro-groups on their catalytic activity in alkane hydroxylation. The introduction of nitro-group proved to lower the product yields. During the catalytic oxidation, a significant amount of Fe(II) species is present in the cases of nitro-substituted complexes, while the unsubstituted Fe–TPA complex was rapidly oxidized to Fe(III) state. Although theoretical calculations predicted that introducing nitro-groups should facilitate H-atom abstraction from alkane by *cis*-oxo-hydroxo-iron(V) species, the present experimental study demonstrated that such energetically unfavorable species cannot be obtained in the reaction condition.

In Chapter 3, the author investigated the effects of nitro-substitution to the Fe(II)–TPA complex on the electronic structure in more detail from both experimental and theoretical aspects. The introduction of nitro groups on the TPA-type ligand stabilizes the low-spin state of the ferrous complex, which is caused by significant π back-bonding interactions between iron(II) and 4-nitropyridine ligand. The DFT calculation revealed that introducing the nitro groups stabilizes $d\pi$ orbitals more than $d\sigma$ orbitals, which is more prominent with the low-spin state than with the high-spin state.

In summary of Part I, the author studied two important factors during aerobic oxidation processes; activation of molecular oxygen and hydrocarbon by Fe(II)–TPA and active intermediate derived Fe(II)–TPA, respectively. The results obtained in Part I also points out that 1) it is necessary for effective catalysis not only to activate molecular oxygen but also to successfully generate an active intermediate, and that 2) ease of formation of the active intermediate plays a significant role rather than reactivity of the active intermediate.

In Part II, the enhancement in the photocatalytic activity and the selectivity was developed using Nb₂O₅-based photocatalysts from the aspect of kinetics and by inhibition of the formation of active oxygen species, respectively. In addition, a specific photoactivation mechanism discovered in the photocatalysis of Nb₂O₅ was advanced and discussed in detail.

In Chapter 4, the author demonstrated that selective photooxidation of amines to imines proceeded over Nb₂O₅ through a similar reaction mechanism to that of alcohol over Nb₂O₅; oxidative dehydrogenation of amine to corresponding imine via photoactivation of the surface complex consisted of dissociatively adsorbed amine (amide species) and Nb₂O₅. The substrate screening revealed that a variety of amines including primary, secondary, and bicycloamine derivatives were also oxidized to imine. In contrast to alcohol oxidation, a primary imine produced by dehydrogenation of the corresponding primary amine is immediately hydrolyzed into aldehyde and converted to a dimerized imine.

In Chapter 5, it was found that aerobic photooxidation of hydrocarbon proceeded over Nb₂O₅ with higher selectivity than that over TiO₂. However, mechanistic study revealed that the photoactivation mechanism of hydrocarbon over Nb₂O₅ was different from that for alcohol and

amine involving photoactivation of surface complex. The proposed mechanism is typical Langmuir-Hinshelwood mechanism including C–H activation by positive holes and O₂ reduction by excited electrons, followed by combination of the resulting alkyl radical and superoxide. ESR study suggests that the higher selectivity of Nb₂O₅ for partial oxidation products than TiO₂ is due to the absence of O₃⁻, which is highly active for the complete oxidation of hydrocarbons.

In Chapter 6, the author prepared a variety of metal loaded Nb₂O₅ photocatalysts (M/Nb₂O₅; M = Pt, Rh, Ru, Ni, Cu, and Ag) and discovered the positive but counterintuitive effect of Cu on photocatalytic activity in alcohol oxidation in contrast to other metals. The author demonstrated that Cu/Nb₂O₅ catalyst exhibited higher activity than bare Nb₂O₅ without lowering selectivity toward a wide scope of alcohols including primary, secondary, aliphatic and aromatic ones. In particular, 1-phenylethanol was almost quantitatively converted to acetophenone in a solvent-free condition. This is the first example that aerobic photooxidation of alcohol proceeded quantitatively even under solvent-free condition

In Chapter 7, the author investigated the mechanism of alcohol photooxidation over Cu/Nb₂O₅ in detail and elucidated the role of Cu in enhancement of the photocatalytic activity in alcohol oxidation. The reaction mechanism for Cu/Nb₂O₅ is essentially the same as that for bare Nb₂O₅, except that redox of Cu(II)–Cu(I) is involved instead of that of Nb(V)–Nb(IV). The roles of Cu were found to be an effective desorption site (Cu(I)) to promote desorption of the product and a redox promoter to accelerate the conversion from radical intermediate to the product (Cu(II)). The proposed photoactivation mechanism was supported by DFT calculations in a similar fashion to the case of amine oxidation.

In Chapter 8, the author modified the composition of Cu species on Cu/Nb₂O₅ by pretreatment in order to optimize the positive role of Cu in alcohol photooxidation. Photocatalytic activity twice as high as that of as-prepared Cu/Nb₂O₅ was obtained by optimized pretreatment; oxidation at 393 K after the reduction. The photocatalytic activity in alcohol oxidation varied according to the fraction of Cu₂O species estimated by XAFS spectroscopy. The obtained result suggested that the presence of Cu₂O at the outermost layer of the Cu particle as an efficient desorption site was the crucial factor in enhancement of the photocatalytic activity.

In Chapter 9, a series of TiO₂ catalysts covered with Nb₂O₅ (Nb₂O₅/TiO₂, loading of Nb₂O₅;

0–5 mol%) was prepared to inhibit formation of the highly oxidizing oxygen anion radical, O_3^- for selective photocatalytic oxidation. The author demonstrated that selectivity in alcohol photooxidation was enhanced with increase in surface coverage of TiO_2 with Nb_2O_5 . ESR study supported that formation of O_3^- was successfully inhibited upon Nb_2O_5 coating and O_3^- completely disappeared over monolayer coverage (3.5 mol% Nb_2O_5 loading). 3 mol% Nb_2O_5/TiO_2 exhibited higher selectivities than TiO_2 at a comparable conversion level in the oxidation of not only 1-pentanol but also other secondary alcohols such as 2-pentanol, 3-pentanol, cyclohexanol.

As an overview of Part II, the selective photocatalytic oxidation of alcohols, amines, and hydrocarbons using Nb_2O_5 -based photocatalysts was established. Among these systems, molecular oxygen plays different two roles. For oxygenation of hydrocarbon, molecular oxygen literally acts as an oxygen source to be incorporated into substrate. But, for oxidative dehydrogenation of alcohol and amine, molecular oxygen is virtually employed as an acceptor of electrons and protons taken up from substrate. In both cases, however, the achieved high selectivities owe a great deal to the lack of O_3^- over the Nb_2O_5 -based photocatalysts. The result obtained in Part II proves the strategy to inhibit the formation of active oxygen species effective and provides a new promising basis for selective photooxidation. In addition, the photocatalysis of Nb_2O_5 shows some specific photocatalytic properties; the effect of Cu and in-situ doping. The role of Cu discovered and elucidated in this study, promotion of desorption, points out that one should focus attention on not only promotion of charge separation, but also acceleration of a rate-determining process among the overall catalytic cycle even from the viewpoint of photocatalysis. The in-situ doping effect occurs for oxidation of alcohol or amine, whereas the photooxidation of hydrocarbon proceeds only via band gap excitation of Nb_2O_5 . The crucial difference between these two photoactivation systems is whether the substrate is dissociatively adsorbed. This unique photo-activation mechanism by direct electron transition from the surface donor level provides us attractive ways for removing the limit of band gap energy, and utilization of the visible light.

List of Publications

Part I

Chapter 1.

1. Efficient Aerobic Oxidation of Hydrocarbons Promoted by High-Spin Nonheme Fe(II) Complexes Without Any Reductant
Shinya Furukawa, Yutaka Hitomi, Tetsuya Shishido, and Tsunehiro Tanaka
Inorganica Chimica Acta, **2011**, 378, 19.

Chapter 2.

2. Alkane Hydroxylation Catalyzed by a Series of Mononuclear Non-Heme Iron Complexes Containing 4-Nitropyridine Ligands.
Yutaka Hitomi, Shinya Furukawa, Masakazu Higuchi, Tetsuya Shishido, and Tsunehiro Tanaka
Journal of Molecular Catalysis A: Chemical, **2008**, 288, 83.

Chapter 3.

3. π Back-Bonding of Iron(II) Complexes Supported by Tris(pyrid-2-ylmethyl)amine and Its Nitro-Substituted Derivatives
Shinya Furukawa, Yutaka Hitomi, Tetsuya Shishido, Kentaro Teramura, and Tsunehiro Tanaka
The Journal of Physical Chemistry A, **2011**, 115, 13589

Part II

Chapter 4.

4. Selective Amine Oxidation Using Nb₂O₅ Photocatalyst and O₂
Shinya Furukawa, Yasuhiro Ohno, Tetsuya Shishido, Kentaro Teramura,
and Tsunehiro Tanaka
ACS Catalysis, **2011**, *1*, 1150.
5. Mechanistic Study on Selective Photooxidation of Amines over Nb₂O₅:
Direct Electron Transfer from Adsorbed Species to Conduction Band
Shinya Furukawa, Yasuhiro Ohno, Tetsuya Shishido, Kentaro Teramura,
and Tsunehiro Tanaka
To be submitted.

Chapter 5.

6. Reaction Mechanism of Selective Photooxidation of Hydrocarbons over Nb₂O₅
Shinya Furukawa, Tetsuya Shishido, Kentaro Teramura, and Tsunehiro
Tanaka
The Journal of Physical Chemistry C, **2011**, *115*, 19320.

Chapter 6.

7. Solvent-free Aerobic Alcohol Oxidation Using Cu/Nb₂O₅: Green and
Highly Selective Photocatalytic System
Shinya Furukawa, Ayaka Tamura, Tetsuya Shishido, Kentaro Teramura,
and Tsunehiro Tanaka
Applied Catalysis B: Environmental, **2011**, *110*, 216.

Chapter 7

8. Reaction Mechanism and the Role of Copper in the Photooxidation of Alcohol over Cu/Nb₂O₅
Shinya Furukawa, Yasuhiro Ohno, Tetsuya Shishido, Kentaro Teramura, and Tsunehiro Tanaka
ChemPhysChem, **2011**, *12*, 2823.

Chapter 8

9. XAFS Study of Cu/Nb₂O₅ as a Photocatalyst for Alcohol Photooxidation: Correlation between Oxidation State of Cu and Photocatalytic Activity
Shinya Furukawa, Daisuke Tsukio, Tetsuya Shishido, Kentaro Teramura, and Tsunehiro Tanaka
To be submitted.

Chapter 9

10. Photocatalytic Oxidation of Alcohols over TiO₂ covered with Nb₂O₅
Shinya Furukawa, Tetsuya Shishido, Kentaro Teramura, and Tsunehiro Tanaka
ACS Catalysis, in revision.

Publications not Included in the Present Thesis

11. Alkane Metathesis by Tandem Catalytic System: Dehydrogenation and Hydrogenation over PtSn/Al₂O₃, and Metathesis over Re₂O₇/Al₂O₃
Shinya Furukawa, Tetsuya Shishido, Kentaro Teramura, and Tsunehiro Tanaka
Submitted.